



UNIVERSITEIT VAN PRETORIA  
UNIVERSITY OF PRETORIA  
YUNIBESITHI YA PRETORIA

# Effect of Carbide Additives on the Structure and Behaviour of Polycrystalline Diamond

By  
Kaveshini Francis

Submitted in fulfilment of the requirements for the degree of  
Doctor of Philosophy

Department of Materials Science and Metallurgical Engineering,  
University of Pretoria

Supervisors: Prof. J de Villiers and Prof. W Stumpf

2017

© University of Pretoria

## **ABSTRACT**

*It is widely known that the addition of vanadium carbide to tungsten carbide significantly enhances the performance of the tungsten carbide tool by improving the hardness as well as the abrasion resistance of the material. This thesis describes the addition of different concentrations of vanadium carbide to polycrystalline diamond (PCD), and investigates the microstructure and behaviour of the PCD. It was observed that a (V,W)C<sub>x</sub> mixed carbide phase was formed in the PCD together with residual vanadium carbide in solution with the cobalt binder. The (V,W)C<sub>x</sub> carbide deposited predominantly at the WC-Co/diamond interface. The 1wt% vanadium carbide enhanced PCD showed the presence of tungsten carbide evenly distributed within the PCD, whereas the 3wt% vanadium carbide enhanced PCD and the 5wt% vanadium carbide enhanced PCD revealed the absence of tungsten carbide in the sintered PCD.*

*Both TEM and SEM analysis confirmed the presence of the (V,W)C<sub>x</sub> mixed carbide phase within the PCD. The sandstone milling test revealed the vanadium carbide enhanced PCD to be more thermally stable with approximately 40% improvement in performance, whilst both the Paarl Granite Turning test and Vertical borer tests showed the vanadium carbide enhanced PCD to be more wear resistant than the standard cobalt based PCD.*

*Heat treatment experiments were undertaken to determine the thermal stability of the (V,W)C<sub>x</sub> mixed carbide phase. Using hot stage XRD, the (V,W)C<sub>x</sub> mixed carbide phase was found to be stable up to a temperature of 1100 °C. In addition, the vanadium carbide enhanced PCD showed a reduced amount of graphite being formed during hot stage XRD analysis. This suggests that the vanadium carbide enhanced PCD would be more thermally stable during tool use as compared to the conventional PCD.*

*Other carbide additives such as molybdenum carbide, chromium carbide and titanium carbide were also investigated. The Cr<sub>3</sub>C<sub>2</sub> did not seem to react with the WC in the PCD to form a mixed carbide. The addition of titanium carbide to the vanadium carbide enhanced PCD led to the formation of a proposed mixed (Ti,V,W)C<sub>x</sub> phase. Vertical borer test results showed that the VC–TiC enhanced PCD exhibited superior durability.*

*The addition of vanadium carbide and chromium carbide to fine grained PCD was also investigated in terms of abnormal grain growth (AGG). It was observed that the grain size of the AGG in the standard PCD ranged from 100-400  $\mu\text{m}$  with an AGG region of 250-300  $\mu\text{m}$ , the vanadium carbide doped PCD showed an AGG size of 100-200  $\mu\text{m}$  with an AGG region of 250-300  $\mu\text{m}$  and the chromium carbide doped PCD showed an AGG size of 100-250  $\mu\text{m}$  with an AGG region of 650-700  $\mu\text{m}$ . The exaggerated AGG present in the chromium carbide doped PCD was likely due to the increase in the carbon activity in the PCD.*

*From this body of work, two patents were filed. A patent was filed by Kaveshini Naidoo et al. with the publication number: US2010285335A1 that described the performance improvement of the vanadium carbide enhanced PCD. An additional patent was filed by Kaveshini Naidoo et al. with the publication number: US2015151410A1 that described the performance improvement of the VC-TiC enhanced PCD.*

## **ACKNOWLEDGEMENTS**

Professor Johan de Villiers, the promotor of the work. A special thank you for the constructive discussions and for motivating me to complete the thesis.

Professor Waldo Stumpf, for affording me the time to complete the work, and believing in the merit of the work.

Element Six, for supporting the work and providing me with the resources to complete the work.

Mr Brett Lancaster, for helping me with the hot stage XRD work and for the fruitful discussions regarding my findings.

Dr Johan Westraadt, for the TEM work performed on my samples and for being very helpful in general.

Ms Zandi Mkhonto, for helping me with the various analyses on my samples, much appreciated.

Ms Anine Ras (deceased), a very dear friend, for helping me to structure my thesis. Thank you for believing in me, motivating me, discussing my findings, and being an inspiration to me.

And finally, a special thank you to my family and friends for believing in me, holding me accountable for completing the thesis, and for offering me both support and advice.

### Declaration

I declare that this thesis is my own unaided work, except where otherwise acknowledged. It is being submitted for the degree of Doctor of Philosophy at the University of Pretoria. It has not been submitted before for any degree or examination at any other university

Signed: .....

Date: .....

## **DEDICATION**

This work is dedicated to my mom who taught me the value of patience, hard work and perseverance. You were always a pillar of strength in my life and I finally accomplished one of the dreams you had for me. You will always remain close to my heart.

Love always.

## Table of Contents

### Chapter One: Polycrystalline Diamond

1.1 Background .....	1
1.2 Manufacture of PCD .....	7
1.2.1 Types of PCD .....	14
1.2.2 Limitations of PCD .....	15
1.2.3 Graphitisation .....	16
1.2.4 Oxidation .....	17
1.2.5 Thermal Expansion .....	18
1.3 Metal Carbide additions to Tungsten Carbide and Steel .....	19
1.3.1 Metal Carbide additions to Steel .....	19
1.3.2 Metal Carbide additions to Tungsten Carbide .....	20
1.3.3 Stability, Solubility and Wettability of Metal Carbides .....	22
1.4 Metal Carbide additions to Polycrystalline Diamond .....	27
1.4.1 Additives to PCD .....	27
1.4.2 Displacement of Cobalt .....	28
1.4.3 Oxidation of Cobalt .....	28
1.4.4 CTE Mismatch .....	29
1.4.5 Promote Diamond Intergrowth .....	29
1.4.6 Precipitation Hardening .....	29
1.4.7 Stabilisation of the cobalt phase .....	30
1.5 Aim of the Study .....	31
1.6 Hypotheses .....	32

### Chapter Two: Addition of Vanadium Carbide to PCD

2.1 Background .....	34
2.2 Experimental .....	35
2.3 Brief description of Analysis Techniques .....	39
2.3.1 X-ray Diffraction (XRD) .....	39
2.3.2 Scanning Electron Microscopy (SEM) .....	41
2.3.3 Malvern Analysis .....	42

2.3.4 X-ray Tomography .....	42
2.3.5 Transmission Electron Microscopy (TEM).....	43
2.4 Results .....	44
2.4.1 XRD analysis of powder .....	44
2.4.2 Sintering of PCD .....	48
2.4.2.1 Experiment 1 .....	48
2.4.2.2 Experiment 2.....	51
2.4.2.3 Sintering of PCD with 3wt% (1.85vol%) VC .....	56
2.4.3 PCD sintered with varying VC concentration .....	73
2.4.4 Behaviour Testing .....	79
2.5 Discussion .....	90
2.6 Conclusion.....	97
2.7 Recommendations.....	99

### Chapter Three: Heat Treatment of PCD

3.1 Background .....	100
3.2 Experiments .....	101
3.2.1 Terminated Press Runs .....	101
3.2.2 Heat treatment of the VC and diamond powder mix.....	101
3.2.3 Hot Stage XRD Analysis .....	102
3.3 Results .....	103
3.3.1 Terminated Press Runs .....	103
3.3.1.1 Sintering time reduced to 10%.....	103
3.3.1.2 Sintering time reduced to 50% .....	104
3.3.2 Heat treatment of the VC and diamond powder mix.....	106
3.3.3 Hot stage XRD analysis .....	113
3.3.3.1 Standard PCD.....	113
3.3.3.2 5wt% VC enhanced PCD.....	117
3.4 Discussion .....	122
3.5 Conclusion.....	127
3.6 Recommendation .....	127



## Chapter Four: Addition of Other Carbides to PCD

4.1 Background .....	128
4.2 Experimental .....	129
4.3 Results .....	129
4.3.1 Mo <sub>2</sub> C addition to PCD .....	129
4.3.2 TiC addition to PCD .....	136
4.3.3 Cr <sub>3</sub> C <sub>2</sub> addition to PCD .....	146
4.3.4 TiC-VC addition to PCD .....	153
4.3.5 Image Analysis of PCD containing various Carbides .....	159
4.3.6 Vertical Borer testing of VC-TiC enhanced PCD .....	160
4.4 Discussion .....	161
4.5 Conclusion.....	166
4.6 Recommendations.....	167

## Chapter Five: Grain Growth of PCD

5.1 Background .....	168
5.2 Experimental .....	171
5.3 Results .....	172
5.3.1 Analysis of the 0.5 μm PCD Compact.....	172
5.3.2 Analysis of the 0.5 μm PCD Compact containing 3wt% VC .....	175
5.3.3 Analysis of the 0.5 μm PCD Compact containing 3wt% Cr <sub>3</sub> C <sub>2</sub> .....	179
5.4 Discussion .....	182
5.5 Conclusion.....	185
5.6 Recommendations.....	186

## Chapter Six: Conclusion and Recommendations

6.1 Summary and Conclusions.....	187
6.2 Recommendations.....	190
REFERENCES .....	192
APPENDIX ONE .....	204
APPENDIX TWO .....	206
APPENDIX THREE.....	212

APPENDIX FOUR.....218  
APPENDIX FIVE.....224  
APPENDIX SIX.....230  
APPENDIX SEVEN.....236

## LIST OF FIGURES

Figure 1.1: Roller cone bit .....	1
Figure 1.2: Comparison of footage drilled for Diamond bits and Tricone bits .....	2
Figure 1.3: Average Bit Life for Roller cone bits and Diamond bits .....	3
Figure 1.4: Illustration showing the various diamond synthesis regimes .....	3
Figure 1.5: PCD insert .....	4
Figure 1.6: Land-based Oil Rig .....	5
Figure 1.7: Off shore drilling rig .....	6
Figure 1.8: Drill Bit .....	7
Figure 1.9: Brazing of PCD inserts into a bit .....	7
Figure 1.10: Schematic showing formation of a PCD cutter .....	8
Figure 1.11: Carbide substrate showing an example of a non-planar interface .....	9
Figure 1.12: Effect of nitrogen on the colour of the diamond crystals .....	10
Figure 1.13: Stages of Sintering .....	11
Figure 1.14: Frenkel and Kuczynski Model .....	12
Figure 1.15: Schematic showing infiltration of the cobalt binder into the PCD table: (a) Diamond particles placed on top of the WC substrate, (b) Infiltration of cobalt from the substrate into the diamond powder bed, (c) Liquid phase sintering of the diamond particles forming a polycrystalline compact .....	12
Figure 1.16: Scanning electron microstructure (SEM) of a typical PCD showing the presence of diamond appearing as dark grey particles, cobalt binder appearing as the light grey phase and small tungsten carbide particles shown as the bright white phase ..	13
Figure 1.17: PCD interface structure .....	14
Figure 1.18: Schematic showing the primary problems associated with PCD, i.e. the inter-relationship between graphitisation, oxidation and thermal expansion .....	15
Figure 1.19: Image showing micro-cracking of PCD .....	17
Figure 1.20: Gibbs Free Energy of Formation for various Carbides, normalised to one metal atom .....	22
Figure 1.21: Enthalpy of formation wetted by the cobalt eutectic melt .....	24
Figure 1.22: Graph showing the d orbital distribution of different metals .....	26
Figure 1.23: Schematic of carbide particles deposited at the diamond-binder interface ..	28
Figure 1.24: Co-W Phase Diagram .....	31

Figure 2.1: Pre-composite assembly for the sintering of solid PCD .....	37
Figure 2.2: Pre-composite assembly for the sintering of PCD infiltrated with a first layer of 3wt% VC powder and a second layer of 20wt% Co foil.....	37
Figure 2.3: Pre-composite assembly of PCD admixed with 3wt% VC and sintered on a WC substrate .....	38
Figure 2.4: Schematic of a high pressure vehicle .....	39
Figure 2.5: Belt Press.....	39
Figure 2.6: Schematic of X-Ray Diffraction .....	40
Figure 2.7: Schematic of the scanning electron microscope (SEM).....	41
Figure 2.8: Laser Diffraction Particle Sizing .....	42
Figure 2.9: Schematic of the principle of X-ray tomography.....	43
Figure 2.10: Schematic of a Transmission electron microscope (TEM) .....	44
Figure 2.11: X-ray Diffraction pattern for the vanadium carbide powder .....	45
Figure 2.12: SEM microstructures of the powder mix consisting predominantly of diamond, and a combination of VC, WC and cobalt – A (500x mag), B (1000x mag), C (2000x mag) and D (4000x mag) .....	46
Figure 2.13: Various components of the powder mix .....	46
Figure 2.14: Malvern distribution of the VC powder .....	47
Figure 2.15: Malvern distribution of the diamond-VC powder mix.....	47
Figure 2.16: Microstructural images of the standard PCD: A (bottom PCD, i.e. PCD near the foil), B (bulk PCD), C (top PCD).....	48
Figure 2.17: X-ray image of the standard PCD .....	49
Figure 2.18: EDS map of the standard solid PCD, showing the concentration of carbon, oxygen, cobalt and tungsten as a function of PCD distance .....	50
Figure 2.19: XRD pattern of the standard solid PCD .....	51
Figure 2.20: Microstructural images of the PCD infiltrated with VC: A (bottom PCD, i.e. PCD near the foil), B (bulk PCD), C (top PCD) .....	52
Figure 2.21: Image showing the VC layer at the bottom of the PCD.....	52
Figure 2.22: Image showing the EDS spectrum of the VC layer, identified by ‘Spectrum 2’ .....	53
Figure 2.23: EDS Profile for PCD infiltrated with VC powder, showing the concentration of carbon, cobalt, tungsten and vanadium as a function of PCD distance .....	53

Figure 2.24: XRD pattern for the PCD infiltrated with VC powder .....	55
Figure 2.25: Microstructural images of the standard PCD and the PCD containing 3wt% VC: A (interface structure of the standard PCD), B (interface structure of the PCD containing 3wt% VC), C (above interface structure of the standard PCD), D (above interface structure of the PCD containing 3wt% VC), E (top surface microstructure of the standard PCD), F (top surface microstructure of the PCD containing 3wt% VC) .....	58
Figure 2.26: EDS analysis of the standard PCD .....	59
Figure 2.27: EDS analysis of the PCD containing 3wt% VC .....	60
Figure 2.28: Image Analysis of the Std PCD and PCD containing 3wt% VC: A (diamond area comparison), B (binder area comparison), C (diamond contiguity comparison) and D (WC phase area comparison) .....	62
Figure 2.29: X-ray image of the sintered samples: A (Standard PCD) and B (PCD containing 3wt% VC).....	63
Figure 2.30: HAADF (High Angle Annular Dark Field) STEM image and EDS analysis of the binder in the PCD containing 3wt% VC.....	64
Figure 2.31: TEM mapping of the binder pool in the PCD containing 3wt% VC.....	65
Figure 2.32: TEM Mapping of binder pools for the PCD containing 3wt% VC.....	66
Figure 2.33: Stem HAADF image of the binder stitching and the TEM mapping of the area .....	67
Figure 2.34: XRD patterns of the sintered PCD: A (XRD pattern of the standard PCD), B (XRD pattern of the PCD containing 3wt% VC) and C (XRD pattern of the overlay of the two samples).....	69
Figure 2.35: XRD pattern showing the shift in the cobalt peak position .....	70
Figure 2.36: XRF analysis of the surface of the PCD containing 3wt% VC showing the four different quadrants .....	72
Figure 2.37: Microstructural comparisons: A (Std PCD), B (PCD containing 1wt% VC), C (PCD containing 3wt% VC) and D (PCD containing 5wt% VC).....	74
Figure 2.38: Image analysis results: A (Diamond Area), B (Binder Area), C (Diamond Contiguity), D (WC phase area) and E (Binder pool size).....	75
Figure 2.39: X-ray images: A (standard PCD), B (PCD containing 1wt% VC), C (PCD containing 3wt% VC) and D (PCD containing 5wt% VC) .....	76

Figure 2.40: XRD Patterns for PCD containing vanadium carbide: A (PCD containing 1wt% VC), B (PCD containing 3wt% VC) and C (PCD containing 5wt% VC) .....	78
Figure 2.41: Schematic of milling test .....	80
Figure 2.42: Schematic of PCD cutter removing rock material as it cuts across the rock	80
Figure 2.43: Sandstone Milling Test.....	81
Figure 2.44: Schematic of the Paarl Granite Turning Test .....	81
Figure 2.45: Equipment used for Paarl Granite Turning Test.....	82
Figure 2.46: Paarl Granite test results of the standard PCD and the PCD containing VC	83
Figure 2.47: Optical images of the wear scar after 45 min exposure to PGT testing: (A) Standard PCD, (B) PCD containing 5wt% VC.....	84
Figure 2.48: SEM images of the Standard PCD after 45min exposure to PGT testing: (A) Backscatter image of the wear scar, (B) Secondary image of the wear scar .....	84
Figure 2.49: SEM images of the PCD containing 5wt% VC after 45 min exposure to PGT testing: (A) Backscatter image of the wear scar, (B) Secondary image of the wear scar ..	85
Figure 2.50: SEM images of the top surface of the wear scar: (A) Standard PCD, (B) PCD containing 5wt% VC .....	86
Figure 2.51: Overlay of the XRD patterns for the Standard PCD and PCD containing 5wt% VC after exposure to 45 min wear testing (phases taken from the ICSD database) .....	87
Figure 2.52: Overlay of the XRD patterns showing graphitisation of the Standard PCD and PCD containing 5wt% VC after exposure to 45min wear testing.....	88
Figure 2.53: Schematic of the VB test.....	89
Figure 2.54: VB comparison between the standard PCD and PCD containing 3wt% VC	89
Figure 2.55: Image of the wear scar: (a) Standard PCD, (b) VC enhanced PCD.....	90
Figure 2.56: Schematic of carbide particles deposited at the diamond-binder interface ..	92
Figure 2.57: Ratio of V:W in the mixed carbide - measured using EDS analysis .....	93
Figure 2.58: V-W-C ternary phase diagram showing the formation of the (V,W)Cx mixed carbide .....	94
Figure 2.59: Cobalt peak shift .....	95
Figure 2.60: Graph illustrating the addition of VC to carbon steel and the effect on the overall hardness of the tool .....	96
Figure 3.1: Heat treatment of diamond powder in a tube furnace .....	102

Figure 3.2: SEM microstructure of the VC enhanced PCD sintered at 10% of the original sintering time.....	103
Figure 3.3: EDS analysis of the binder pool.....	104
Figure 3.4: SEM microstructure of the 3wt% VC enhanced PCD sintered at 50% of the original sintering time .....	105
Figure 3.5: EDS analysis of a carbide particle .....	106
Figure 3.6: PCD bulk showing presence of cracks.....	106
Figure 3.7: SEM microstructure of the powder mixture containing VC, WC, Co and diamond at room temperature.....	107
Figure 3.8: SEM microstructure of the powder mixture containing VC, WC, Co and diamond post heat treatment at 1200 °C .....	108
Figure 3.9: XRD pattern of the powder mixture containing VC, W, Co and diamond post heat treatment at 1200 °C .....	109
Figure 3.10: SEM microstructure of the powder mixture containing VC, WC, Co and diamond post heat treatment at 1300 °C .....	110
Figure 3.11: XRD pattern of powder mixture containing VC, WC, Co and diamond post heat treatment at 1300 °C .....	110
Figure 3.12: SEM microstructure of the powder mixture containing VC, WC, Co and diamond post heat treatment at 1400 °C .....	111
Figure 3.13: XRD pattern of powder mixture containing VC, WC, Co and diamond post heat treatment at 1400 °C .....	111
Figure 3.14: XRD quantification of the powder mixture containing VC, WC, Co and diamond: (A) Heat treated powder mixture at 1200 °C, (B) Heat treated powder mixture at 1400 °C.....	112
Figure 3.15: XRD pattern of the standard PCD at 25 °C .....	113
Figure 3.16: XRD pattern of the standard PCD at 750 °C.....	114
Figure 3.17: XRD pattern of the standard PCD at 800 °C .....	115
Figure 3.18: XRD pattern of the standard PCD at 950 °C.....	115
Figure 3.19: Optical image of the PCD after heat treatment at 950 °C .....	116
Figure 3.20: SEM image of the surface of the standard PCD post heat treatment at 950 °C.....	117

Figure 3.21: EDS analysis of the surface of the standard PCD post heat treatment at 950 °C .....	117
Figure 3.22: XRD pattern of the 5wt% VC enhanced PCD at room temperature .....	118
Figure 3.23: XRD pattern of the 5wt% VC enhanced PCD at 950 °C .....	120
Figure 3.24: XRD pattern of the 5wt% VC enhanced PCD at 1000 °C .....	120
Figure 3.25: XRD pattern of the 5wt% VC enhanced PCD at 1100 °C .....	120
Figure 3.26: XRD pattern of the 5wt% VC enhanced PCD at 25 °C (post heat treatment) .....	121
Figure 3.27: Co-V Phase Diagram [104] .....	121
Figure 3.28: SEM image of the VC enhanced PCD post heat treatment.....	122
Figure 3.29: XRD pattern showing the overlay of the $C_4V_{3.2}W_{0.8}$ and $C_7V_8$ peaks as a function of temperature .....	123
Figure 3.30: Ratio of $C_4V_{3.2}W_{0.8}:C_7V_8$ in the 5wt% VC – diamond powder mix exposed to different temperatures .....	124
Figure 3.31: Model showing the proposed formation of the (V,W)C <sub>x</sub> mixed carbide.....	125
Figure 3.32: TEM mapping of the binder pool in the PCD containing 3wt% VC.....	125
Figure 3.33: XRD overlay of the standard PCD and 5wt% VC enhanced PCD.....	126
Figure 4.1: SEM microstructures of PCD containing 3wt% Mo <sub>2</sub> C .....	130
Figure 4.2: SEM microstructure of PCD containing 3wt% Mo <sub>2</sub> C: (a) microstructure of the PCD showing binder pools, (b) and (c) EDS analysis of binder pools showing the presence of Mo <sub>2</sub> C .....	131
Figure 4.3: XRD pattern of PCD containing 3wt% Mo <sub>2</sub> C taken at 25 °C .....	132
Figure 4.4: XRD quantification of the PCD containing 3wt% Mo <sub>2</sub> C.....	133
Figure 4.5: Mo-W-C Ternary Phase Diagram [89].....	133
Figure 4.6: XRD pattern of 3wt% enhanced Mo <sub>2</sub> C PCD taken at 950 °C.....	135
Figure 4.7: XRD pattern of 3wt% enhanced Mo <sub>2</sub> C PCD taken at 25 °C post heat treatment.....	135
Figure 4.8: SEM and EDS analysis of the Mo <sub>2</sub> C enhanced PCD post heat treatment ...	136
Figure 4.9: SEM microstructure of PCD containing 3wt% TiC .....	137
Figure 4.10: SEM microstructure of a binder pool in the 3wt% TiC enhanced PCD: (a) microstructure of the binder pool, (b) EDS spectrum of the TiC carbide particulate, (c) EDS spectrum of WC deposit .....	138



Figure 4.11: XRD pattern of PCD containing 3wt% TiC taken at 25 °C .....	140
Figure 4.12: XRD quantification of the PCD containing 3wt% TiC .....	140
Figure 4.13: XRD pattern of 3wt% enhanced TiC taken at 900 °C.....	142
Figure 4.14: XRD pattern of 3wt% enhanced TiC taken at 1000 °C.....	142
Figure 4.15: XRD pattern of 3wt% enhanced TiC taken at 1100 °C.....	143
Figure 4.16: XRD pattern of 3wt% enhanced TiC taken at 25 °C post heat treatment ...	143
Figure 4.17: XRD pattern of 3wt% enhanced TiC – overlay of the diamond peak .....	144
Figure 4.18: SEM and EDS analysis of the TiC enhanced PCD post heat treatment ....	145
Figure 4.19: SEM microstructure of PCD containing 3wt% Cr <sub>3</sub> C <sub>2</sub> .....	146
Figure 4.20: EDS Spectra of the binder pools for the Cr <sub>3</sub> C <sub>2</sub> enhanced PCD .....	147
Figure 4.21: XRD pattern of PCD containing 3wt% Cr <sub>3</sub> C <sub>2</sub> .....	148
Figure 4.22: XRD quantification of the PCD containing 3wt% Cr <sub>3</sub> C <sub>2</sub> .....	149
Figure 4.23: XRD pattern of PCD containing 3wt% Cr <sub>3</sub> C <sub>2</sub> taken at 700 °C .....	151
Figure 4.24: XRD pattern of PCD containing 3wt% Cr <sub>3</sub> C <sub>2</sub> taken at 750 °C.....	151
Figure 4.25: XRD pattern of PCD containing 3wt% Cr <sub>3</sub> C <sub>2</sub> taken at 1100 °C .....	152
Figure 4.26: XRD overlay of the CoO <sub>4</sub> W peak at different temperatures .....	152
Figure 4.27: SEM and EDS analysis of the Cr <sub>3</sub> C <sub>2</sub> enhanced PCD post heat treatment .	153
Figure 4.28: SEM microstructures of PCD containing 1.5wt% TiC and 1.5wt% VC .....	154
Figure 4.29: XRD pattern of PCD containing 1.5wt% VC and 1.5wt% TiC.....	155
Figure 4.30: XRD pattern of the C <sub>2</sub> TiV and C <sub>2</sub> TiW phases showing peak shift.....	155
Figure 4.31: XRD pattern of PCD containing 1.5wt% VC and 1.5wt% TiC taken at 25°C post heat treatment .....	158
Figure 4.32: SEM and EDS analysis of the VC-TiC enhanced PCD post heat treatment .....	158
Figure 4.33: Image Analysis Data for PCD containing different carbides.....	160
Figure 4.34: Graph showing the vertical borer comparison between the standard PCD, VC enhanced PCD and VC-TiC enhanced PCD.....	161
Figure 4.35: Optical images of the wear scar post VB: (a) Standard PCD, (b) VC enhanced PCD, (c) VC-TiC enhanced PCD.....	161
Figure 4.36: XRD overlay of the diamond peak at room temperature (blue), 1100 °C (green) and at 25 °C post heat treatment (red) for the 3wt% Mo <sub>2</sub> C enhanced PCD .....	162

Figure 4.37: SEM comparison of the microstructures post heat treatment: (a) Mo <sub>2</sub> C enhanced PCD, (b) TiC enhanced PCD and (c) Cr <sub>3</sub> C <sub>2</sub> enhanced PCD .....	163
Figure 4.38: Overlay of the graphite (002) peak appearing in the VC-TiC enhanced PCD and in the VC enhanced PCD .....	164
Figure 4.39: Wetting of Metallic carbides by liquid cobalt [60].....	165
Figure 5.1: Continuous and Discontinuous (abnormal) grain growth .....	169
Figure 5.2: Optical image of the 0.5 μm sintered PCD showing areas of abnormal grain growth (AGG) and normal grain growth (NGG) of the diamond crystallites.....	173
Figure 5.3: SEM image of the 0.5 μm sintered PCD compact showing AGG at the WC-Co/diamond interface: (a) AGG at the interface, (b) Measurement of grain size.....	174
Figure 5.4: SEM image of 0.5 μm sintered PCD showing normal grain growth: (a) Bulk PCD, (b) Measurement of grains .....	174
Figure 5.5: SEM image of 0.5 μm sintered PCD showing large grains in the AGG region .....	175
Figure 5.6: Optical image of the 0.5 μm sintered PCD doped with 3wt% VC .....	176
Figure 5.7: SEM image of the 0.5 μm sintered PCD compact doped with 3wt% VC, showing AGG at the WC-Co/diamond interface: (a) AGG at the interface, (b) Measurement of grain size.....	177
Figure 5.8: SEM image of 0.5 μm sintered PCD doped with 3wt% VC showing normal grain growth .....	178
Figure 5.9: SEM image of 0.5 μm sintered PCD doped with 3wt% VC showing large grains in the AGG region.....	178
Figure 5.10: Optical image of the 0.5 μm sintered PCD doped with 3wt% Cr <sub>3</sub> C <sub>2</sub> .....	179
Figure 5.11: SEM image of the 0.5 μm sintered PCD compact doped with 3wt% Cr <sub>3</sub> C <sub>2</sub> , showing AGG at the WC-Co/diamond interface: (a) AGG at the interface, (b) Measurement of grain size.....	180
Figure 5.12: SEM image of 0.5 μm sintered PCD doped with 3wt% Cr <sub>3</sub> C <sub>2</sub> showing normal grain growth .....	181
Figure 5.13: SEM image of 0.5 μm sintered PCD doped with 3wt% Cr <sub>3</sub> C <sub>2</sub> showing large grains in the AGG region.....	181
Figure 5.14: Solubility curve of diamond in the cobalt liquid [140].....	182

Figure 5.15: AGG comparison of: (a) Std PCD, (b) VC doped PCD and (c) Cr<sub>3</sub>C<sub>2</sub> doped PCD ..... 184

Figure 5.16: TEM analysis of the 3wt% VC addition to coarse grain PCD ..... 184

## LIST OF TABLES

Table 1.1: Coefficient of Linear Expansion for various metals, values taken at room temperature.....	18
Table 1.2: Wetting angle of various metals with diamond .....	26
Table 1.3: Data showing solubility of different metals in cobalt at 1400 °C .....	27
Table 1.4: Micro Hardness of Metal Carbides .....	30
Table 2.1: Matrix of experiments carried out on solid PCD .....	36
Table 2.2: Average EDS values for the elements in the solid PCD (Standard PCD) .....	50
Table 2.3: EDS Analysis of the VC Phase and the (V,W)C <sub>x</sub> Phase .....	54
Table 2.4: Average EDS values for the elements in the PCD infiltrated with VC .....	55
Table 2.5: ICP results showing Co and W content for solid sintered PCD .....	56
Table 2.6: EDS analysis of the binder pool showing the ratio of V:W .....	60
Table 2.7: EDS Quantification of the binder pools using the TEM .....	66
Table 2.8: XRD Data for the standard PCD and the PCD containing 3wt% VC .....	70
Table 2.9: Parameters used for the calculation of molar volume .....	71
Table 2.10: Volume Data for the various sintering reactions .....	72
Table 2.11: XRF analysis results for the PCD containing 3wt% VC .....	73
Table 2.12: Rietveld Analysis of PCD containing various VC concentrations .....	79
Table 2.13: EDS analysis of the wear scar area for the standard PCD .....	85
Table 2.14: EDS analysis of the wear scar area of the PCD containing 5wt% VC .....	86
Table 2.15: Measure of graphitisation from the XRD patterns for the Standard PCD and PCD containing 5wt% VC after exposure to 45min wear testing.....	88
Table 2.16: Peak positions for shift of cobalt peak .....	95
Table 2.17: Hardness measurements of PCD components .....	97
Table 3.1: Hot Stage XRD parameters.....	102
Table 3.2: XRD phases present in the 5wt% VC enhanced PCD during heat treatment	119
Table 3.3: EDS Analysis of the various phases in the heat treated PCD .....	122
Table 4.1: Source and Particle size of the various carbide powders .....	129
Table 4.2: EDS semi-quantification of the PCD binder pools in the 3wt% Mo <sub>2</sub> C enhanced PCD .....	132
Table 4.3: XRD phases present in the Mo <sub>2</sub> C enhanced PCD during heat treatment .....	134

Table 4.4: EDS analysis of the various phases in the heat treated Mo <sub>2</sub> C enhanced PCD .....	136
Table 4.5: EDS data for the images shown in Figure 4.43 .....	139
Table 4.6: EDS analysis (atomic %) of the binder pools .....	139
Table 4.7: XRD phases present in the TiC enhanced PCD during heat treatment.....	141
Table 4.8: XRD phases present in the TiC enhanced PCD during heat treatment.....	145
Table 4.9: EDS Analysis of the various phases in the heat treated TiC enhanced heat treated PCD .....	146
Table 4.10: EDS data for the spectra shown in Figure 4.51 .....	148
Table 4.11: XRD phases present in the Cr <sub>3</sub> C <sub>2</sub> enhanced PCD during heat treatment ...	150
Table 4.12: EDS Analysis of the various phases in the heat treated Cr <sub>3</sub> C <sub>2</sub> enhanced heat treated PCD .....	153
Table 4.13: EDS Analysis of the PCD containing 1.5wt% TiC and 1.5wt% VC.....	154
Table 4.14: XRD phases present in the VC-TiC enhanced PCD during heat treatment	157
Table 4.15: EDS Analysis of the various phases in the heat treated VC-TiC enhanced heat treated PCD .....	158
Table 4.16: Micro Hardness of Metal Carbides .....	166

## LIST OF ABBREVIATIONS

PCD	Polycrystalline Diamond
GE	General Electric
SEM	Scanning Electron Microscope
CTE	Coefficient of Thermal Expansion
WC	Tungsten Carbide
VC	Vanadium Carbide
TiC	Titanium carbide
Cr <sub>3</sub> C <sub>2</sub>	Chromium Carbide
MoC	Molybdenum Carbide
XRD	X-Ray Diffraction
XRF	X-Ray Fluorescence
ICP	Inductively Coupled Plasma
TEM	Transmission Electron Microscope
NbC	Niobium Carbide
Fcc	Face centred Cubic
Bcc	Body Centred Cubic
Co	Cobalt
PGT	Paarl Granite Turning
VB	Vertical Borer
EDM	Electro Discharge Machining
EDS	Energy Dispersive Spectroscopy
IA	Image Analysis
SiO <sub>2</sub>	Silica Oxide
RIR	Reference Intensity Ratio
HAADF	High Angle Annular Dark Field
LSW	Lifshitz, Slyozov and Wagner
ICSD	Inorganic Crystal Structure Database

# CHAPTER ONE

## POLYCRYSTALLINE DIAMOND (PCD)

### 1.1 Background

Polycrystalline diamond (PCD) is predominantly used for oil and gas drilling applications [1] [2]. It is believed that the Chinese knew the art of drilling several hundred feet of rock back in 1700 BC [3]. They would pound a single diamond stone into a suitable brass alloy, which acted as a tool holder. This was a method to hold the diamond and manually impact the rock without shattering the brittle diamond. Hundreds of workers would 'drill' man-sized holes, mostly over 70 m (230 ft) in depth, to gain access to fresh water.

Prior to the introduction of PCD inserts for drilling applications, a roller cone bit was effectively used (refer to Figure 1.1). Roller cone bits cut rock using a 'crushing' action whereas PCD bits cut rock using a 'shearing' action. PCD bits cost up to five times more than conventional bits, the PCD bits must therefore provide outstanding performance to offset the bit costs [4].

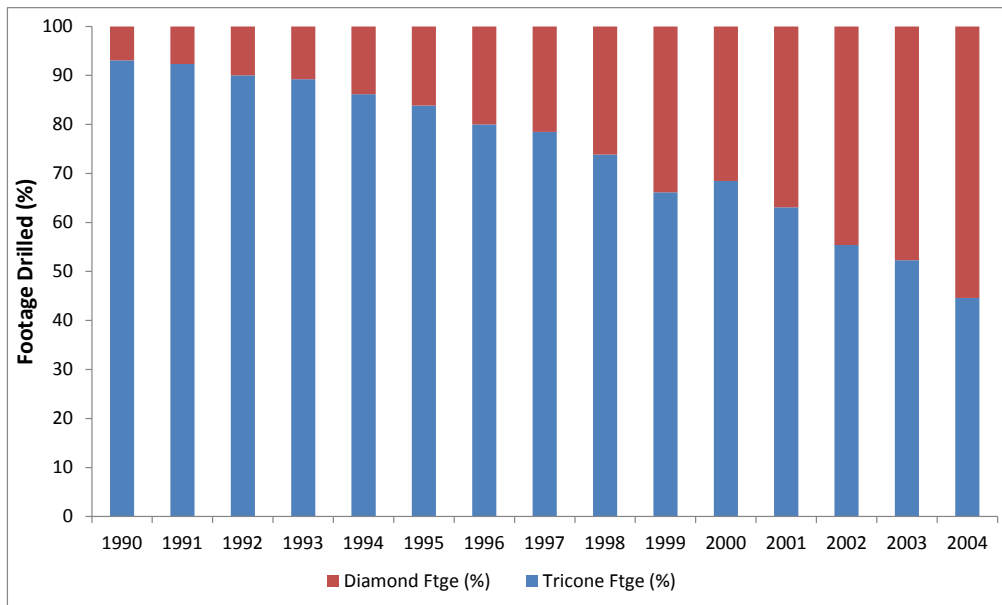


**Figure 1.1: Roller cone bit [5]**

The advent of PCD has greatly improved the speed, efficiency and effectiveness of oil and gas drilling over the past 30 years. PCD cutters were first developed by General Electric (GE) in 1973 and since then have revolutionized the oil and gas industry [ [6], [7]].

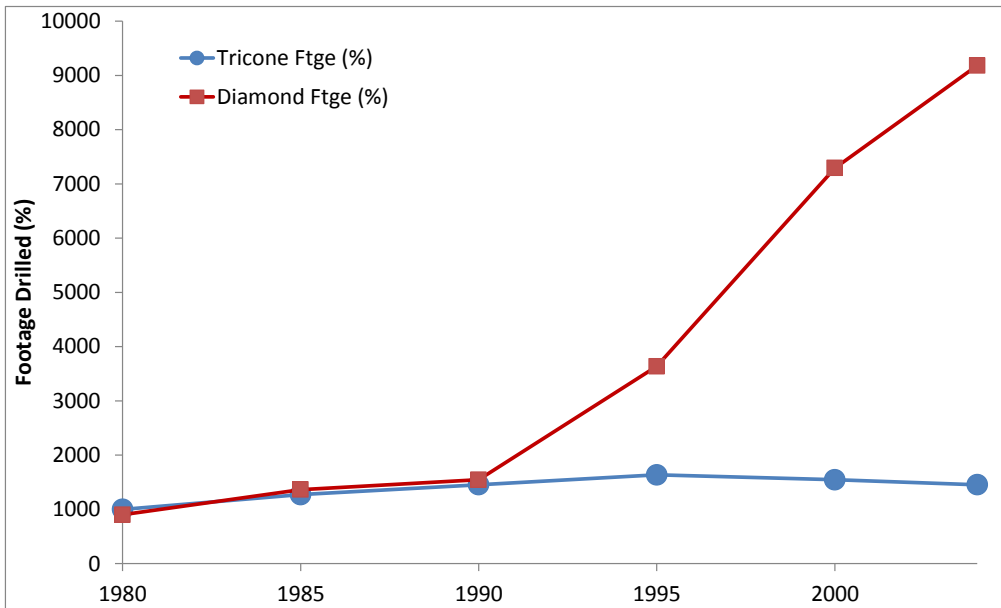
Essentially, GE used synthetic monocrystalline diamond which was loaded onto a tungsten carbide substrate and sintered at high pressures and temperatures to produce a 13 mm diameter compact having a 0.5 mm diamond layer thickness.

Figure 1.2 shows the gradual displacement of Tricone bits with diamond bits. According to Security DBS, in 2003 the split of footage drilled was 60% roller cone and 40% fixed cutter. Figure 1.3 shows the average bit life for Roller cone bits and Diamond bits. The Diamond bit footage (over the life of a bit) took off rapidly in 1995 due to the growing rental/repair of PCDs.



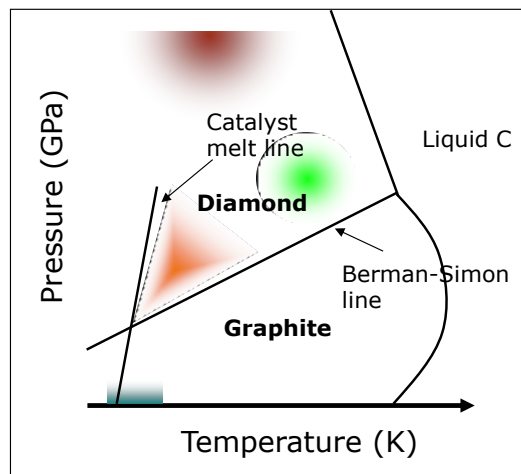
**Figure 1.2: Comparison of footage drilled for Diamond bits and Tricone bits [8]**





**Figure 1.3: Average Bit Life for Roller cone bits and Diamond bits [8]**

To better understand and appreciate the sintering of PCD, it is essential to understand the synthesis of diamond particles. A powder mixture of graphite, iron and nickel in the correct ratio is placed in a reaction vessel and subjected to higher pressures and temperatures typically in the order of 5.5 GPa and 1400 °C.



- Catalysed synthesis: above 5 GPa / 1300°C
- Non-catalysed synthesis: above 15 GPa / 2500°C
- CVD synthesis: 1 atm, ~750-1250°C
- Shock-wave synthesis: above ~30 GPa / 1000°C

**Figure 1.4: Illustration showing the various diamond synthesis regimes [9] [10]**

Figure 1.4 shows an illustration of the various synthesis regimes that are used for the manufacture of synthetic diamond crystals. Although graphite can be transformed to diamond in the absence of a catalyst, this requires very high pressures and temperatures and in terms of the efficiency of production, this is not quite feasible. The most economical method of synthesizing diamond is by the addition of a catalyst, and the most common catalysts that are used are iron and nickel [11]. The ratio of the iron and nickel can vary depending on the type of diamond required. The synthesized diamond is then recovered using acid digestion and processed into various size fractions. The micron fraction (usually less than 30  $\mu\text{m}$ ) is typically used for the sintering of PCD.

Although PCD is predominantly used for the Oil and Gas Industry, it also finds extensive application in the aerospace and automotive industries [12] [13]. Figure 1.5 shows a picture of the PCD insert that is generally manufactured. It consists of a PCD table sintered onto a tungsten carbide substrate. This insert is then brazed into pockets of a drill bit. The thickness of the PCD varies depending on the application. For example, precision machining applications require the PCD table to have a thickness in the range of 0.2 to 0.6 mm [14] in order to maintain the cutting efficiency. Oil and Gas applications require the PCD table to have a thickness ranging from 2 mm to 4 mm in order to maintain the durability.



**Figure 1.5: PCD insert**

Figure 1.6 shows images of a typical oil rig that is used in the drilling of Oil and Gas. There are two types of oil rigs, namely offshore rigs (refer to Figure 1.7) and rigs that are based inland. The PCD inserts used to drill offshore must be able to withstand greater impact, whilst the PCD inserts used in the inland drilling operations must possess both

impact and abrasion resistance [15]. Impact resistance is defined as a material's ability to resist the force of a sudden impact. In the case of Oil and Gas drilling, impact occurs between the PCD insert and the rock. The consequence of impact is the chipping and spalling of the PCD table, and this reduces the ability of the cutter to perform its task. Abrasion resistance on the other hand is defined as a process of wearing away a surface by friction. It is imperative that the PCD cutter has very good wear resistance in order to maintain its sharp cutting edge and improve cutting efficiency. The most important criteria in drilling are increased rate of penetration (ROP) and higher tool durability, allowing the driller to complete the well using as few bits as possible.



**Figure 1.6: Land-based Oil Rig [16]**



**Figure 1.7: Off shore drilling rig [17]**

Figure 1.8 provides a closer look at the drill bit. The bit consists of 6 blades which have pockets mounted on them for the easy insertion of the PCD cutter. Depending on the drill bit manufacturer, the bit design can vary from a 5 blade design to a 6 blade design to even an eight blade design. The greater the number of blades inserted onto the bit, the more aggressive the drilling conditions become. The PCD cutters are brazed into the bit using an oxy-acetylene flame (refer to Figure 1.9), and usually reach a temperature of approximately 800 °C during the brazing process.

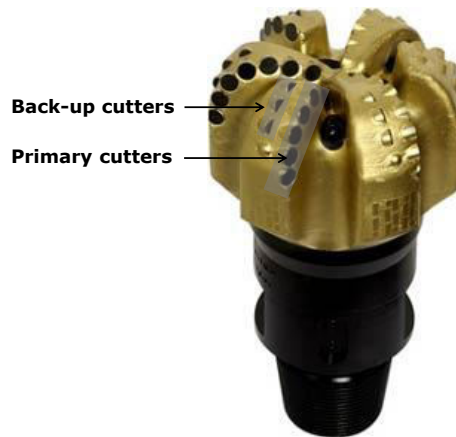


**Figure 1.8: Drill Bit**

Each blade consists of two rows of cutters, i.e. the first row of cutters are the primary cutters used predominantly for the drilling of the rock and the second row of cutters are called the back-up cutters and these offer support to the frontline cutters. The back-up cutters are usually smaller than the frontline cutters. During the drilling operation, the temperature of the drill bit can increase considerably and in order to prevent this drastic increase in temperature, highly fluid mud is circulated as the coolant, and is also used to flush rock chips back to the surface.



**Figure 1.9: Brazing of PCD inserts into a bit [16]**

## 1.2 Manufacture of PCD inserts

PCD is usually made by sintering diamond powders in the temperature range 1400 °C to 1500 °C at pressures of 5 GPa to 7 GPa [18], by using suitable metallic solvent sintering aids [19]. There are different grades of diamond that can be sintered and these range

from fine grained PCD to coarse grained PCD. Essentially, the diamond micron powder is placed on top of the tungsten carbide substrate, as shown in Figure 1.10. The tungsten carbide substrate typically consists of predominantly tungsten carbide, 13% cobalt and 6% carbon. The cobalt that is present in the substrate infiltrates the diamond powder and this enables liquid phase sintering.

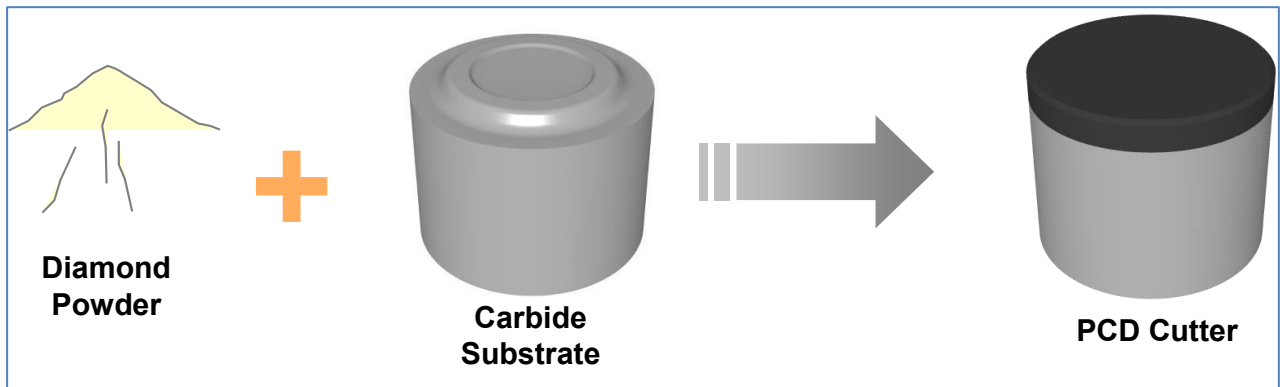


**Figure 1.10: Schematic showing formation of a PCD cutter**

There are two types of substrate interfaces, namely planar interfaces and non-planar interfaces. A planar interface has a tendency to increase the residual stress between the sintered diamond table and the carbide substrate, leading to possible delamination during tool operation, i.e. lower durability [20]. Initial PCD cutters were made using planar interfaces, which then evolved to the use of non-planar interfaces to better distribute the residual stress across the cutter.

Figure 1.11 shows an example of a non-planar interface. Residual stress is an artifact of the stress resulting from the sintering conditions experienced by the cutter during the manufacturing process. Residual stresses are usually generated during the cooling process in the sintering cycle once the sintering of the PCD is complete. The coefficient of thermal expansion mismatch between the carbide interface and the PCD causes the carbide to shrink more than the PCD, leading to potential delamination of the PCD layer.

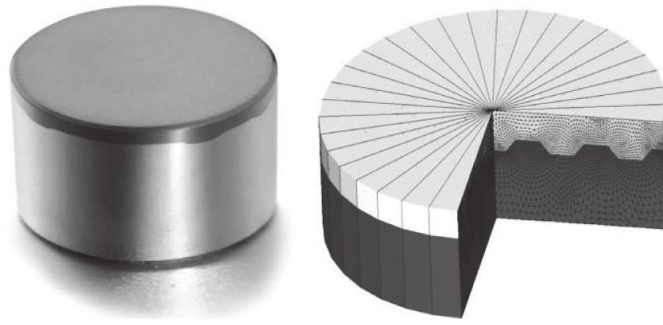


**Figure 1.11: Carbide substrate showing an example of a non-planar interface [21]**

After purification of the pre-composite unit containing the diamond powder at high temperatures under vacuum to remove all residual impurities, the unit is placed in an insulated capsule and sintered at high pressures and temperatures. Typical gaseous impurities are oxygen and nitrogen. During the high temperature treatment, partial graphitization of the diamond particles occur and this increases the reactivity of the diamond surface during the sintering process. It is critical to remove the oxygen present as this can adversely affect the sintering of the PCD.

The nitrogen atoms substitute the carbon atoms and result in the yellow colouration of synthetic diamond during the synthesis stage. Figure 1.12 explains the occurrence of this phenomenon. The nitrogen atom has 5 valence electrons and these electrons can be donated into the empty orbitals of the conduction band, enabling the absorption of blue and violet light leading the yellow appearance of the diamond. The left diagram in Figure 1.12 shows the effect of minute concentrations of nitrogen on the colour of the synthesized diamond, i.e. the energy required to excite an electron from the donor level to the conduction band is 4 eV resulting in the formation of colourless diamond. In contrary, the right diagram in Figure 1.12 shows that at a few nitrogen atoms per million carbon atoms, the donor level is broadened and energies greater than 2.2 eV can excite an electron from the donor level to the conduction band. The absorption of these higher energies (blue and violet light) results in the yellow color of the diamond.

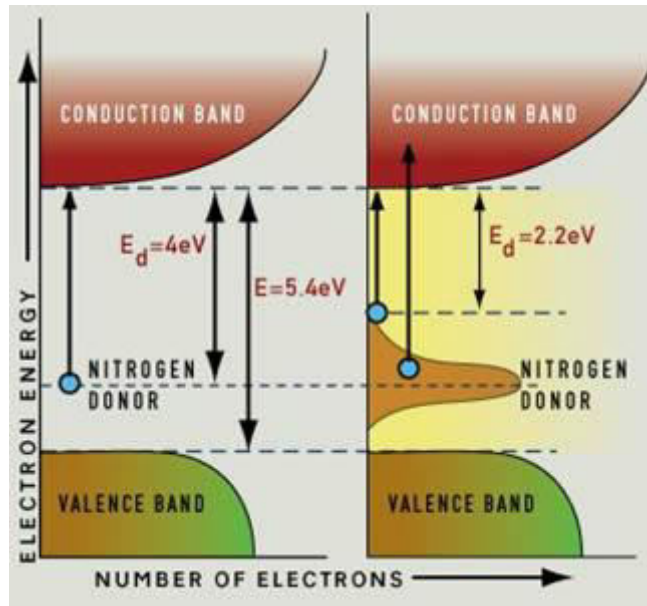


**Figure 1.12: Effect of nitrogen on the colour of the diamond crystals [22]**

There are three distinctive phases that the PCD undergoes during sintering, namely cold compaction, hot compaction and liquid phase sintering [23]. During cold compaction, the diamond particles are forced together due to only the pressure being applied. The force exerted on the particles results in the crushing of the particles due to point-to-point contact. In general, a coarse unimodal diamond mix will result in greater compaction as compared to a mixture of coarse particles and fine particles. The reason for this is that the fine particles tend to cushion the coarser particles therefore hindering excessive crushing. Effective crushing of the particles is essential in achieving high levels of green density.

Hot compaction occurs when the heat is applied and this enables plastic deformation of the diamond particles [24]. The heat applied is insufficient to cause the metal sintering aid to melt. During liquid phase sintering, the metal sintering aid in the tungsten carbide substrate melts, and infiltrates the PCD thereby allowing the diamond to saturate the cobalt by dissolution and re-precipitate as regrown diamond particles [25]. The most common sintering aid used for the sintering of PCD is cobalt, although other sintering aids such as iron and nickel-manganese have been used.



The various stages of sintering are shown in Figure 1.13. Particle to particle necking typically occurs according to Figure 1.14 in general sintering dynamics. The sintering of PCD is however slightly different in that the carbon from the diamond particles firstly dissolve in the sintering aid and re-precipitate as regrown diamond. The carbon dissolution process involves the electron transfer between the empty d orbitals of the sintering aid such as cobalt and the electrons in the pi orbitals of carbon [11].

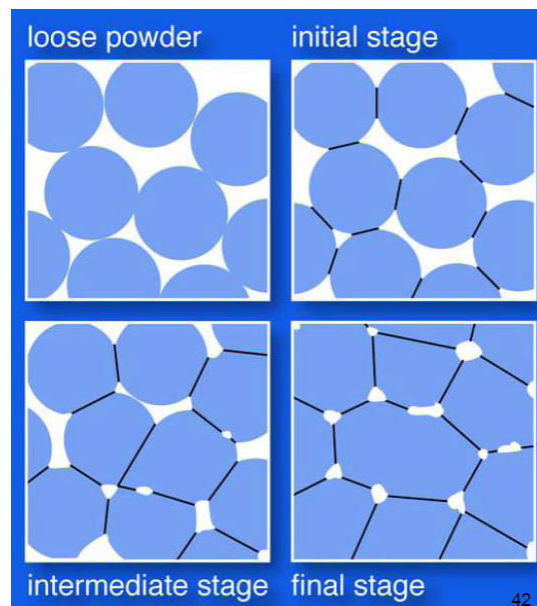


**Figure 1.13: Stages of Sintering [24]**

One of the reasons why cobalt is an effective sintering aid is because half of its d orbitals are filled with electrons whilst the other half is empty. A metal such as copper where the d orbitals are fully occupied with electrons acts as a poor sintering aid due to its inability to accept electrons from the carbon atom. Conversely, elements such as vanadium and tantalum where the d orbitals are almost devoid of electrons, can readily accept electrons from the carbon atom thereby forming a very strong bond with carbon, usually in the form of metal carbides. Due to this phenomenon, carbide formers are poor transition metal catalysts because they have a tendency to preferably form metal carbides instead of dissolving the carbon present to form diamond.

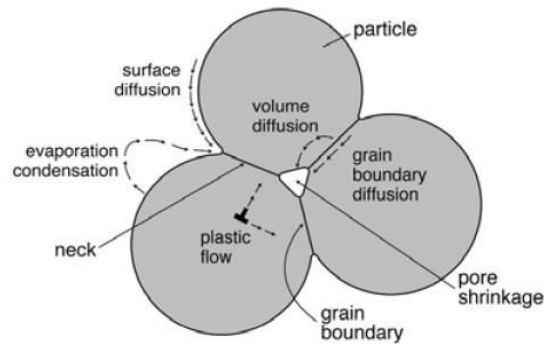


**Figure 1.14: Frenkel and Kuczynski Model [24]**

Figure 1.15 shows the infiltration of the cobalt binder from the tungsten carbide substrate into the PCD table, thereby creating a firm bond between the substrate and the PCD table. The infiltration of the cobalt from the tungsten carbide substrate typically occurs at 1400 °C and 5.5 GPa.

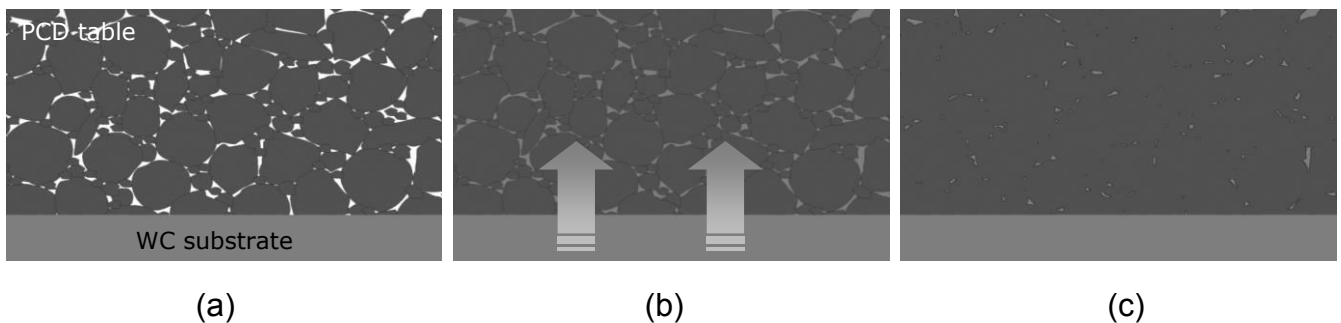


**Figure 1.15: Schematic showing infiltration of the cobalt binder into the PCD table: (a) Diamond particles placed on top of the WC substrate, (b) Infiltration of cobalt from the substrate into the diamond powder bed, (c) Liquid phase sintering of the diamond particles forming a polycrystalline compact**

After sintering, there is residual binder remaining in the open pores of the sintered material which can be removed at a later stage by leaching of the binder out of the PCD using acid media. After sintering of the PCD, the cupping material is removed and the PCD is machined in order to attain the required specifications. Figure 1.16 shows the scanning electron microstructure (SEM) of a typical PCD. The microstructure was taken in the backscatter mode where the lighter elements such as carbon appear darker, and the heavier elements such as tungsten carbide appears lighter. The dark grey grains are

diamond and the light grey pools are the binder which comprises a combination of cobalt, tungsten and carbon. The white particles are tungsten carbide. During the admixing process, tungsten carbide seeds are introduced into the diamond powder mix by the tungsten carbide milling media. During liquid phase sintering, the tungsten carbide from the substrate dissolves into the cobalt binder. The cobalt binder then infiltrates the PCD. The tungsten present in the cobalt binder precipitates onto the existing tungsten carbide seeds, resulting in grain growth of the tungsten carbide precipitate.

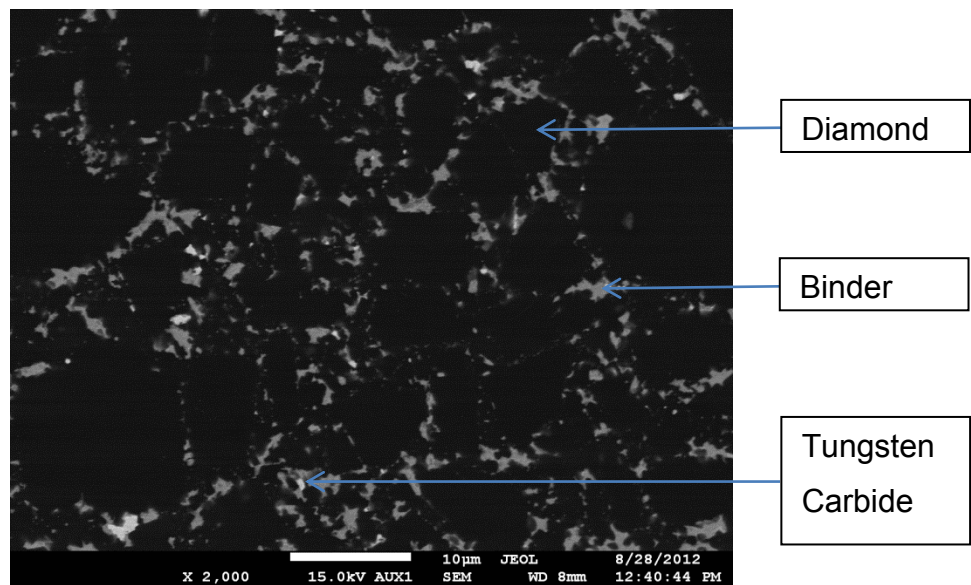


**Figure 1.16: Scanning electron microstructure (SEM) of a typical PCD showing the presence of diamond appearing as dark grey particles, cobalt binder appearing as the light grey phase and small tungsten carbide particles shown as the bright white phase**

Figure 1.17 shows the typical structure of a PCD interface showing the acicular tungsten carbide particles and the cobalt pooling area. As the cobalt from the substrate diffuses into the PCD table at an elevated temperature and pressure, the tightly bonded tungsten carbide network breaks apart slightly, producing the acicular particles at the interface.

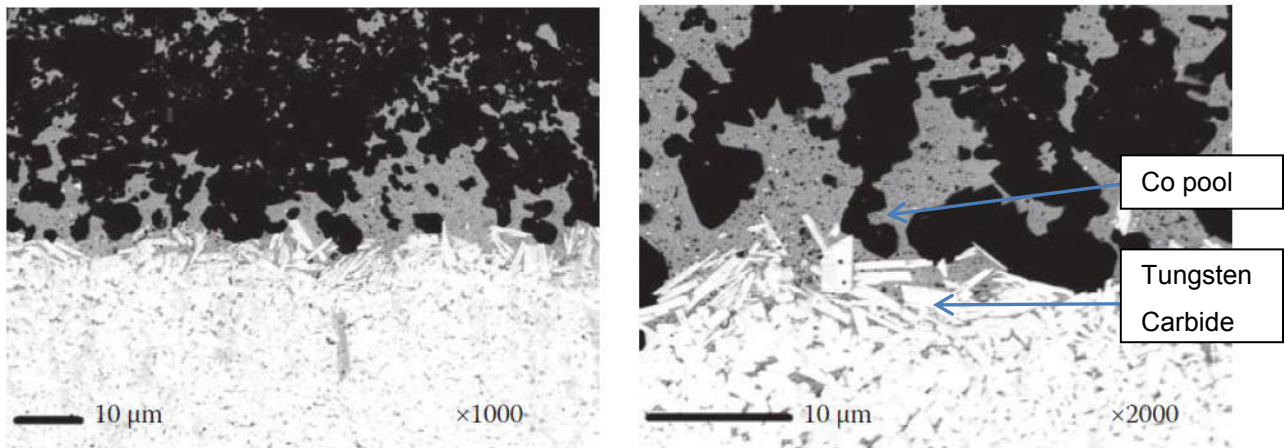


**Figure 1.17: PCD interface structure [21]**

### 1.2.1 Types of PCD

There are various types of PCD manufactured for different purposes. Fine grain PCD for example is normally categorized as PCD having a particle size of less than 6 μm. The finer the PCD grain size, the more abrasion resistant the PCD [26]. Abrasion resistant PCD is ideally used to drill hard rock formations. This type of PCD has a tendency to readily spall as a function of drilling time and speed. The cutting edge of the PCD is constantly kept sharp and smooth as the drilling operation proceeds. However, if a chip forms on the cutting edge of the PCD during the drilling operation, the PCD begins to crack, then spall and in severe cases, the entire PCD can delaminate. Conversely, coarse grain PCD is used for general purpose and impact resistant applications, with lower abrasion resistance requirements.

According to Bellin et al. [6], the sintering process is faster if both the pressure and temperature is increased. This is best expressed in Equation 1-1.

$$\text{Log } (d\rho/dt) \sim -D_1 P^* / (RT) \dots \text{Equation 1-1}$$

where  $P^*$  is the average effective pressure,  $\rho$  is the powder apparent density,  $t$  is time,  $D_1$  is the carbon diffusivity in the molten metal sintering aid,  $R$  is the ideal gas constant and  $T$

is the temperature. In addition, when sintering PCD using smaller grain sizes, higher temperatures and pressures are usually required. This is explained in Equation 1-2.

$$P^* \sim (4a^2 / (Z\chi^2)) \cdot P_{appl} \dots \text{Equation 1-2}$$

where  $a$  is the average particle size,  $\chi$  is the radius of the contact area between two spherical particles,  $Z$  is the number of surrounding particles and  $P_{appl}$  is the external pressure applied to the system.

### 1.2.2 Limitations of PCD

Although the introduction of PCD for drilling applications has revolutionized the Oil and Gas industry, there are a few limitations that PCD experiences. The most common problems associated with PCD are graphitisation, oxidation and thermal expansion (refer to Figure 1.18). These three categories will be discussed in further detail.

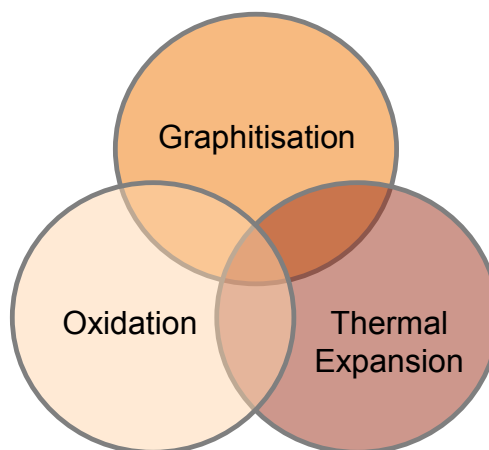


**Figure 1.18: Schematic showing the primary problems associated with PCD, i.e. the inter-relationship between graphitisation, oxidation and thermal expansion**

### 1.2.3 Graphitisation

Graphitisation is the formation of graphite when the PCD is exposed to elevated temperatures [6]. Graphite is formed by the reverse catalysis of diamond to graphite under high temperatures and atmospheric pressure, in the presence of a binder such as cobalt. Graphite is a much weaker material in comparison to PCD, and the presence of graphite in the PCD causes localized weak points along the PCD whereby the PCD can fracture, chip or spall leading to the ultimate failure of the PCD cutter.

One method to overcome graphitization is to leach the cobalt from the surface of the PCD [27] [28] [29]. This is effectively achieved using acid mixtures such as hydrochloric acid, aqua regia (i.e. one part nitric acid and three parts hydrochloric acid) or caustic materials such as sodium hydroxide, potassium hydroxide or halogen gasses. During the leaching process, it is imperative that the carbide substrate attached to the PCD is protected, and this is best accomplished using a fixture that can withstand the harsh acidic or caustic environment that the PCD is exposed to. Leaching is a post treatment that is carried out after the PCD is sintered and processed.

Taking it a step further, work has been carried out to mask certain areas on the top surface of the PCD to produce selective leaching of the binder [30]. This reduces the hazardous waste produced by the leaching process and further ensures that only the PCD exposed to the cutting surface is free from the metal binder. In addition, work has been done by Naidoo et al. to re-infiltrate the leached PCD with low melting point additives [31]. One of the advantages of this invention is to offer the PCD additional strength during tool operation as compared to the structure containing open porosity post leaching. Low melting point additives such as copper and gold do not adversely interact with the diamond to form graphite. Other inert additives may be infiltrated into the PCD post leaching such as silicon [32].

To avoid a two stage process which can become quite costly, extensive research is continuously being carried out to sinter PCD that is more thermally stable. One method of doing this is to use a sintering aid that is active during the sintering process but is inactive post sintering. An example is the sintering of PCD using carbonate binders such as

calcium carbonate [33]. This binder system however requires higher temperatures and pressures in the region of 2200 °C and 8 GPa. Other non-metallic catalytic systems may also be employed for example the use of magnesium carbonate in combination with ammonium chloride [34] or metal oxoanions such as molybdates, tungstates, vanadates and phosphates [35].

#### 1.2.4 Oxidation

Oxidation is the process whereby an element or compound combines chemically with oxygen. In PCD, both the binder and diamond particles can be oxidized if the PCD is exposed to elevated temperatures. Diamond oxidises to form gaseous carbon monoxide and carbon dioxide, whereas cobalt oxidises to form either  $\text{Co}_3\text{O}_4$  or the more stable  $\text{CoO}$ . Both of these oxidation reactions are exothermic.

Shi et al. investigated the thermal degradation of PCD compacts introduced by induction heating and observed that when cobalt present in the PCD oxidises to form cobalt oxide, micro-cracking of the PCD layer occurs [36]. In addition, bulge like formations also occur. This is most probably due to the molar volume increase when cobalt transitions from the cobalt metal to the cobalt oxide phase.

Figure 1.19 shows an image of the extreme micro-cracking on the surface of the PCD as a result of the oxidation of the cobalt binder.

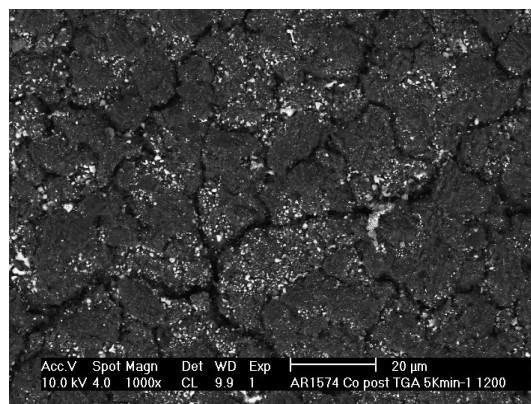


**Figure 1.19: Image showing micro-cracking of PCD**

### 1.2.5 Thermal Expansion

Due to the significantly different thermal expansion rates of the binder (which comprises cobalt and tungsten carbide) and the diamond matrix, the PCD is susceptible to thermal degradation, i.e. the binder expands at a substantially greater rate. As the binder expands, it creates pressure on the diamond-to-diamond bonds, expanding and weakening them. This combined with the external forces acting on the PCD cutter, the bonds begin to break thereby causing accelerated degradation of the PCD [30].

Table 1.1 shows the coefficient of linear expansion for the various metals as compared to diamond. It is obvious from Table 1.1 that the difference between cobalt and diamond is significant.

**Table 1.1: Coefficient of Linear Thermal Expansion for various metals, values taken at room temperature [37] [38]**

<b>Metal</b>	<b>Coefficient of Linear Thermal Expansion (<math>10^{-6}/\text{C}</math>)</b>
Copper	16.5
Nickel	13.4
Cobalt	13.0
Chromium	4.9
Molybdenum	4.8
Tungsten	4.5
Silicon	3.0
Tungsten Carbide	5.8 <sup>a</sup>
Titanium Carbide	7.4
Vanadium Carbide	7.2
Zirconium carbide	6.7
Niobium carbide	6.6
Tantalum carbide	6.3
Chromium carbide	10.3
Molybdenum carbide	4.9/



Diamond	1.0
a. [39]	

On application of heat, cobalt tends to expand much more than diamond, and this may lead to possible cracking of the PCD. A possible solution to this PCD limitation is to try to introduce an additive to PCD which has a closer CTE to diamond, or replace the existing binder with an alternative binder having a closer CTE to the diamond. From Table 1.1, it is clear that the transition metal carbides show a closer CTE to diamond as compared to the transition metal catalysts, viz. cobalt and nickel.

### 1.3 Metal Carbide additions to Tungsten Carbide and Steel

There has been a large volume of work carried out to investigate the effect of various carbide additions on the properties of tungsten carbide and steel. The general findings were that the addition of carbides such as vanadium carbide, titanium carbide, niobium carbide and chromium carbide improved the properties of tungsten carbide especially the hardness. This was achieved by primarily controlling the grain growth of the sintered tungsten carbide. It must be noted that the hardening mechanisms observed in steel may not necessarily be the same as those found in cemented carbides or polycrystalline diamond.

#### 1.3.1 Metal Carbide additions to Steel

Popandopula et al. investigated the addition of metal carbides to high speed steel [40]. Their findings showed that  $M_6C$  carbides were the principal carbides formed in the steel, with metastable  $M_7C_3$  and  $M_3C$  carbides formed regardless of whether the carbon in the steel was high or low. Their findings also revealed an increase in the red hardness (i.e. heat resistance) of the steel.

Qi et al. showed an increase in abrasion resistance when vanadium is added to high chromium cast iron hardfacing metal [41]. Qu et al. and Sapate et al. revealed that high

chromium cast iron exhibited excellent wear resistance at a low-stress state when its microstructure contained  $M_7C_3$ -type carbides [42] [43].

Wei et al. studied the relationship between the hardness and wear resistance of high speed steel, and found that the wear resistance was dependent on the amount, morphology and distribution of vanadium carbide [44] [45].

Li et al. showed that the addition of vanadium to steel improved both the mechanical and impact properties of the material by dispersion and dislocation strengthening of the material [46].

### 1.3.2 Metal Carbide additions to Tungsten Carbide

Tungsten carbide is used for most metal cutting operations and there is always a drive to improve the properties for high speed machining of steel. This material has attracted great interest from both academics and engineers owing to its high hardness and wear resistance, high melting point and chemical inertness. It is widely used in industries such as aerospace, oil and gas, semiconductor, wear parts and automotive [47].

Weidow et al. investigated the addition of various metal carbides to tungsten carbide and observed that titanium carbide was the most effective in controlling the grain growth of tungsten carbide, which resulted in an increase in the hardness of the material [48].

Sugiyama et al. explored the addition of vanadium carbide to tungsten carbide and detected the formation of  $(W,V)C_x$  thin layers at the  $WC/Co$  interfaces. They suggested that the  $(W,V)C_x$  thin layers are formed during the liquid phase sintering stage and that the grain growth inhibition due to vanadium carbide doping is closely related to the formation of the  $(W,V)C_x$  layers [49]. Vanadium carbide is widely used in the tungsten carbide industry to control grain growth of the tungsten carbide grains and in doing so, improve the overall properties of the tungsten carbide cutting tool. Sometimes, a combination of grain growth inhibitors is used to enhance the properties of tungsten carbide [50].

Marshall et al. state that both chromium carbide and vanadium carbide act as grain growth inhibitors in tungsten carbide but since chromium carbide is more soluble in the binder phase, it is not as effective as vanadium carbide [51]. They furthermore state that chromium doping lowers the melting point on the WC–Co phase diagram and hence the hcp phase of cobalt is not as suppressed in chromium-doped material as compared to vanadium-doped materials.

It is a known fact that when vanadium carbide is added to tungsten carbide as a grain growth inhibitor, the microstructure shows the presence of large (V,W) $C_x$  mixed carbide grains. The addition of more than about 2 wt% vanadium (i.e. above the solubility limit of vanadium for the liquid binder) creates a problem during liquid state sintering in that the vanadium dissolves in the liquid binder and then re-precipitates as very large grains of (W,V) $C_x$  resulting in very brittle material [52].

Attempts have also been made to reduce the grain size of (W,V) $C_x$  cubic carbides by replacing half of the of the vanadium atoms with titanium atoms producing WC–VC–TiC–Co. Titanium was added because its solubility in the liquid binder phase is lower than that of vanadium. This was successful and the addition of titanium with vanadium is still employed today in the making of tungsten carbide tools [53]. Other investigations were also carried out to reduce the cubic carbide grain sizes by sintering the materials in the presence of nitrogen, as it decreases the solubility of vanadium during sintering [54] [55].

Hashe et al. later found that by pre-alloying the (V,W) $C_x$  powder, finer cubic carbide grains were attained which showed superior properties such as higher hardness [56]. This was attributed to the elimination of the driving force for nucleation and growth of the (V,W) $C_x$  cubic carbide.

Besides carbide additives being used as grain growth inhibitors, the addition of carbides to WC-Co influences the tungsten carbide grain morphology. Chromium carbide generates partly rounded tungsten carbide grains [57], whilst the addition of vanadium carbide introduces sharp triangular grains [58].

In general, there seems to be numerous successful investigations into the improvement of the properties of tungsten carbide by the addition of carbides to the mixture prior to sintering.

### 1.3.3 Stability, Solubility and Wettability of Metal Carbides

Figure 1.20 shows the Gibbs free energy of formation of various carbides, plotted using data obtained from the Smithells Metals Reference Book [59]. The vertical red dashed line in the graph depicts the temperature at which the PCD is sintered. Prior to discussing the graph, it must be noted that the sintering environment of the PCD differs from the environment in which the data for the graph was collected, i.e. the PCD is exposed to a cobalt rich environment at high pressures. The graph is therefore indicative of what to expect during sintering when using the various carbide additives.

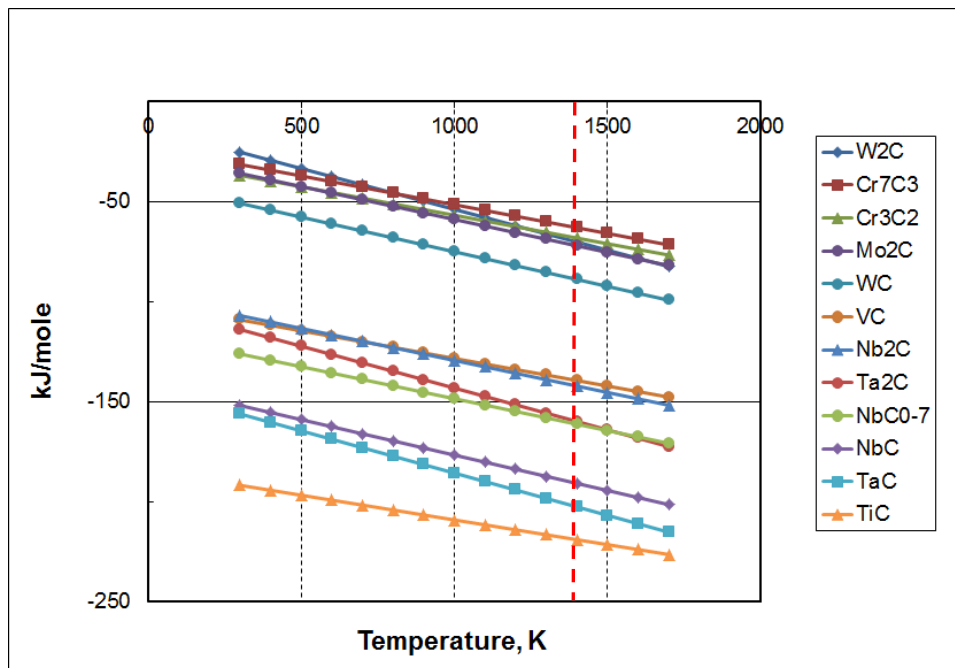


**Figure 1.20: Gibbs Free Energy of Formation for various Carbides, normalised to one metal atom [59]**

At room temperature, the most stable carbide seems to be titanium carbide, and the least stable carbide is tungsten carbide.

Room Temperature:  $\text{Cr}_3\text{C}_2 \ll \text{Mo}_2\text{C} \ll \text{WC} \ll \text{VC} \ll \text{Ta}_2\text{C} \ll \text{NbC} \ll \text{TaC} \ll \text{TiC}$   
-----> increasing stability

Sintering Temperature:  $\text{Cr}_3\text{C}_2 \ll \text{Mo}_2\text{C} \ll \text{WC} \ll \text{VC} \ll \text{Ta}_2\text{C} \ll \text{NbC} \ll \text{TaC} \ll \text{TiC}$   
-----> increasing stability

The carbide present in standard PCD is tungsten carbide. From Figure 1.20, it is seen that certain carbides are more stable than tungsten carbide either at room temperature or higher.

Figure 1.21 shows a graph depicting the wetting of metallic carbides by liquid cobalt. The surface energies of a system dictate the wettability of the solid by the liquid according to Equation 1-3.

$$\gamma_s = \gamma_{sl} + \gamma_L \cos \theta \dots \dots \dots \text{Equation 1-3}$$

Where,

- $\gamma_s$  = Surface energy of the solid
- $\gamma_{sl}$  = Solid-liquid interfacial energy
- $\gamma_L$  = Surface tension of the liquid
- $\theta$  = Wetting angle

The surface tension of the liquid is measured by the sessile drop method and the wetting angle can be directly measured using the drop.

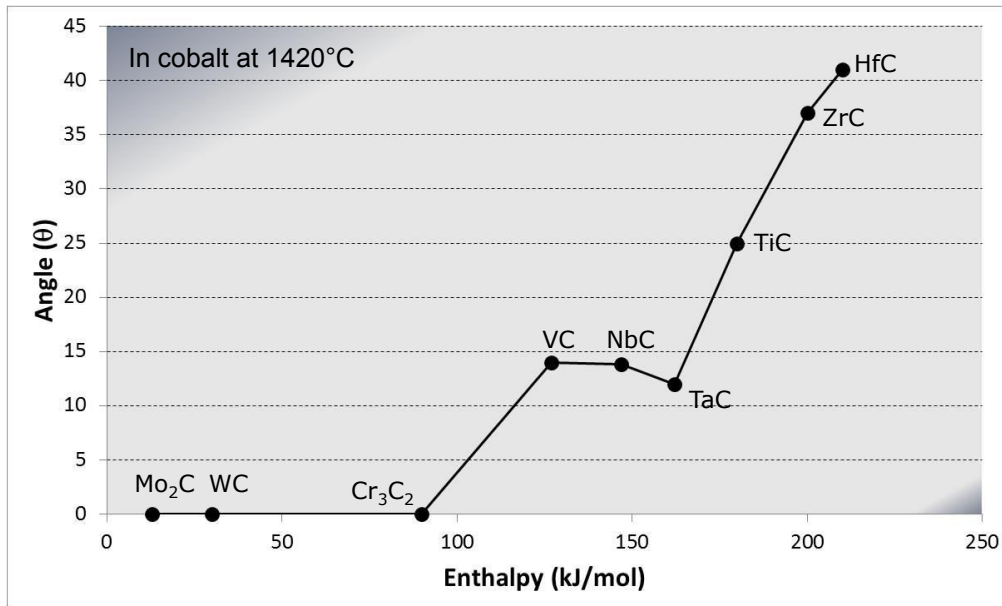


**Figure 1.21: Enthalpy of formation wetted by the cobalt eutectic melt [60]**

If the carbide has good wettability with cobalt, it will go into solution with cobalt much easier. According to Figure 1.21, the wetting angle of carbides such as VC, NbC, TaC, and TiC is much higher than Mo<sub>2</sub>C, WC or Cr<sub>3</sub>C<sub>2</sub>. In general, the more stable the carbide, the less the wetting. The melting points of pure nickel and cobalt metal are 1453 °C and 1495 °C respectively. The measurements employing nickel and cobalt were made at 1380 °C and 1420 °C respectively. At these temperatures, all carbides are expected to have formed eutectic melts with the two metals. Figure 1.20 illustrates that WC, Cr<sub>3</sub>C<sub>2</sub> and Mo<sub>2</sub>C are much less stable than TiC and TaC at room temperature. The wetting angle data in Figure 1.21 further substantiates this.

It is expected that Mo<sub>2</sub>C, WC and Cr<sub>3</sub>C<sub>2</sub> would go into solution with cobalt more readily than VC, NbC or TiC. It can be inferred that the addition of Cr<sub>3</sub>C<sub>2</sub> to PCD would most probably enhance solution strengthening in the PCD whilst the addition of VC would enhance precipitation hardening within the PCD compact.

Table 1.2 shows the wetting angle of various metals with diamond. There seems to be three categories of metals, viz. metals that have a high wetting angle with diamond (i.e. Cu, Ag, Au, Pt, Pd), metals that have an average wetting angle with diamond (i.e. Ni, Co, Fe, Mn) and metals that have a low wetting angle with diamond (i.e. Cr, V, Ti). Metals

with filled d orbitals such as Cu have very little interaction with diamond because there is no electron transfer between the d orbitals of the metal and the pi orbitals of the carbon in diamond (refer to Figure 1.22). Coupled to this, the low adhesion energy and high interfacial energy of this category of metals makes interaction with diamond virtually impossible.

The second group of metals such as Co has partially filled d orbitals and can therefore easily accept electrons from the p orbitals of carbon, making interaction with diamond possible. It is for this reason, that Co can enable sintering of diamond particles since it facilitates the dissolution and re-precipitation of carbon to form diamond particles. Adversely, since the reactivity and wettability of Co with diamond is high, Co can easily graphitise the diamond during tool use at ambient conditions.

The third group of metals such as V has almost empty d orbitals and hence the interaction of the d orbitals of these metals with the pi orbitals of diamond is very strong. This group of metals have a tendency to combine with carbon to form stable carbides thereby locking the carbon within its structure.

Table 1.3 shows the solubility data for various metals in cobalt taken from their binary phase diagrams [61]. Chromium has the highest solubility in cobalt with titanium having the lowest solubility. This is in agreement with the graph depicting the wetting of metallic carbides by cobalt shown in Figure 1.21.

**Table 1.2: Wetting angle of various metals with diamond [62]**

Metal	Pressure (GPa)	Temp (K)	Wetting Angle ( $\theta$ )	Adhesion Energy ( $\text{J}\cdot\text{m}^{-3}$ )	Interfacial Energy ( $\text{J m}^{-2}$ )
Cu	5.5	1620	150	0.18	7.43
Ag	5.5	1620	140	0.21	6.99
Au	5.5	1620	130	0.41	7.03
Pt	7.5	2370	45	3.07	5.03
Pd	7.5	2370	38	2.68	5.12
Ni	6.5	1970	30	3.36	4.75
Co	6.5	1970	26	3.52	4.63
Fe	7.0	2070	20	3.59	4.56
Mn	7.0	2070	17	2.15	5.25
Cr	7.0	2070	12	3.17	4.74
V	8.0	2470	7	3.79	4.42
Ti	8.0	2470	10	3.10	4.77

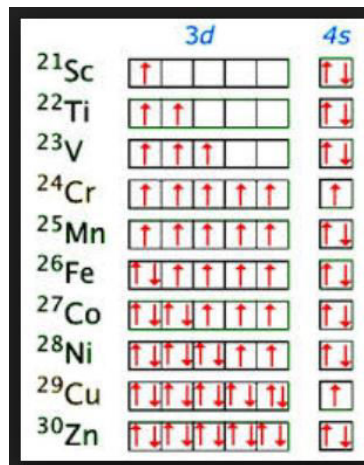


**Figure 1.22: Graph showing the d orbital distribution of different metals [63]**



**Table 1.3: Data showing solubility of different metals in cobalt at 1400 °C**

<b>Metal</b>	<b>Solubility of metal in Cobalt at 1400 °C</b>
Vanadium	23at%
Titanium	6.5at%
Molybdenum	18at%
Chromium	55at%

#### 1.4 Metal Carbide additions to Polycrystalline Diamond

##### 1.4.1 Additives to PCD

The three categories of problems associated with PCD need to be addressed both individually and as a whole, i.e. most often the result of the PCD degradation is not limited to just one cause but a combination of failures that lead to its demise. It is known that the cobalt based PCD can easily graphitize and oxidise, whilst at the same time degrade due to the coefficient of thermal mismatch between the binder and diamond at elevated temperatures. As mentioned, one possible solution to the problem is to replace the transition metal cobalt with a binder that does not aid in the graphitization of diamond, is not prone to oxidation and has a closer CTE to diamond.

A potential replacement is the use of magnesium carbonate or calcium carbonate as a binder system [33] [64]. Although this would seem like an easy solution, the sintering of a magnesium or calcium carbonate based PCD requires higher temperatures and pressures in the region of 8 GPa and >2000 °C. Given the high demands for PCD cutters and drive for lowering the production costs, this binder system is not currently feasible. Hence alternatives need to be investigated.

One of the alternatives as mentioned is to leach the top surface of the PCD thereby removing the cobalt binder that is in contact with the rock at the cutting edge. This is a relatively simple process but is heavily patented and often requires the payment of royalties especially if deeper leach depths are required. Hence, a simpler method to alleviate the problem is to add carbides to the diamond powder prior to sintering. The

carbides may be admixed to the diamond powder, infiltrated from a shim or powder layer at the PCD – substrate interface or coated onto the diamond particles prior to sintering. There are various advantages of adding carbides to PCD and these are outlined below.

#### 1.4.2 Displacement of Cobalt

The carbide would displace some of the cobalt present in the PCD thereby reducing the extent of graphitization, oxidation and CTE mismatch in the sintered PCD. In addition, it is likely that the carbides would precipitate at the diamond-binder interface within the PCD thereby further protecting the diamond from harm (refer to Figure 1.23).

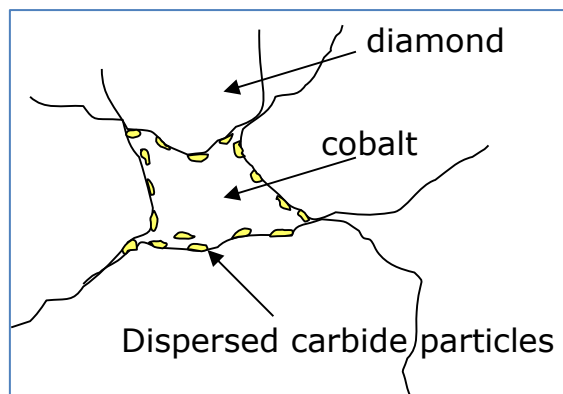


**Figure 1.23: Schematic of carbide particles deposited at the diamond-binder interface**

#### 1.4.3 Oxidation of Cobalt

The PCD would become more oxidation resistant, owing to there being less binder present in the PCD. Also, the carbide in solution with the binder may further stabilize the binder thereby hindering the oxidation of the binder. It is known that carbides such as vanadium carbide enhance both the corrosion resistance and oxidation resistance of a material [65].

#### 1.4.4 CTE Mismatch

Carbides generally have a coefficient of thermal expansion much lower than that of the cobalt metal. By displacing the cobalt metal with the metal carbide, the overall CTE of the PCD is expected to be much closer to the tungsten carbide substrate. The residual stress between the PCD and the substrate is expected to reduce, especially during sintering.

#### 1.4.5 Promote Diamond Intergrowth

Most carbides do not adversely affect diamond intergrowth, except for silicon carbide where the cobalt reacts with the silicon carbide to form the inert cobalt silicide prior to diamond intergrowth.

#### 1.4.6 Precipitation Hardening

Precipitation hardening is another advantage that carbide additives bestow on PCD. The carbide precipitates in the cobalt binder pools and increases the hardness of the PCD compact. Table 1.4 shows the micro hardness values for some of the metal carbides. In PCD, the hardness of diamond is  $7000 \text{ kg/mm}^2$ , the hardness of tungsten carbide is  $2100 \text{ kg/mm}^2$  and the hardness of cobalt is  $1043 \text{ kg/mm}^2$  [66].

When carbide are added to PCD, some of the cobalt present in the PCD is displaced by the carbide. So for example, if vanadium carbide is added to PCD, vanadium carbide has a higher hardness than tungsten carbide and will therefore impart a higher overall hardness to the PCD compact which will probably result in an increase in abrasion resistance.

**Table 1.4: Micro Hardness of Metal Carbides [38]**

<b>Metal Carbide</b>	<b>Micro Hardness (kg/mm<sup>2</sup>)</b>
Diamond	7000 <sup>a</sup>
VC <sub>0.97</sub>	2900
TiC	2900
HfC <sub>0.99</sub>	2700
ZrC <sub>0.97</sub>	2600
TaC <sub>0.99</sub>	2500
NbC <sub>0.99</sub>	2400
WC	2100
Mo <sub>2</sub> C	1500
Cr <sub>3</sub> C <sub>2</sub>	1300

a [67]

#### 1.4.7 Stabilisation of the cobalt phase

There are two cobalt phases, i.e. an hcp stable phase and an fcc metastable phase. According to the cobalt phase diagram in Figure 1.24, the hcp phase transitions to the fcc phase at 422 °C. In PCD, the fcc phase of cobalt is present. Huang et al. observed that the hcp phase of cobalt can be changed to the fcc phase and vice versa using varying ball: powder ratios during the ball milling process [68]. They noticed that when using a ball: powder ratio = 80 with a frequency of 1.6 Hz, the hcp phase completely converted to the fcc phase, and depending on the ball: powder ratio and frequency, the fcc phase can partly or completely convert to the hcp phase. This implies that during the PCD tool use, the fcc phase of cobalt could be converted to the hcp phase due to the hammering action of the tool against the rock interface.

In a study performed by Guillermet [69], the molar volume of the hcp phase of cobalt was found to be  $6.72 (\text{m}^3 \cdot \text{mol}^{-1})10^6$  and the molar volume of the fcc phase of cobalt was found to be  $6.75 (\text{m}^3 \cdot \text{mol}^{-1})10^6$  at room temperature. It was further shown that as the temperature increases to 1600K, the difference in the molar volume between the fcc and hcp phase decreases and eventually equalizes at temperatures greater than 1600K.

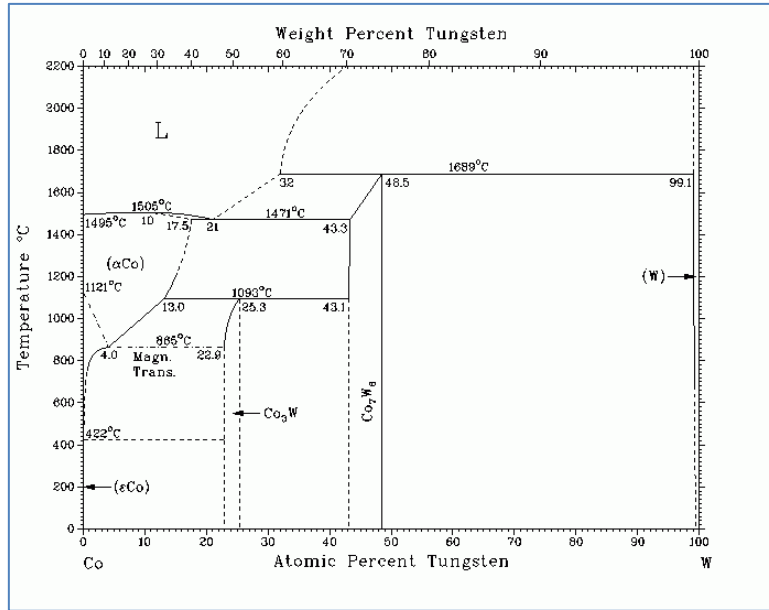


**Figure 1.24: Co-W Phase Diagram [61]**

One possible solution is to stabilize the fcc phase of cobalt using another element. At present the fcc phase of cobalt is stabilized by the presence of tungsten atoms in the cobalt lattice. Other carbides such as vanadium could further stabilize the fcc cobalt phase thus reducing or even eliminating any phase transformation that might occur.

### 1.5 Aim of the Study

The aim of this thesis is to investigate the effect of the addition of various carbides to the structure and performance of polycrystalline diamond. The focus of the study will predominantly be based on the addition of vanadium carbide to PCD. Vanadium carbide was chosen since it showed a huge benefit when added to tungsten carbide in terms of improving the properties of the material. The interaction of vanadium with tungsten will be explored in terms of whether vanadium carbide remains as 'vanadium carbide' in the PCD or whether it combines with the residual tungsten to form a mixed carbide.

The stability of the carbides present in the PCD will be examined using hot stage XRD. During tool use, the tool is exposed to high temperatures especially at the tool-rock interface. It is essential to determine the potential reaction of the carbide during tool use. Furthermore, the extent of graphitisation in the presence of the carbide additive will also

be studied, and a mechanism proposed for the formation and dissolution of the carbide (if this phenomenon is shown to occur).

In addition, other carbides will also be added to PCD, viz. chromium carbide which also results in tungsten carbide with an enhanced wear performance, titanium carbide which reduces the grain growth of the (V,W)C<sub>x</sub> carbide formed in tungsten carbide and molybdenum carbide which is known to be beneficial to the properties of tungsten carbide. Hot stage XRD of these carbides will also be investigated.

To investigate the addition of the various carbide additions to PCD, diamond particles with an average grain size will be used. It is known that the finer the diamond grain size, the more difficult it is to sinter as the kinetics of the sintering environment enhances grain growth. Hence, the addition of carbides to reduce grain growth in PCD will also be investigated. The carbides to be considered are vanadium carbide and chromium carbide. The rationale for choosing these particular two carbides is that their behaviour is opposite to each other in that vanadium carbide is less soluble than chromium carbide in the cobalt binder solution. The effect of these two carbide additives is expected to be different.

## 1.6 Hypotheses

Based on the vast research carried out on improving the properties of tungsten carbide and steel, it is expected that the addition of carbides to PCD will enhance the behaviour of PCD. Mixed carbides such as (W,M)C<sub>x</sub> are expected to form within the PCD structure instead of the M<sub>6</sub>C carbides that are commonly formed in steel. Some of the mixed carbides are expected to form at the diamond-binder interface (i.e. precipitation hardening) and some are expected to remain in the binder solution (i.e. solution strengthening).

Carbides are generally stable compounds with respect to disassociation, so it is expected that the newly formed mixed carbide will be stable as well, i.e. it should not dissociate on the application of heat. The carbide additive is expected to reduce the extent of

graphitisation in the PCD tool. Furthermore, the stabilisation of the cobalt binder should improve with the addition of the carbide.

In terms of grain growth, both the addition of vanadium carbide and chromium carbide is expected to reduce the grain growth of the PCD especially at the diamond-tungsten carbide interface and the diamond-cobalt interface.

## CHAPTER TWO

### ADDITION OF VANADIUM CARBIDE TO PCD

#### 2.1 Background

The most commonly used carbide as a grain growth inhibitor of tungsten carbide is vanadium carbide. In suppressing grain growth, the carbide additives create a harder and more wear-resistant material [53], [70]. The added VC does not remain as VC in the sintered product, but reacts with the tungsten present in the tungsten carbide to form a mixed (V,W)C<sub>x</sub> carbide. However, adding more than 1wt% VC results in the precipitation of very large grains of cubic (W,V)C<sub>x</sub> which lead to a material with poorer properties. Hashe et al state that in their investigations, a core-rim structure in (V,W)C<sub>x</sub> was formed with the core having a higher vanadium concentration than the rim [53].

Bonny et al. showed that the addition of VC/Cr<sub>3</sub>C<sub>2</sub> improved the hardness of the tungsten carbide material and reduced grain growth [71]. They also found that the wear performance of the tool improved. Arenas et al. found that the addition of VC to tungsten carbide increased the contiguity of the carbide network and increased the overall toughness of the material [72], whereas Soleimanpour et al. showed that although the addition of VC to tungsten carbide resulted in the increase in hardness of the compact, the transverse rupture strength was compromised [73]. In general, the addition of VC to WC-Co promotes an overall improvement in the properties of the tool, and based on the extensive research carried out, it seems likely that similar improvements in tool performance would be observed on addition of VC to PCD.

VC was therefore added to polycrystalline diamond to investigate the effect on the microstructure and resulting behaviour of the compact. Two sets of experiments were carried out, viz. PCD sintered directly onto a tungsten carbide substrate with a diamond powder mix containing admixed VC placed on top of the substrate, and the second experiment was a solid sintered PCD with VC infiltration from a powder bed. The infiltration of VC from a powder bed placed at the PCD-tungsten carbide substrate interface was expected to provide a higher degree of homogeneity of the VC within the sintered PCD as compared to the admixing of the VC with the diamond prior to sintering.



For the admixing route, it is always good practice for the additive to be an order of magnitude smaller than the matrix material in order to provide acceptable homogeneity [74]. According to German [74], the more homogeneous the additive distribution prior to liquid phase sintering, the more rapid the densification during sintering. Hence, large additive particle sizes are detrimental.

Besides admixing, there are other methods of introducing the VC additive to the diamond matrix for example depositing fine particles of VC onto the diamond thus producing a more homogeneous distribution of VC in the diamond matrix. Jin et al. synthesised WC–Co–Cr<sub>3</sub>C<sub>2</sub>–VC nanocomposite powders using water soluble salts of ammonium metatungstate, cobalt nitrate, ammonium dichromate, ammonium vanadate and glucose [75]. Can et al. further describes sol gel processes to coat abrasive particles with various metals and carbides [76]. These coating methods could be used to develop an effective technique to deposit VC particles onto diamond prior to sintering. The study of suitable coating techniques was not part of the scope of this investigation.

## 2.2 Experimental

The VC powder used in the experiments was obtained from HC Starck (HV 160). The particle size analysis was performed using a Malvern Mastersizer 2000, X-ray diffraction analysis was done using a Panalytical X'Pert Pro fitted with an Anton Paar HTK1400 non-ambient stage, X-ray fluorescence analysis was carried out using a XRF PW2400, Scanning electron microscopy analysis was performed using both a Jeol JSM 7500 and a Philips XL30 instrument, Inductively Coupled Plasma analysis was undertaken using a Spectro Ciros<sup>ccd</sup>, and 3D X-ray analysis was done using an X-Tech instrument. Diamond powder with an average particle size of 10 µm was obtained from Element Six and used as the matrix material. The diamond powder consisted of a multimodal feed with different quantities of diamond fractions combined. Varying concentrations of VC was added to the diamond powder with the concentrations ranging from 1 – 5wt%. The average particle size of the VC powder was 3 µm.

PCD compacts are generally sintered on a tungsten carbide substrate and this relies on the cobalt from the substrate infiltrating into the diamond layer to enable sintering. Another type of PCD that could be sintered, is solid PCD, i.e. PCD that is not attached to a substrate. One of the advantages of sintering a solid PCD is that a VC interlayer or shim could be used to infiltrate the VC into the diamond layer such that the PCD absorbs only the amount of additive it requires ensuring that there is no excess additive. A matrix of experiments was performed to investigate the different sintering methods (refer to Table 2.1).

**Table 2.1: Matrix of experiments carried out on solid PCD**

<b>Experiment Number</b>	<b>Description</b>
1	PCD infiltrated with a layer of cobalt foil, with no VC powder addition, (i.e. Standard solid PCD). 20wt% (9vol%) of cobalt foil was introduced, with the remaining PCD being diamond.
2	PCD infiltrated with a first layer of 3wt% (1.85vol%) VC powder and a second layer of 20wt% (9vol%) Co foil
3	PCD admixed with 3wt% (1.85vol%) VC and sintered on a WC substrate

The 20wt% (9vol%) cobalt foil was chosen as an infiltrant concentration as there is approximately 15wt% - 20wt% binder in the sintered PCD. In order to assess whether a solid VC doped PCD can be sintered using the modified sintering method, a standard PCD containing no VC was initially sintered prior to assessing the infiltration of a VC layer into the PCD (Experiment 2). The pre-composite assembly for Experiment 1 (i.e. standard PCD) is shown in Figure 2.1. It comprises cobalt foil placed at the bottom of the canister material with a layer of diamond powder on top. The canister material is made up of a refractory metal. The substrate is then encased in a separate canister as to prevent the melting and infiltration of the cobalt from the substrate into the diamond powder, and the substrate canister placed on top of the diamond powder with kaowool as the separation medium. The whole assembly is then encapsulated, and subjected to elevated pressures and temperatures to enable the sintering of the PCD.

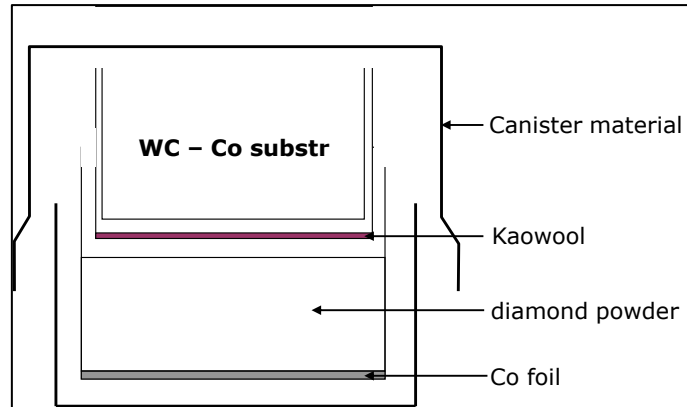


**Figure 2.1: Pre-composite assembly for the sintering of solid PCD**

The pre-composite assembly for Experiment 2 is shown in Figure 2.2. In this experiment, the PCD is infiltrated with a first layer of 3wt% VC powder and a second layer of 20wt% Co foil.

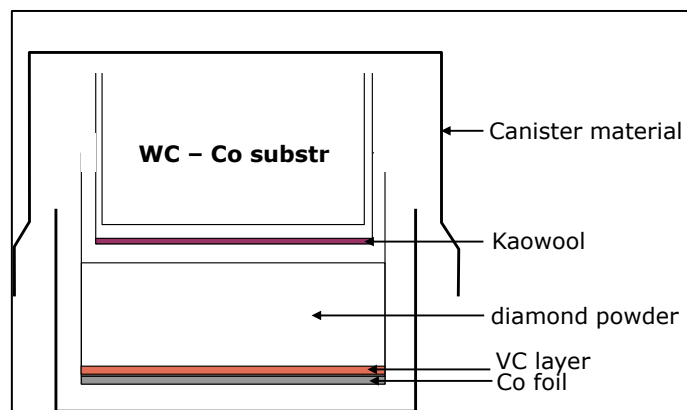


**Figure 2.2: Pre-composite assembly for the sintering of PCD infiltrated with a first layer of 3wt% VC powder and a second layer of 20wt% Co foil**

For Experiment 3, the diamond powder, VC powder and a small fraction of cobalt was admixed using a Planetary ball mill. The WC balls used in the admixing process were abraded by the diamond particles thereby introducing WC particulates into the powder matrix. The presence of the WC particulates in the powder mix is necessary in order to hinder the formation of larger plumes within the PCD which is quite common during the sintering process and generally appears at the interface. Plumes are formed by the

deposition of tungsten that is dissolved in the cobalt onto a freshly nucleated tungsten carbide seed. There is an observed reduction in plume formation when there are many tungsten carbide seeds initially present in the powder material prior to sintering.

To prepare the pre-composite, the diamond powder was placed in a canister with the substrate placed on top of the powder (refer to Figure 2.3). The canister was then encapsulated and subjected to high pressures and temperatures generally in the order of 5.5 GPa – 7.7 GPa, and 1400 °C – 1600 °C. Refer to Figure 2.4 and Figure 2.5 for a schematic and a picture of the belt press typically used for the sintering of the VC based PCD.

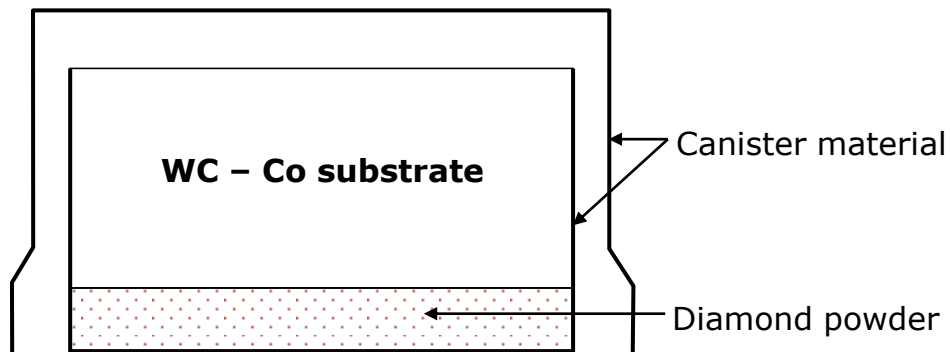


**Figure 2.3: Pre-composite assembly of PCD admixed with 3wt% VC and sintered on a WC substrate**

Post sintering, the samples were lapped and the outer diameter ground to remove the capsule cupping material. In order to get a representative idea of the microstructure, the sample was cross-sectioned using an Electro Discharge Machine (EDM), further lapped to remove any EDM residue on the surface of the sample and then polished. It is imperative to analyse a polished surface to ensure that a clear image is obtained and that the electrons are not scattered.

In addition to analysing the structure of the PCD containing VC, the PCD was subjected to a few behavioural tests such as Paarl Granite Log Test and a Sandstone Milling Test to determine its wear behaviour and thermal resistance.

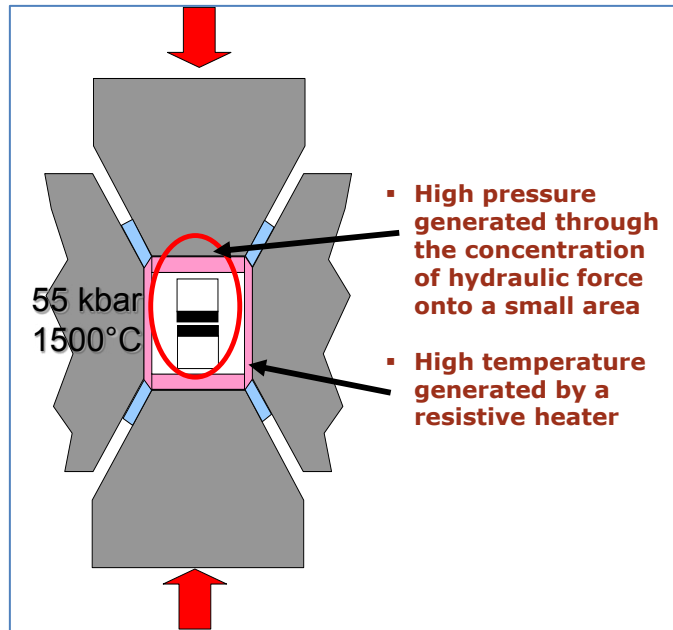


**Figure 2.4: Schematic of a high pressure vehicle**



**Figure 2.5: Belt Press**

## 2.3 Brief description of Analysis Techniques

### 2.3.1 X-Ray Diffraction (XRD)

XRD is an analytical technique that focuses on the X-ray scattering from crystalline materials. Each material produces a unique X-ray "fingerprint" of X-ray intensity versus

scattering angle that is characteristic of its crystalline atomic structure [77]. X-rays are electromagnetic radiation of exactly the same nature as light but of shorter wavelength ( $10^{-10}$  m = 1 Angstrom). So x-rays are ideal to probe interatomic distances which are typically of that order [78]. Figure 2.6 shows the schematic of the principle of x-ray diffraction. X-rays from an x-ray tube are generally targeted at a sample, which in turn diffracts the incoming X-rays but also emits characteristic x-rays excited from the sample.

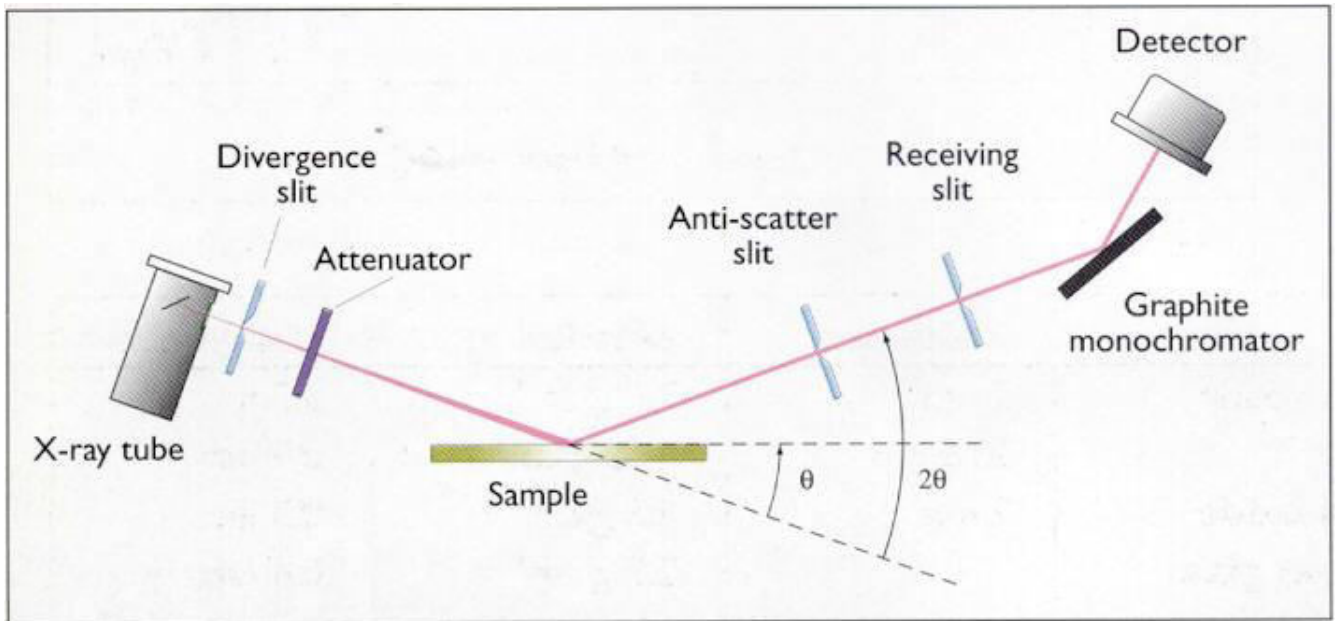


**Figure 2.6: Schematic of X-Ray Diffraction [77]**

The relationship describing the angle at which a beam of X-rays of a particular wavelength diffracts from a crystalline surface is known as Bragg's Law [79]:

$$2d\sin\theta = n\lambda$$

$\lambda$  = wavelength of the x-ray

$\theta$  = scattering angle

$n$  = integer representing the order of the diffraction peak.

$d$  = inter-plane distance of (i.e. atoms, ions, molecules)

### 2.3.2 Scanning Electron Microscopy (SEM)

SEM analysis involves the interaction of a beam of primary electrons (produced by an electron gun) with the material being examined. When the primary electron beam strikes the sample, three main types of emissions occur, namely secondary electrons, backscattered electrons and X-rays (refer to Figure 2.7). These emissions emanate either from the surface of the sample or within the sample.

The secondary electrons are emitted from the surface of the sample and are used to determine the sample topography. Backscattered electrons are emitted from deeper within the specimen, and these electrons provide information related to the atomic number of the specimen. Finally, the emitted X-rays can be used in conjunction with an X-ray detector to determine which elements are present in the sample. This technique of X-ray emission is called Energy Dispersive Spectroscopy (EDS).

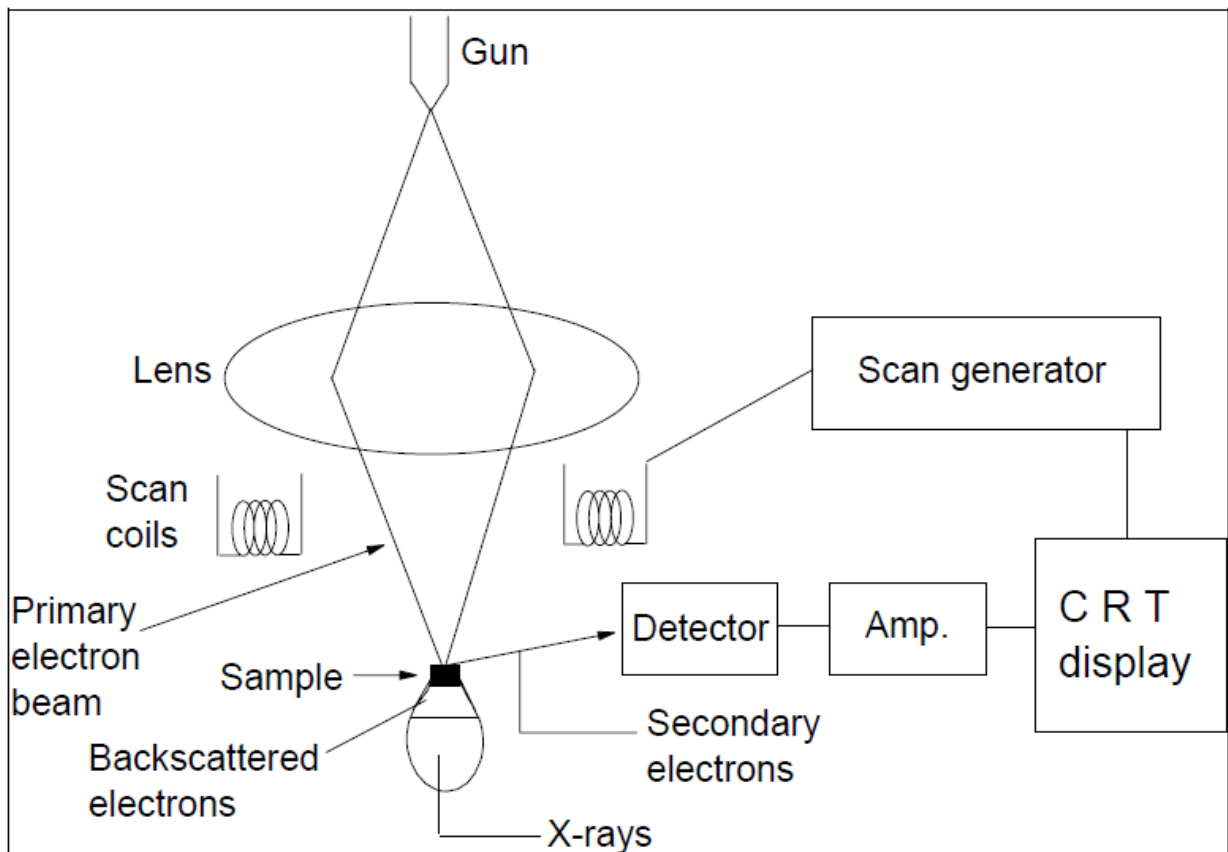


**Figure 2.7: Schematic of the scanning electron microscope (SEM). Modified extract from [80]**

EDS is generally used to determine the elemental composition of a material. A focused beam of electrons bombards the sample, and an x-ray spectrum is emitted. In principle, all elements from atomic number 4 (Be) to 92 (U) can be detected, although not all instruments are equipped for 'light' elements ( $Z < 10$ ) [81].

### 2.3.3 Malvern Analysis

The technique of laser diffraction is based on the principle that particles passing through a laser beam will scatter light at an angle that is directly related to their size [82]. The observed scattering angle increases as the particle size decreases. Large particles would scatter light at narrow angles with high intensity, whereas small particles scatter at wider angles but with low intensity. The primary measurement that generally has to be carried out within a laser diffraction system is the capture of the light scattering data from the particles under study (refer to Figure 2.8). Typically, a system consists of a laser which provides light at a fixed wavelength, a sample presentation system to ensure that the material under test passes through the laser beam as a homogeneous stream of particles and a series of detectors which are used to measure the light pattern produced over a wide range of angles.

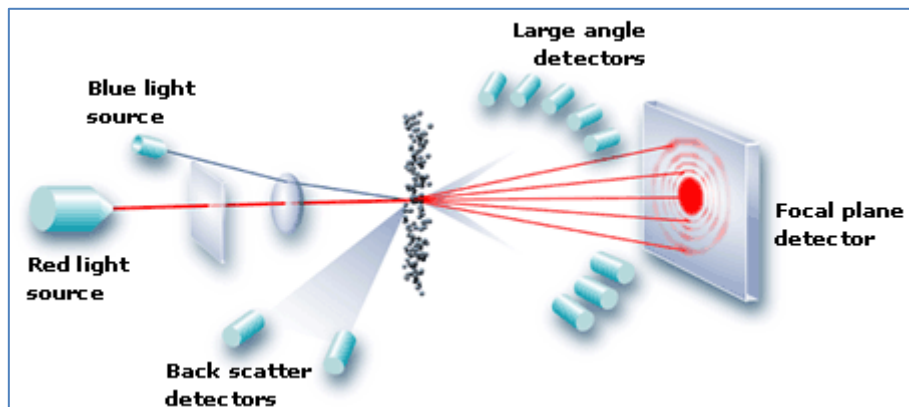


**Figure 2.8: Laser Diffraction Particle Sizing [82]**

### 2.3.4 X-ray Tomography

The basis of X-ray tomography is X-ray radiography. Essentially, an x-ray beam is directed onto a sample and the transmitted beam is recorded on a detector (refer to



Figure 2.9). According to the Beer–Lambert law, the ratio of the number of transmitted to incident photons is related to the integral of the absorption coefficient of the material along the path that the photons follow through the sample [83]. In the area of the photoelectric effect, the absorption coefficient is linked to the density, the atomic number and the energy (that is when the beam is monochromatic) by using an empirical law. The resulting image is a super-imposed projection of a volume in a 2D plane. The typical way to get 3D information is to perform a large number of radiographs while rotating the sample between 0° and 180°.

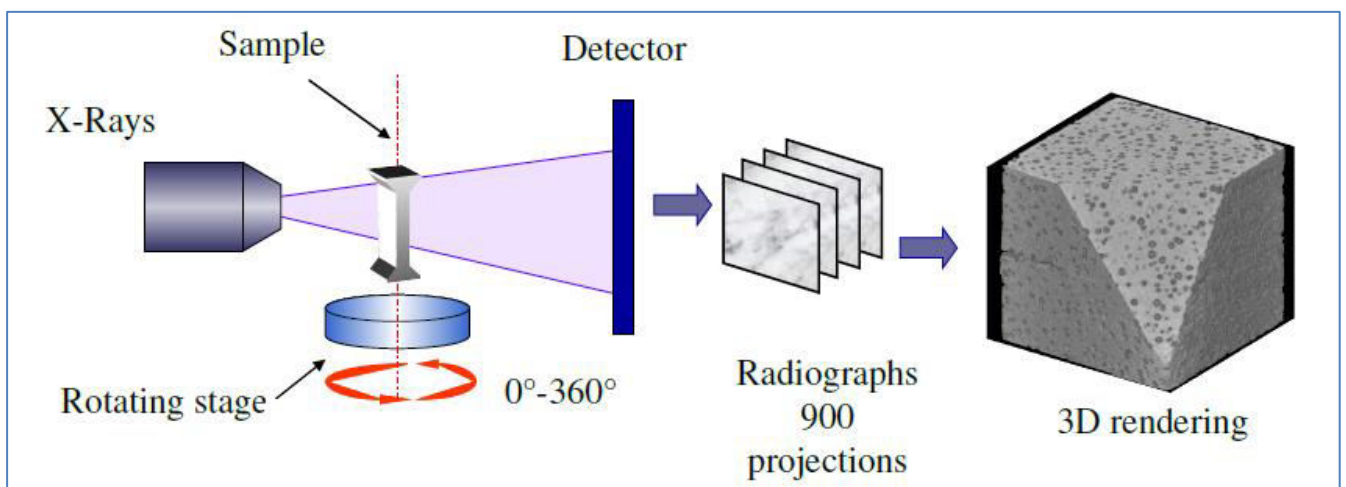


**Figure 2.9: Schematic of the principle of X-ray tomography [84]**

### 2.3.5 Transmission Electron Microscopy (TEM)

TEM allows the visualization of thin slices of material with nanometre resolution. A TEM operates much like a light microscope, but uses electrons instead of visible light, since the wavelength of electrons is much smaller than visible light [85]. A schematic of the TEM is shown in Figure 2.10.

TEM uses high energy electrons (up to 300 kV accelerating voltage) which are accelerated to nearly the speed of light [86]. The electron beam behaves like a wave front with wavelength about a million times shorter than light waves. When an electron beam passes through a thin-section specimen of a material, the electrons are scattered. A sophisticated system of electromagnetic lenses focuses the scattered electrons into an

image or a diffraction pattern. There are various modes that the TEM can operate, viz. the imaging mode provides a highly magnified view of the specimen, the diffraction mode displays accurate information about the local crystal structure and the nano-analytical mode provides information on the elemental composition of the material.

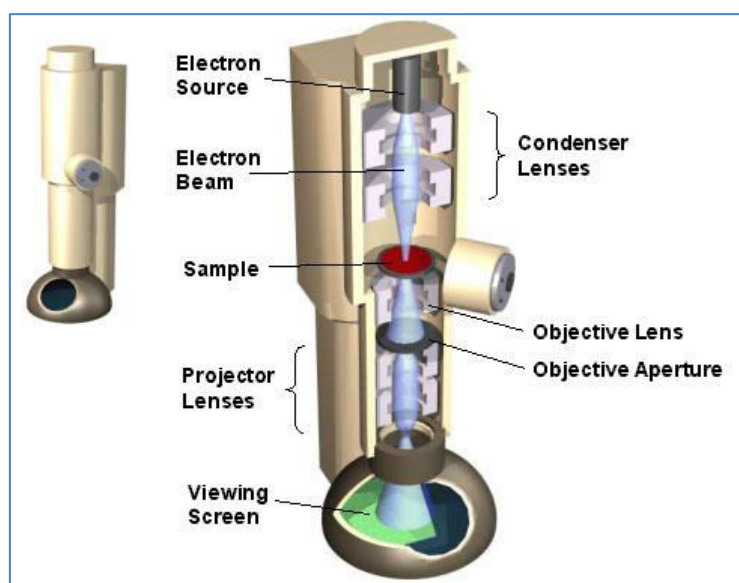


**Figure 2.10: Schematic of a Transmission electron microscope (TEM) [85]**

## 2.4 Results

### 2.4.1 XRD analysis of powder

X-ray diffraction analysis was done using a Panalytical X'Pert Pro fitted with an Anton Paar HTK1400 non-ambient stage. A cobalt tube was used with  $K\alpha = 1.789\text{\AA}$ . In addition, the PANalytical HighScore Plus (version 3.0) and the ICSD database (version 1.5) software packages were used.

X-ray diffraction (XRD) analysis was carried out on the vanadium carbide powder that was used in the sintering experiments. The XRD was scanned from  $20^\circ 2\theta$  to  $90^\circ 2\theta$  to cover the whole spectrum, with a step size of  $0.0170^\circ 2\theta$  and a scan step time of 29.84

seconds. Major VC peaks appear at  $43.68^{\circ}2\theta$  and  $50.87^{\circ}2\theta$  (refer to Figure 2.11), and no impurities were found to be present in the raw material. The most stable phase of VC was found to be  $C_7V_8$ .

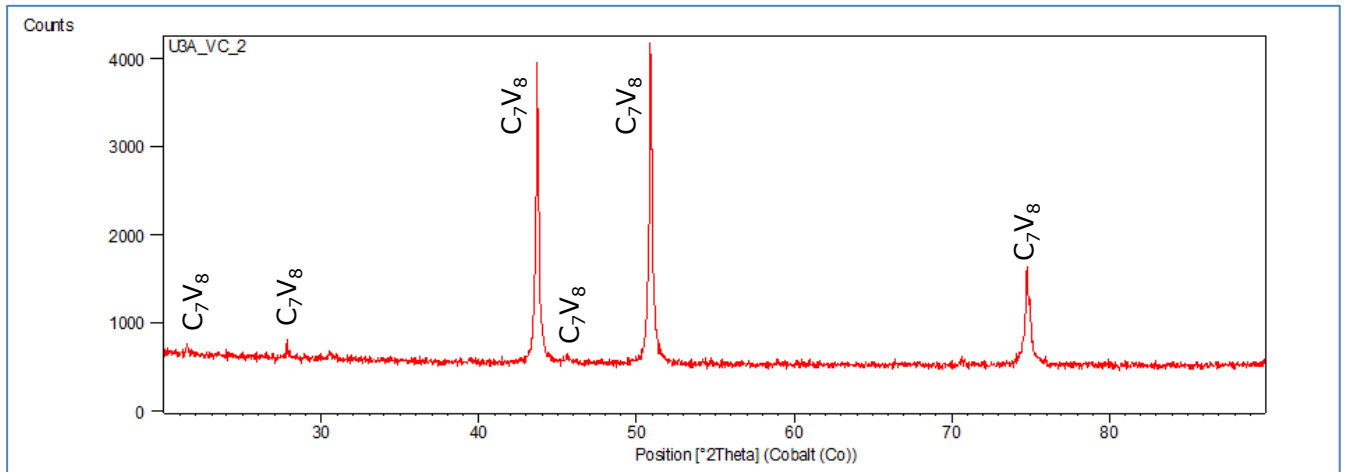


**Figure 2.11: X-ray Diffraction pattern for the vanadium carbide powder**

Scanning Electron Microscopy (SEM) was also carried out on the VC powder as well as the powder mix in order to determine the homogeneity, particle shape and size of the powder mix.

Figure 2.12 shows the SEM microstructures of the powder mix for the VC containing PCD consisting predominantly of diamond, 3wt% VC, admilled WC and 1wt% cobalt at various magnifications. The powder mix was dispersed onto carbon tape and then analysed. The diamond particles are blocky, angular and vary in shape. Figure 2.13 shows the various components of the powder mix. In an SEM image, the lighter the atomic mass of the particle, the darker the particle appears on the image, e.g. the mass of carbon appears much lighter than the mass of tungsten, and therefore the appearance of carbon is much darker than the appearance of WC. The VC appears as 'fluffy' particulates, whereas the cobalt is present as spherical particles. The WC varies in particle size as these particles have been abraded from the WC milling media. In general, the mix looks homogeneous, and the VC additive is much smaller than the diamond matrix which is the major constituent.

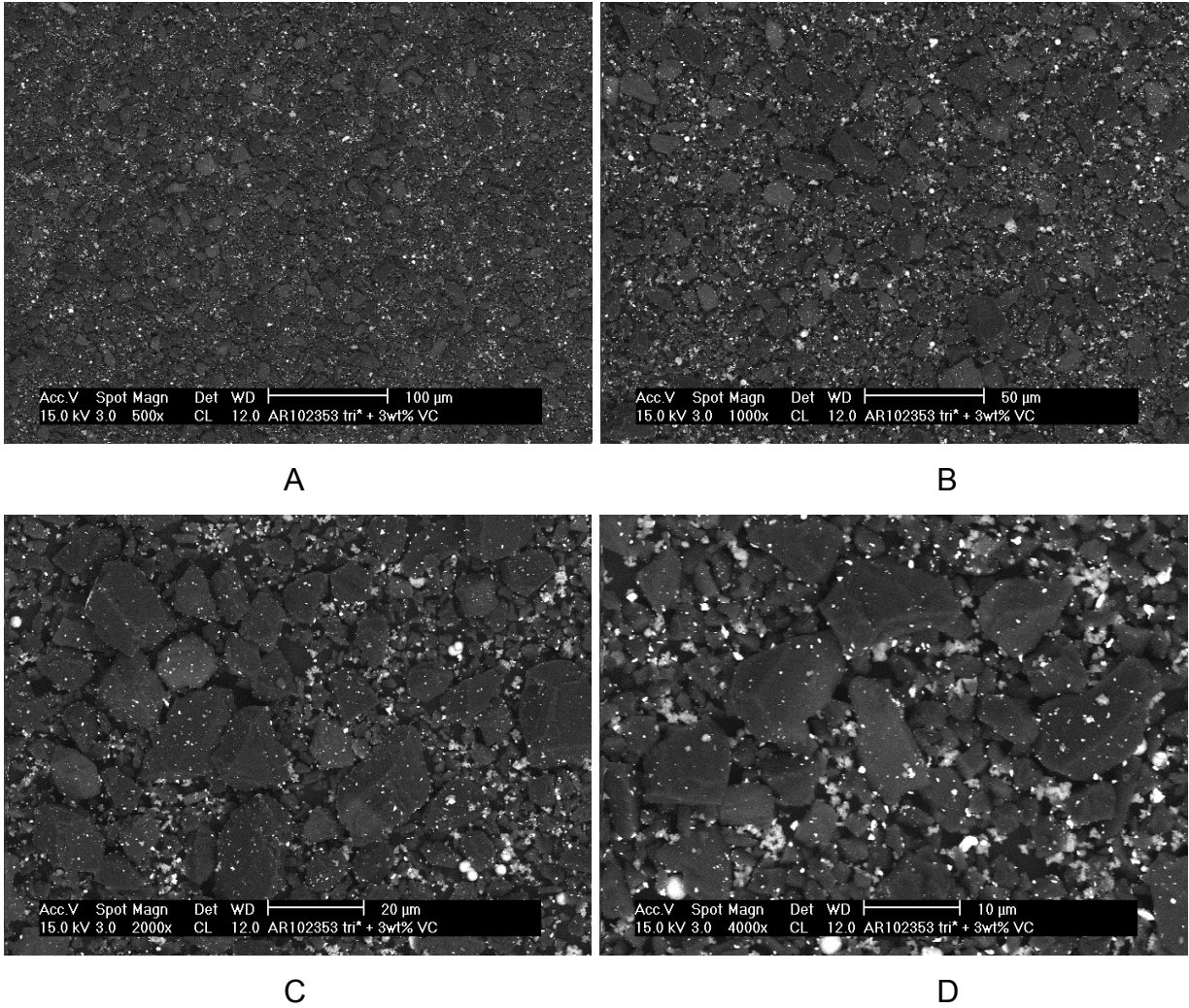


**Figure 2.12: SEM microstructures of the powder mix consisting predominantly of diamond, and a combination of VC, WC and cobalt – A (500x mag), B (1000x mag), C (2000x mag) and D (4000x mag)**

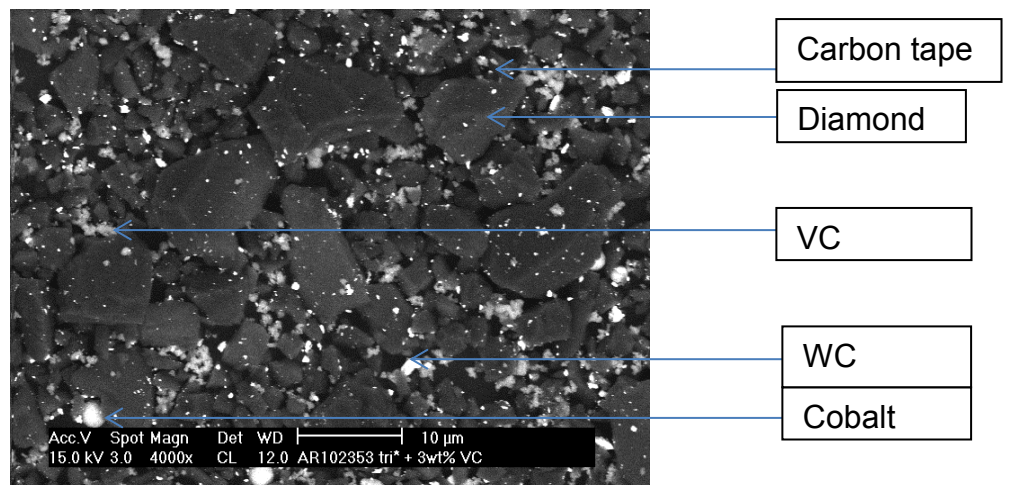


**Figure 2.13: Various components of the powder mix**

Malvern analysis is generally used to determine the particle size of a sample. Figure 2.14 shows the Malvern distribution of the VC powder and Figure 2.15 shows the Malvern distribution of the diamond – VC powder mix. The volume weighted mean  $D[4,3]$  for the VC powder was 3.08  $\mu\text{m}$ , and the volume weighted mean for the powder mix was 9.97  $\mu\text{m}$ . The Malvern distribution in Figure 2.15 shows a major peak with a minor shoulder peak. This is most probably indicative of a coarser fraction and a finer fraction of particles.

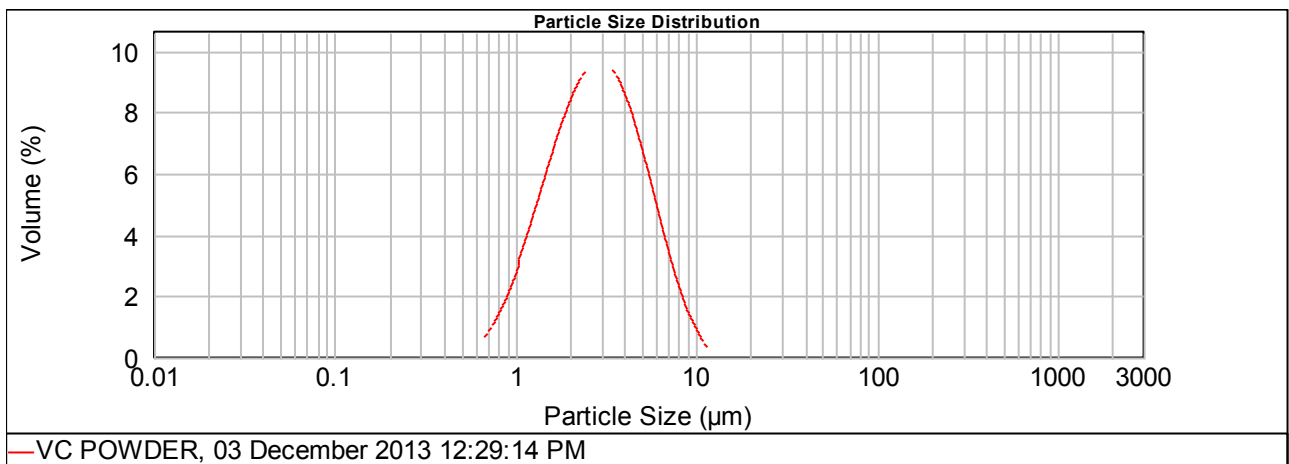


**Figure 2.14: Malvern distribution of the VC powder**

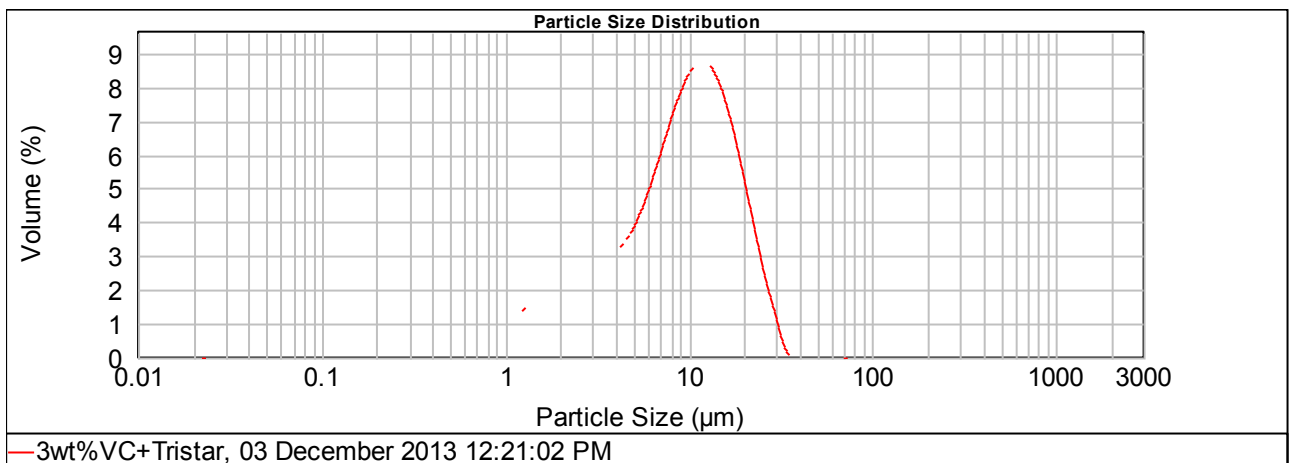


**Figure 2.15: Malvern distribution of the diamond-VC powder mix**

## 2.4.2 Sintering of PCD

### 2.4.2.1 Experiment 1: Sintering of solid PCD containing no VC

A solid PCD is a PCD that is not attached to a WC substrate. A new technique of sintering had to be developed for the sintering of the solid PCD. Therefore, in order to assess whether a solid VC doped PCD can be sintered using the modified sintering method, a standard PCD containing no VC was initially sintered prior to assessing the infiltration of a VC layer into the PCD. Figure 2.16 shows the microstructural images of the standard PCD. This was shown to be well sintered from the bottom of the PCD (i.e. region of the cobalt foil) to the top of the PCD.

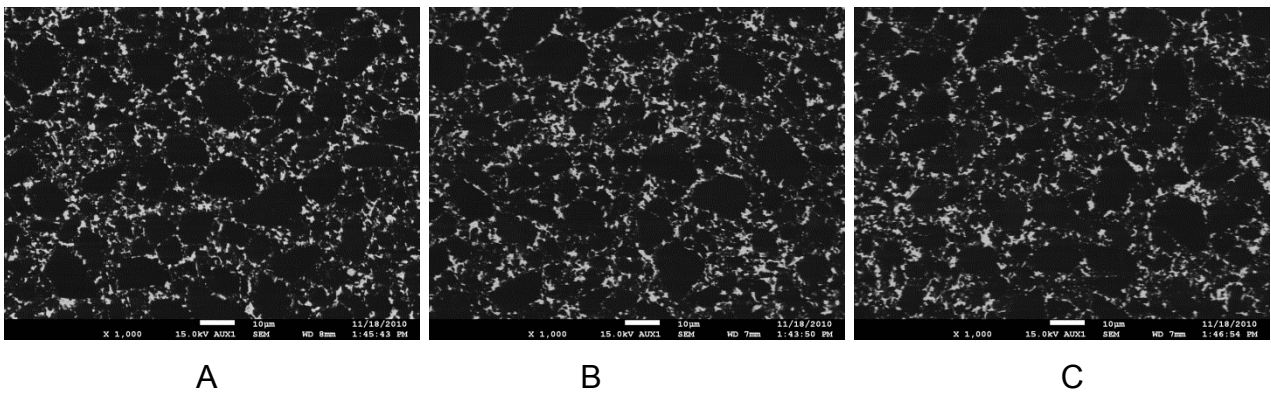


**Figure 2.16: Microstructural images of the standard PCD: A (bottom PCD, i.e. PCD near the foil), B (bulk PCD), C (top PCD)**

X-ray tomography analysis was performed on the samples. The power of the x-ray was 14.9W with a magnification of 6x. The x-ray image of the standard PCD (shown in Figure 2.17) shows no evidence of cracks or the presence of plumes. The lighter shade in the image is the PCD and the darker shade is the magnetic stub which holds the PCD.

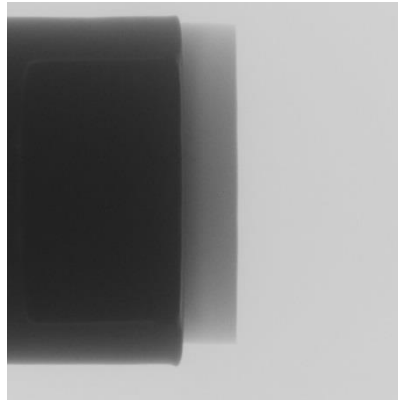


**Figure 2.17: X-ray image of the standard PCD**

EDS mapping was performed on the sample to determine the levels of cobalt and tungsten in the PCD (refer to Figure 2.18). The zero point on the x-axis refers to the cobalt foil – PCD interface. The carbon content was found to be lower in the cobalt foil regime (demarcated by the smallest distance) and gradually increased in the PCD layer as a function of distance. The cobalt foil interlayer can clearly be seen in the image shown in Figure 2.18.

There is always oxygen present in the PCD and this cannot be avoided, although the presence of oxygen is always minimised. Oxygen has a tendency to compete with carbon for solubility in cobalt [11], i.e. as the concentration of oxygen in the PCD increases, the solubility of carbon in the binder pool decreases. If the solubility of carbon in the binder pool decreases, the quality of sintering deteriorates. According to the EDS profile, the oxygen content in the cobalt foil region seems much higher than the oxygen content in the PCD.

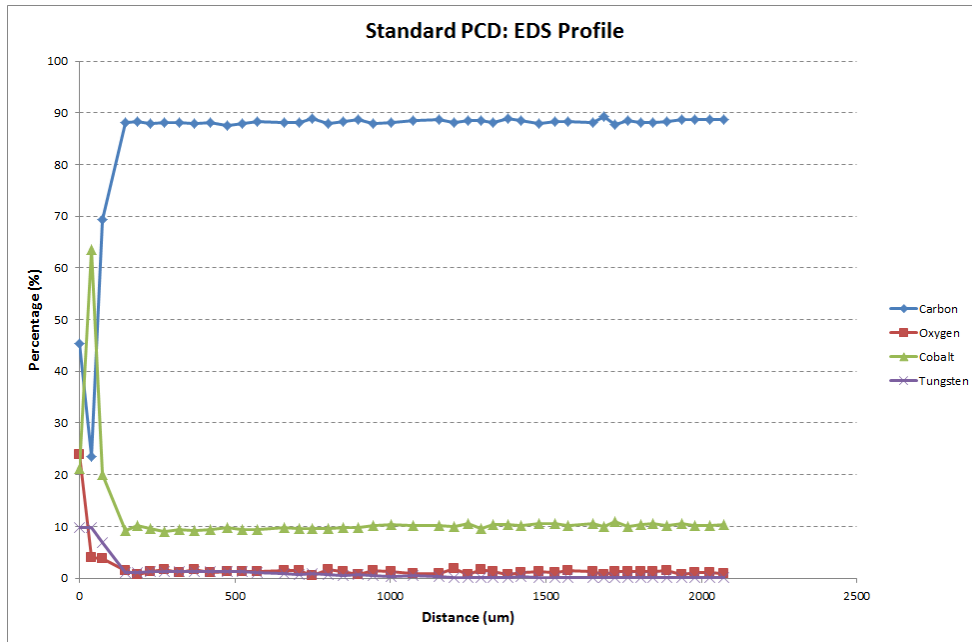


**Figure 2.18: EDS map of the standard solid PCD, showing the concentration of carbon, oxygen, cobalt and tungsten as a function of PCD distance**

The cobalt content is initially high in the cobalt foil region, which is to be expected, and then rapidly decreases to a fairly constant concentration of 10%. Similarly, the tungsten content is initially higher and then reduces to very low levels in the PCD. As mentioned previously, the tungsten is introduced to the PCD during the ball milling process, and not intentionally added to the PCD.

Table 2.2 shows the average EDS values for the elements found in the PCD. Since PCD consists primarily of diamond, the element with the highest concentration is carbon. The tungsten content is low since the only source of tungsten was from the milling media. The standard deviation values are high due to the heterogeneous nature of the material being analysed.

**Table 2.2: Average EDS values for the elements in the solid PCD (Standard PCD)**

	Carbon	Oxygen	Cobalt	Tungsten
Mean	85	1.9	12	1.1
Standard Deviation	12	4	8	2



XRD analysis was carried out on the sintered compact (refer to Figure 2.19). The peaks are labelled according to the phases present in the database. The pattern shows the presence of diamond, tungsten carbide (WC) and tungsten dissolved in cobalt ( $\text{Co}_{0.87}\text{W}_{0.13}$ ). The reference peak for  $\text{Co}_{0.87}\text{W}_{0.13}$  according to the ICSD database occurs at  $59.853^\circ 2\theta$ , whilst the observed  $\text{Co}_{0.87}\text{W}_{0.13}$  peak shown in Figure 2.19 appears at  $59.752^\circ 2\theta$ . Due to the close proximity of the peak positions, it can be inferred that the peak observed is the Co-W solid solution.

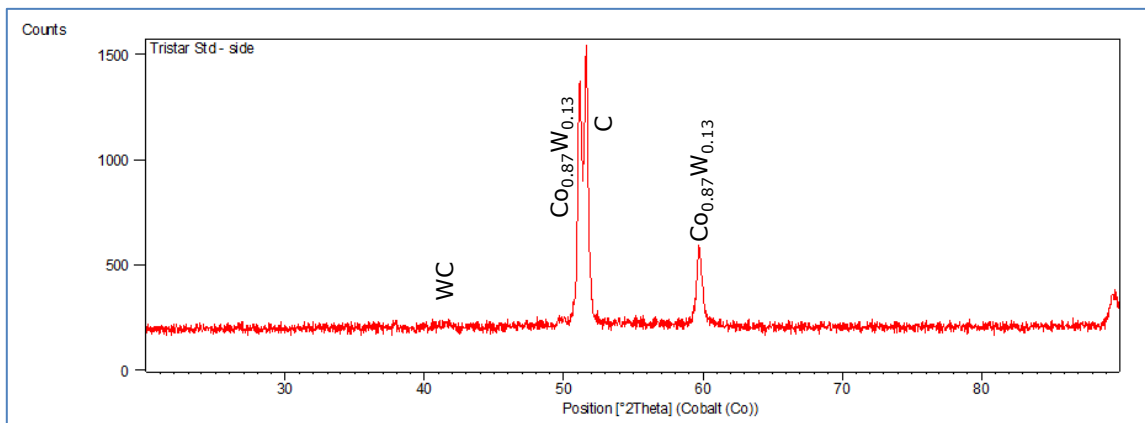


**Figure 2.19: XRD pattern of the standard solid PCD**

Generally, the sintering of the standard solid PCD was successful and could be used as a reference to analyse the other sintering methods.

#### 2.4.2.2 Experiment 2: Sintering of PCD infiltrated with a first layer of 3wt% (1.85vol%) VC powder and a second layer of 20wt% (9vol%) Co foil

The rationale for this experiment was to determine the quality of PCD obtained by infiltrating the PCD with VC powder instead of admixing VC into the diamond powder. Figure 2.20 shows the microstructural images of the solid PCD with VC infiltration. The sintering of the PCD seems to be compromised with large binder pools appearing in the sintered structure, especially at the bottom and at the top of the PCD. This observation was consistent throughout the sample.

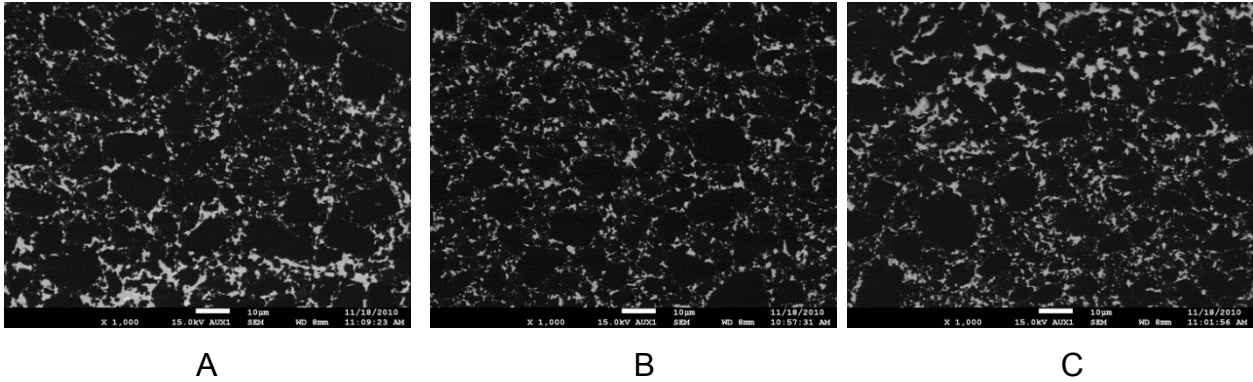


**Figure 2.20: Microstructural images of the PCD infiltrated with VC: A (bottom PCD, i.e. PCD near the foil), B (bulk PCD), C (top PCD)**

Figure 2.21 shows the VC layer at the bottom of the PCD and Figure 2.22 shows the EDS spectrum of the VC layer. The layer at the bottom of the PCD comprises three distinct phases, viz. (V,W)C<sub>x</sub> phase, VC phase and the canister material (i.e. NbC). It would appear that the tungsten from the admixed diamond diffused into the VC layer to form the (V,W)C<sub>x</sub> phase.

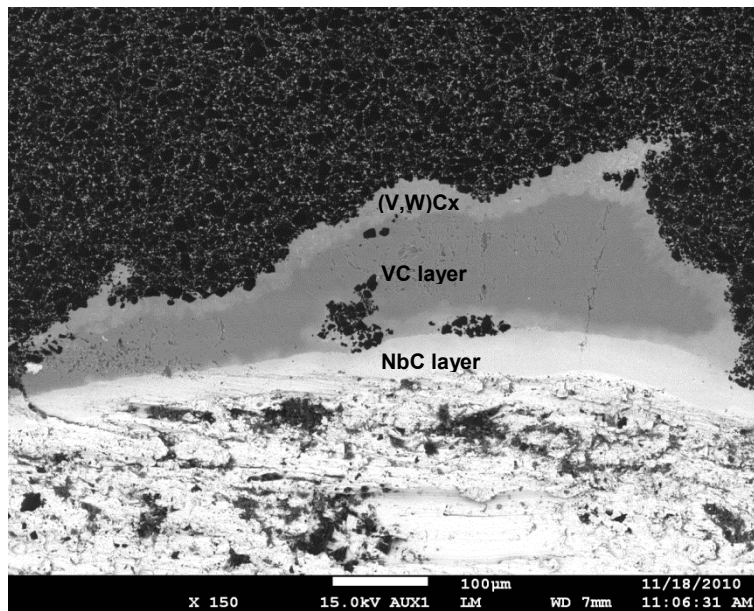


**Figure 2.21: Image showing the VC layer at the bottom of the PCD**

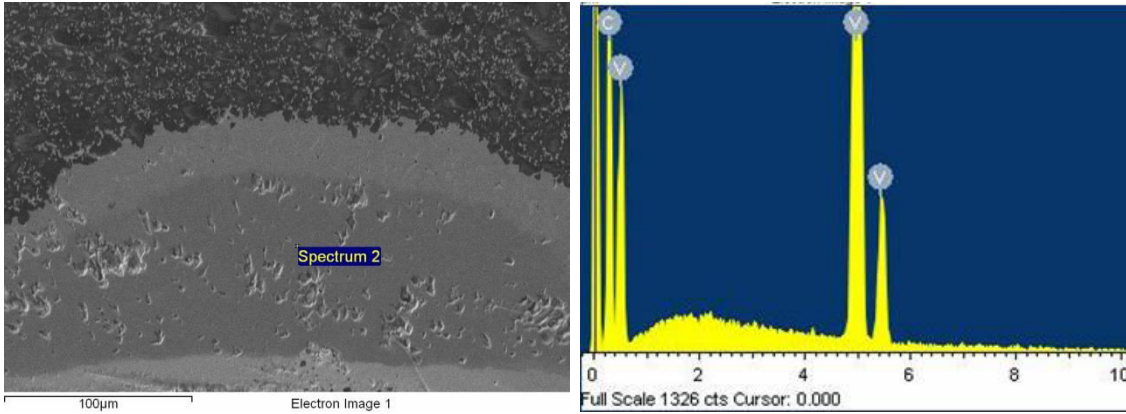


**Figure 2.22: Image showing the EDS spectrum of the VC layer, identified by 'Spectrum 2'**

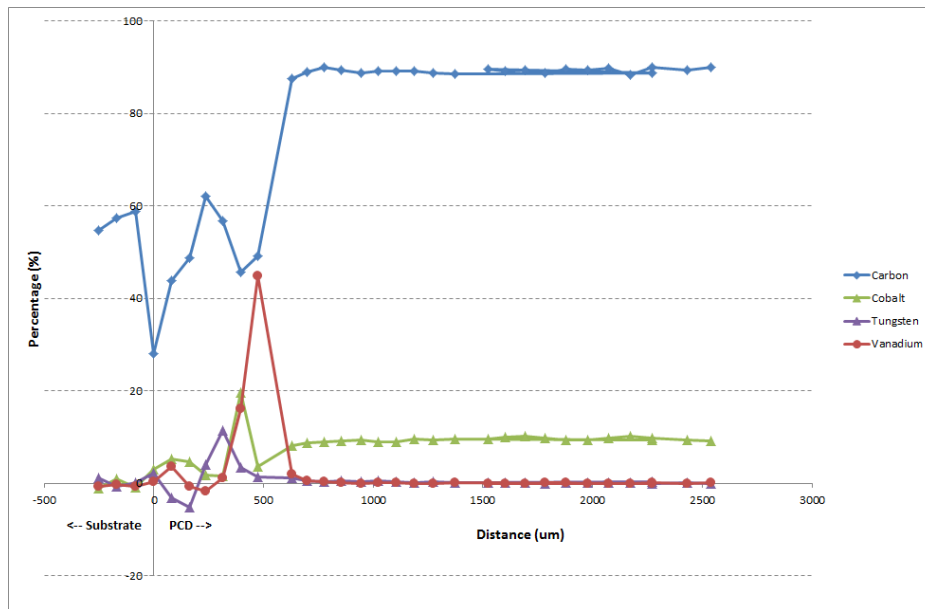


**Figure 2.23: EDS Profile for PCD infiltrated with VC powder, showing the concentration of carbon, cobalt, tungsten and vanadium as a function of PCD distance**

The EDS profile is shown in Figure 2.23. The cobalt content is low as the profile is taken from the VC layer, and gradually increases to average at approximately 9vol%. The VC content sharply increases in the regime of the VC layer and then abruptly decreases significantly in the PCD. The amount of WC shown in the PCD is also very low. Below

500  $\mu\text{m}$ , in addition to the elements present in Figure 2.23, there appeared to be a large concentration of oxygen present which is not displayed on the graph. The oxygen seemed to be present predominantly in the infiltration layer. The EDS profile implies that the VC has not effectively infiltrated the PCD and seems to have combined with the residual tungsten in the diamond powder to form a (V,W) $\text{C}_x$  phase.

**Table 2.3: EDS Analysis of the VC Phase and the (V,W) $\text{C}_x$  Phase normalised to 8 carbon atoms**

Phase	Analysis No.	Carbon (at%)	Vanadium (at%)	Tungsten (at%)	Cobalt (at%)	Observed Stoichiometry
VC	1	53.67	45.9	-	-	$\text{V}_{6.84}\text{C}_8$
	2	49.94	49.86	-	-	$\text{V}_{7.99}\text{C}_8$
	3	49.86	50.14	-	-	$\text{V}_{8.04}\text{C}_8$
	4	50.88	49.11	-	-	$\text{V}_{7.72}\text{C}_8$
	5	50.29	49.71	-	-	$\text{V}_{7.91}\text{C}_8$
	6	49.25	50.75	-	-	$\text{V}_{8.24}\text{C}_8$
	7	46.31	53.69	-	-	$\text{V}_{9.27}\text{C}_8$
	8	49.18	50.82	-	-	$\text{V}_{8.27}\text{C}_8$
	9	48.37	51.62	-	-	$\text{V}_{8.54}\text{C}_8$
	10	52.68	47.32	-	-	$\text{V}_{7.19}\text{C}_8$
(V,W) $\text{C}_x$	1	49.47	42.89	2.38	5.26	$\text{V}_{6.94}\text{W}_{0.38}\text{Co}_{0.85}\text{C}_8$
	2	49.04	41.21	2.34	7.41	$\text{V}_{6.72}\text{W}_{0.38}\text{Co}_{1.21}\text{C}_8$
	3	48.38	42.01	2.45	7.16	$\text{V}_{6.95}\text{W}_{0.47}\text{Co}_{1.36}\text{C}_8$
	4	48.74	45.19	2.73	3.34	$\text{V}_{7.42}\text{W}_{0.45}\text{Co}_{0.55}\text{C}_8$
	5	51.68	42.63	2.55	3.14	$\text{V}_{6.60}\text{W}_{0.39}\text{Co}_{0.49}\text{C}_8$
	6	49.32	42.51	2.49	5.67	$\text{V}_{6.90}\text{W}_{0.40}\text{Co}_{0.92}\text{C}_8$
	7	48.52	44.58	2.81	4.08	$\text{V}_{7.35}\text{W}_{0.46}\text{Co}_{0.67}\text{C}_8$
	8	47.85	41.65	2.55	7.94	$\text{V}_{6.96}\text{W}_{0.43}\text{Co}_{1.33}\text{C}_8$
	9	49.86	46.97	2.68	0.50	$\text{V}_{7.54}\text{W}_{0.43}\text{Co}_{0.80}\text{C}_8$
	10	48.94	48.59	1.93	0.53	$\text{V}_{7.94}\text{W}_{0.32}\text{Co}_{0.09}\text{C}_8$

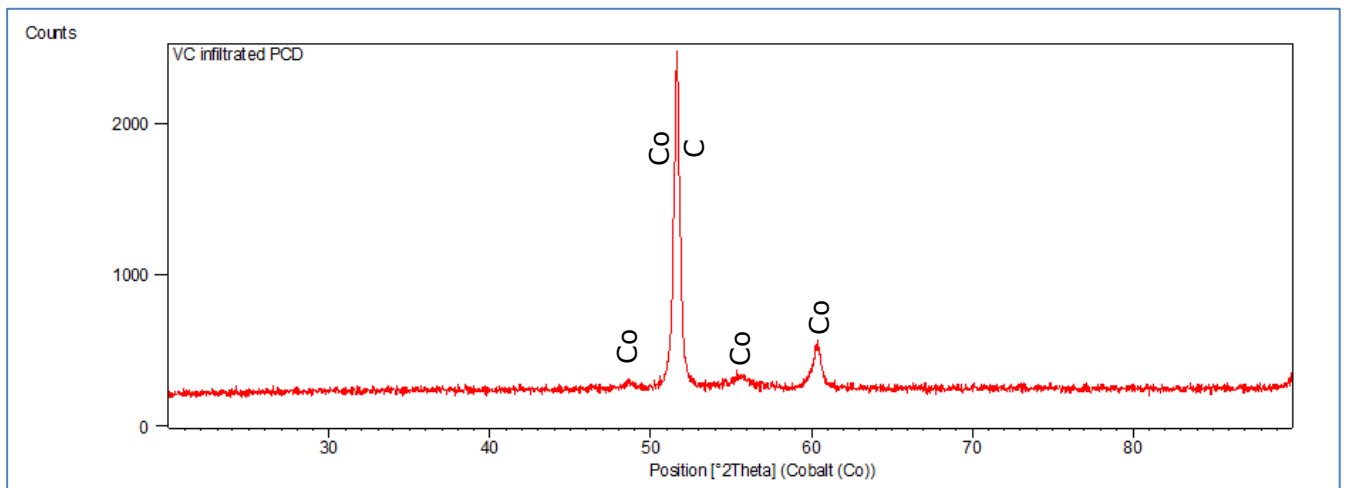
Table 2.3 shows the EDS analysis of the VC phase and the (V,W)C<sub>x</sub> phase. The table also shows the proposed stoichiometry based on the atomic percentage levels of the elements present. Using the average EDS values and removing the cobalt content, the stoichiometry of the (V,W)C<sub>x</sub> phase was found to be C<sub>4.1</sub>V<sub>3.7</sub>W<sub>0.2</sub>.

Table 2.4 shows the average EDS values for the elements found in the PCD. Since PCD consists primarily of diamond, the element with the highest concentration is carbon. Both the tungsten and vanadium content is low.

**Table 2.4: Average EDS values for the elements in the PCD infiltrated with VC**

	Carbon	Oxygen	Cobalt	Tungsten	Vanadium
Mean	89.20	0.88	9.45	0.29	0.18
Std Deviation	0.58	0.42	0.47	0.27	0.43

XRD analysis was carried out on the sintered compact (refer to Figure 2.24). The pattern shows the presence of diamond and cobalt. There does not seem to be a sufficient quantity of either WC or VC to be detected by the XRD analysis.



**Figure 2.24: XRD pattern for the PCD infiltrated with VC powder**

ICP analysis was performed on the standard solid PCD and the PCD with VC infiltration to determine the levels of cobalt and tungsten within the PCD (refer to Table 2.5). Although standard PCD typically contains 20wt% binder (combination of cobalt and

tungsten), the solid PCD seems to contain slightly less binder, i.e. 17.2%. The PCD with VC infiltration shows a lower cobalt content as compared to the standard PCD and a much lower tungsten content. The low cobalt content could be due to VC forming a barrier for cobalt diffusion into the PCD, and the low tungsten content could be as a result of the combination of the residual tungsten in the PCD with the VC to form a (V,W)C<sub>x</sub> phase.

**Table 2.5: ICP results showing Co and W content for solid sintered PCD**

<b>Sample</b>	<b>Co (%)</b>	<b>W (%)</b>	<b>Total Binder</b>
Standard PCD	16.7	0.5	17.2
VC infiltrated PCD	14.0	<0.1	14.0

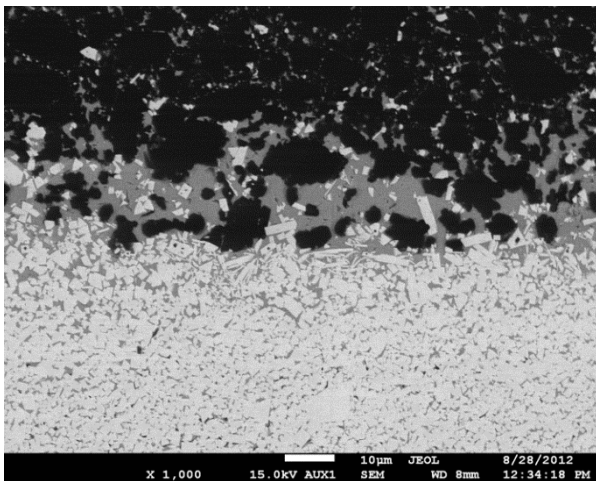
The feasibility experiments show that PCD can be sintered separate from the substrate, but PCD sintered by infiltration from a VC interlayer was found to be unsuccessful. The method for the addition of VC to PCD was hence chosen to be admixing into the diamond powder prior to sintering.

#### 2.4.2.3 Sintering of PCD with 3wt% (1.85vol%) VC admixed into the diamond powder and sintered onto a WC substrate

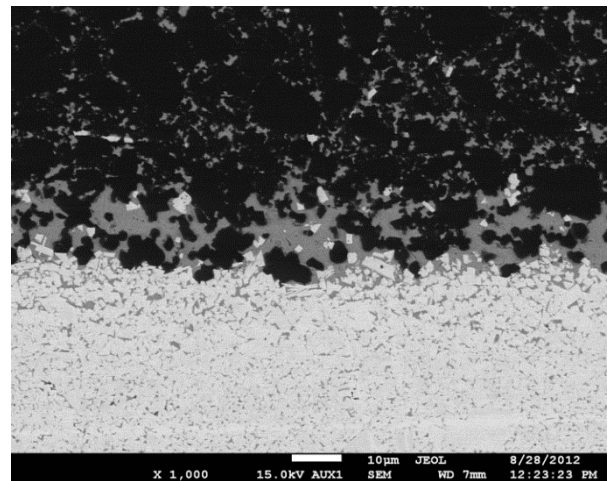
Figure 2.25 shows the microstructural images of the standard PCD sintered onto a WC substrate and the PCD containing 3wt% VC. Both sets of microstructures seem similar, i.e. there is adequate diamond-diamond bonding, and the interface looks acceptable. At the interface, the acicular tungsten carbide grains are clearly visible and there is sufficient cobalt pooling to ensure that the bond between the PCD and the substrate is strengthened. The above interface structures show high levels of tungsten carbide precipitates. This is quite a normal observation as it is well known that the excess tungsten dissolved in the cobalt binder precipitates near the interface on the existing tungsten carbide seeds, and this leads to high levels of tungsten carbide being present

near the interface. Sometimes, the tungsten dissolved in the cobalt binder precipitates as larger tungsten carbide grains called plumes.

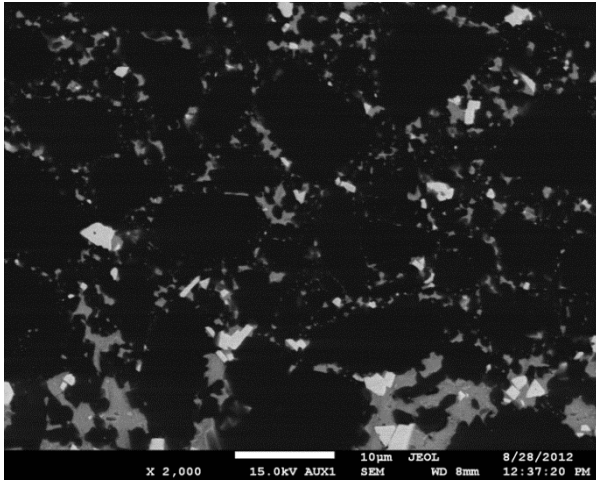
The vanadium carbide particles in the PCD are not very visible in Figure 2.25. However, when Figure 2.25E is compared with Figure 2.25F, there is a clear difference in the microstructure. Figure 2.25E shows the presence of tungsten carbide particles whereas there are no visible tungsten carbide particulates present in Figure 2.25F. From this observation, it can be inferred that the vanadium present in the PCD reacts with the tungsten to form a mixed carbide phase that is different from either vanadium carbide or tungsten carbide. The images of the top surface of the PCD shows some larger diamond grains that are bonded to adjacent grains with cobalt 'stitching' at the boundary of the grains. The 'stitching' phenomenon is basically a number of tiny cobalt pools bonded together.



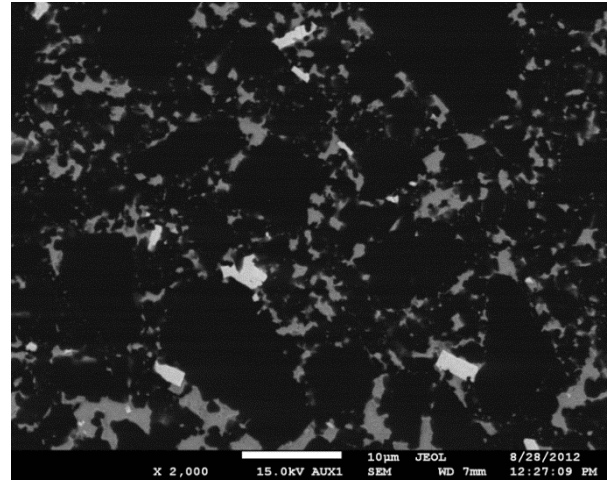
A



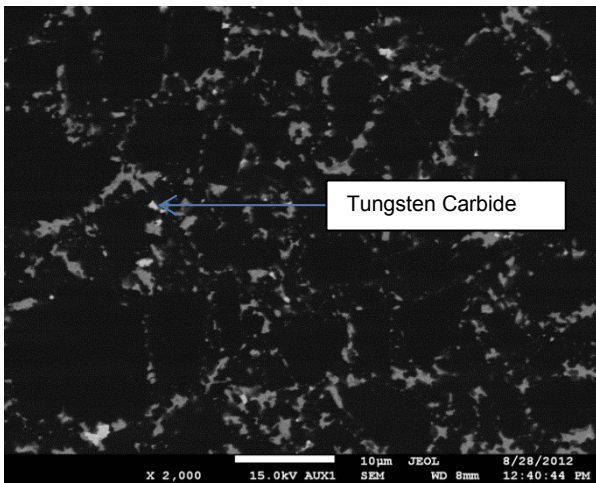
B



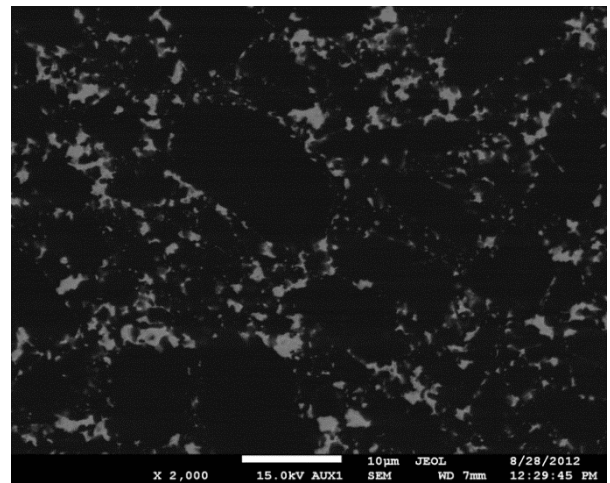
C



D



E



F

**Figure 2.25: Microstructural images of the standard PCD and the PCD containing 3wt% VC: A (interface structure of the standard PCD), B (interface structure of the PCD containing 3wt% VC), C (above interface structure of the standard PCD), D (above interface structure of the PCD containing 3wt% VC), E (top surface microstructure of the standard PCD), F (top surface microstructure of the PCD containing 3wt% VC)**

EDS analysis was carried out on the samples. It is important to note that the excitation volume of the PCD sample that emits the secondary X-rays is of the order of 10 micrometers in size. In the samples where the PCD was doped by VC, most carbide particles formed are less than 10 micrometers. This means that any analysis of the carbide particles would also include excited X-rays of the surrounding area, i.e. diamond.



Therefore, the carbon content of the carbides will usually be in excess, and the analysis would not be as accurate.

Spectra were taken at two areas of the PCD, i.e. the overall PCD and the binder pool. The EDS spectrum for the standard PCD is shown in Figure 2.26 and the EDS spectrum for the PCD containing 3wt% VC is shown in Figure 2.27. From the spectrum in Figure 2.26, it is clear that the standard PCD contains carbon, cobalt and WC which is to be expected. The spot analysis of the cobalt pool for the PCD containing 3wt% VC shows the presence of carbon, cobalt, tungsten and vanadium. The vanadium-tungsten particulate seems to precipitate at the binder pool.

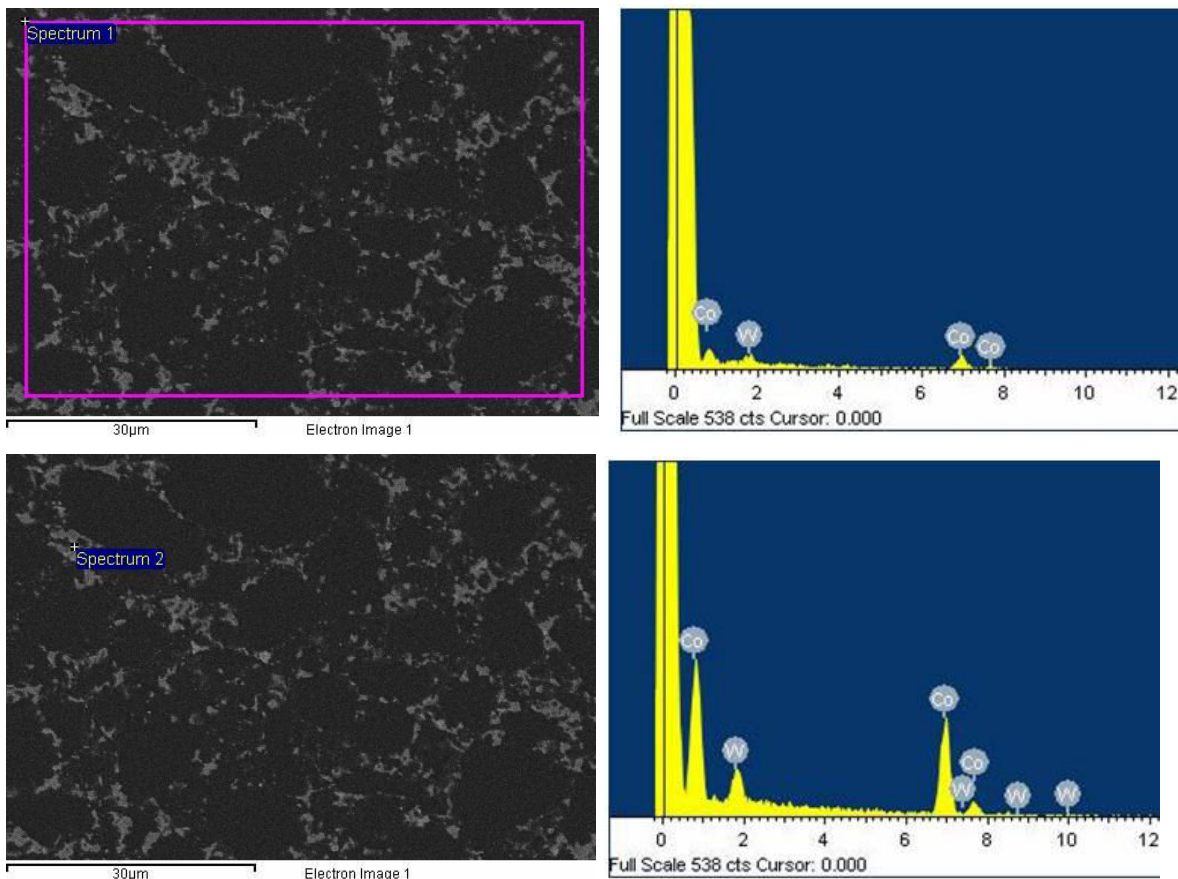


**Figure 2.26: EDS analysis of the standard PCD**

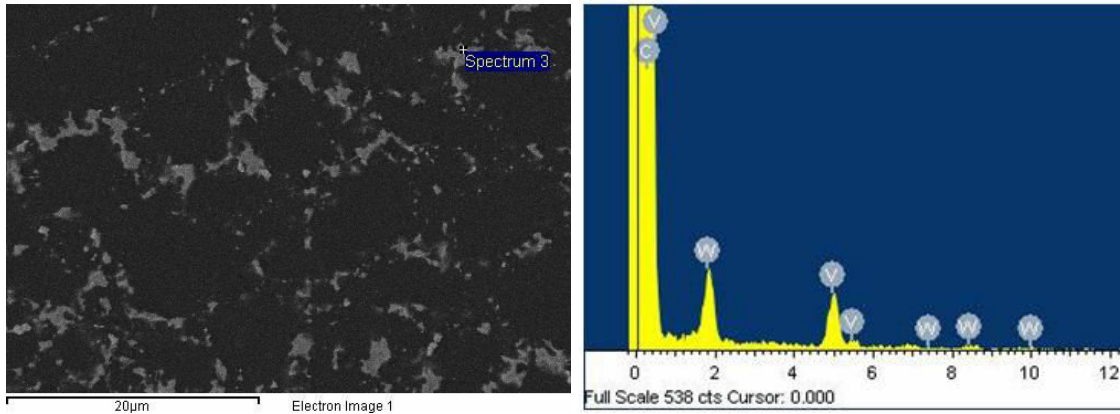


**Figure 2.27: EDS analysis of the PCD containing 3wt% VC**

The binder pools of the VC enhanced PCD were analysed using EDS (refer to Table 2.6). The atomic composition and ratio of the carbon, vanadium and tungsten atoms could not be attained due to the overwhelming presence of diamond particles and the large area of the EDS spot analysis. Generally, the size of the interaction volume increases with accelerating voltage. Hence, the ratio of vanadium and tungsten was determined. Table 2.6 shows the average measured ratio of vanadium: tungsten as 73:27 using EDS. The binder pool comprises the mixed carbide deposition, vanadium in solution with cobalt and tungsten in solution with the cobalt.

**Table 2.6: EDS analysis of the binder pool showing the ratio of V:W**

<b>Spectrum</b>	<b>V (at. %)</b>	<b>W (at. %)</b>	<b>Ratio of V:W (%)</b>
EDS 1	2.27	0.60	79:21
EDS 2	7.15	2.82	72:28
EDS 3	5.84	2.21	73:27
EDS 4	5.91	2.49	70:30
EDS 5	10.91	4.12	73:27
EDS 6	6.79	2.81	71:29
EDS 7	3.86	1.26	75:25
EDS 8	8.17	3.12	72:28
EDS 9	8.89	3.41	72:28
EDS 10	3.70	1.46	72:28
EDS 11	6.38	2.43	72:28
EDS 12	7.25	2.66	73:27

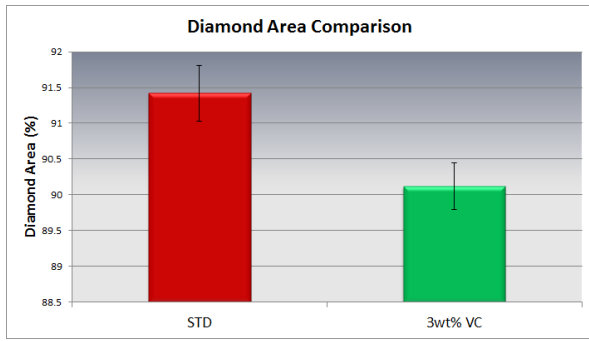
Image analysis was carried out on the samples to try to differentiate them. The method essentially measures the average diamond grain size, the binder pool size, diamond area, binder area, and the diamond contiguity of an image. Generally, it is known that the finer the diamond grain size, the smaller the binder pool size, and the higher the binder content. The binder area and the diamond area are inter-related. The lower the binder content, the more thermally stable the PCD becomes. In general, the higher the diamond content of the PCD, the more abrasion resistant the PCD.

Contiguity is defined as a continuous mass, or a series of features in contact or proximity. It is measured using a formula derived by Golovchan and Litoshenko, shown in Equation 2-1 [87], where C is contiguity,  $V_f$  is cobalt volume fraction, a and b are constants with values 0.64 and 0.39 and S is a measure of the spread in grain size. Diamond contiguity relates to the percentage of diamond particles in contact with each other.

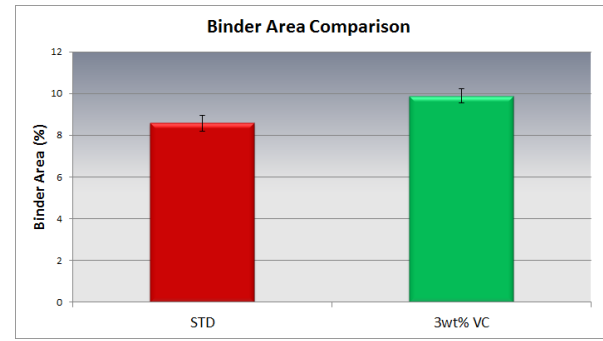
$$C = 1 - V_f^a (\exp bS)$$

**Equation 2-1**

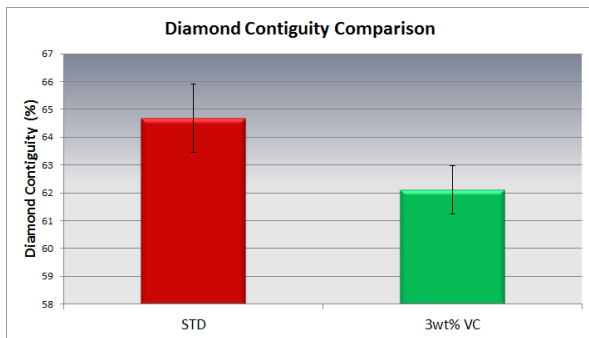
Sixteen images each at a 1000x magnification were used for the image analysis measurements. According to the image analysis data, the average diamond grain size, which was calculated using the mean chord length, for the standard PCD was similar to the sample containing 3wt% VC (i.e. Std PCD:  $8.14 \pm 3.46 \mu\text{m}$ , 3wt% VC PCD:  $7.95 \pm 3.62 \mu\text{m}$ ). The grain size of the PCD was not expected to change as a result of the addition of VC. Likewise, there was no significant difference observed in the binder pool size between the two samples (i.e. Std PCD:  $1.87 \pm 1.02 \mu\text{m}$ , 3wt% VC PCD:  $2.01 \pm 0.97 \mu\text{m}$ ). Figure 2.28 shows the image analysis comparison of the standard PCD and the PCD sample containing 3wt% VC.



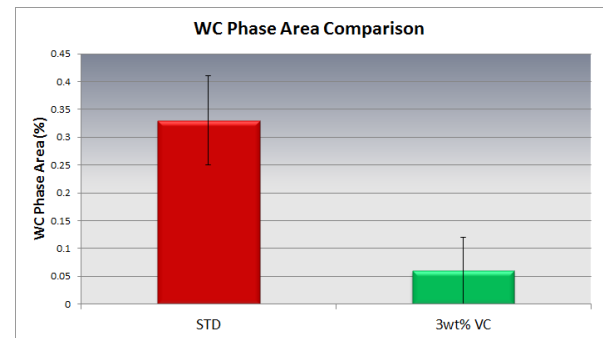
A



B



C

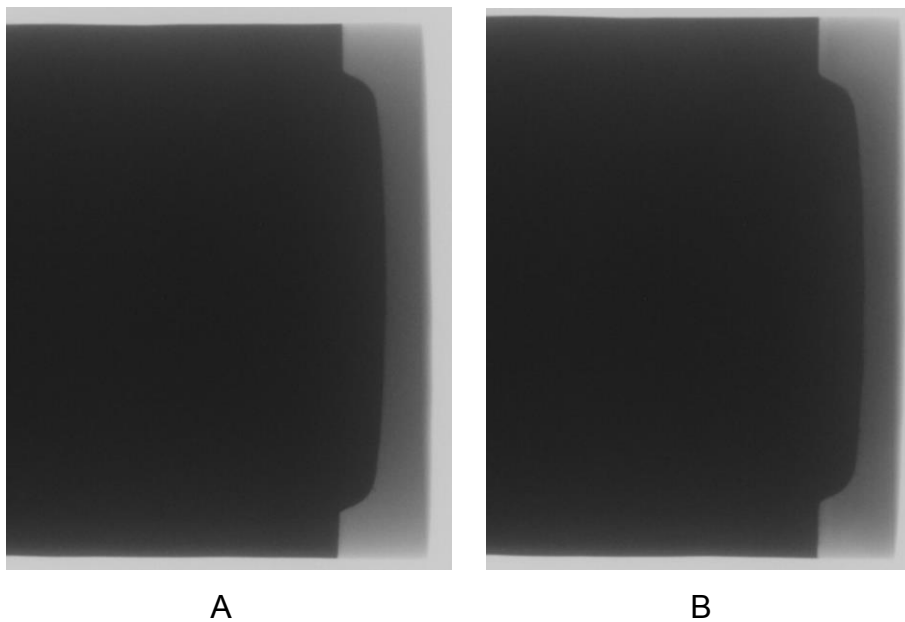


D

**Figure 2.28: Image Analysis of the Std PCD and PCD containing 3wt% VC: A (diamond area comparison), B (binder area comparison), C (diamond contiguity comparison) and D (WC phase area comparison)**

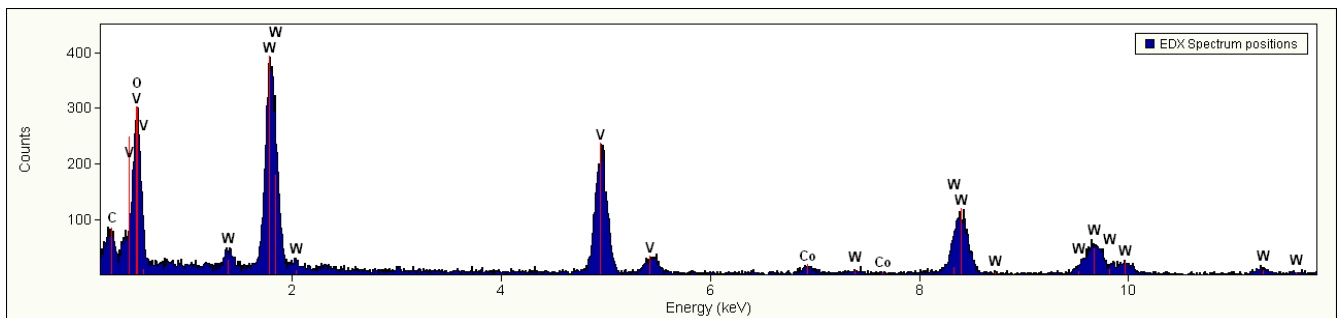
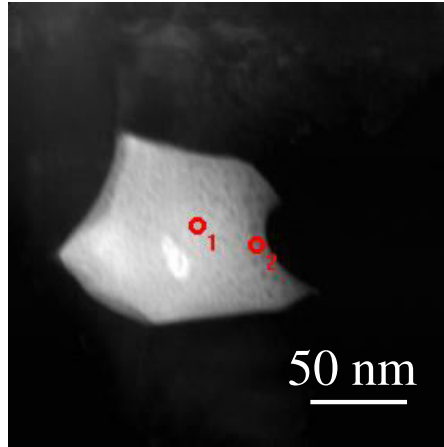
As mentioned previously, the diamond area and the binder area are inter-related. The 3wt% VC sample shows a significant decrease in diamond content and a significant increase in binder content. This result is not surprising since additional binder in the form of VC was intentionally added to the PCD. Figure 2.28C shows the diamond contiguity of the standard to be higher than the 3wt% VC sample. This is most probably due to the high binder content present in the PCD, i.e. less diamond-diamond contact. A low diamond contiguity is not necessarily cause for concern, and this may positively affect the performance of the material especially in drilling applications. The WC phase area of the standard seems much higher than the 3wt% VC sample. This again is to be expected since the microstructure of the VC containing PCD shows a decrease in the amount of WC present (refer to Figure 2.25F).

Figure 2.29 shows the x-ray tomography images of the sintered samples. The substrate can clearly be seen as the darker contrast showing the obvious WC substrate profile, and the lighter shade is the PCD. The x-ray analysis is usually used to detect the presence of anomalies in the sintered compact. Examples of anomalies are fine cracks, plumes or contaminants. From the images shown in Figure 2.29, both samples are well sintered with no obvious defects present. If defects were to be present in the sintered compact, the x-ray equipment could be calibrated to measure the dimensions of the defect.



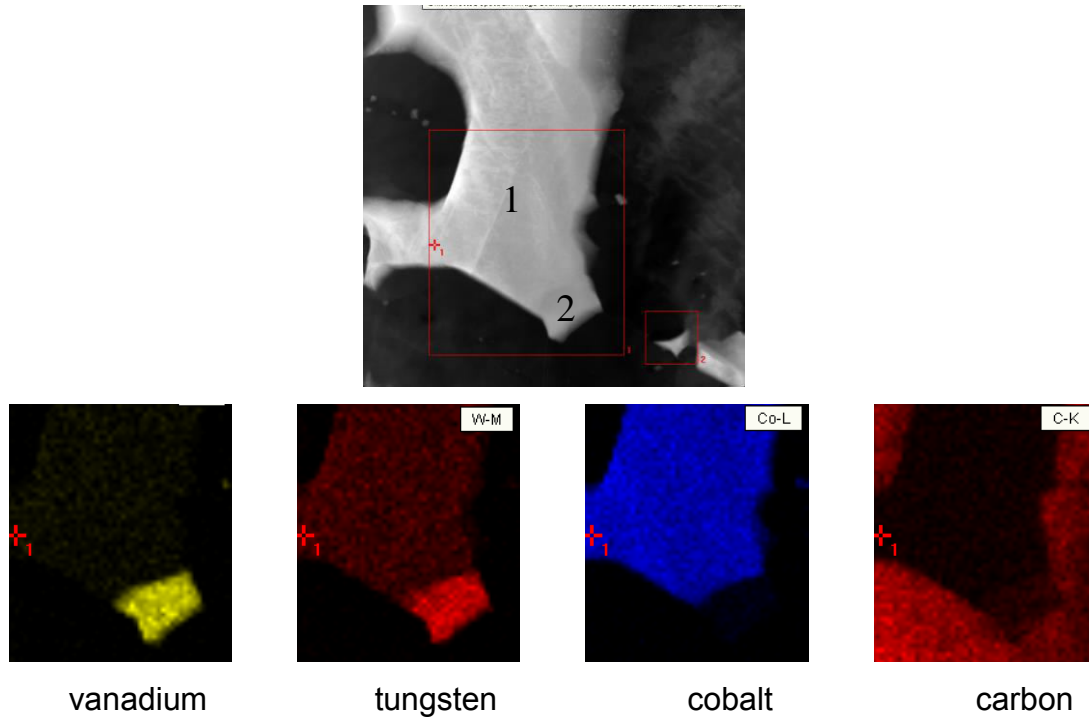
**Figure 2.29: X-ray image of the sintered samples: A (Standard PCD) and B (PCD containing 3wt% VC)**

The microstructures of the PCD containing 3wt% VC do not clearly show the presence of the VC. Hence Transmission Electron Microscopy (TEM) analysis was carried out on the sample by Dr Johan Westraadt at NMMU. A thin specimen of the PCD containing 3wt% VC was prepared using ion beam milling and then analysed using the TEM (refer to Figure 2.30). An area of the binder pool in the sample was analysed to qualify the elements present in the specific section of the material. EDX analysis showed the area to consist predominantly of a mixture of vanadium and tungsten with a small amount of dissolved cobalt.



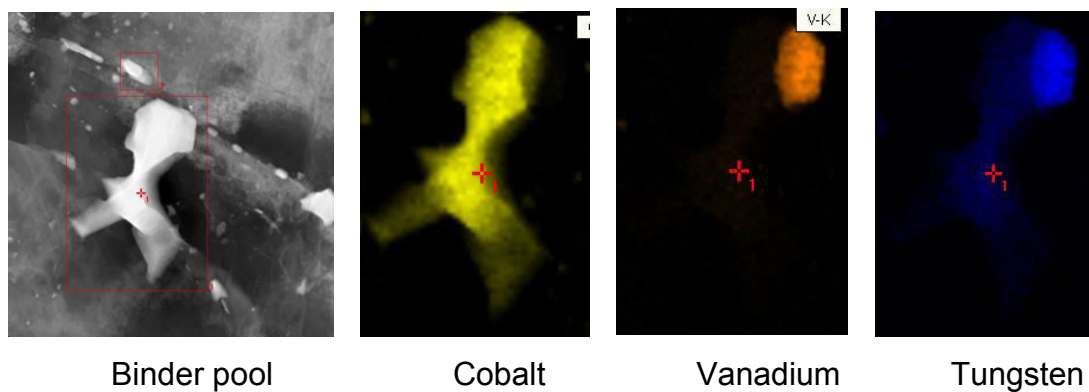
**Figure 2.30: HAADF (High Angle Annular Dark Field) STEM image and EDS analysis of the binder in the PCD containing 3wt% VC**

TEM mapping was carried out on a different area of the binder (refer to Figure 2.31). Area 1 showed the presence of 3.66at% tungsten, 0.12at% vanadium, 69.70at% cobalt and 26.52at% carbon, and area 2 consisted of 13at% tungsten, 27at% vanadium, 2at% cobalt and 58at% carbon. From the image, there is a clear phase contrast between the two areas being analysed, i.e. area 1 (marked in black) seems to have a lighter shade of grey than area 2. Generally, the heavier the atomic mass, the lighter the appearance of the element. Area 1 consists predominantly of cobalt, with a significant amount of dissolved WC, whereas area 2 consists primarily of VC and a significant amount of WC.



**Figure 2.31: TEM mapping of the binder pool in the PCD containing 3wt% VC**

The TEM mapping clearly shows the presence of a combination of vanadium and tungsten occurring in area 2. The area also contains cobalt which is the transition metal sintering aid that enables sintering to occur. The surrounding area comprises carbon which is essentially the diamond particles surrounding the binder. Additional images of binder pools and TEM mapping is shown in Figure 2.32. In these images, the mixed carbide particle consisting predominantly of vanadium and tungsten is clearly visible and appears as a lighter grey shade.



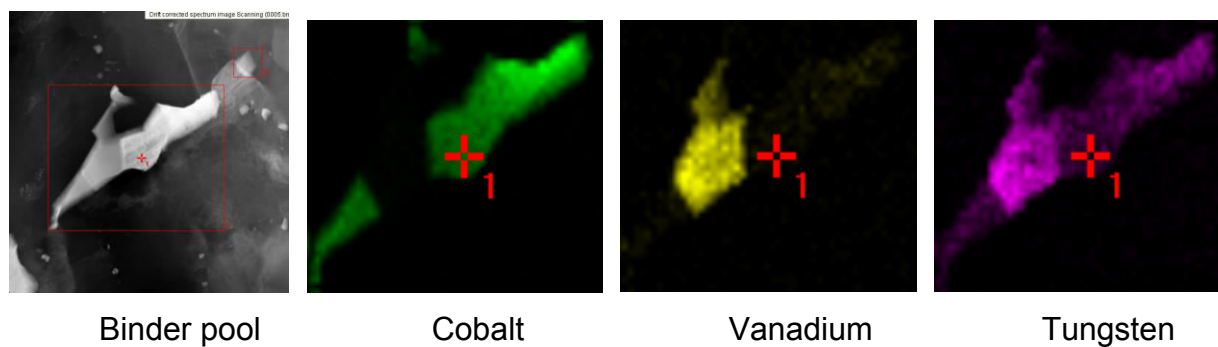


**Figure 2.32: TEM Mapping of binder pools for the PCD containing 3wt% VC**

Additional EDS quantification using the TEM was carried out to determine the V:W ratio (the images are shown in Appendix One). The measured data is shown in Table 2.7. The average ratio of V:W was found to be  $78:22 \pm 4.4$  which appears higher than the ratio of V:W calculated using the SEM, i.e.  $73:27 \pm 2.3$ .

**Table 2.7: EDS Quantification of the binder pools using the TEM**

Analysis	Carbon (at%)	Cobalt (at%)	Vanadium (at%)	Tungsten (at%)	V:W Ratio
EDS 1	57.64	1.51	31.65	9.20	77:23
EDS 2	93.57	0.41	4.55	1.47	76:24
EDS 3	88.21	0	8.61	3.18	73:27
EDS 4	84.79	0.42	11.41	3.38	77:23
EDS 5	87.77	0.56	8.87	2.80	76:24
EDS 6	89.57	0	9.01	1.42	86:14

Tiny cobalt pools usually appear between two adjacent diamond particles, and this is commonly referred to as 'cobalt stitching'. Essentially, the name describes the stitching together of the diamond particles forming an interconnected bond. Figure 2.33 reflects this phenomenon. The stitching area consists mainly of the cobalt binder with dissolved tungsten and vanadium.



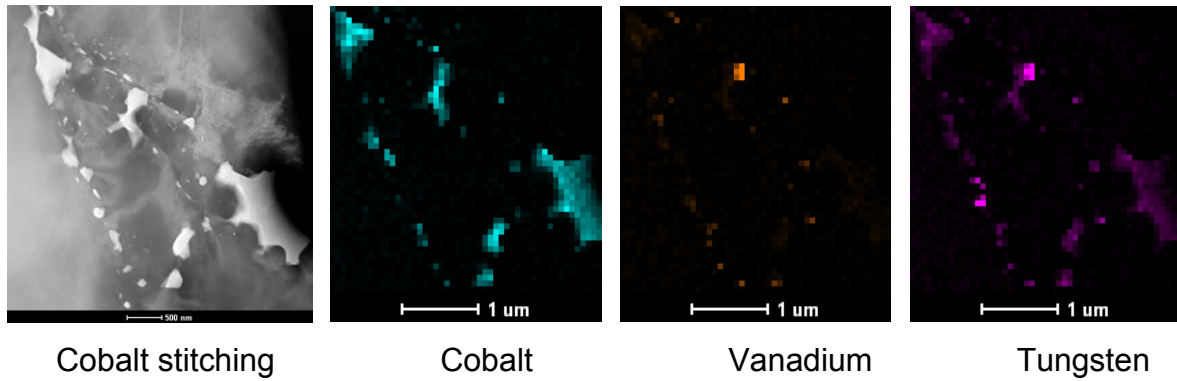


**Figure 2.33: Stem HAADF image of the binder stitching and the TEM mapping of the area**

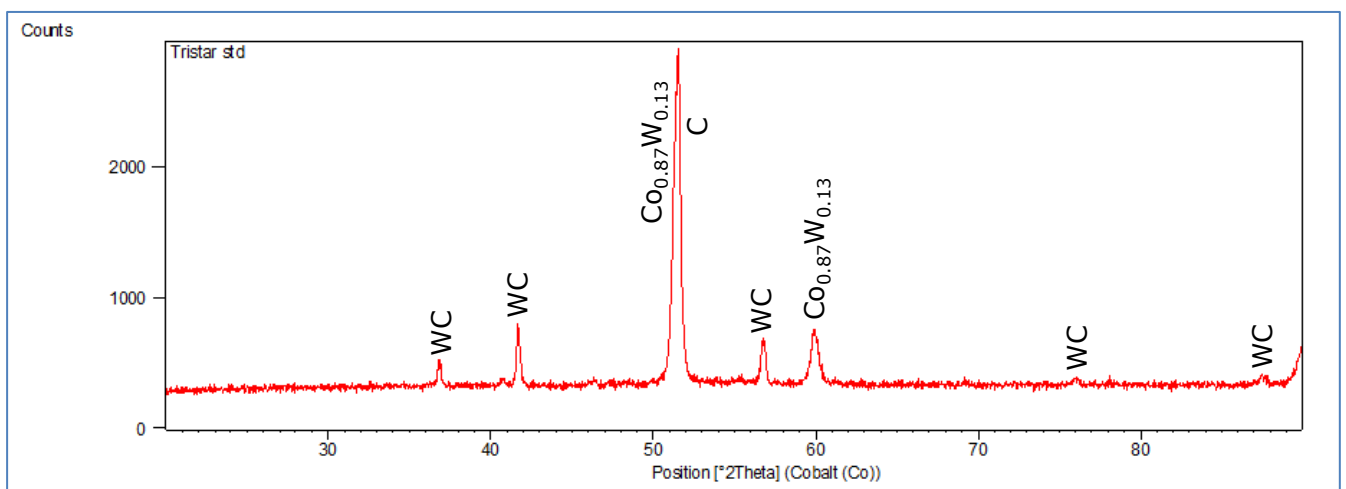
Figure 2.34 shows the XRD patterns for the standard PCD and the PCD containing 3wt% VC, and Table 2.8 shows the XRD data including the lattice constants (taken from the database) for the various phases. Note that the labels of the peaks on the XRD patterns denote the compositions of the phases in the database. The standard PCD contains stoichiometric WC, diamond and tungsten in solution with cobalt. As a result of the quenching process during sintering, tungsten is usually found in solution with the cobalt. Basically, the tungsten freezes in the cobalt when the PCD compact is cooled from a sintering temperature of 1400 °C to room temperature. An interesting observation is that when tungsten is dissolved in cobalt, the cobalt peak position shifts, appearing at  $59.92^{\circ}2\theta$  instead of  $60.28^{\circ}2\theta$ . This phenomenon occurs as a result of tungsten atoms having an atomic radius of 139 pm substituting itself in the cobalt lattice [88]. Since the atomic radius of cobalt is 125 pm, the presence of tungsten expands the lattice and this results in the shift of the cobalt peak position.

The XRD pattern of the PCD containing 3wt% VC shows the presence of a new phase, i.e. labelled as  $C_4V_{3.2}W_{0.8}$  in the database. This is typically referred to as a (V,W)Cx mixed carbide phase. The phase has a cubic structure and contains more VC as compared to WC. Generally, VC has a cubic structure whilst WC has a hexagonal structure. It would seem that the tungsten dissolves into the VC particle to form the mixed carbide, thus resulting in a cubic structure being formed. Interestingly, there is no free WC present in the PCD. This observation would infer a strong interaction between the vanadium and tungsten species. The cobalt pool contains dissolved vanadium, and the

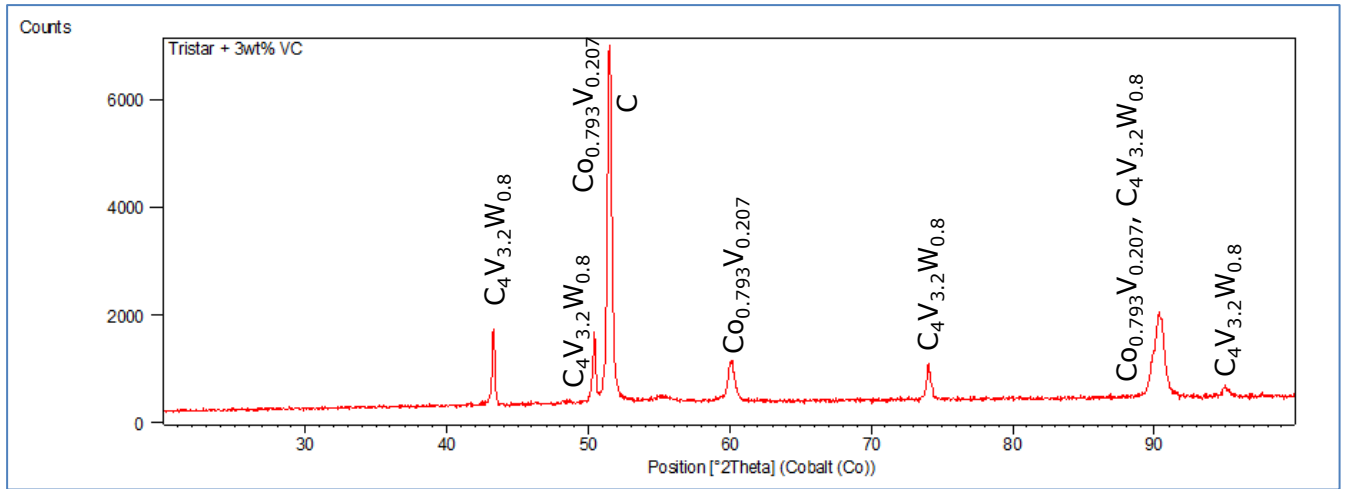
peak is shifted slightly towards the left relative to pure cobalt. The atomic radius of vanadium is 134 pm.

Figure 2.34C shows an overlay of the standard PCD and the PCD containing VC. The cobalt peak position (with a peak reflection of 200) is shifted slightly to the left (i.e. higher d-spacing) and occurs at  $59.92^\circ 2\theta$  (refer to Figure 2.35). When comparing the standard PCD with the PCD containing VC, the tungsten dissolved in the cobalt creates a greater peak shift to the left as compared to the vanadium dissolved in the cobalt. In addition, stoichiometric WC is absent in the PCD containing VC.

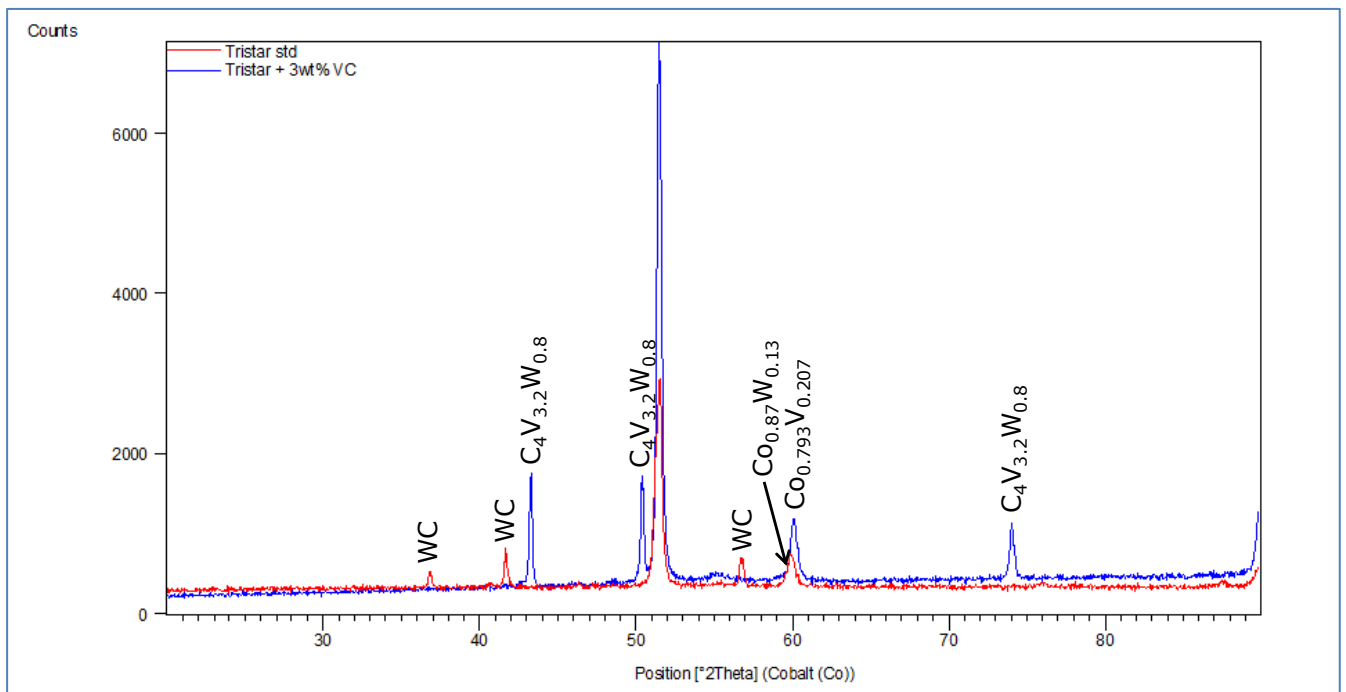
The XRD analysis which was based on the peak positions revealed that the chemical formula of the mixed carbide could be  $C_4V_{3.2}W_{0.8}$  (according to the ICSD database). However, there could be a multitude of vanadium and tungsten compositions since the vanadium and tungsten form a solid solution. The TEM elemental composition of the mixed carbide particle showed the presence of 13at% tungsten, 27at% vanadium, 2at% cobalt and 58at% carbon (refer to Figure 2.31). If we remove the cobalt value and normalise the concentration of the elements based on four carbon atoms, we attain the following chemical formula:  $C_4V_{1.86}W_{0.90}$ . From the EDS analysis performed on the VC enhanced PCD using the SEM (refer to Table 2.6), the ratio of vanadium to tungsten was found to be 73:27 which is close to the XRD ratio of vanadium to tungsten, i.e. 80:20. Furthermore Table 2.7 shows the average ratio of vanadium: tungsten to be 78:22 which is in close proximity to the observed XRD ratio of vanadium: tungsten (i.e. 80:20).



A



B



C

**Figure 2.34: XRD patterns of the sintered PCD: A (XRD pattern of the standard PCD), B (XRD pattern of the PCD containing 3wt% VC) and C (XRD pattern of the overlay of the two samples)**

**Table 2.8: XRD Data for the standard PCD and the PCD containing 3wt% VC**

Phase	Peak position ( $^{\circ}2\theta$ )	a = b (Å)	c (Å)	Calculated Density ( $\text{g}/\text{cm}^3$ )	Volume (Å <sup>3</sup> )	Crystal structure
WC	36.87; 41.69; 56.71; 76.02; 87.57	2.9070	2.8370	15.67	20.76	Hexagonal
Co <sub>0.87</sub> W <sub>0.13</sub>	51.27; 59.92	3.5860		10.82	46.11	Cubic
Diamond	51.64	3.5600		3.54	45.12	Cubic
Co <sub>0.793</sub> V <sub>0.207</sub>	51.48; 60.06; 90.33	3.5660		8.63	45.35	Cubic
C <sub>4</sub> V <sub>3.2</sub> W <sub>0.8</sub>	43.29; 50.42; 74.05; 90.33; 94.96	4.1980		8.04	73.98	Cubic

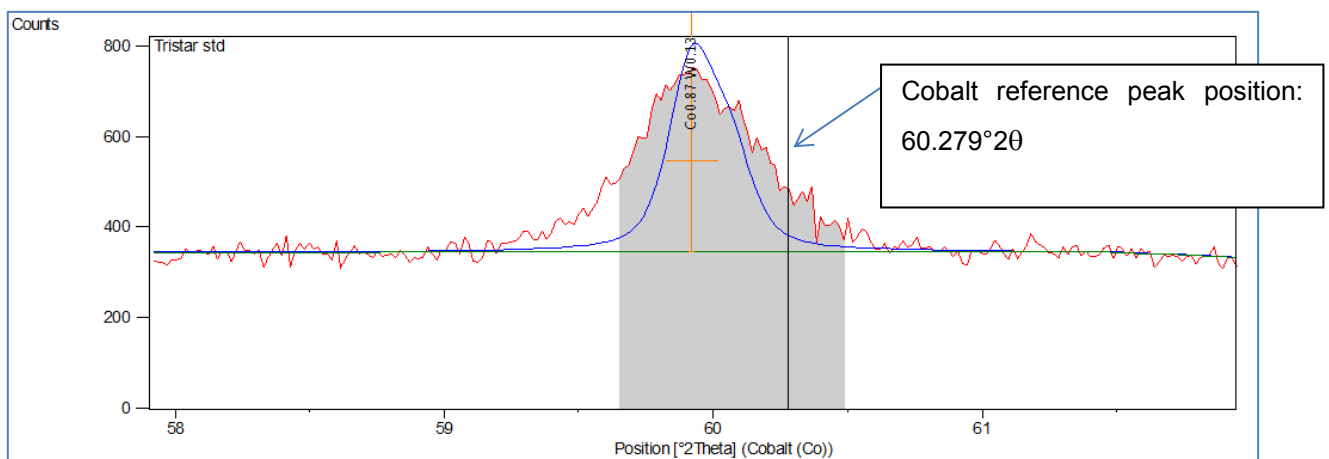
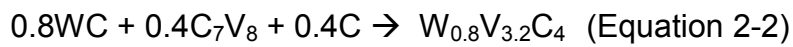


**Figure 2.35: XRD pattern showing the shift in the cobalt peak position: blue line depicts the calculated peak and the red line depicts the experimental peak**

The molar volume change was calculated for the PCD containing VC to determine whether the formation of the (V,W)Cx particle would increase the molar volume of the PCD. An increase in the molar volume may lead to the initiation of cracks primarily due to expansion and contraction. The lattice constants (i.e. a, b and c) together with the number of atoms per unit cell (i.e. z) were used in the calculation. The volume of the cubic structure is given by  $a^3$  and the volume of the hexagonal structure is given by  $a^2c \sin 60^\circ$  (refer to Table 2.9). Equation 2-2 describes the formation of the (V,W)Cx mixed carbide.



The theoretical volume of the starting constituents were calculated and compared to the theoretical volume of the resulting product. The percentage difference was found to be - 3.518%, which clearly shows a reduction in molar volume, hence no volume expansion is expected.

**Table 2.9: Parameters used for the calculation of molar volume**

Parameter	WC	C <sub>7</sub> V <sub>8</sub>	C	→	W <sub>0.8</sub> V <sub>3.2</sub> C <sub>4</sub>
a	2.907	8.33	3.567		4.198
b	2.907	8.33	3.567		4.198
c	2.837	8.33	3.567		4.198
z	1	4	8		1

Table 2.10 shows the theoretical and practical volume calculations for the standard PCD (i.e. PCD containing no additives) and for the PCD containing vanadium carbide. The practical calculation was performed using the unit cell values obtained from the XRD patterns for the given sample, together with Rietveld refinement, whereas the theoretical calculations were done using the theoretical values. Reaction 1 shows the formation of the (V,W)Cx product and reaction 2 shows the formation of products in the standard PCD. In both of the reactions shown in Table 2.10, there is no volume expansion occurring when the products are formed.

**Table 2.10: Volume Data for the various sintering reactions**

No	Reaction	Theoretical (% volume difference)	Practical (% volume difference)	Expansion
1	$0.8WC + 0.4C_7V_8 + 0.4C$ $\rightarrow W_{0.8}V_{3.2}C_4$	-3.518	-3.519	No
2	$1.13WC + 0.87Co + 0.87C$ $\rightarrow WC + Co_{0.87}W_{0.13} + C$ (Std reaction)	-0.496	-0.870	No

X-ray Fluorescence (XRF) analysis was carried out on the surface of the PCD containing VC to determine whether there was a concentration difference for the various elements (refer to Figure 2.36). Four different positions were investigated and the results appear in Table 2.11. The vanadium concentration seems consistent across the surface of the PCD. This implies a homogeneous distribution of vanadium in the PCD.

Conversely, both position 2 and position 3 shows higher levels of tungsten on the surface of the PCD. This region is denoted as the hot side of the cutter since the PCD was more exposed to the heater sleeve during sintering. Essentially, the higher the temperature, the more tungsten gets dissolved in the cobalt during sintering, and the more tungsten is carried into the PCD.

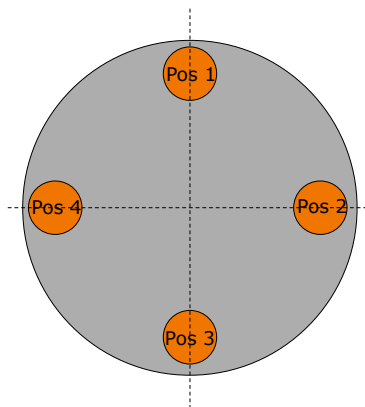


**Figure 2.36: XRF analysis of the surface of the PCD containing 3wt% VC showing the four different quadrants**

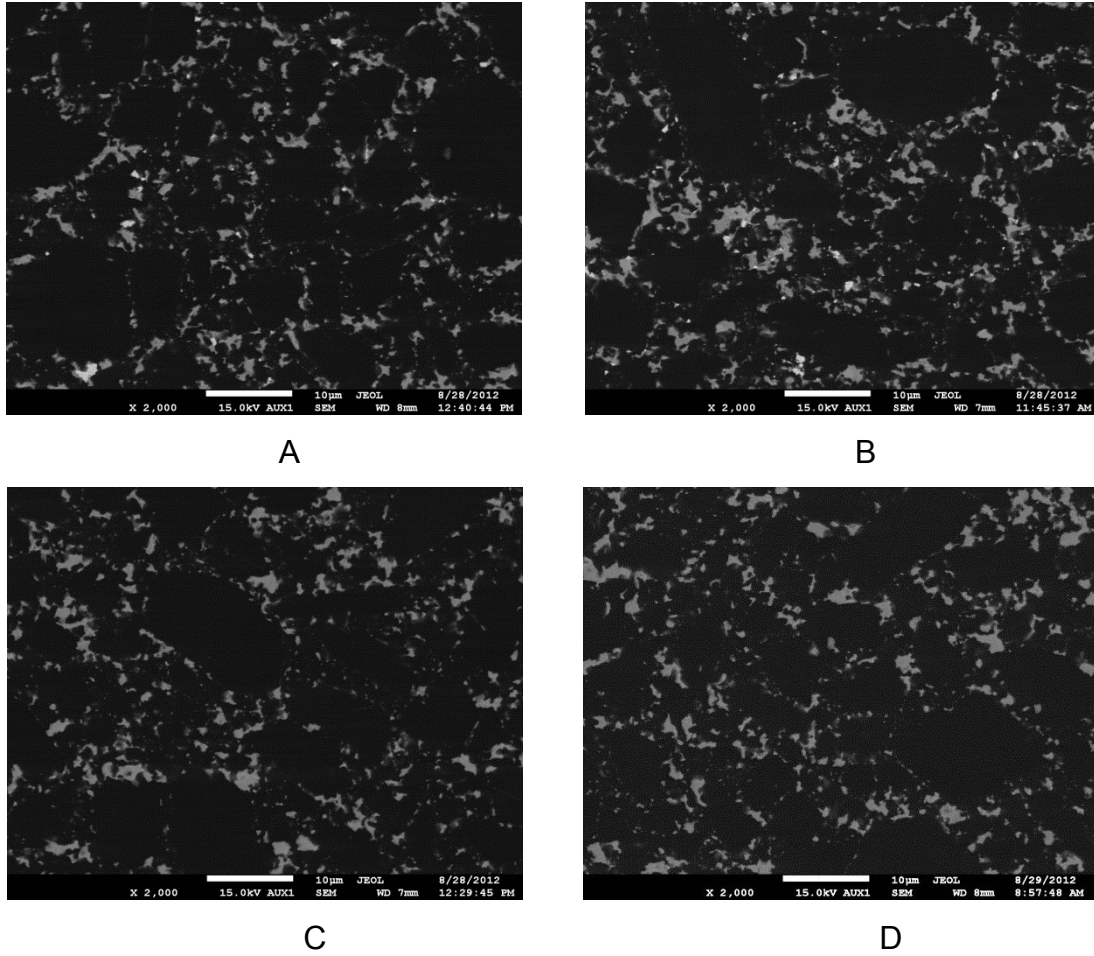
**Table 2.11: XRF analysis results (wt%) for the PCD containing 3wt% VC**

<b>Element</b>	<b>Position 1</b>	<b>Position 2</b>	<b>Position 3</b>	<b>Position 4</b>
Vanadium	12.58	12.32	12.37	12.65
Cobalt	67.32	61.25	63.01	62.91
Tungsten	20.10	26.44	24.63	24.44

### 2.4.3 PCD sintered with varying VC concentration

The investigation up to this point has been focused on using 3wt% VC. So far, the critical findings were that a mixed (V,W)C<sub>x</sub> phase formed with the absence of free VC or free WC especially towards the surface of the PCD. To continue with the investigation, different concentrations of VC additions were studied, namely 1wt% (0.61vol%), 3wt% (1.85vol%) and 5wt% (3.11vol%) VC (refer to Figure 2.37).

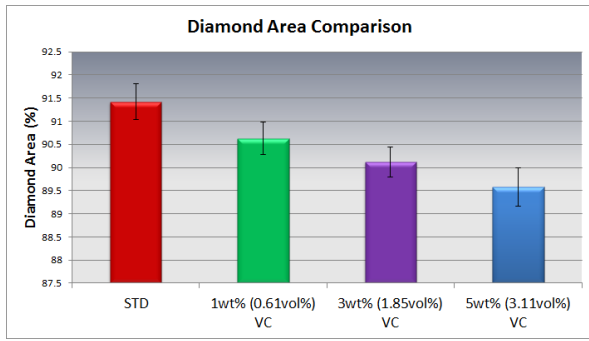
Visually, there appears to be not much difference in the microstructures appearing in Figure 2.37. The standard PCD and the PCD containing 1wt% VC shows evidence of WC precipitation at the binder – diamond interface, whereas WC seems absent in the PCD containing 3wt% VC and 5wt% VC. This observation could be explained by the assumption that the PCD containing 1wt% VC had insufficient VC to combine with the WC to form the (V,W)C<sub>x</sub> mixed carbide, hence the presence of residual WC near the surface of the PCD.



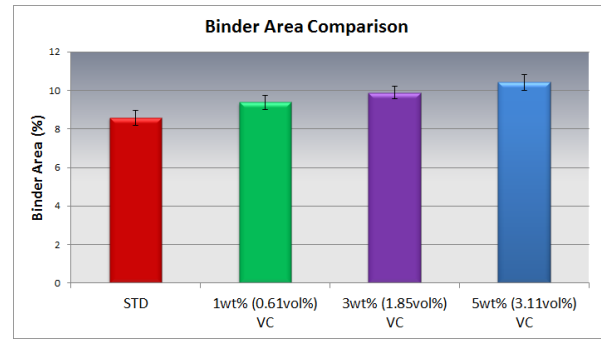
**Figure 2.37: Microstructural comparisons: A (Std PCD), B (PCD containing 1wt% VC), C (PCD containing 3wt% VC) and D (PCD containing 5wt% VC)**

Image analysis data is shown in Figure 2.38. As the vanadium concentration in the PCD increases, the diamond area decreases and the binder content increases. The diamond area and binder content are interchangeable. A decrease in diamond area is expected to reduce the abrasion resistance of the diamond compact, but this is not always the case.

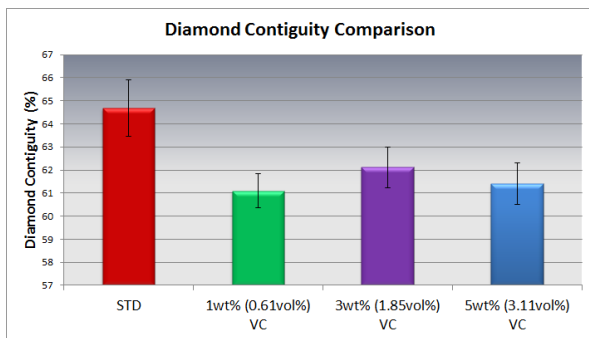




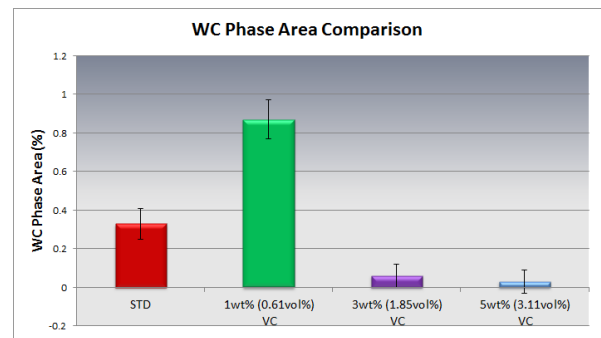
A



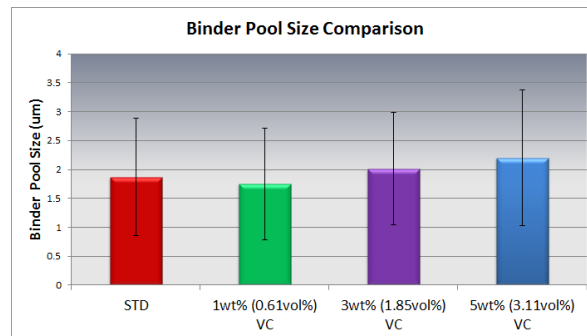
B



C



D

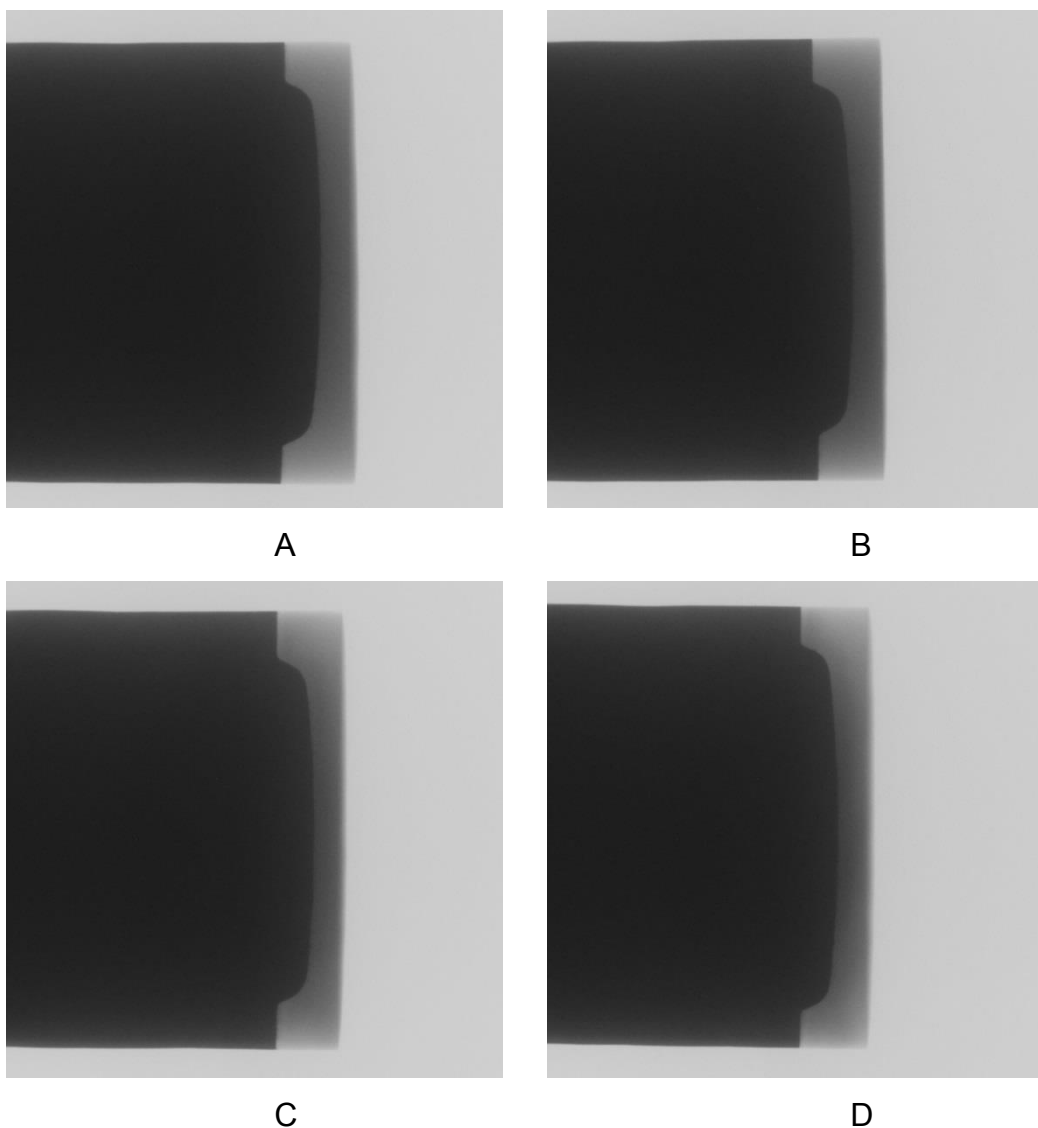


E

**Figure 2.38: Image analysis results: A (Diamond Area), B (Binder Area), C (Diamond Contiguity), D (WC phase area) and E (Binder pool size)**

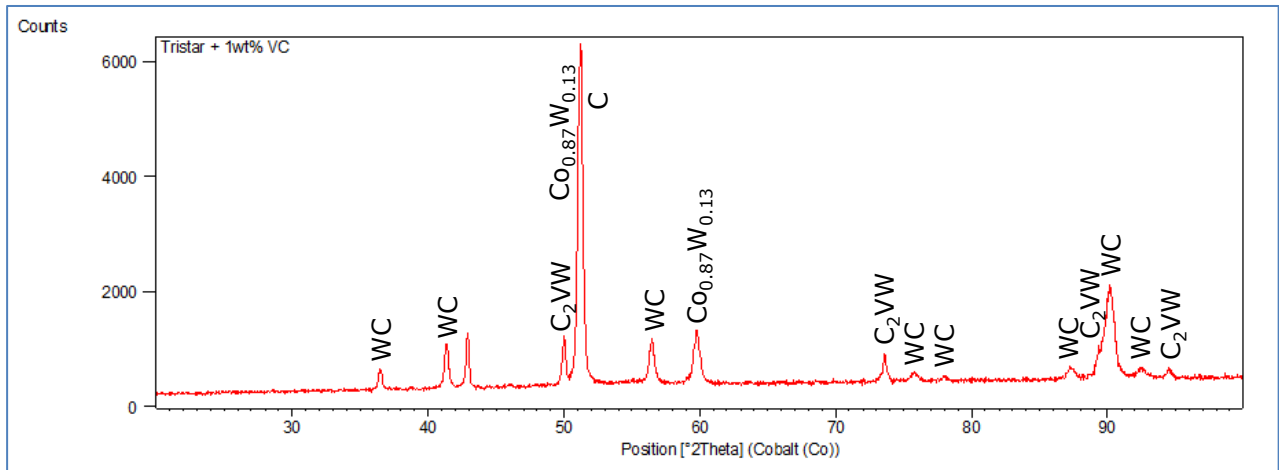
The diamond contiguity of the PCD containing VC seems more-or-less similar, although significantly lower than the standard PCD. There seems to be no difference between the various VC additions. The WC phase area shows a distinct trend between the standard PCD and the PCD containing 3wt% and 5wt% VC, i.e. as the concentration of VC increases, the amount of WC present in the PCD decreases. However, the PCD containing 1wt% VC does not seem to follow this trend.

Figure 2.38E shows an interesting graph of binder pool size as a function of VC concentration. It seems that as the VC concentration in the PCD increases, the binder pool size also increases but is however not significantly different to the standard PCD. The increase in binder pool size is expected and can possibly be attributed to the precipitation of larger (V,W)C<sub>x</sub> particles in the binder pool (i.e. nucleation and growth of the (V,W)C<sub>x</sub> particles as the concentration increases). The x-ray images of the PCD containing VC are shown in Figure 2.39. All the images appear to be similar, i.e. no evidence of plumes or cracks present in the PCD.

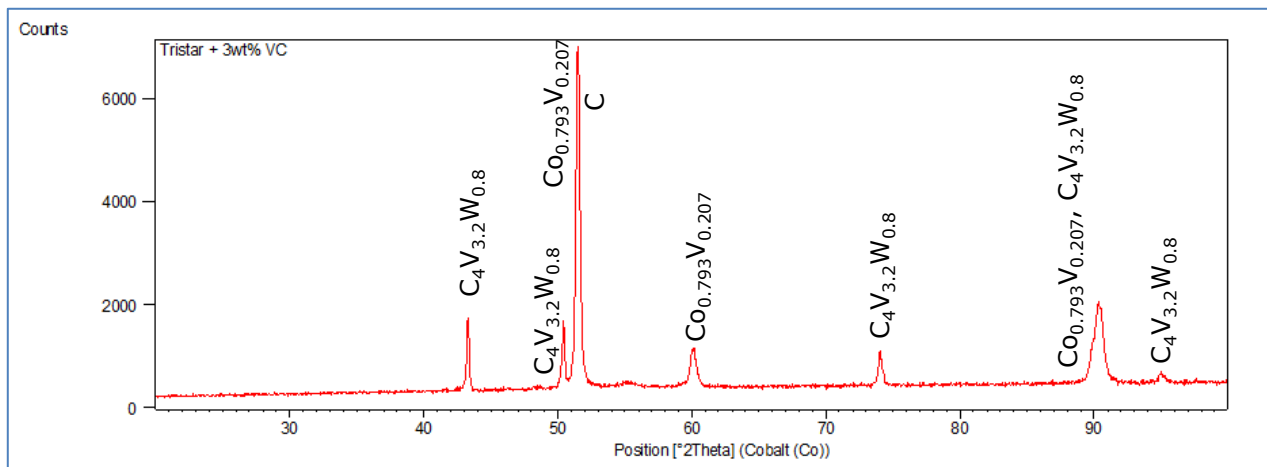


**Figure 2.39: X-ray images: A (standard PCD), B (PCD containing 1wt% VC), C (PCD containing 3wt% VC) and D (PCD containing 5wt% VC)**

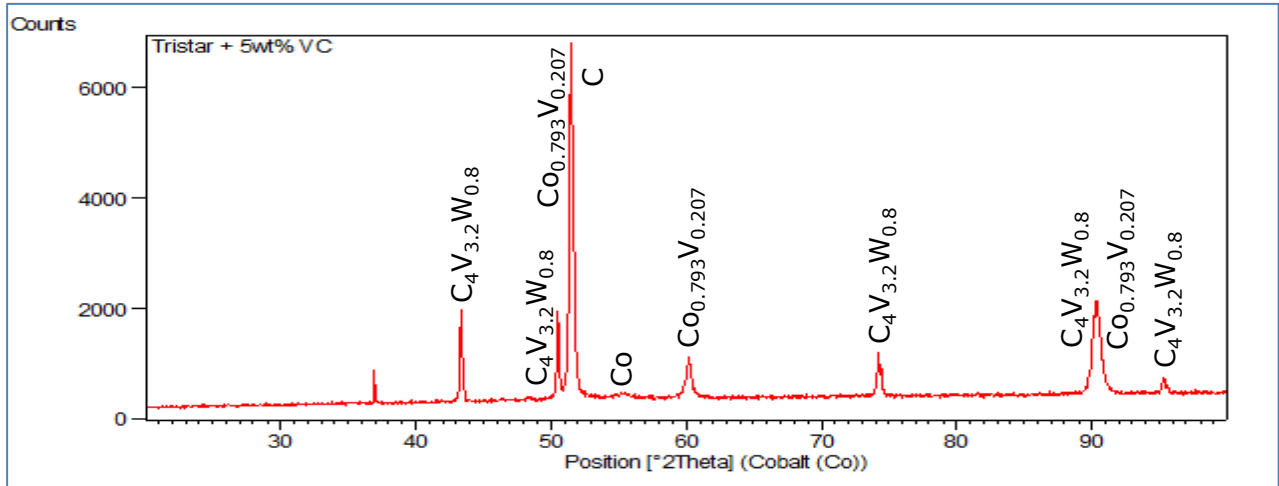
XRD analysis of the PCD containing VC is shown in Figure 2.40. In the PCD containing 1wt% VC, clear peaks showing the presence of WC are observed. This agrees with the observation made in Figure 2.37B that the microstructure shows the appearance of WC precipitates in the binder pool.



A



B



C

**Figure 2.40: XRD Patterns for PCD containing vanadium carbide: A (PCD containing 1wt% VC), B (PCD containing 3wt% VC) and C (PCD containing 5wt% VC)**

In the PCD containing 3wt% VC, we have seen the formation of a  $C_4V_{3.2}W_{0.8}$  mixed carbide (according to the ICSD database), however in the PCD containing 1wt% VC, we observe the presence of a different phase, namely  $C_2V_1W_1$  (according to the ICSD database). Since the  $C_2V_1W_1$  phase and the  $C_4V_{3.2}W_{0.8}$  phase have similar diffraction peaks, they seem to differ mainly in their respective unit cell size. The lattice parameter for the  $C_4V_{3.2}W_{0.8}$  and  $C_2V_1W_1$  phases were found to be 4.1980Å and 4.2260Å respectively. The  $C_2V_1W_1$  phase contains less vanadium as compared to tungsten and the ratio of vanadium to tungsten is 1:1. This implies that a reduced amount of vanadium is present in the PCD to combine with the residual tungsten, and hence the appearance of free tungsten carbide in the binder pools. In addition, there is more tungsten dissolved in the cobalt in the 1wt% VC sample as evidenced by the formation of the  $Co_{0.87}W_{0.13}$  phase, and the absence of the  $Co_{0.793}V_{0.207}$  phase. Contrary to the 1wt% VC sample, the 5wt% VC sample exhibits the same phase formation as the 3wt% VC sample.

Rietveld analysis was carried out on the PCD containing 3wt% VC (results shown in Table 2.12). It is clear from the Rietveld analysis that the 1wt% enhanced PCD sample contains a higher concentration of WC than the 3wt% VC enhanced PCD or the 5wt% VC

enhanced PCD. Furthermore, the amount of the carbide phase increases as the concentration of the VC additive increases.

**Table 2.12: Rietveld Analysis of PCD containing various VC concentrations**

Phase	1wt% VC in PCD	3wt% VC in PCD	5wt% VC in PCD
$C_4V_{3.2}W_{0.8}$	-	5	6
$C_2VW^a$	4	-	-
WC	1	<1	<1
Diamond	88	90	89
$Co_{0.87}W_{0.13}$	7	-	-
$Co_{0.793}V_{0.207}$	-	5	5

<sup>a</sup>  $C_2VW$  and  $C_4V_{3.2}W_{0.8}$  are essentially the same phase but with different cell sizes

<sup>b</sup> Distinction between  $Co_{0.87}W_{0.13}$  and  $Co_{0.793}V_{0.207}$  are tenuous at best, and could be the same phase

#### 2.4.4 Behaviour Testing

Thus far, the microstructure and phase composition of the PCD containing VC has been established. The question remains as to the performance of the material. It is assumed that since the VC displaces some of the binder in the PCD, the resultant PCD would possess a higher thermal stability and abrasion resistance. Thermal stability is an extremely important factor in assessing the performance of a cutter. Generally, the binder is used as a sintering aid for the transformation of carbon into diamond at elevated pressures and temperatures. In the absence of high pressures, especially during the drilling application where elevated temperatures are reached, the cobalt in the PCD can graphitise the meta-stable diamond back to its stable form, i.e. graphite. This then 'softens' the PCD and results in early failure of the tool. Since VC doping of the PCD table results in a decreased amount of cobalt binder, the PCD is thought to be more thermally stable.

To investigate the thermal stability of the PCD, a milling test was performed on the material. Essentially, the PCD sample is clamped onto a fixture and the sample is then exposed to a block of sandstone. The cutting action is such that the cutter is exposed to the rock for half the revolution and exposed to air during the second half of the revolution. This is depicted in the schematic shown in Figure 2.41. This type of cutting action is termed interrupted cutting. During the rotation of the cutter, the cutters move along the rock as it cuts (schematic shown in Figure 2.42). The debris emerging from the cutting action is removed by water, which is also used to cool the cutter as it cuts along the rock.

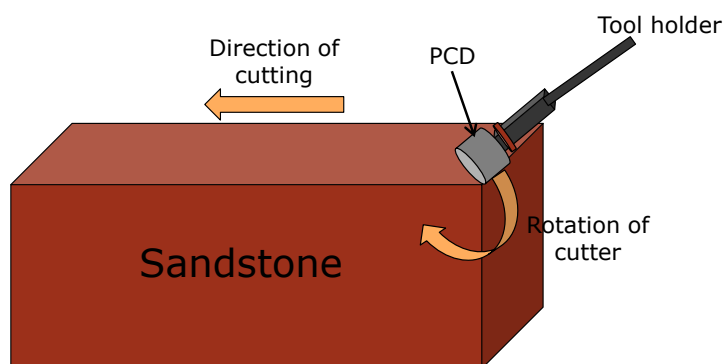


**Figure 2.41: Schematic of milling test**

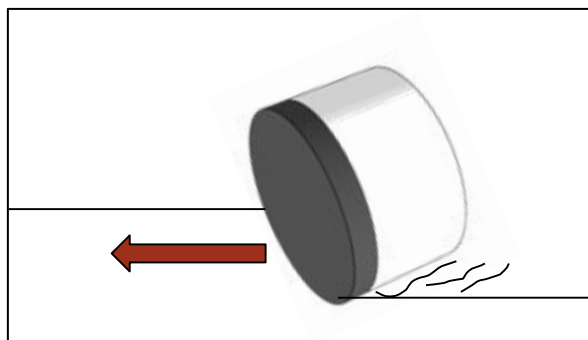


**Figure 2.42: Schematic of PCD cutter removing rock material as it cuts across the rock**

Figure 2.43 shows the result of the Sandstone Milling test. Essentially, the longer the length of the cut before the tool fails, the better the performance of the cutter. On the graph, the blue colour shows the minimum cutting length, the red colour shows the average cutting length and the yellow colour displays the maximum cutting length of the cutter. Two cutters were tested in total. On comparison of the performance of these two

cutters, it is seen that the PCD containing VC performs approximately 40% better than the standard PCD. As mentioned, the milling test is more of a measure of the thermal stability of the cutter and does to an extent measure the abrasion resistance of the cutter as well.

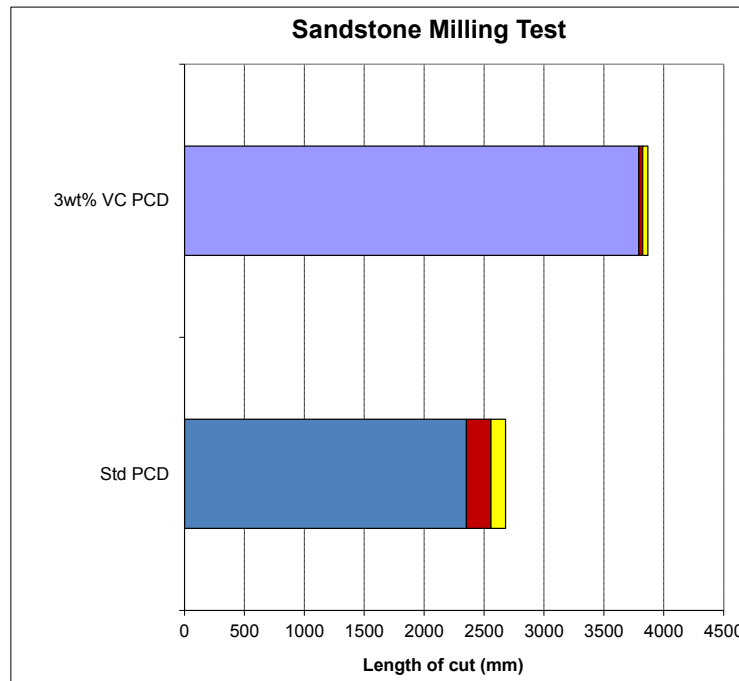


**Figure 2.43: Sandstone Milling Test**

A more defined test for abrasion resistance is the Paarl Granite Turning test (refer to Figure 2.44 for the schematic of the test, and Figure 2.45 for the equipment used for the test). In this test, the edge of the PCD is exposed to the rotating Paarl granite rock until a wear scar develops on the edge of the cutter surface. The wear scar length is measured to determine the abrasion resistance of the cutter. This test is performed dry, i.e. there is no coolant flowing over the cutter to reduce the temperature.

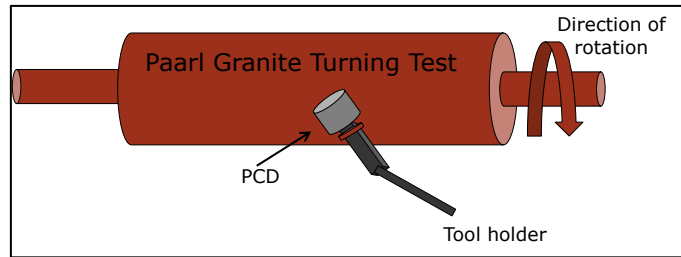


**Figure 2.44: Schematic of the Paarl Granite Turning Test**

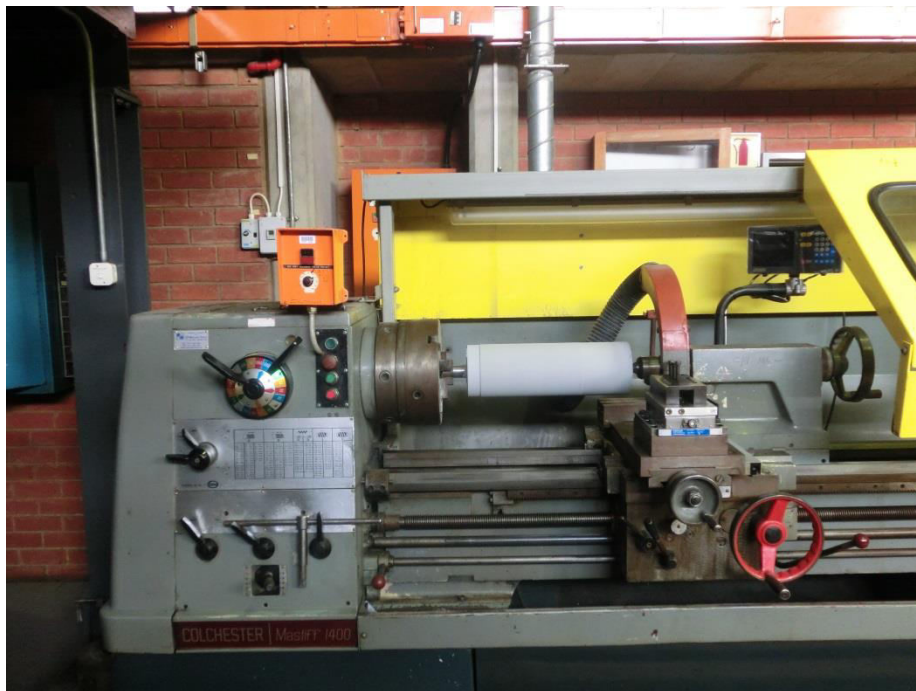


**Figure 2.45: Equipment used for Paarl Granite Turning Test**

Figure 2.46 shows the Paarl Granite test results of the standard PCD and the PCD containing VC. Both the standard PCD and the PCD containing VC were exposed to the Paarl granite bar for three minutes. It is clear that the VC doped PCD has a significantly better abrasion resistance, i.e. the lower the wear scar length, the better the abrasion resistance of the cutter.



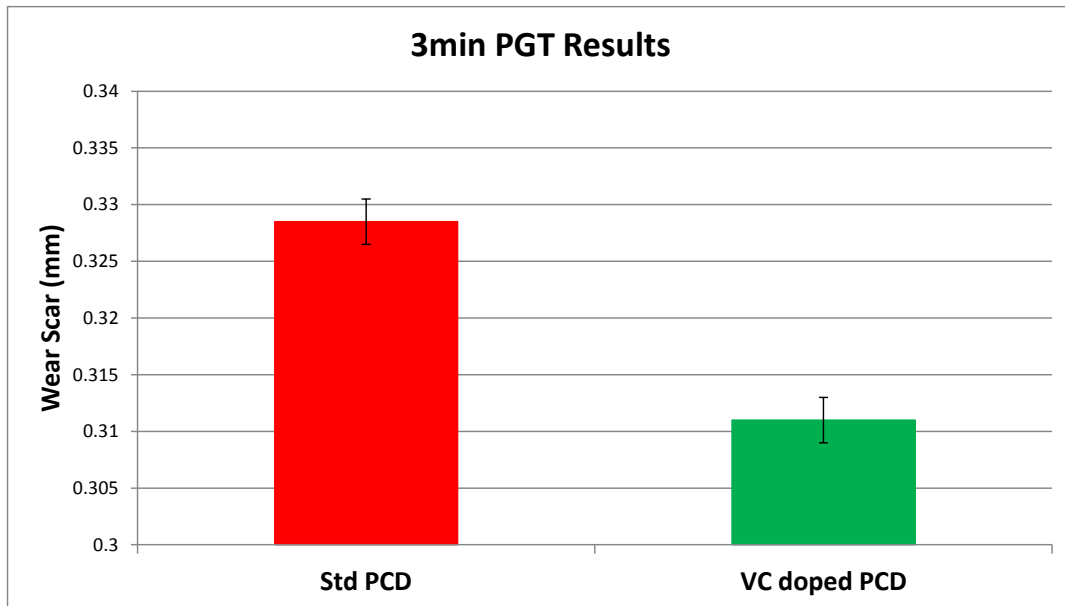
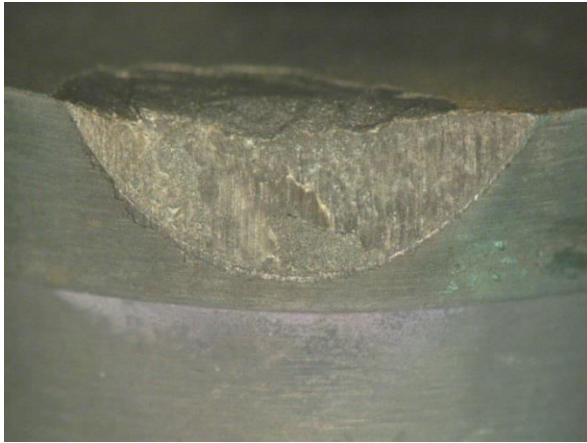
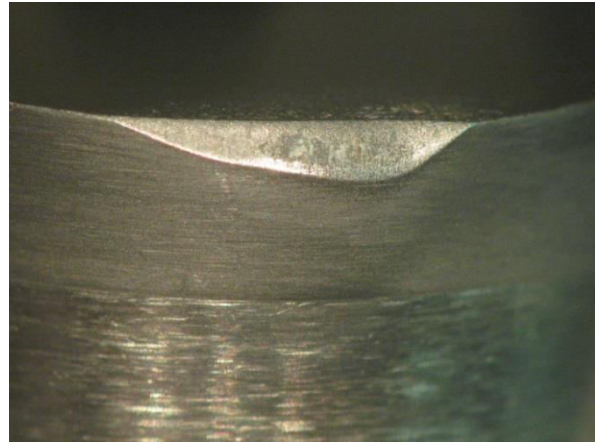


**Figure 2.46: Paarl Granite test results of the standard PCD and the PCD containing VC**

In order to fully assess the wear behaviour of the standard PCD and the PCD containing VC, the PCD was exposed to a Paarl Granite Turning test for a period of 45 min. The test was carried out dry, i.e. no coolant water was used to cool the surface of the PCD during cutting. Figure 2.47 shows the optical image of the wear scar after 45 min exposure to PGT testing. The wear scar of the standard PCD has a much larger area (i.e. area = 10.9 mm<sup>2</sup>) as compared the wear scar of the PCD containing 5wt% VC (area = 2.73 mm<sup>2</sup>). Furthermore, the wear scar of the PCD containing VC seems smooth whereas the wear scar of the standard PCD seems rough. The standard PCD shows a woody wear with PCD spalling on the surface of the cutter.



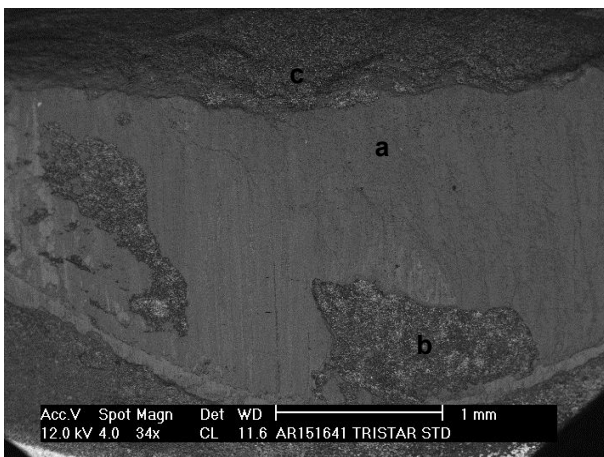
A



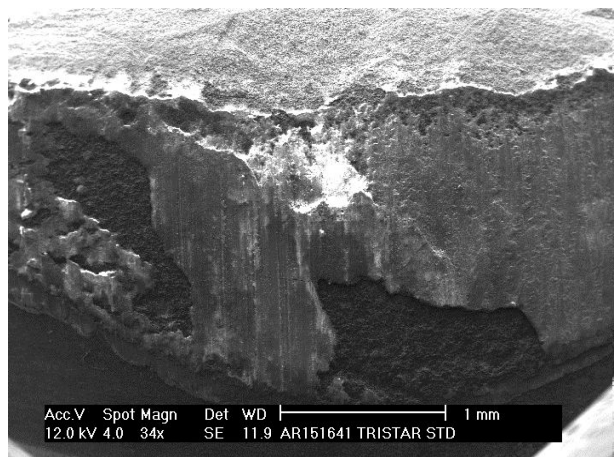
B

**Figure 2.47: Optical images of the wear scar after 45 min exposure to PGT testing: (A) Standard PCD, (B) PCD containing 5wt% VC**

A closer examination of the wear scar was performed using the SEM (refer to Figure 2.48). The secondary electron image provides more information on the topography of the PCD. Table 2.13 shows the elemental composition of the wear scar area. Area (a) shows the granite rock residue on the surface of the PCD with the components of the rock typically being  $\text{SiO}_2$ . Area (b) shows the exposed diamond and area (c) shows the top surface of the PCD. Both area (b) and area (c) contains smaller quantities of  $\text{SiO}_2$  residue from the rock.



A



B

**Figure 2.48: SEM images of the Standard PCD after 45min exposure to PGT testing: (A) Backscatter image of the wear scar, (B) Secondary image of the wear scar**

**Table 2.13: EDS analysis of the wear scar area for the standard PCD, elements in wt%**

Area	C	O <sub>2</sub>	Fe	Na	Al	Si	K	Ca	Co
a	18.56	40.13	4.36	2.31	6.12	24.83	2.59	1.11	-
b	79.95	11.71	-	-	0.55	2.18	-	-	5.60
c	82.25	9.06	-	-	-	1.19	-	-	7.50

Figure 2.49 shows the SEM images of the PCD containing 5wt% VC after 45 min exposure to PGT testing. The images are similar to the standard PCD in terms of the SiO<sub>2</sub> deposit on the surface of the wear scar. Table 2.14 shows the EDS analysis results. Based on the extent of SiO<sub>2</sub> pick up from the granite rock, it is very difficult to assess the oxidation of the cutter and draw a comparison between the standard PCD and the PCD containing 5wt% VC to determine which cutter is more oxidation resistant.

The SEM images of the top surface of the wear scar are shown in Figure 2.50. The numerous SiO<sub>2</sub> deposits can be clearly seen.

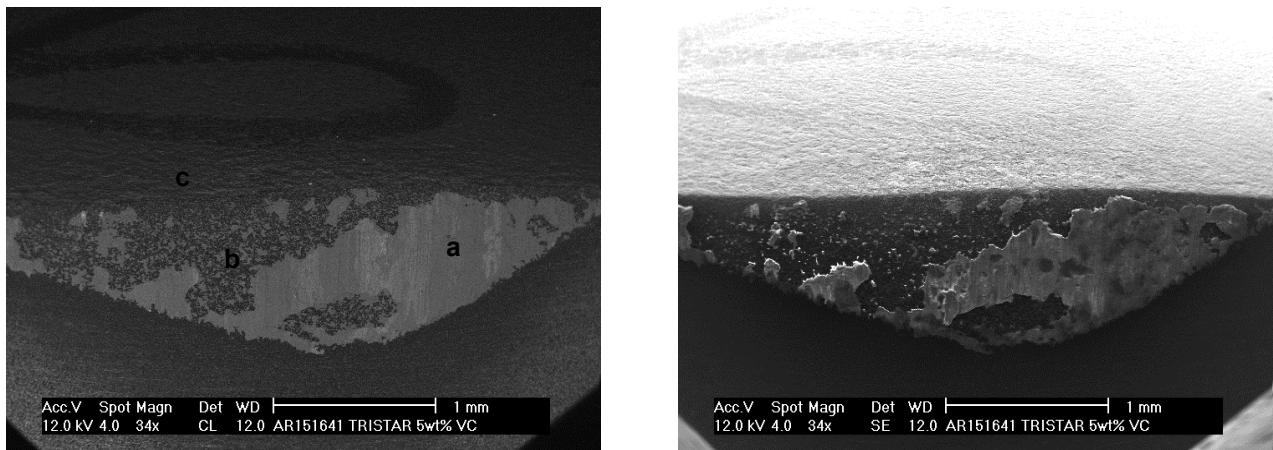
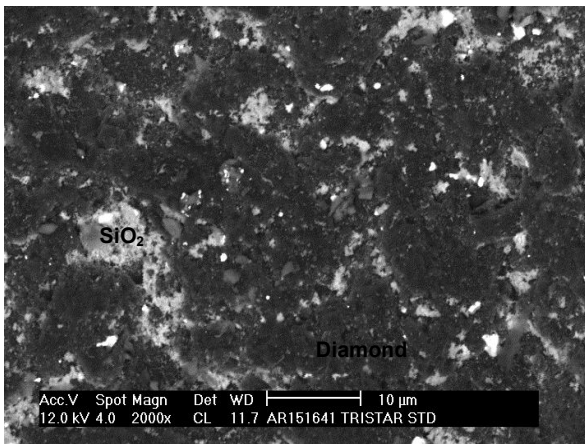


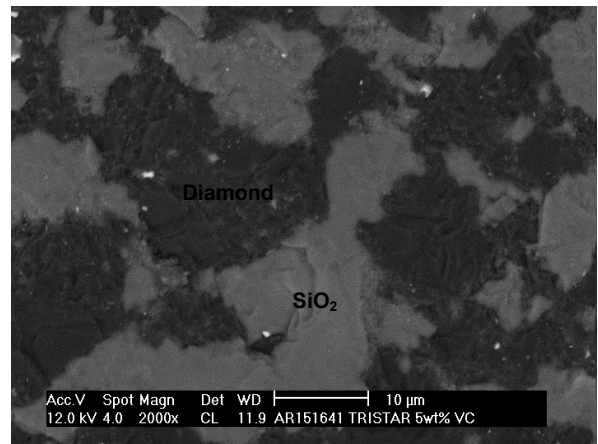
**Figure 2.49: SEM images of the PCD containing 5wt% VC after 45 min exposure to PGT testing: (A) Backscatter image of the wear scar, (B) Secondary image of the wear scar**

**Table 2.14: EDS analysis of the wear scar area of the PCD containing 5wt% VC, elements in wt%**

Area	C	O <sub>2</sub>	Mg	Na	Al	Si	K	Ca	Co
a	14.10	43.74	1.40	3.22	7.70	23.69	4.71	-	1.45
b	74.92	18.13	-	-	0.46	6.49	-	-	-
c	40.42	38.75	-	2.21	3.73	12.58	2.21	-	-



A



B

**Figure 2.50: SEM images of the top surface of the wear scar: (A) Standard PCD, (B) PCD containing 5wt% VC**

XRD analysis was performed on both the standard PCD and the PCD containing 5wt% VC after 45 min exposure to PGT testing. Figure 2.51 shows the overlay of the two samples, where the red graph depicts the standard PCD and the blue graph shows the PCD containing 5wt% VC. XRD analysis could not detect the presence of SiO<sub>2</sub> on the surface of the PCD. This is most likely due to the SiO<sub>2</sub> preferentially being deposited on the surface of the wear scar rather than on the top surface of the PCD. No oxides could be detected in either of the XRD patterns.

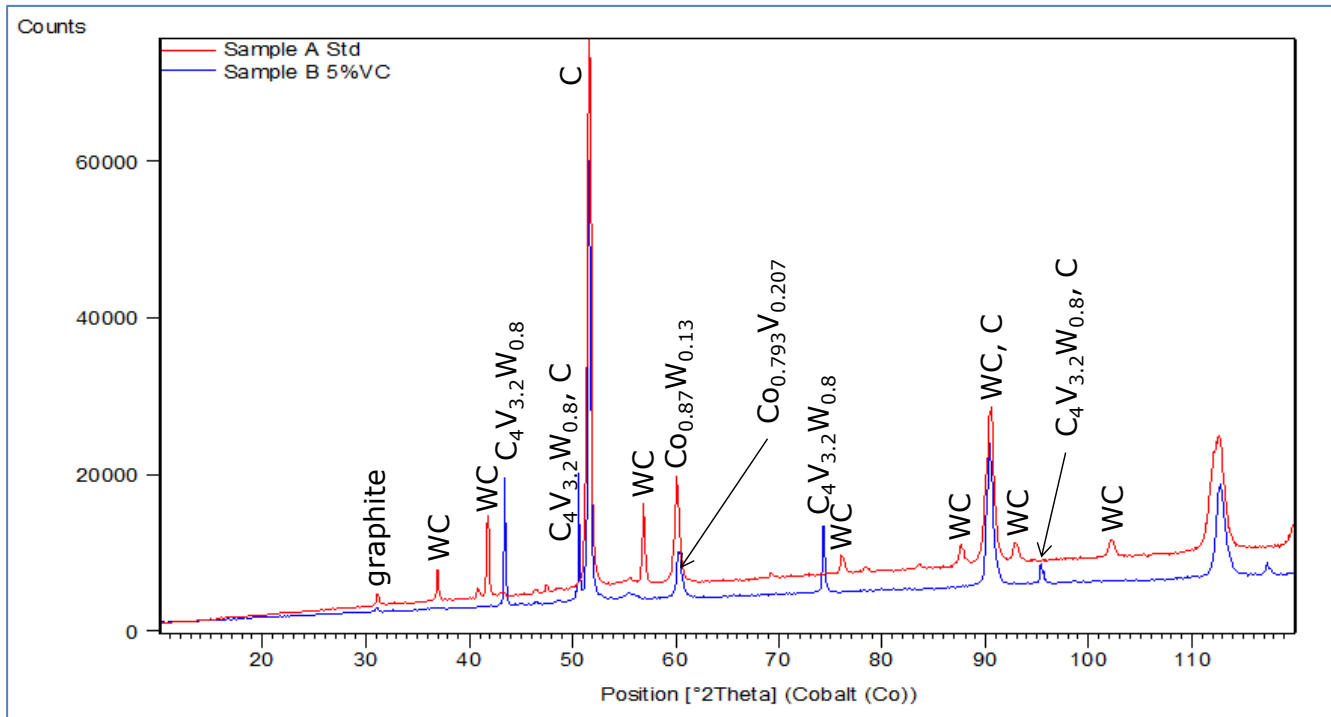


**Figure 2.51: Overlay of the XRD patterns for the Standard PCD and PCD containing 5wt% VC after exposure to 45 min wear testing (phases taken from the ICSD database)**

As expected, the standard PCD seems to graphitise more readily than the PCD containing 5wt% VC (refer to Figure 2.52). The red graph represents the standard PCD and the blue graph shows the PCD containing 5wt% VC. Table 2.15 shows the graphite peak area and the graphite peak height for both of the samples tested. According to the XRD patterns, the PCD containing 5wt% VC seems to be approximately 90% more resistant to graphitisation as compared to the standard PCD. The calculation was based on the graphite peak area in both of the XRD patterns.

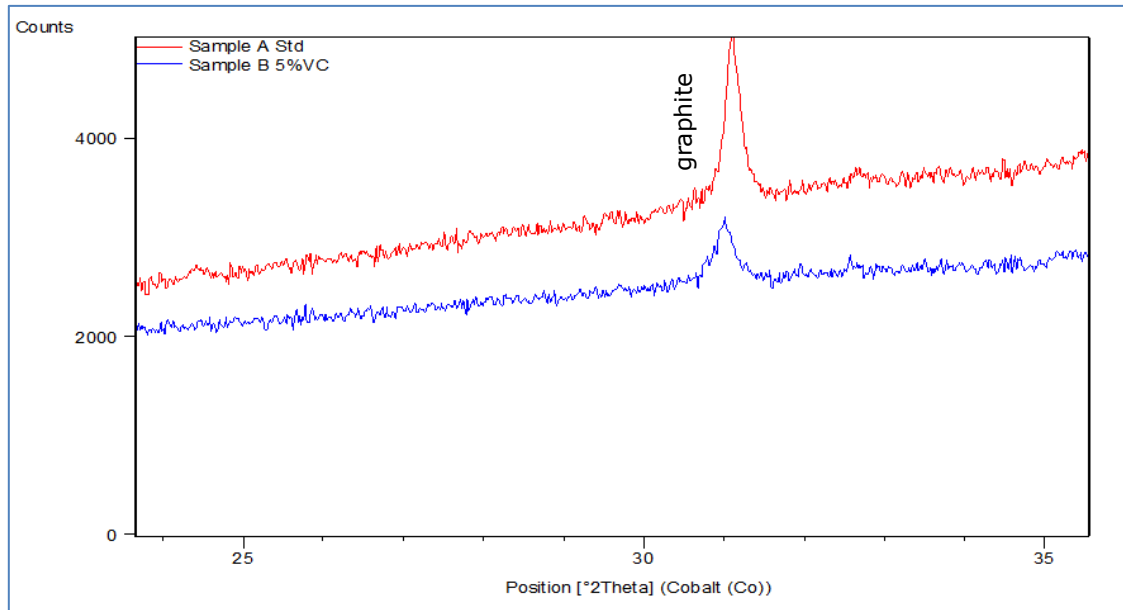


**Figure 2.52: Overlay of the XRD patterns showing graphitisation of the Standard PCD and PCD containing 5wt% VC after exposure to 45min wear testing**

**Table 2.15: Measure of graphitisation from the XRD patterns for the Standard PCD and PCD containing 5wt% VC after exposure to 45 min wear testing**

Sample	Graphite Peak Height (cts)	Graphite Peak Area (cts)
Standard PCD	1627.448	187.9854
PCD containing 5wt% VC	600.6689	99.1184

The PGT test focuses on testing the abrasion resistance of a cutter whereas the Milling Test focuses on assessing the thermal stability of the cutter. The vertical borer (VB) test is a combination of the PGT test and the sandstone milling test. In addition, the VB test also assesses the impact resistance of the cutter. Figure 2.53 shows the schematic of the VB test. The hexagonal shaped granite rock rotates clockwise whilst the PCD cutter moves from the edge of the rock towards the centre of the rock. The cutting distance of the rock as a function of the wear scar generated on the PCD edge is measured. Essentially, the performance of the cutter is measured on the cutting distance as a function of the wear scar area. The cutting distance is determined by measuring the distance the cutter repeatedly travels from the edge of the rock to the centre. It is

preferable that the cutting distance is maximised whilst maintaining a small wear scar area. The end point of the test is usually determined by the failing of the PCD cutter by spalling, or by a pre-determined cutting distance (i.e. the test is stopped at a given cutting distance and samples are compared to each other).

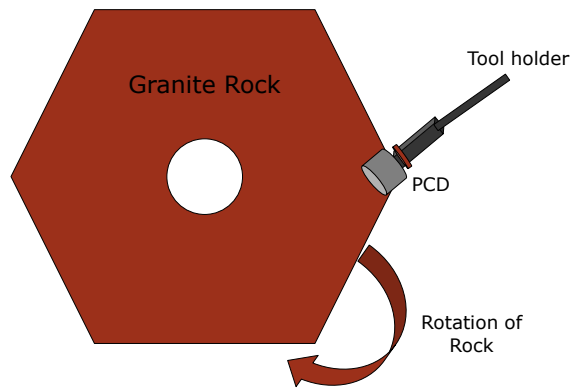


**Figure 2.53: Schematic of the VB test**

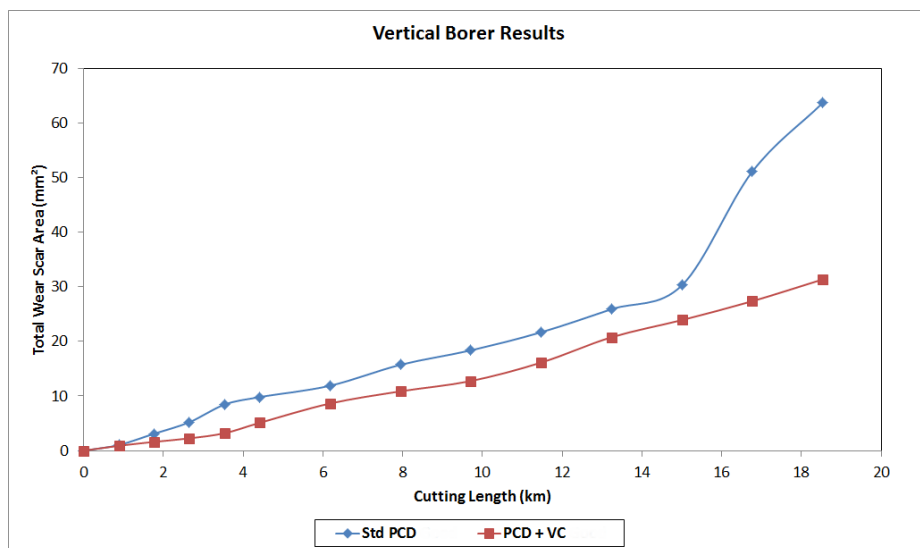


**Figure 2.54: VB comparison between the standard PCD and PCD containing 3wt% VC**

Figure 2.54 shows the VB comparison between the standard PCD and the PCD containing 3wt% VC. In this test, the durability of the tool (i.e. length of cut) seems similar for both the standard PCD and the PCD containing VC. However, the abrasion resistance

of the PCD containing VC is much better than the standard PCD. Abrasion resistance is assessed by measuring the wear scar length as a function of the cutting distance, i.e. the smaller the wear scar, the more abrasion resistant the cutter. An increase in the abrasion resistance of the PCD infers a more powerful cutting action and a more effective tool. Overall, the performance of the PCD containing VC seems superior to the standard PCD. Figure 2.55 shows the wear scar area of the standard PCD and the VC enhanced PCD post VB testing. The wear scar on the standard PCD is rough, with the presence of PCD chipping and spalling on the surface of the PCD. The wear scar on the VC enhanced PCD shows a smooth worn cutter with the absence of chipping or spalling. Ideally, a PCD insert showing this type of wear behaviour would be more durable during tool use.

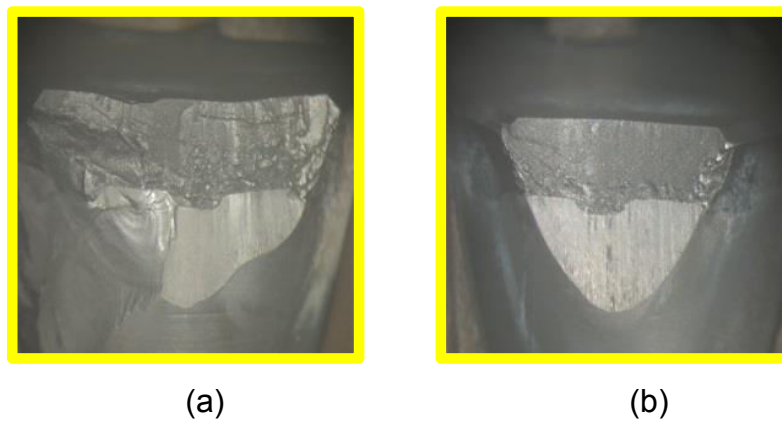


**Figure 2.55: Image of the wear scar: (a) Standard PCD, (b) VC enhanced PCD**

## 2.5 Discussion

Vanadium carbide is widely used in the tungsten carbide industry to improve the properties of the tool by controlling the grain growth of the WC particles. It was assumed that the addition of VC to PCD would result in similar benefits in terms of improving the properties of the PCD. When comparing hardness values of the various constituents (i.e. VC = 2900 kg/mm<sup>2</sup>, WC = 2100 kg/mm<sup>2</sup>, Co = 1043 kg/mm<sup>2</sup>), the PCD was expected to contain particles within it having a higher hardness value.



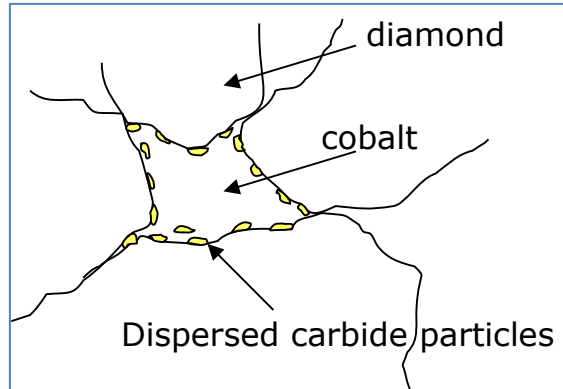
In general, PCD is manufactured by allowing the cobalt to infiltrate the PCD from the substrate. The reason for this is to enhance crushing of the diamond particles during cold compaction prior to hot compaction and plastic deformation. The admixing of cobalt particles into the diamond matrix reduces the extent of diamond-diamond crushing and hence compromises densification. For this reason, the infiltration of VC into the PCD from a VC powder layer was thought to be beneficial. Unfortunately, this was not possible due to the VC layer acting as a barrier against cobalt infiltration.

The observed barrier phenomenon is best explained by the low solubility of VC in Co (temperature = 1400°C/800°C, solubility = 1.5%/1%). Furthermore, the vanadium carbide reacted with the WC from the diamond powder mix to form a mixed (V,W)C<sub>x</sub> carbide, and this newly formed phase hindered any further infiltration of the cobalt from the substrate into the PCD. As a result, the sintered PCD contained less cobalt and tungsten.

In order to try to salvage the idea of infiltrating a vanadium source into the diamond layer, a layer of vanadium powder was also used as an infiltration source. Regrettably, this experiment did not work, although the PCD contained the standard amount of cobalt.

One of the major issues highlighted concerning the degradation of PCD is the graphitisation of the compact during the brazing of the drill bit into the drill pocket, and during tool use. Since it was shown that VC seems to be a good barrier for cobalt infiltration, it is likely that the presence of VC would also reduce the extent of graphitisation within the PCD. This will be investigated in a subsequent chapter in the thesis.

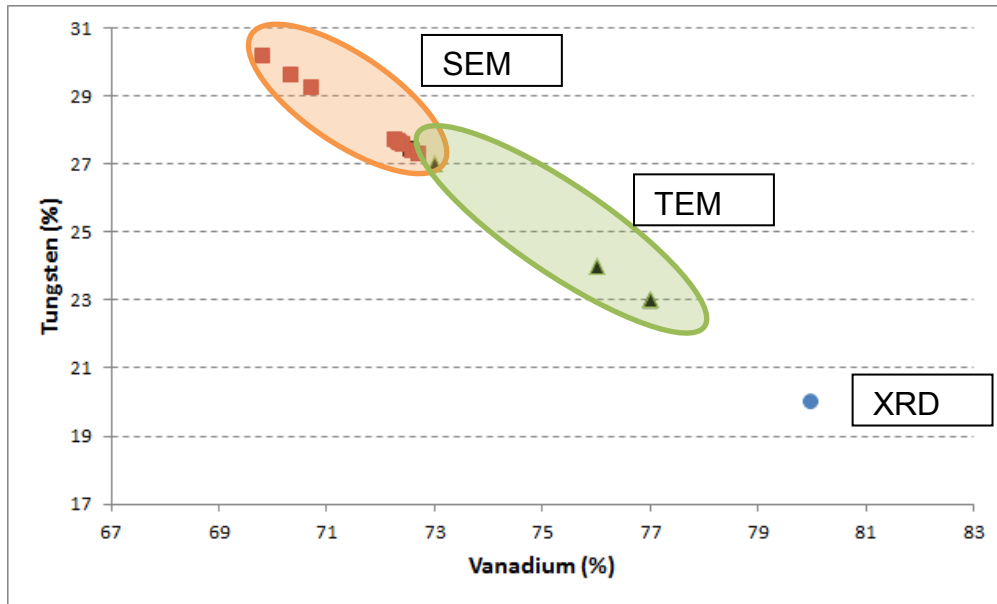
Another important aspect is the deposition of the mixed carbide in the PCD compact. It is thought that if the mixed carbide deposits along the diamond-binder interface (refer to Figure 2.56), it will protect the diamond against extensive graphitisation by acting as a barrier between the diamond and the cobalt binder. It is known that cobalt could easily graphitise the diamond at elevated temperatures and ambient pressures.



**Figure 2.56: Schematic of carbide particles deposited at the diamond-binder interface**

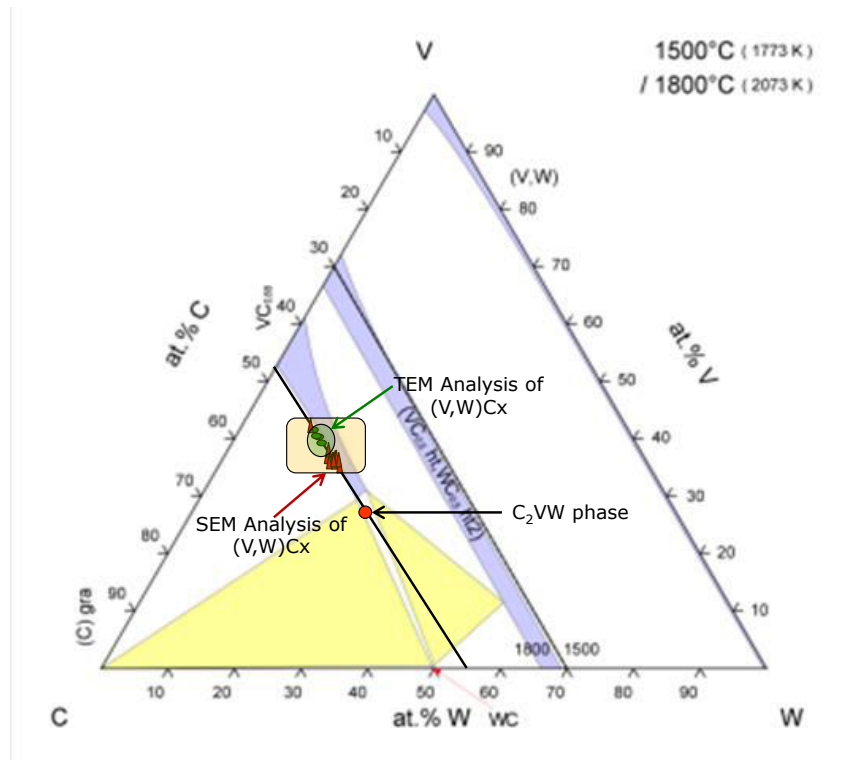
According to the TEM images shown in Figure 2.31 and Figure 2.32, the mixed carbide has a tendency to deposit at the diamond-binder interface, and in so doing is expected to partially hinder graphitisation.

Figure 2.57 shows the V:W ratio in the mixed carbide as analysed on the TEM, SEM and the XRD. According to the ICSD XRD database, the approximate or probable formula for the mixed carbide appears to be  $C_4V_{3.2}W_{0.8}$ . Vanadium and tungsten form a solid solution with a range of concentrations. Using the TEM, the formula for the mixed carbide was found to be  $C_4V_{1.86}W_{0.90}$ . The TEM shows the tungsten content in the mixed carbide to be slightly higher than the XRD. There is a scatter of results for both the SEM and the TEM due to the EDS analysis being done on a slightly wider area which comprises the mixed carbide particles, diamond and the cobalt binder. If the emitted x-rays were focused solely on the mixed carbide particle, then the formula for the mixed carbide could be more accurately determined.



**Figure 2.57: Ratio of V:W in the mixed carbide - measured using EDS analysis**

Figure 2.58 shows the V-W-C ternary phase diagram. For the addition of 3wt% VC to the PCD, two phases form, namely (V,W)C<sub>x</sub> solid solution and carbon. Both the EDS data for the TEM and SEM were plotted on the phase diagram. The TEM data showed a narrow range, whereas the SEM data showed an expected wider range. The EDS data obtained for both the TEM and SEM agrees with the XRD phases observed as evidenced by their location on the phase diagram. For the addition of 1wt% VC to the PCD, a three phase solution forms, namely C<sub>2</sub>VW (phase taken from the ICSD database), WC and carbon. There is agreement with the phase diagram, when the proposed C<sub>2</sub>VW phase is plotted onto the phase diagram.



**Figure 2.58: V-W-C ternary phase diagram [89] showing the formation of the (V,W)Cx mixed carbide**

One of the hypothesis mentioned previously stated that the substitution of vanadium atoms into the cobalt lattice is expected to distort the crystal lattice of the fcc structure of cobalt, thereby stabilising the structure and hindering it from transforming back to the hcp structure. The cobalt peak shift for the standard PCD, 3wt% VC enhanced PCD and 5wt% VC enhanced PCD are shown in Figure 2.59. In addition, the peak positions are outlined in Table 2.16. The standard PCD shows a greater peak shift for the cobalt peak when compared to the reference cobalt peak position. This effect lessens as the amount of VC addition to the PCD increases.

The result can best be explained by taking the atomic radius of tungsten (i.e. 139 pm) and vanadium (i.e. 134 pm) into consideration. The tungsten atom is slightly larger and is therefore able to distort the cobalt lattice to a greater extent. It would seem that as the VC concentration increases, the distortion of the cobalt peak lessens. The atomic concentration of tungsten in the proposed  $\text{Co}_{0.87}\text{W}_{0.13}$  phase is 13%, whilst the concentration of vanadium in the proposed  $\text{Co}_{0.793}\text{V}_{0.207}$  phase is 21%. This could imply

that the substitution of the tungsten atom into the cobalt crystal lattice is more effective in stabilising the fcc phase of cobalt than the substitution of the vanadium atom. However, the observed peak shift could also possibly be explained by the differences in composition. Nevertheless, the addition of VC to PCD seems to maintain the cubic structure of cobalt according to the XRD traces.

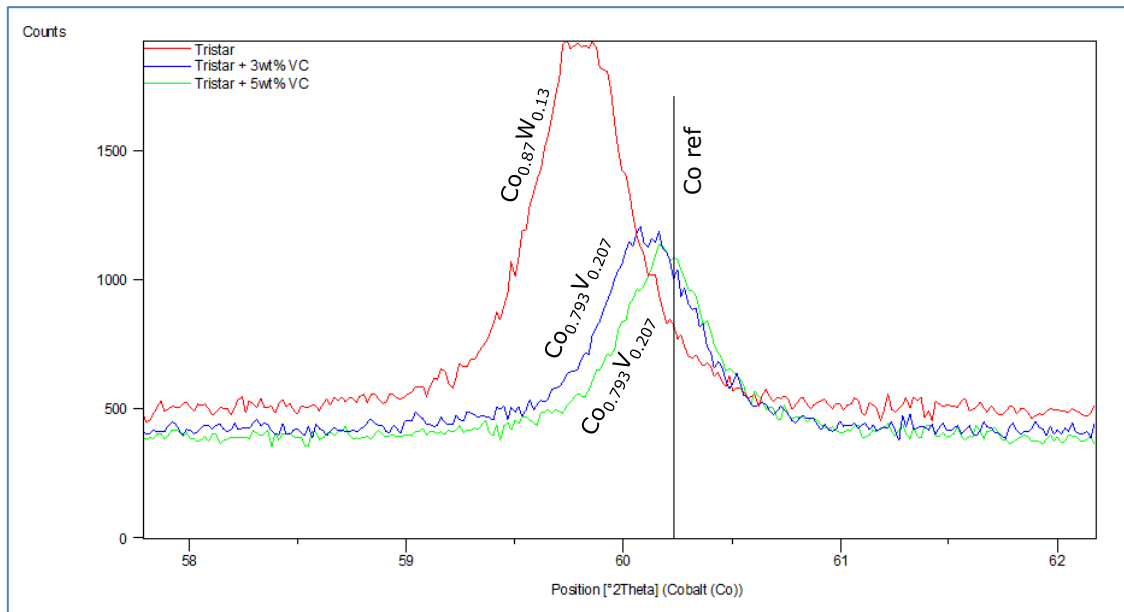


**Figure 2.59: Cobalt peak shift**

**Table 2.16: Peak positions for shift of cobalt (200) peak**

Sample	Phase	Peak position (°2θ)
Cobalt reference peak	Co	60.28
Standard PCD	$\text{Co}_{0.87}\text{W}_{0.13}$	59.92
3wt% VC in PCD	$\text{Co}_3\text{V}$	60.06
5wt% VC in PCD	$\text{Co}_3\text{V}$	60.20

The milling test shows the VC enhanced PCD to be thermally stable, the PGT tests show an increase in the abrasion resistance of the VC enhanced PCD, and the VB test shows an increase in the overall performance of the VC enhanced PCD. The question remains as to the reasons for the improvement in the behaviour of the PCD when it is doped with VC. To help explain the phenomena observed, it is pertinent to take into consideration the

structure of the VC enhanced PCD and its associated behaviour. In the standard PCD, WC precipitates in the binder pool more so near the interface of the PCD and less at the surface of the PCD. PCD doped with VC contains a mixed carbide that precipitates mostly in the binder pools.

The addition of VC to carbon steels was found to increase the hardness of the tool (refer to Figure 2.60) [90]. Similarly, the addition of VC to WC-Co also improved the hardness of the tool. It was therefore expected that the addition of VC to PCD would increase the hardness of the tool as well.

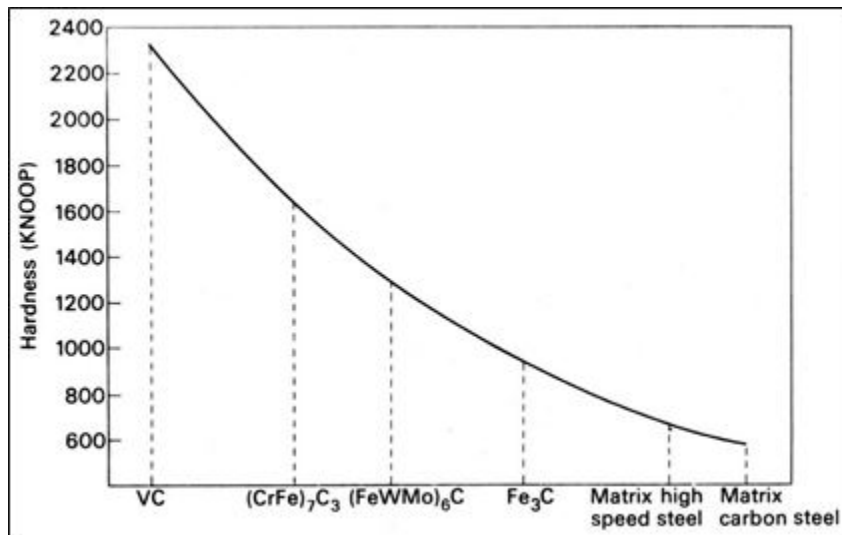


**Figure 2.60: Graph illustrating the addition of VC to carbon steel and the effect on the overall hardness of the tool**

Table 2.17 shows hardness values for the various components found in the PCD. The presence of both WC and VC within the PCD has the potential to harden the binder pool. However, there is a fine balance between having an ultra-hard brittle material and a soft ductile material. A brittle material generally has a tendency to chip and spall on impact, whereas a ductile material possesses higher toughness but would lack the wear resistance required.

**Table 2.17: Hardness measurements of PCD components [91] [92]**

<b>Element / Compound</b>	<b>Vickers Hardness (HV) MN n<sup>-2</sup></b>
Cobalt	1043
Tungsten Carbide	2400
Vanadium Carbide	2800

Lay et al. found that thin layers of mixed carbide precipitated at the Co/WC interface [93] and Christensen et al. observed that vanadium segregated at the carbon rich boundaries and increased the grain boundary strength [94]. It is therefore highly possible that the VC addition to PCD strengthens the grain boundaries which is enabled by the segregation of the (V,W)C<sub>x</sub> mixed carbide at the Co/diamond interface. The PCD compact is also stabilised and strengthened by the precipitation hardening of the binder phase by the deposition of the (V,W)C<sub>x</sub> mixed carbide phase.

Using ab initio total energy calculations, Sun et al showed that the incorporation of tungsten into the cubic VC structure increases both the bulk modulus and the shear modulus [95]. They suggested that the presence of tungsten in the VC may slightly increase the hardness of the cubic VC phase.

## 2.6 Conclusion

The addition of VC to PCD showed the powder mix to be homogenous with an even distribution of vanadium carbide, tungsten carbide and cobalt particles in the diamond matrix. Infiltration of a VC layer (positioned at the interface between the WC substrate and the diamond powder) into the PCD was unsuccessful due to the VC acting as a barrier to the infiltrating cobalt. The VC was therefore admixed with the diamond particles. The VC enhanced PCD showed no significant quantity of WC in the PCD microstructure. This implies that most the residual WC which was both admixed prior to sintering and swept up into the PCD from the substrate during sintering combined with the cubic VC to form a cubic mixed carbide phase with the formula (V,W)C<sub>x</sub>. The mixed carbide was found to be rich in carbon and vanadium.

X-ray tomographic analysis showed the PCD to be well sintered with no anomalies or cracks present in the PCD. TEM analysis revealed that the (V,W)C<sub>x</sub> phase deposited at the diamond-binder interface. Molar volume calculations yielded no increase in volume with the formation of the mixed carbide, hence there was no need for concern regarding the expansion within the PCD table on formation of the (V,W)C<sub>x</sub> phase.

XRF analysis indicated a homogeneous distribution of the VC on the surface of the PCD. Sometimes, owing to the temperature gradient within a capsule during sintering, infiltration of the cobalt from the substrate may occur more rapidly on one edge as compared to the other. Usually the cobalt has dissolved tungsten and/or vanadium in it and this could result in the uneven distribution of the additive on the surface of the PCD.

XRD analysis showed no residual tungsten carbide present in the VC enhanced PCD with VC addition levels of 3wt% (1.85vol%). Other additive levels were also investigated, viz. 1wt% (0.61vol%) VC and 5wt% (3.11vol%) VC. For the 1wt% VC enhanced PCD, the mixed carbide had the formula C<sub>2</sub>VW with a stoichiometric 1:1 ratio V:W according to the ICSD XRD database. The XRD pattern of this sample showed residual WC present in the PCD with no vanadium dissolved in the cobalt binder. The 5wt% VC enhanced PCD seemed to have the similar microstructure and XRD pattern as compared to the 3wt% VC enhanced PCD.

Mechanical testing proved that the VC enhanced PCD possesses improved behaviour properties. The sandstone milling test revealed the VC enhanced PCD to be more thermally stable with approximately 40% improvement, whilst both the PGT and VB tests showed the PCD to be more wear resistant. The reason for the superior performance of the VC enhanced PCD was explained by the precipitation hardening of the (V,W)C<sub>x</sub> phase within the PCD and the segregation of the (V,W)C<sub>x</sub> towards the Co/diamond interface.

Thus far, results show that the VC enhanced PCD shows potential as a new developed product for oil and gas drilling in order to increase the lifespan of the tool. To this effect, a patent was filed by Kaveshini Naidoo et al. with the publication number:



US2010285335A1 that described the performance improvement of the VC enhanced PCD [96].

## 2.7 Recommendations

In this study it was found that using 1wt% VC as a dopant produced residual WC in the PCD. It is therefore recommended to determine the performance of the PCD doped with different quantities of VC in order to establish what the optimum VC dopant concentration regime is. In addition, it would be interesting to determine the optimum VC concentration to be added to PCD to provide a microstructure that is free of any residual WC.

A few mechanisms that could be responsible for the improved performance of the VC doped PCD were highlighted in this study, but this requires further investigation to be fully substantiated.

## CHAPTER THREE

### HEAT TREATMENT OF THE PCD

#### 3.1 Background

The most common use of PCD is in machining and drilling applications [97] [2]. During these applications, especially drilling, the PCD is exposed to very high temperatures. Generally, during the manufacture of PCD, cobalt is used as a sintering aid which enables the conversion of graphite into diamond at elevated temperatures and pressures [98]. Diamond is known to be meta-stable at ambient pressures and temperatures. However, during tool operation at elevated temperatures, the cobalt is able to reverse catalyse the conversion of diamond into graphite since ambient pressures are present. Even prior to tool use, the PCD is usually brazed onto the drill bit using an oxy-acetylene flame and the possibility of PCD degradation is extremely high [3], and is found to be more evident in PCD containing finer diamond grains.

The formation of graphite leads to a 55% molar volume increase and this could lead to the cracking of the PCD table [99]. A typical microstructural crack in PCD was previously shown in Figure 1.19. Microstructural cracking could have various causes, for example if the coefficient of thermal mismatch between the diamond and the binder is high, it could cause the diamond table to form micro cracks which could lead to tool failure especially when the tool is exposed to the harsh drilling or cutting conditions. This effect is usually exacerbated by exposure to elevated temperatures where the cobalt (having a CTE value of  $13 \times 10^{-6} \text{ m.m}^{-1}.\text{k}^{-1}$ , [100]) expands more rapidly than the diamond (which has a CTE value of  $1 \times 10^{-6} \text{ m.m}^{-1}.\text{k}^{-1}$ , [101]). The other cause could be a molar volume increase as a result of graphitisation of the diamond or oxidation of the binder [36] [102].

Huang et al. investigated the interaction between VC and WC carbides [103]. Pure VC and WC carbides were hot pressed at 1950 °C and 2050 °C for 90 min under a pressure of 30 MPa, using a graphite die. They observed that the (V,W)C<sub>x</sub> phase formed at a faster rate when cobalt was present, and this was probably due to the dissolution of tungsten and carbon into cobalt and precipitation onto the VC grains.

In this study, the focus was on the effect of heat treatment on the stability of the carbide phase in the PCD. In addition, the extent of graphitisation was also investigated.

## 3.2 Experiments

### 3.2.1 Terminated Press Runs

It has been mentioned in previous chapters that the mixed carbide has the formula  $(V,W)C_x$ , but the formation temperature or the time taken for the formation was not known. An experiment was hence structured to investigate this phenomenon. Keeping the pressure and sintering temperature constant, two experiments were carried out, viz. 50% reduction in the original sintering time and 10% reduction in the original sintering time. The sintering pressure and temperature remained at 6.8 GPa and 1400 °C respectively. A diamond powder mix comprising 3wt% (1.85vol%) VC powder was used for the experiments. These experiments were aimed at investigating the kinetics of the reaction. In general, it is very difficult to modify the sintering pressure or temperature of the reaction and this is mainly due to the existence of a small sintering window for PCD formation. The belt press was used to carry out these experiments.

### 3.2.2 Heat treatment of the VC and diamond powder mix

A diamond powder mix comprising 3wt% (1.85vol%) VC powder was heated treated in a tube furnace at three different temperatures (i.e. 1200 °C, 1300 °C and 1400 °C) under a flowing stream of nitrogen gas for 3hrs. Figure 3.1 shows a schematic of the experimental setup.

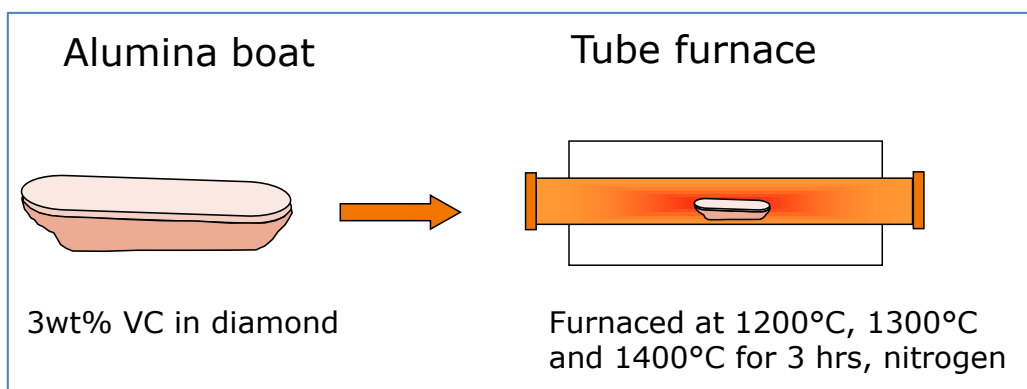


**Figure 3.1: Heat treatment of diamond powder in a tube furnace**

The powder samples were allowed to cool under a constant stream of nitrogen gas prior to removal in order to reduce the extent of oxidation. After removal of the powder from the tube furnace, the samples were analysed using a Panalytical X'Pert Pro XRD and a JSM 7500 Jeol SEM.

### 3.2.3 Hot Stage XRD Analysis

Hot stage XRD analysis was carried out on a standard PCD to determine the onset of graphitization, and to observe any phase changes that may occur. The VC enhanced PCD was also subjected to hot stage XRD to determine the stability of the mixed carbide phase, the onset of graphitization and the stability of the binder phase. The XRD was run from room temperature to a temperature of 1100 °C, with the angle ranging from 0°2θ to 80°2θ. The experiment was carried out under vacuum, at a pressure of 10<sup>-4</sup> - 10<sup>-6</sup> mbar, using the settings outlined in Table 3.1.

**Table 3.1: Hot Stage XRD parameters**

<b>Parameter</b>	<b>Setting</b>	<b>Parameter</b>	<b>Setting</b>
Start Position [°2θ]	20.0237	PSD Mode	Scanning
End Position [°2θ]	79.9517	Spinning	No
Step Size [°2θ]	0.0330	Divergence Slit Type	Automatic
Scan Step Time [s]	29.8450	Anode Material	Co
Scan Type	Continuous	Generator Settings	40 mA, 40 kV

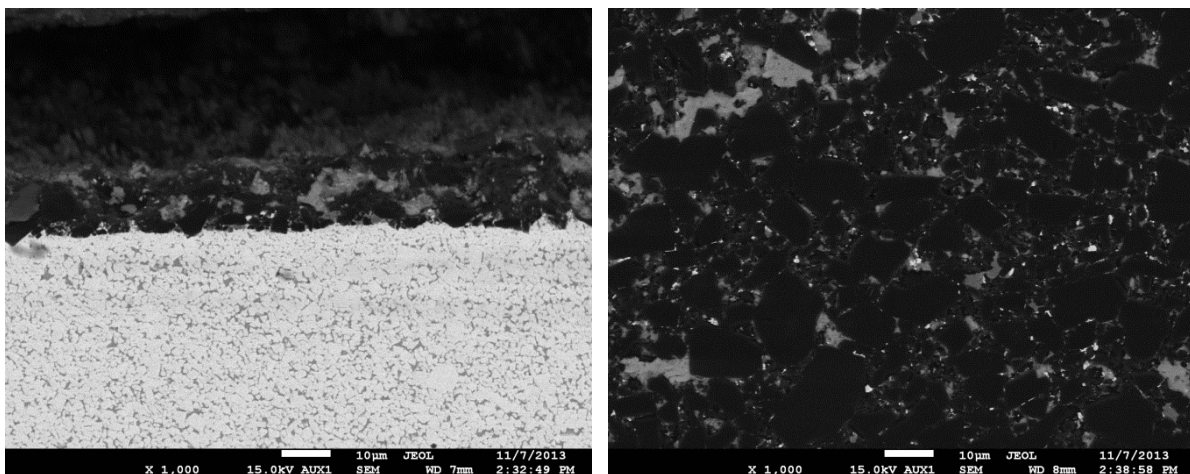
The PCD had to be electro discharge machined from a height of 12 mm to a height of 5 mm in order to fit into the tool holder. The diameter of the PCD remained the same, i.e. 16 mm.

### 3.3 Results

#### 3.3.1 Terminated Press Runs

##### 3.3.1.1 Sintering time reduced to 10% of original sintering time

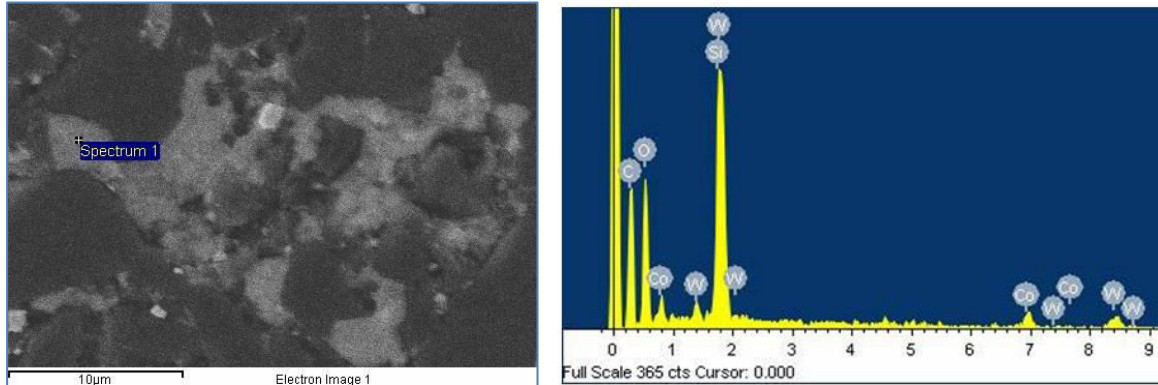
Figure 3.2 shows the SEM microstructure of the 3wt% VC enhanced PCD sintered at 10% of the original sintering time. The interface microstructure looks unreacted indicating that insufficient time was allowed for the cobalt to infiltrate from the substrate into the PCD table. The WC particles at the interface look intact, i.e. there is no acicularity of the WC particles at the interface which is normally an indication of an acceptable sintered PCD structure. Furthermore, there is no cobalt pooling at the interface and the diamond particles are not inter-grown. There appears to be a parallel crack running along the interface which indicates that the PCD has delaminated from the substrate, which is another indication of insufficient bonding of the PCD to the WC substrate.



**Figure 3.2: SEM microstructure of the VC enhanced PCD sintered at 10% of the original sintering time**

The microstructure of the bulk PCD shows the individual diamond grains crushed together with no diamond-diamond bonding. The behavior properties of this type of

microstructure are expected to be poor since the PCD compact has no continuous diamond network and hence no structural strength.



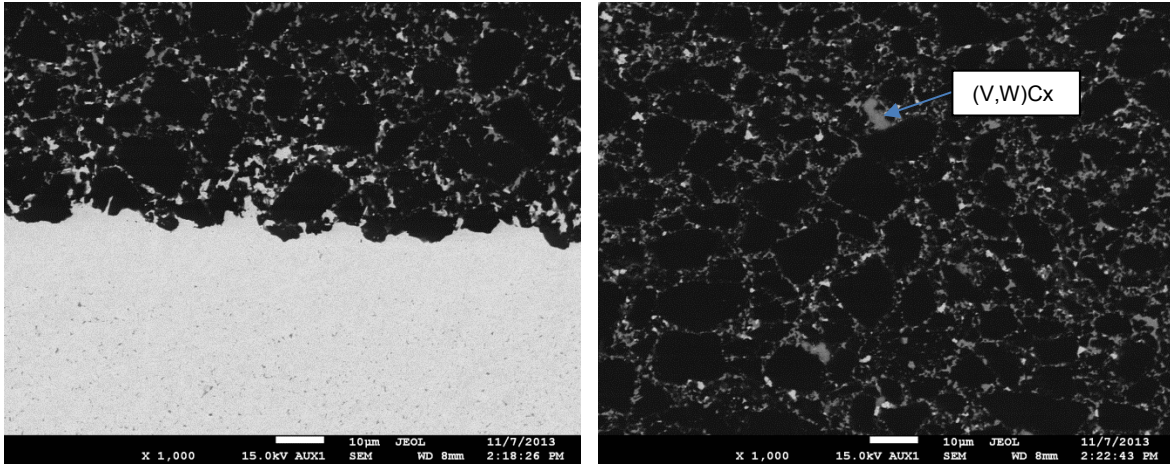
**Figure 3.3: EDS analysis of the binder pool**

Figure 3.3 shows the EDS analysis of the binder pool. Non sintered diamond particles are clearly visible in the binder pools. The binder pool comprises a mixture of cobalt, tungsten, silicon, carbon and oxygen. The presence of vanadium could not be detected in the binder pool. During the polishing of the PCD compact, there was diamond pull out since there was no diamond-diamond bonding to hold the particles together. The hole left behind was filled with the silica residue which is normally used to polish the surface of the PCD for microstructural analysis. The observed microstructure shows that the dwell time was insufficient to attain adequate diamond inter-growth. XRD analysis could not be carried out on the sample due to the extensive amount of cracks present in the sample.

### 3.3.1.2 Sintering time reduced to 50% of the original sintering time

Figure 3.4 shows the SEM microstructure of the 3wt% VC enhanced PCD sintered at 50% of the original sintering time. The interface between the diamond table and the substrate again seems unreacted which indicates inadequate sintering. In addition, there are large individual diamond particles present at the interface with no evidence of cracks present. Exposing the diamond powder mix to a longer sintering time would allow for a more effective bonding of the PCD table with the substrate. The bulk microstructure shows that the PCD is evidently not sintered. Larger diamond grains are surrounded by smaller grains, and there is a lack of diamond inter-growth between the particles. Another

indication of inadequate sintering is that the binder pools contain undissolved diamond particles.



**Figure 3.4: SEM microstructure of the 3wt% VC enhanced PCD sintered at 50% of the original sintering time**

Located within the PCD structure is the deposition of large carbide particles. Figure 3.5 shows the EDS analysis of the carbide particle. According to this analysis, the carbide particle comprises both vanadium and tungsten. It would therefore seem that at a dwell time of 50% of the original sintering time, the condition for the formation of the mixed carbide is energetically favourable. The mixed carbide was not observed in the PCD compact that was sintering at 10% of the original sintering time. Although there was no evidence of cracks at the PCD interface, the bulk PCD still contained both trans-granular and inter-granular cracks (refer to Figure 3.6). Due to the significant amount of cracking of the PCD, the units could not be processed for XRD analysis.

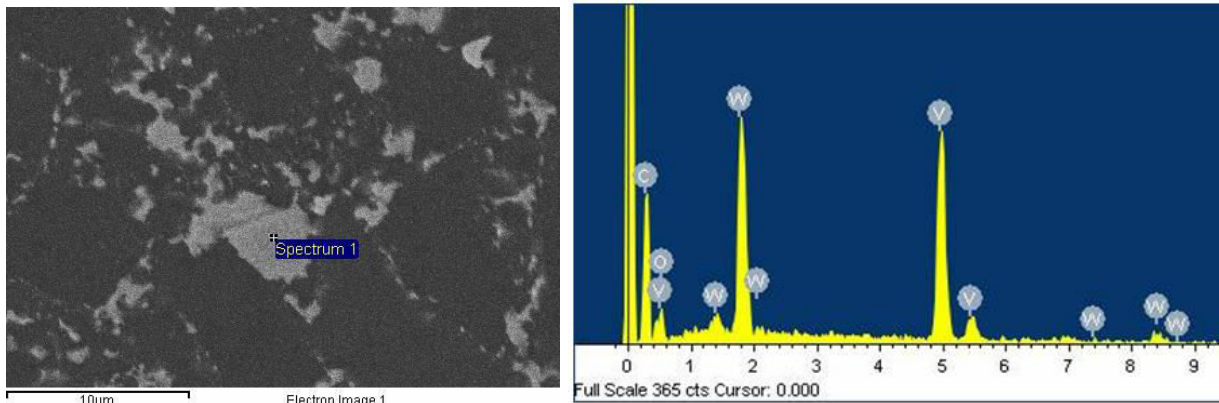


**Figure 3.5: EDS analysis of a carbide particle**

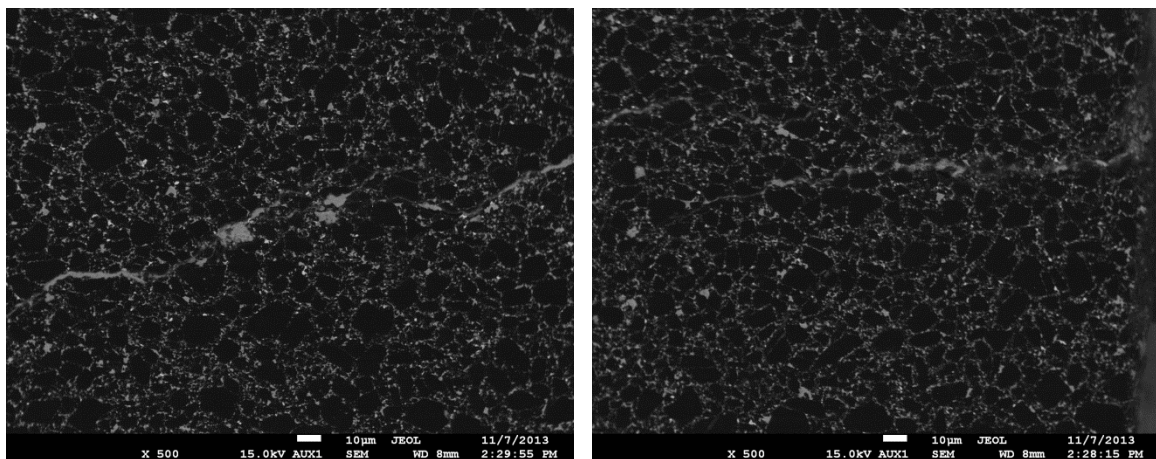


**Figure 3.6: PCD bulk showing presence of cracks**

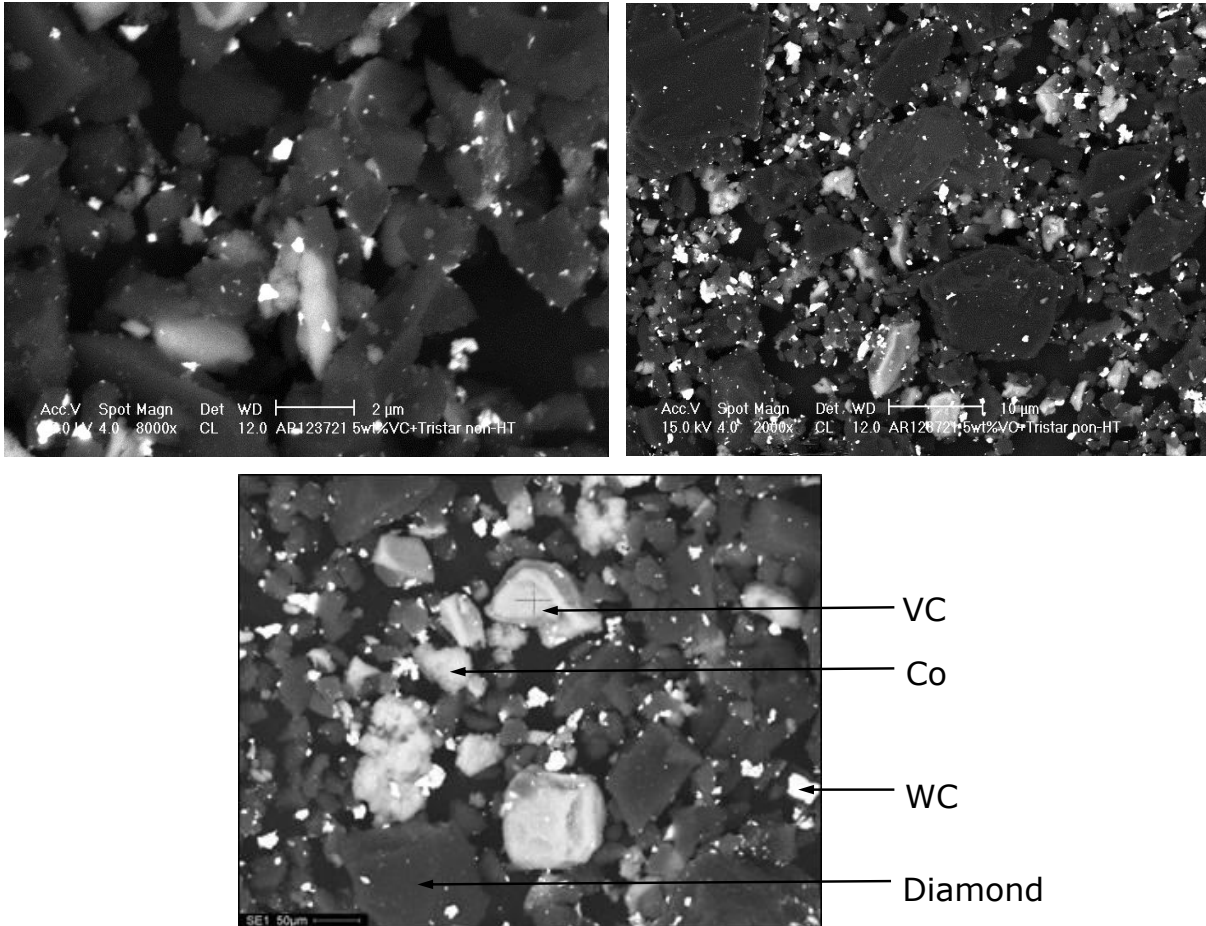
### 3.3.2 Heat treatment of the VC and diamond powder mix

So far the terminated sintering experiments showed the definite presence of the mixed carbide phase when the PCD was sintered at 50% of the original sintering time. It seems that the formation of the mixed carbide phase may be a function of the kinetics of the reaction. The question remains as to the thermodynamics of the formation of the mixed carbide phase, i.e. the temperature of formation.

Figure 3.7 shows the powder mixture of 3wt% VC, 6wt% WC and diamond particles containing 1wt% Co at room temperature. The individual components of the powder mix were combined in a milling pot and milled for 1hr using WC balls as the milling media.



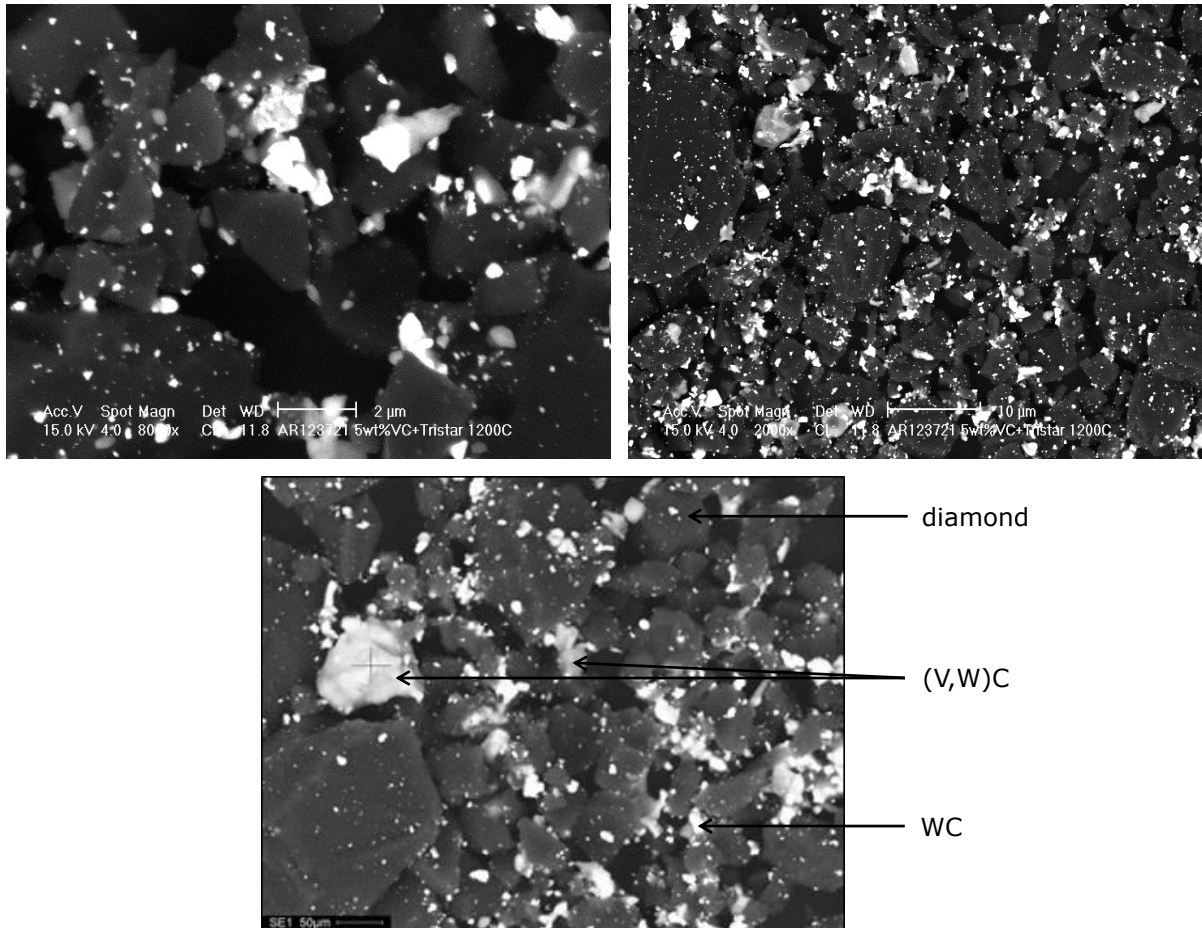
The powder mix seemed homogeneous with the presence of tungsten carbide, cobalt, vanadium carbide and diamond clearly visible.



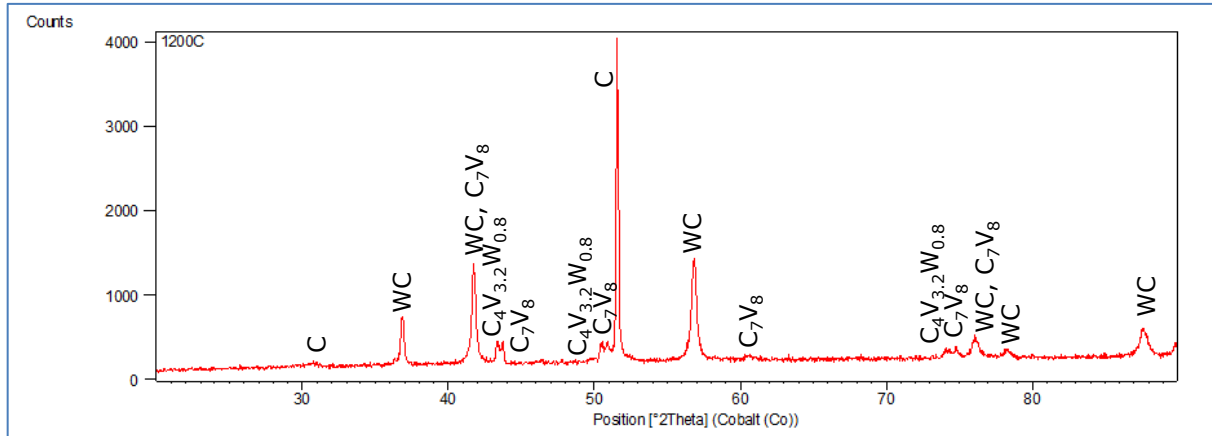
**Figure 3.7: SEM microstructure of the powder mixture containing VC, WC, Co and diamond at room temperature**

The powder mixture comprising VC, WC, Co and diamond particles was then subjected to a temperature of 1200 °C in a tube furnace for 3hrs under a constant flow of nitrogen gas (refer to Figure 3.8). The VC particles seem to have combined with the residual WC particles to form a (V,W)C<sub>x</sub> mixed carbide. The other components of the mix appears quite separate, i.e. no evidence of solid state sintering at this temperature. Figure 3.9 shows the XRD pattern of the powder. At 43.32°2θ and 43.74°2θ there appears two peaks which belong to the (V,W)C<sub>x</sub> phase and C<sub>7</sub>V<sub>8</sub> phase respectively. These peaks again appear at 50.55°2θ and 50.90°2θ. The peaks seem to have equal heights. Other phases present in the PCD are WC and carbon. Although cobalt was added to the powder mix, it could not be

detected using XRD and this is probably owing to cobalt concentration being below the detection limit of the XRD.

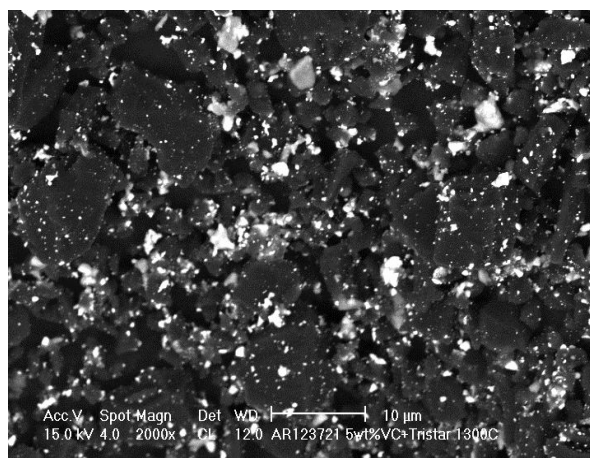
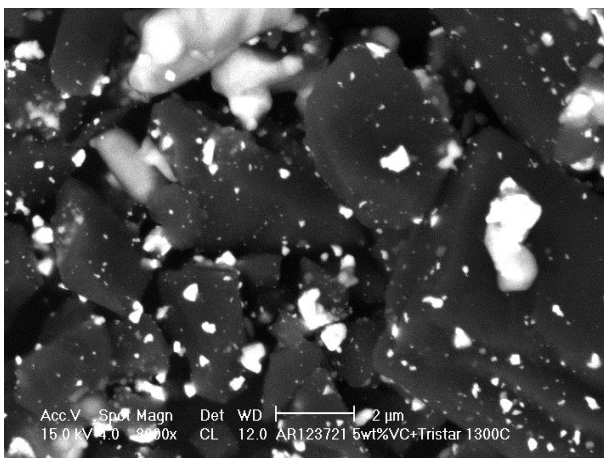


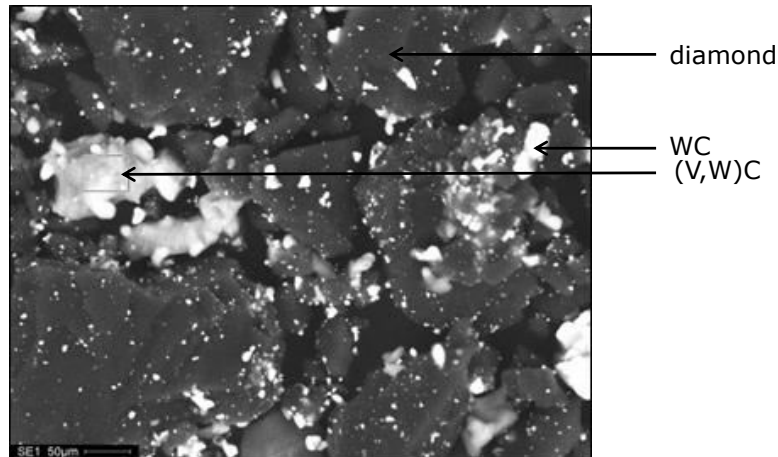
**Figure 3.8: SEM microstructure of the powder mixture containing VC, WC, Co and diamond post heat treatment at 1200 °C**



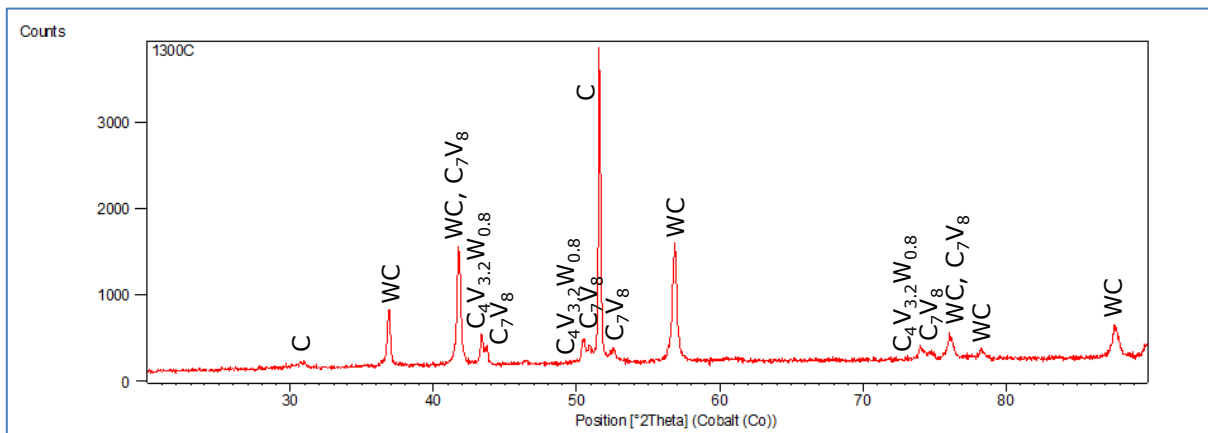
**Figure 3.9: XRD pattern of the powder mixture containing VC, W, Co and diamond post heat treatment at 1200 °C**

Figure 3.10 shows the SEM microstructure of the powder mixture containing VC, WC, Co and diamond post heat treatment at 1300 °C. Some of the particles seem to be interconnected which quite possibly indicates the initiation of solid state sintering. Again the (V,W)C<sub>x</sub> particle is present. XRD analysis shows the presence of WC, diamond, C<sub>4</sub>V<sub>3.2</sub>W<sub>0.8</sub> and C<sub>7</sub>V<sub>8</sub> (refer to Figure 3.11). The C<sub>4</sub>V<sub>3.2</sub>W<sub>0.8</sub> and C<sub>7</sub>V<sub>8</sub> peaks appear at 43.31°2θ and 43.74°2θ respectively, with the peak height of the C<sub>4</sub>V<sub>3.2</sub>W<sub>0.8</sub> phase being higher than the peak height of the C<sub>7</sub>V<sub>8</sub> phase. These twin peaks again appear at 50.45°2θ and 50.92°2θ. The pattern for the powder mix subjected to a temperature of 1300 °C differs from the sample obtained at 1200 °C by the appearance of an additional peak representing the C<sub>7</sub>V<sub>8</sub> phase occurring at 52.60°2θ.





**Figure 3.10: SEM microstructure of the powder mixture containing VC, WC, Co and diamond post heat treatment at 1300 °C**



**Figure 3.11: XRD pattern of powder mixture containing VC, WC, Co and diamond post heat treatment at 1300 °C**

Figure 3.12 shows the SEM microstructure of the powder mixture containing VC, WC, Co and diamond post heat treatment at 1400 °C. The particles seem to be interconnected which is definitely an indication of the presence of solid state sintering. The microstructure shows good homogeneity and distribution of the components. EDS analysis shows the presence of a (V,W) $C_x$  mixed carbide. Figure 3.13 shows the XRD pattern of the powder mix. According to the ICSD XRD database, the phases present are WC, diamond,  $C_4V_{3.2}W_{0.8}$  and  $C_7V_8$ . The peak height of the  $C_4V_{3.2}W_{0.8}$  phases appears much higher than the peak height of the  $C_7V_8$  phase.

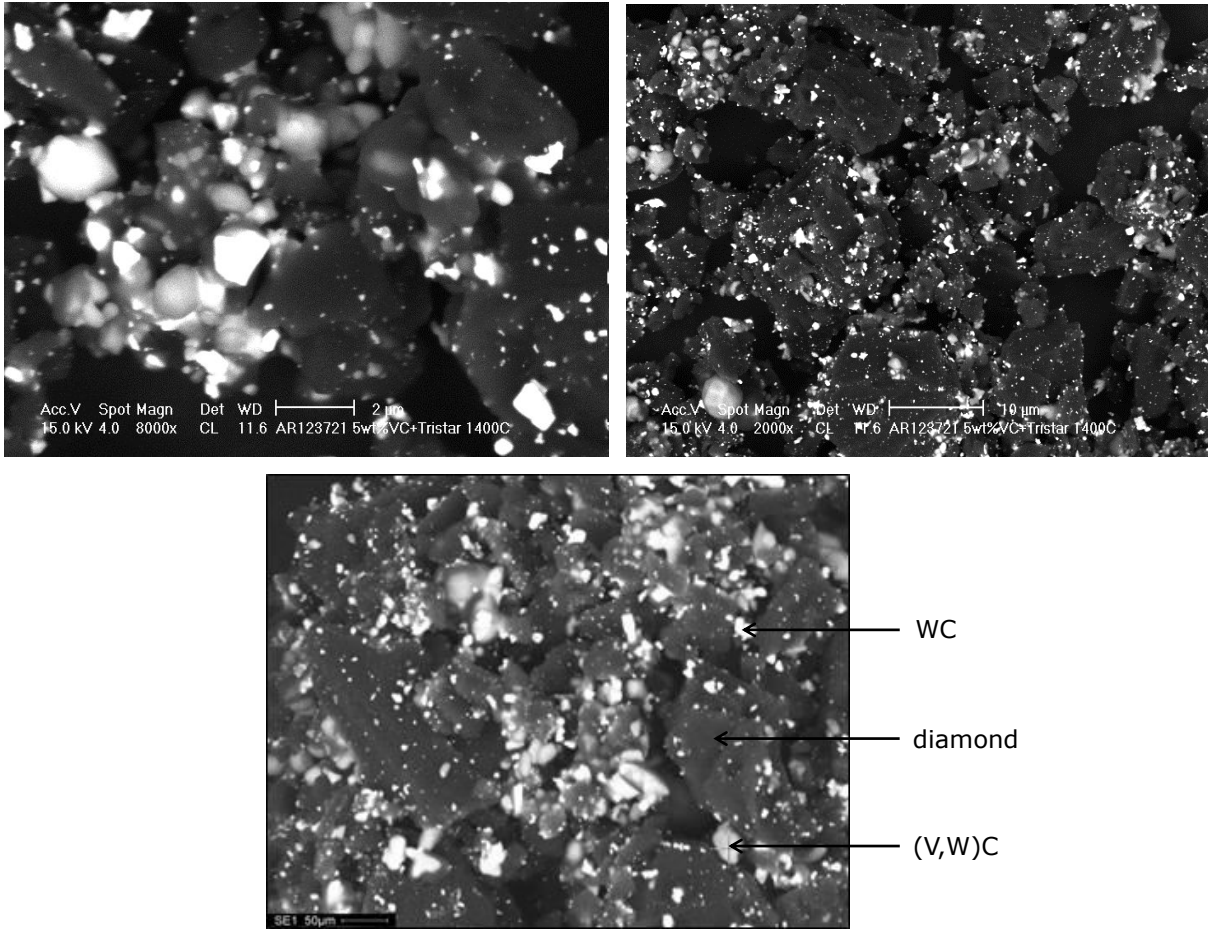


**Figure 3.12: SEM microstructure of the powder mixture containing VC, WC, Co and diamond post heat treatment at 1400 °C**

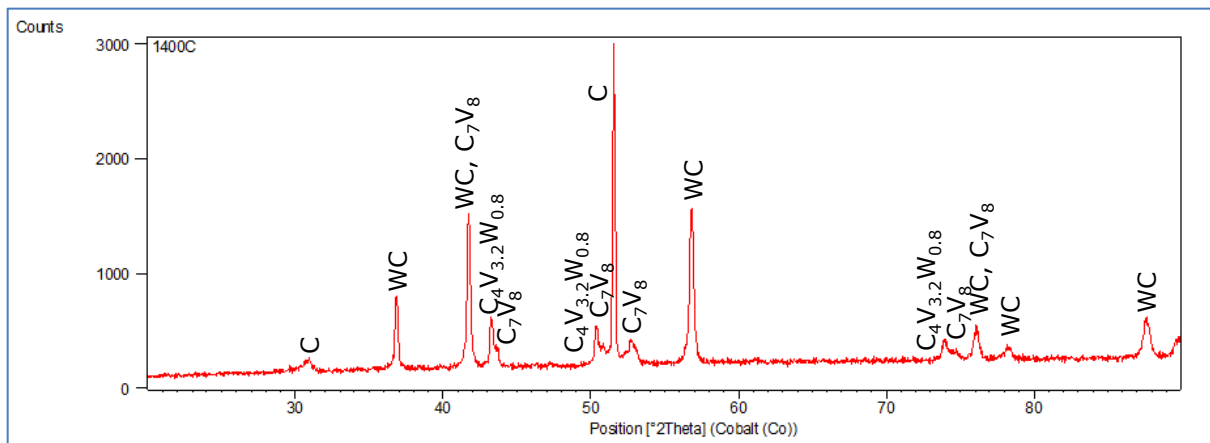
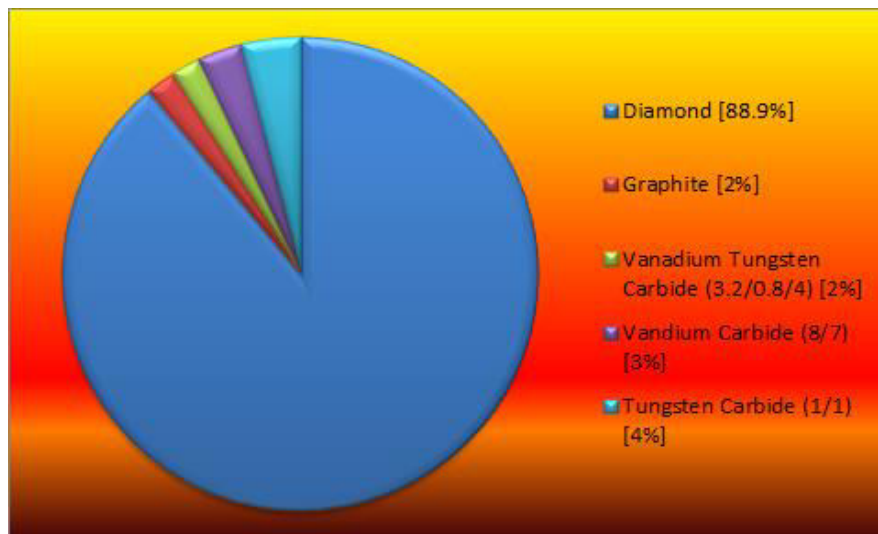
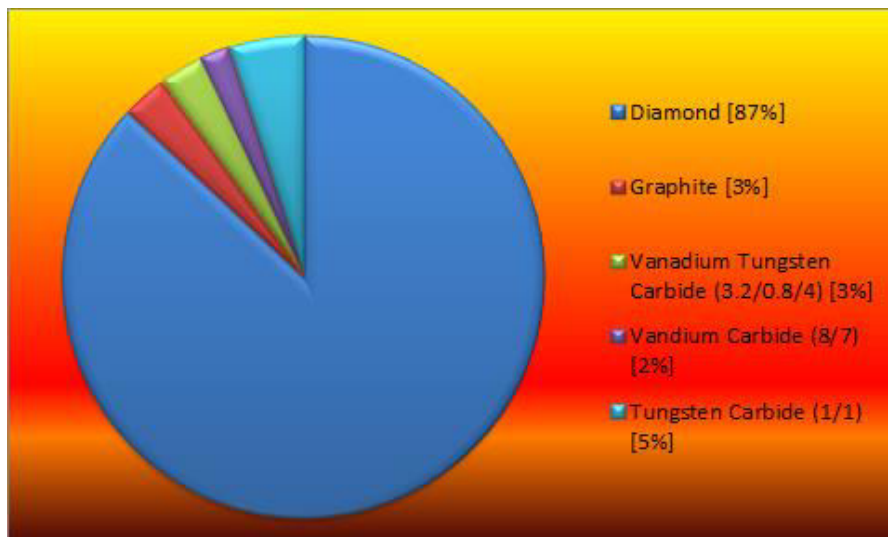


**Figure 3.13: XRD pattern of powder mixture containing VC, WC, Co and diamond post heat treatment at 1400 °C**

Figure 3.14 shows the XRD quantification of the powder mixture containing VC, WC, Co and diamond performed using the Reference Intensity Ratio (RIR) method. It is evident from the XRD quantification that the amount of (V,W)C<sub>x</sub> present in the powder mix is greater in the powder mix subjected to 1400 °C. This implies that at the higher temperatures, the reaction between V<sub>7</sub>C<sub>8</sub> and WC to form the (V,W)C<sub>x</sub> phase is more favourable.



(A)



(B)

**Figure 3.14: XRD quantification of the powder mixture containing VC, WC, Co and diamond: (A) Heat treated powder mixture at 1200 °C, (B) Heat treated powder mixture at 1400 °C**

### 3.3.3 Hot stage XRD analysis of the standard PCD and PCD enhanced with 5wt% VC

#### 3.3.3.1 Standard PCD

Hot stage XRD is a very important tool especially in determining the high temperature behaviour of a reaction. Figure 3.15 shows the XRD pattern of the standard PCD prior to heat treatment. According to the ICSD XRD database, the phases present are WC,  $\text{Co}_{0.87}\text{W}_{0.13}$  and diamond. Tungsten atoms are dissolved in the cobalt lattice and as mentioned previously, the tungsten atoms enhance the phase stability of the cobalt lattice. The XRD peak analysis of the  $\text{Co}_{0.87}\text{W}_{0.13}$  phase shows that the phase has an fcc structure.

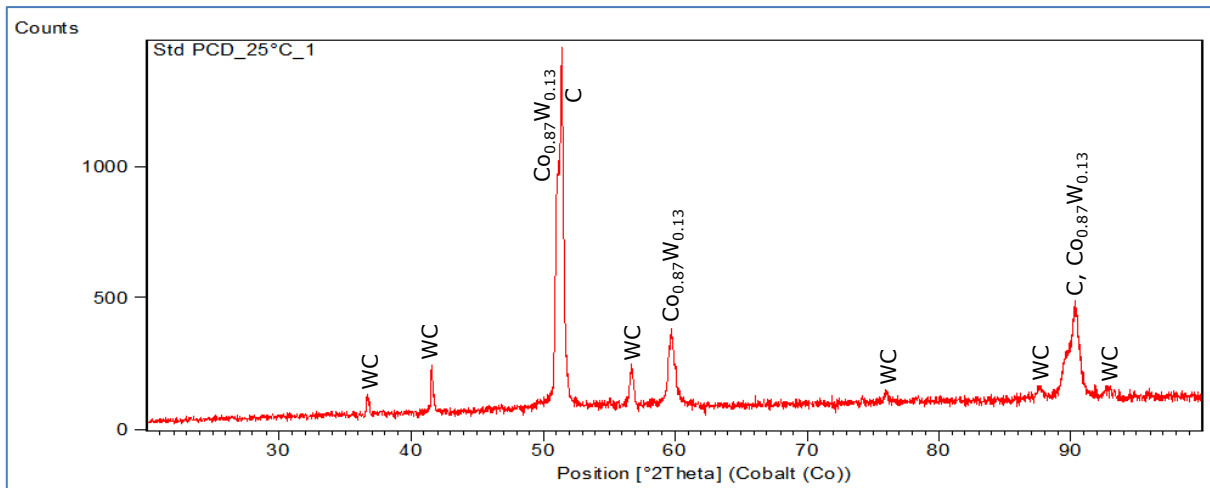
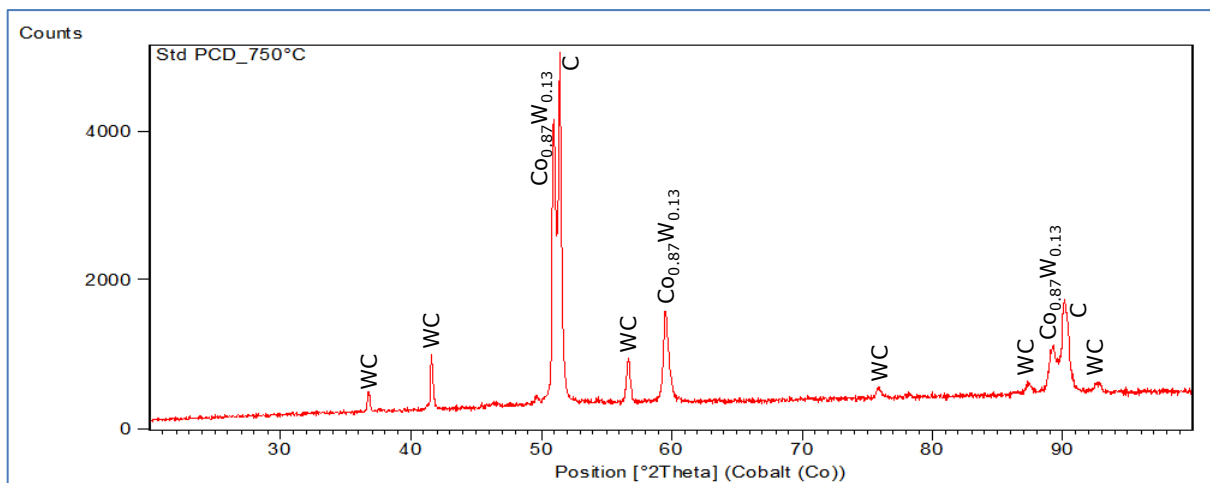
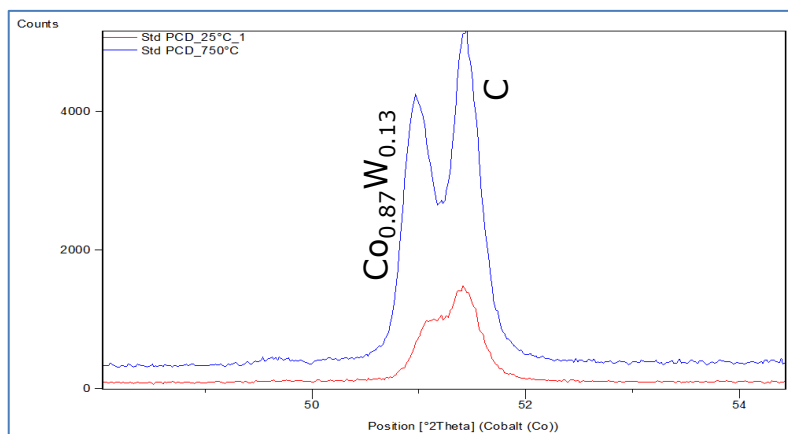


Figure 3.15: XRD pattern of the standard PCD at 25 °C



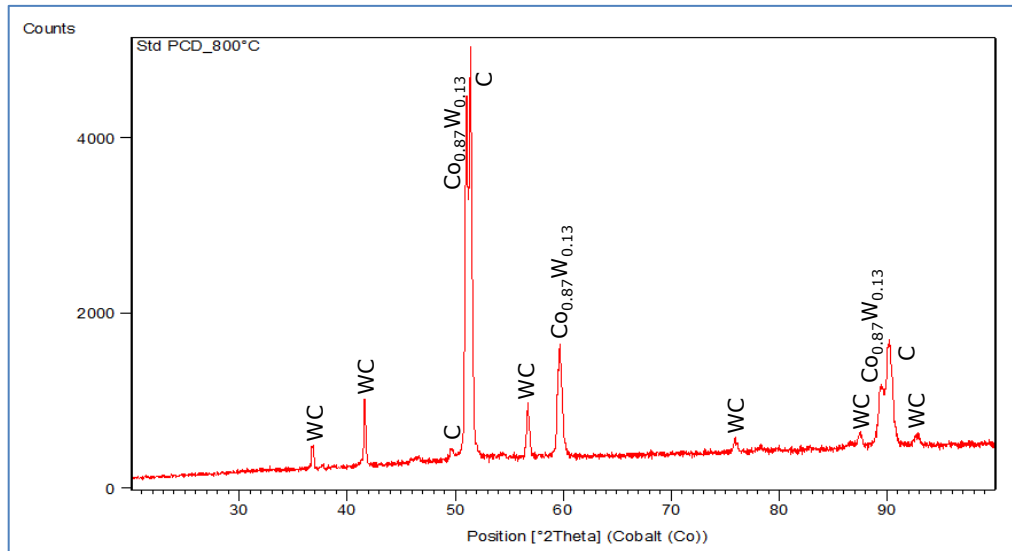


**Figure 3.16: XRD pattern of the standard PCD at 750 °C**

Figure 3.16 shows the XRD pattern of the standard PCD at 750 °C. The typical phases present are WC,  $\text{Co}_{0.87}\text{W}_{0.13}$  and diamond. Interestingly, the peak that appeared at  $51.54^\circ 2\theta$  in the room temperature sample which was a combination of  $\text{Co}_{0.87}\text{W}_{0.13}$  and diamond, becomes de-convoluted at a temperature of 750 °C to form two individual peaks appearing at  $50.95^\circ 2\theta$  and  $51.41^\circ 2\theta$ . These peaks are identified as the  $\text{Co}_{0.87}\text{W}_{0.13}$  phase and the diamond phase. The peak appearing at  $90.26^\circ 2\theta$  is also de-convoluted into the two individual peaks, i.e. the  $\text{Co}_{0.87}\text{W}_{0.13}$  phase and the diamond phase. The  $\text{Co}_{0.87}\text{W}_{0.13}$  remains in the fcc structure. Cobalt has a higher thermal expansion coefficient than diamond and is therefore expected to expand much more than diamond, and hence display a greater peak shift during heat treatment. The difference in the thermal expansion between cobalt and diamond could possibly explain the observed de-convolution of the peaks at higher temperatures.

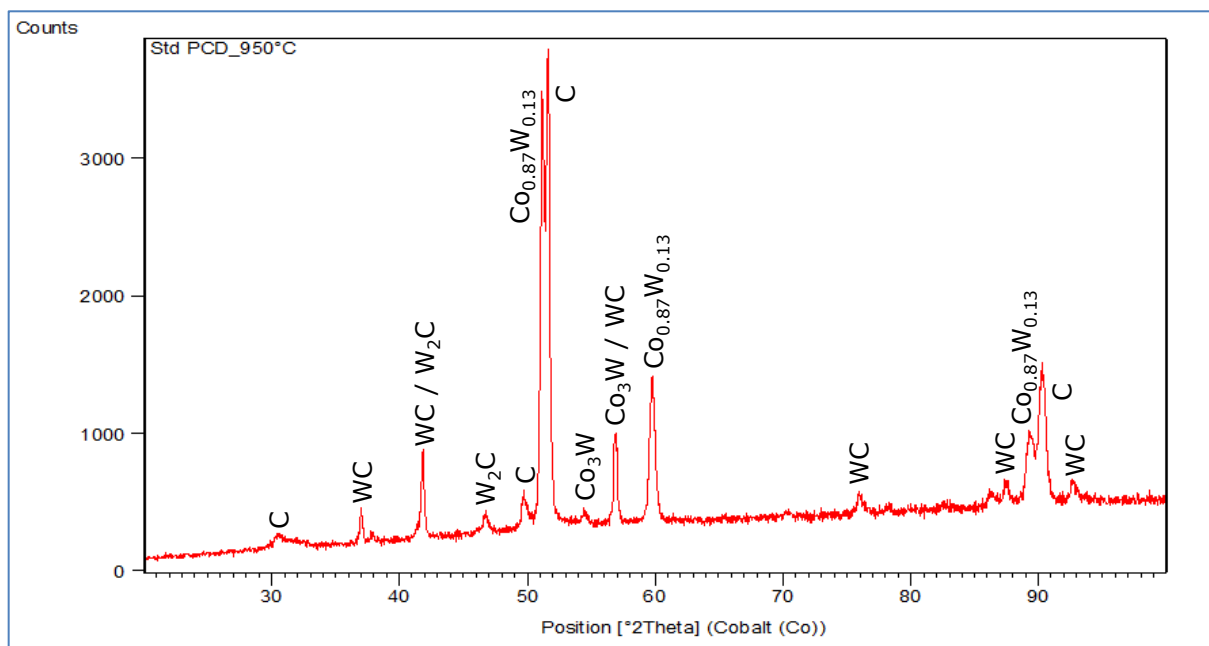
The XRD pattern of the standard PCD at 800 °C is shown in Figure 3.17. The only difference between this pattern and the pattern shown in Figure 3.16 is the distinctive appearance of a diamond peak at  $49.69^\circ 2\theta$ .





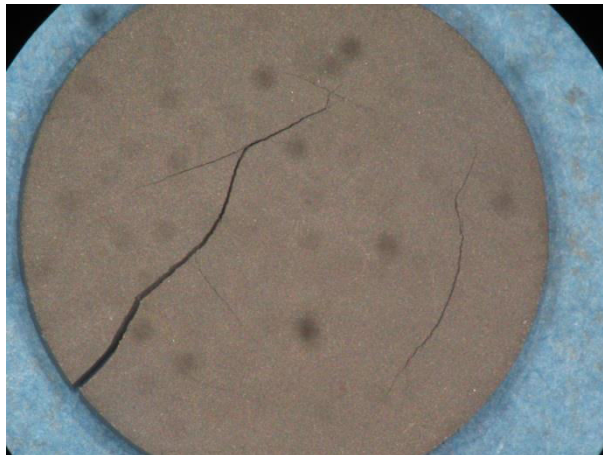
**Figure 3.17: XRD pattern of the standard PCD at 800 °C**

Figure 3.18 shows the XRD pattern of the standard PCD at 950 °C. Three additional phases are present in the PCD namely graphite,  $W_2C$  and  $Co_3W$ . The PCD subjected to 950 °C shows the clear presence of graphite with the primary peak appearing at  $30.49^\circ 2\theta$ . An additional  $Co_3W$  phase appears in the pattern with this phase containing more tungsten than the original  $Co_{0.87}W_{0.13}$  phase.



**Figure 3.18: XRD pattern of the standard PCD at 950 °C**

The optical image of the standard PCD after heat treatment at 950 °C is shown in Figure 3.19. Cracks are present on the surface of the PCD. A closer look at the PCD surface shows the presence of micro cracks. There also seems to be evidence of material on the surface of the PCD which appears as though it might have seeped out from within the PCD (refer to Figure 3.20). EDS analysis of the PCD surface is shown in Figure 3.21. The EDS pattern shows that the material is predominantly cobalt combined with a small quantity of tungsten. It would appear that at elevated temperatures, the cobalt present within the PCD bleeds out from within the PCD and deposits on the surface of the PCD. Since the CTE of diamond is  $1 \times 10^{-6}/\text{C}$  and the CTE of cobalt is  $13 \times 10^{-6}/\text{C}$ , one would expect the cobalt to expand much quicker than the diamond. Due to this expansion as well as the molar volume increase due to the conversion of diamond into graphite, micro cracks could develop on both the surface of the PCD and within the PCD.



**Figure 3.19: Optical image of the PCD after heat treatment at 950 °C**

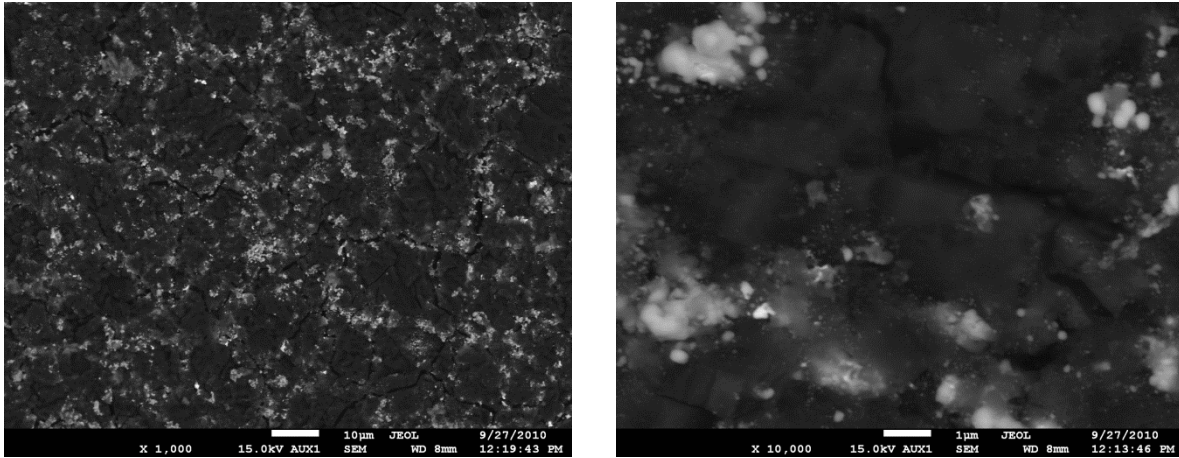


**Figure 3.20: SEM image of the surface of the standard PCD post heat treatment at 950 °C**

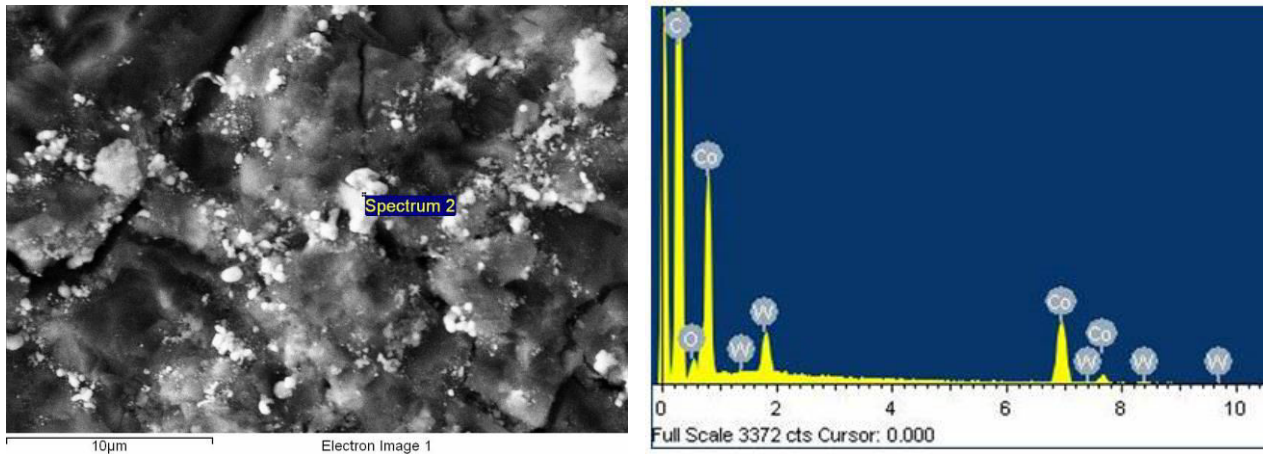


**Figure 3.21: EDS analysis of the surface of the standard PCD post heat treatment at 950 °C**

### 3.3.3.2 5wt% VC enhanced PCD

Hot stage XRD was used to assess the stability of the mixed carbide in order to determine whether any phase change of the metal occurs on the application of heat and to evaluate whether the VC enhanced PCD is more resistant to graphitisation. Figure 3.22 shows the XRD pattern of the VC enhanced PCD at room temperature. The phases present are (V,W)C<sub>x</sub>, Co<sub>0.793</sub>V<sub>0.207</sub> and diamond. Table 3.2 shows the XRD phases present in the VC enhanced PCD and standard PCD as a function of temperature. For the VC enhanced PCD, the phases within the PCD remain constant from room temperature to 900 °C.

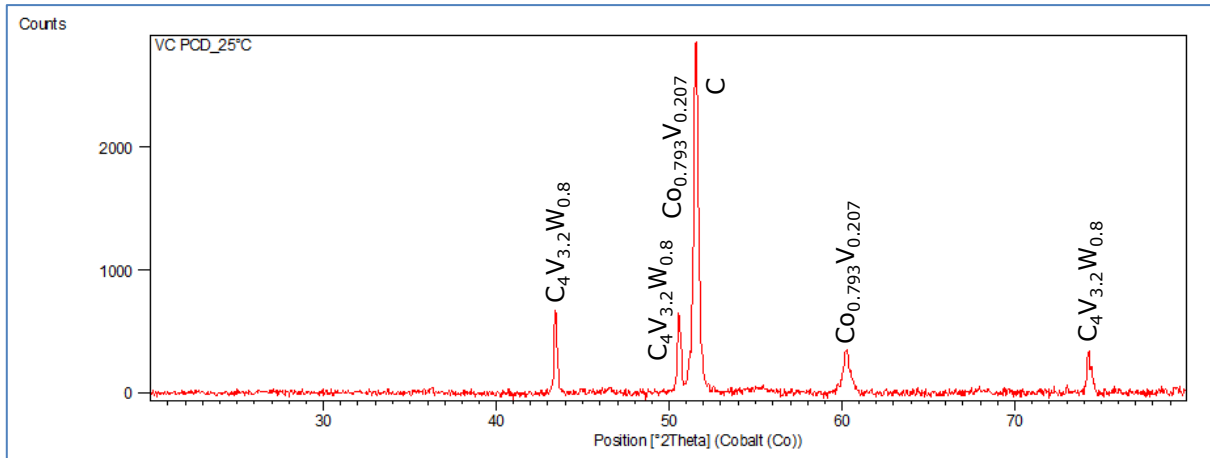


**Figure 3.22: XRD pattern of the 5wt% VC enhanced PCD at room temperature**

At 950 °C, a small bump associated with the formation of graphite appears at 30.56°2θ (refer to Figure 3.23). The XRD pattern taken at 1000 °C and 1100 °C are similar to the pattern taken at 950°C (refer to Figure 3.24 and Figure 3.25). Figure 3.26 shows the XRD pattern post heat treatment at 1100 °C. The peak associated with graphite seems more pronounced and the binder phase seems to consist of a combination of cobalt and vanadium. i.e.  $\text{Co}_{0.793}\text{V}_{0.207}$ . The solubility of vanadium in cobalt at 1400 °C is approximately 24at% and 20wt% (refer to the Co-V phase diagram in Figure 3.27). The XRD patterns suggest that the onset of graphitization seems to begin at 800 °C for the standard PCD and at 950 °C for the VC enhanced PCD. According to the observed XRD patterns, the VC enhanced PCD seems to be more thermally stable than the standard PCD.

**Table 3.2: XRD phases present in the 5wt% VC enhanced PCD and the standard PCD during heat treatment** (Appendix Two shows all the analysed XRD patterns)

Temperature	Phases Present (5wt% VC PCD)	Phases Present (Std PCD)
25°C	(V,W)Cx, CoV, diamond	WC, CoW, diamond
350°C	(V,W)Cx, CoV, diamond	-
400°C	(V,W)Cx, CoV, diamond	-
450°C	(V,W)Cx, CoV, diamond	-
500°C	(V,W)Cx, CoV, diamond	-
550°C	(V,W)Cx, CoV, diamond	-
600°C	(V,W)Cx, CoV, diamond	-
650°C	(V,W)Cx, CoV, diamond	-
700°C	(V,W)Cx, CoV, diamond	WC, CoW, diamond
750°C	(V,W)Cx, CoV, diamond	WC, CoW, diamond
800°C	(V,W)Cx, CoV, diamond	WC, CoW, diamond
850°C	(V,W)Cx, CoV, diamond	WC, CoW, diamond
900°C	(V,W)Cx, CoV, diamond	WC, CoW, diamond
950°C	(V,W)Cx, CoV, diamond, graphite	WC, CoW, Co <sub>3</sub> W, diamond, graphite
1000°C	(V,W)Cx, CoV, diamond, graphite	-
1050°C	(V,W)Cx, CoV, diamond, graphite	-
1100°C	(V,W)Cx, CoV, diamond, graphite	-
25°C (post heat treatment)	(V,W)Cx, CoV, diamond, graphite	WC, CoW, Co <sub>3</sub> W, diamond, graphite

(V,W)Cx represents C<sub>4</sub>V<sub>3.2</sub>W<sub>0.8</sub>, CoV represents Co<sub>0.793</sub>V<sub>0.207</sub>, CoW represents Co<sub>0.87</sub>W<sub>0.13</sub>

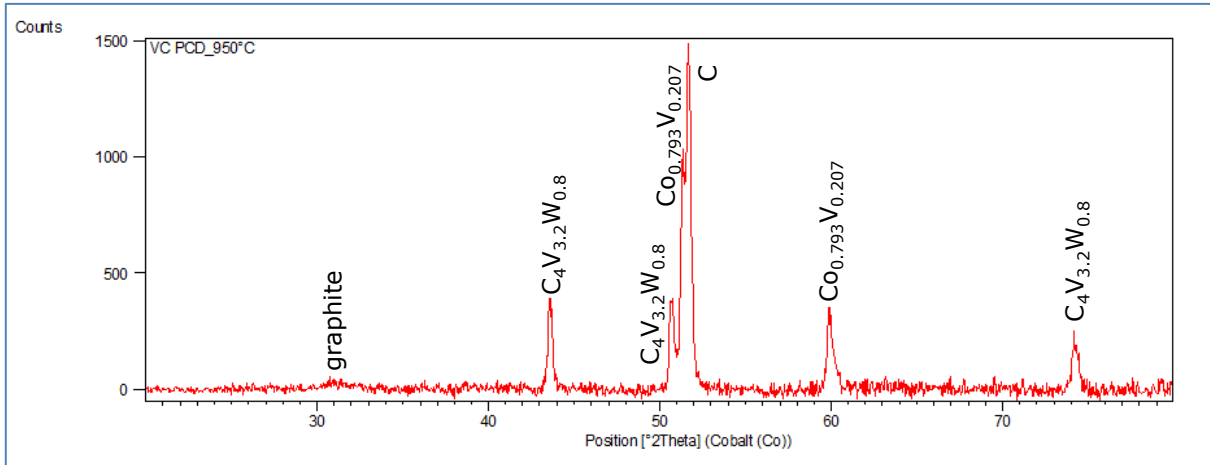


Figure 3.23: XRD pattern of the 5wt% VC enhanced PCD at 950 °C

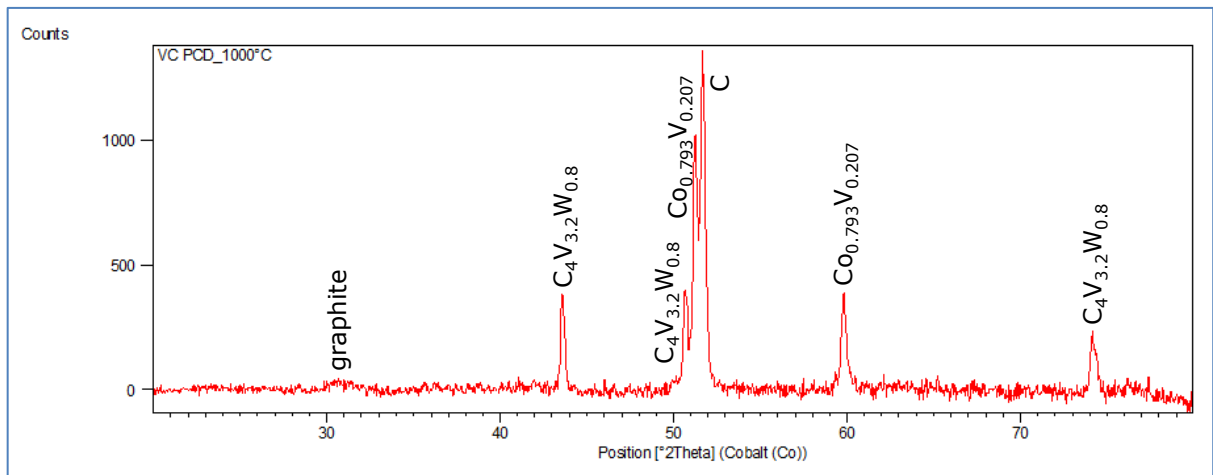


Figure 3.24: XRD pattern of the 5wt% VC enhanced PCD at 1000 °C

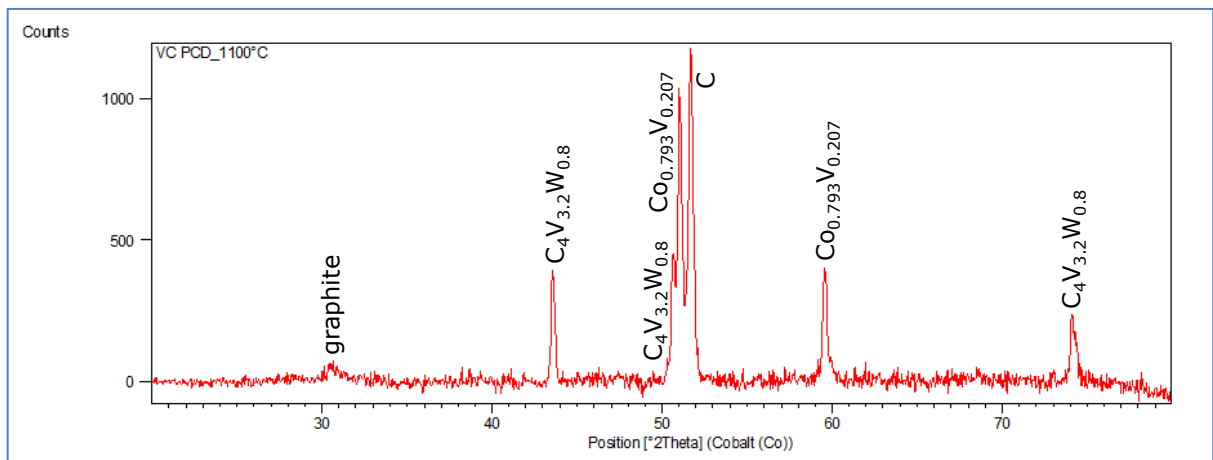
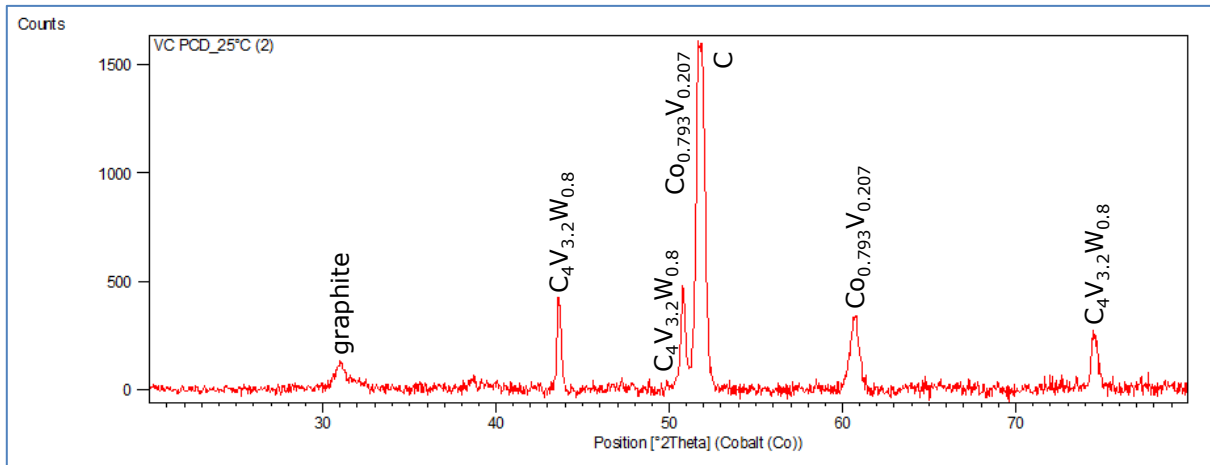
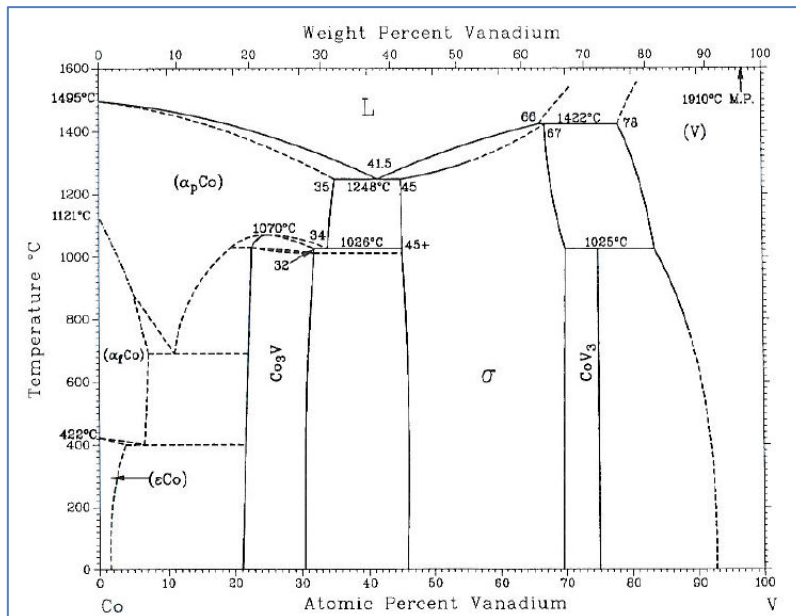


Figure 3.25: XRD pattern of the 5wt% VC enhanced PCD at 1100 °C



**Figure 3.26: XRD pattern of the 5wt% VC enhanced PCD at 25 °C (post heat treatment)**



**Figure 3.27: Co-V Phase Diagram [104]**

Figure 3.28 shows the SEM image and the EDS analysis of the VC enhanced PCD post heat treatment. There are cracks present on the surface of the PCD, and a combination of WC, Co and (V,W)Cx material appear on the PCD surface. Table 3.3 shows the EDS analysis results of the various areas in the heat treated PCD. Area (a) shows a combination of the elements present in the PCD. Area (b) indicates the atomic ratio of V:W to be 77:23, which is more-or-less in agreement with the (V,W)Cx phase determined using the XRD which according to the ICSD database was shown to have the formula of

$C_4V_{3.2}W_{0.8}$  and a calculated V:W ratio of 80:20. Similarly, area (c) is a mixed carbide particle and has a V:W ratio of 76:24. It is difficult to calculate the stoichiometry of the (V,W) $C_x$  phase using EDS analysis due to the overwhelming presence of carbon from the surrounding diamond particles.

It would appear that during the heat treatment of the PCD, the cobalt expanded and seeped out of the PCD leading to extensive amount of cracking observed. The XRD trace also showed the presence of graphite which most probably also initiated cracks due to the molar volume increase from the conversion of diamond into graphite.

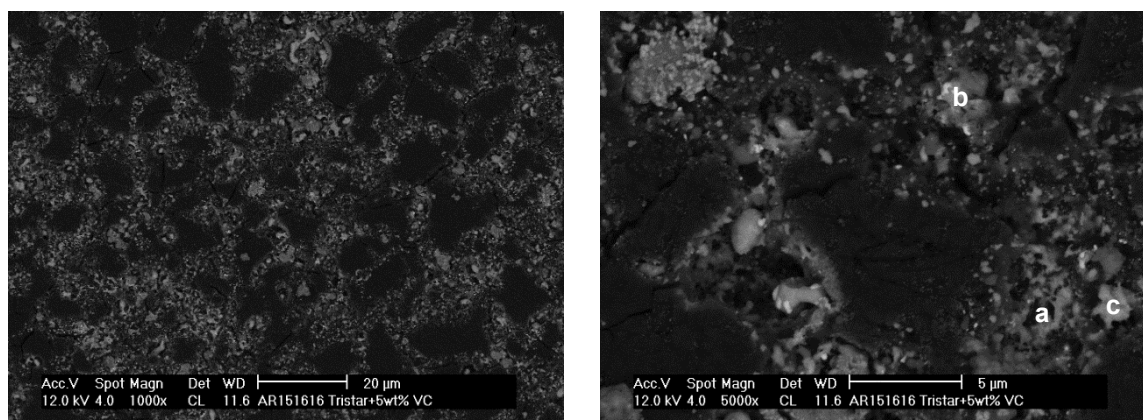


**Figure 3.28: SEM image of the VC enhanced PCD post heat treatment**

**Table 3.3: EDS Analysis of the various phases in the heat treated PCD, values in atomic %**

Area	Carbon	Oxygen	Tungsten	Vanadium	Cobalt
a	90.49	4.18	0.58	1.68	3.08
b	78.27	10.81	1.65	5.58	3.7
c	79.68	8.92	2.01	6.30	3.10

### 3.4 Discussion

The terminated runs carried out showed incomplete sintering of the PCD diamond table at both 10% of the original sintering time and at 50% of the original sintering time. However, at 50% of the original sintering time, the (V,W) $C_x$  mixed carbide was clearly



visible. Due to the difficulties experienced in controlling the terminated sintering experiments using the high pressure vehicle, it was decided to heat treat the 5wt% VC - diamond powder mix at three different temperatures to determine the formation temperature of the mixed carbide, i.e. investigating the reaction at increased temperature.

XRD analysis of the VC-diamond powder showed the ratio of  $C_4V_{3.2}W_{0.8}$ :  $C_7V_8$  to increase as a function of temperature, both the height of the respective peaks as well as the area (refer to Figure 3.29). At 1200 °C, the peak heights for both the  $C_4V_{3.2}W_{0.8}$  and the  $C_7V_8$  phases appear similar. The height of the  $C_4V_{3.2}W_{0.8}$  peak gradually increases as the temperature increases. The values for the peak height and peak area for the  $C_4V_{3.2}W_{0.8}$  and  $C_7V_8$  phases are plotted in Figure 3.30. It was found that as the temperature increased, the ratio of  $C_4V_{3.2}W_{0.8}$ :  $C_7V_8$  also increased, i.e. more of  $C_7V_8$  reacted with tungsten to form the (V,W)C<sub>x</sub> phase. Weidow et al. found that the (V,W)C<sub>x</sub> phase was formed at temperatures around 900 °C – 930 °C after solidification following liquid phase sintering in the manufacturing process [105].

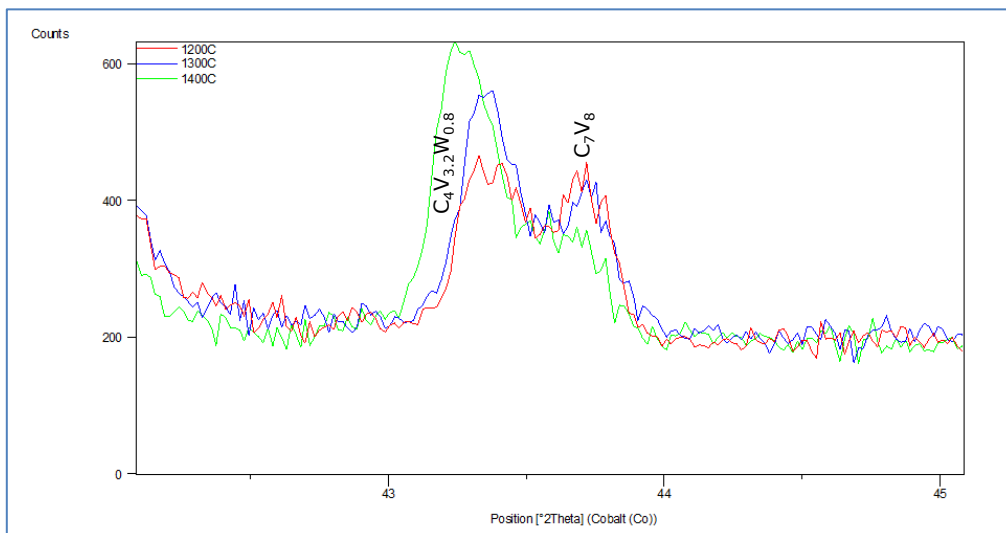


**Figure 3.29: XRD pattern showing the overlay of the  $C_4V_{3.2}W_{0.8}$  and  $C_7V_8$  peaks as a function of temperature**

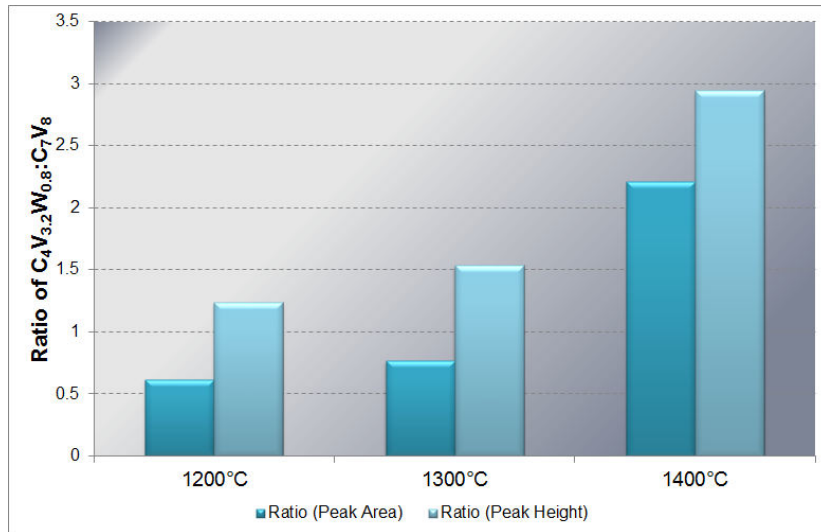


**Figure 3.30: Ratio of  $C_4V_{3.2}W_{0.8}:C_7V_8$  in the 5wt% VC – diamond powder mix exposed to different temperatures**

Figure 3.31 shows the proposed mechanism for the formation of the mixed (V,W)Cx carbide. The reaction between vanadium carbide and tungsten carbide is thermodynamically favourable at higher temperatures. At a temperature of 1200 °C, the XRD pattern contains almost equal amounts of the  $C_4V_{3.2}W_{0.8}$  phase and the un-reacted  $C_7V_8$  phase. The crystal structure of the  $C_7V_8$  phase is cubic and the crystal structure of the WC phase is hexagonal. The  $C_4V_{3.2}W_{0.8}$  phase contains more vanadium atoms than tungsten atoms and maintains a cubic crystal structure. It would therefore seem that the tungsten atoms that are dissolved in the cobalt matrix reacts with the  $C_7V_8$  phase to form a new compound, namely (V,W)Cx (refer to Equation 3-1).

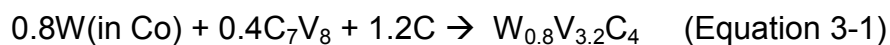
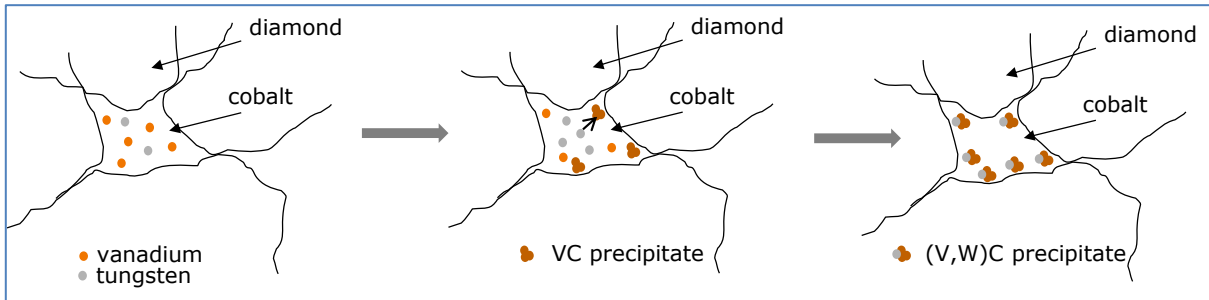
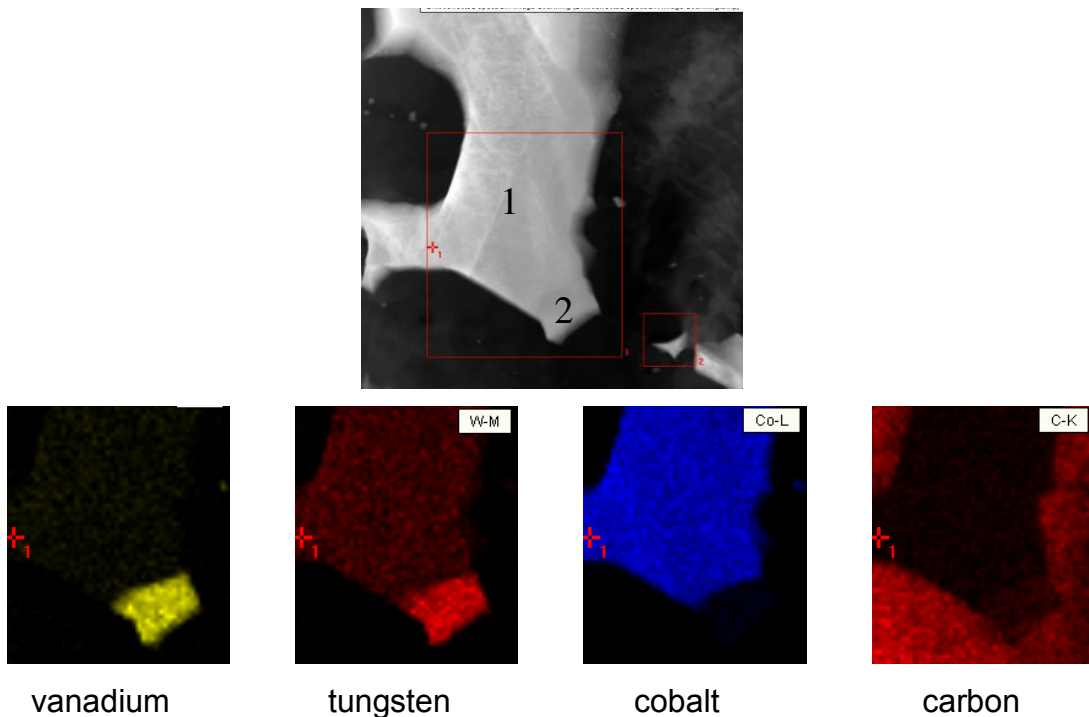


Figure 3.32 shows the TEM microstructure of a mixed carbide particle. The mixed carbide does not comprise a core-rim structure that is rich in VC at its core and shows the formation of the (V,W)Cx mixed carbide at the rim. Based on this observation, it could be assumed that either the vanadium and carbon atoms from the  $V_7C_8$  starting material dissolve in the cobalt binder as individual atoms and re-precipitate with the diffusion of tungsten atoms into the crystal lattice, or the tungsten atoms reacts with the  $V_7C_8$  particle to form the mixed carbide.

It was observed in the previous chapter that PCD sintered using 1wt% VC contained residual WC in the PCD microstructure. This observation can further be explained by the insufficient amount of vanadium atoms present in the PCD to react with all of the residual tungsten atoms dissolved in the cobalt binder, hence leaving behind free WC in the PCD microstructure.



**Figure 3.31: Model showing the proposed formation of the (V,W)Cx mixed carbide**



**Figure 3.32: TEM mapping of the binder pool in the PCD containing 3wt% VC**

The new (V,W)Cx phase seems to be stable on heat treatment of the PCD compact from room temperature to 1100 °C. This suggests that during tool use, no molar volume increase within the PCD compact is expected due to the absence of any phase change of

the (V,W)C<sub>x</sub> mixed carbide. Furthermore, during heat treatment the cobalt binder phase remains in the fcc state and does not revert to the hcp state. This implies that the vanadium dissolved in the cobalt binder stabilises the binder phase.

Figure 3.33 shows the XRD overlay of the standard PCD and the 5wt% VC enhanced PCD at temperatures of 950 °C and 1000 °C. It is clear from the XRD pattern that the extent of graphitisation in the PCD compact is reduced for the PCD containing VC. The advantage of this is that micro-cracking due to the molar transition of diamond to graphite at atmospheric pressure and elevated temperature within the PCD is also reduced. The volume increase for the molar transition of diamond into graphite is 55%.

The phenomenon observed in Figure 3.33 can best be explained by earlier observations that the (V,W)C<sub>x</sub> mixed carbide deposits at the diamond – binder interface thereby protecting the diamond from graphitisation. In addition, the (V,W)C<sub>x</sub> phase in the PCD displaces some of the cobalt binder present and hence the extent of graphitisation is reduced. As mentioned previously, the cobalt binder could catalyse the reverse transformation of diamond into graphite at elevated temperature and ambient pressures. The reduction in the extent of graphitisation in the VC enhanced PCD further explains the observed improvement in the behaviour of the PCD that was previously concluded.

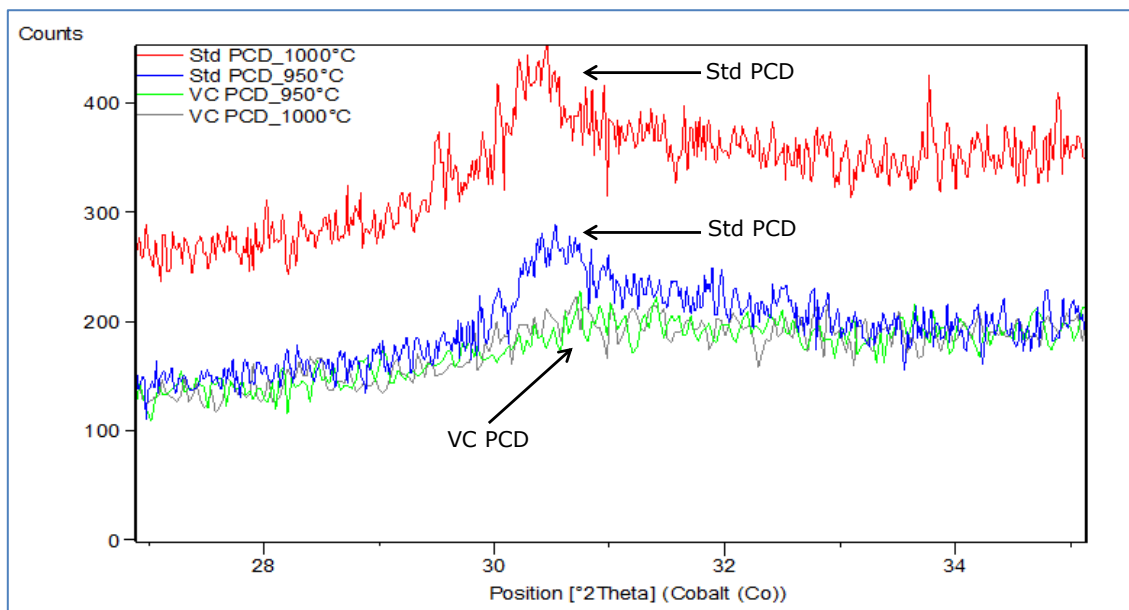


**Figure 3.33: XRD overlay of the standard PCD and 5wt% VC enhanced PCD**

### 3.5 Conclusion

Interrupted high pressure and high temperature press runs were initially carried out to determine the formation temperature of the mixed carbide. These runs were done at 10% of the original sintering time and at 50% of the original sintering time. Unfortunately, the PCD was found to be inadequately sintered comprising both micro and macro cracks.

Micron diamond powder containing 5wt% VC was then heat treated in a tube furnace for 3hrs under a flowing stream of nitrogen. The nitrogen was present to prevent any oxidation of the powder. The heat treatment temperatures were 1200 °C, 1300 °C and 1400 °C. At 1200 °C, the ratio of  $C_4V_{3.2}W_{0.8}:C_7V_8$  (i.e. peak height) was found to be similar. As the temperature of the reaction increased from 1200 °C to 1400 °C, the ratio of the  $C_4V_{3.2}W_{0.8}:C_7V_8$  peak height and peak area also increased. It would appear that as the temperature increased, the reaction between  $C_7V_8$  and WC proceeded towards the formation of the (V,W)Cx phase.

The newly formed (V,W)Cx phase was found to be stable at temperatures up to 1100 °C, with the vanadium atoms stabilizing the fcc cobalt lattice as evidenced by the absence of any hcp cobalt phase present in the sintered PCD. In addition, the presence of VC in the PCD was found to reduce the extent of graphitisation of the PCD.

### 3.6 Recommendation

It is recommended that heat treatment experiments of the diamond powder containing 3wt% VC be broadened to include the formation temperature of the (V,W)Cx phase which occurs at 900 °C – 930 °C.

## CHAPTER FOUR

### ADDITION OF OTHER CARBIDES TO PCD

#### 4.1 Background

Various carbides have been added to WC-Co to change the properties of the carbide material. Hashe et al. discovered that vanadium carbide additions to WC-Co resulted in the formation of very large cubic (W,V)C<sub>x</sub> grains [53]. They found that the addition of small amounts of titanium could be used to control the grain growth of the cubic grains. It was believed that the low solubility of titanium in the binder phase hinders the nucleation and growth of the cubic carbides in the solid state part of the sintering, and that the carbide grains are formed in the liquid state part of the sintering.

Weidow et al. added different carbides to cemented carbide tools in order to improve the properties of the tool during high steel machining [48]. The addition of titanium carbide, zirconium carbide, niobium carbide and tantalum carbide were investigated. All cubic carbide additions to the cemented carbide resulted in lower tungsten carbide grain growth. The material containing both titanium carbide and zirconium addition to the carbide produced the highest hardness due to the formation of the smallest cubic carbide grain size.

Luyckx et al. investigated the additions of C<sub>7</sub>V<sub>8</sub> and Cr<sub>3</sub>C<sub>2</sub> to WC-Co [106]. C<sub>7</sub>V<sub>8</sub> was found to be a more efficient grain refiner than Cr<sub>3</sub>C<sub>2</sub> since Cr<sub>3</sub>C<sub>2</sub> remains in solution whilst C<sub>7</sub>V<sub>8</sub> precipitates on cooling and hence finer tungsten carbide grain sizes were achieved using C<sub>7</sub>V<sub>8</sub>. In general, most carbide additions to WC-Co produced a tool with a higher hardness and improved properties.

This chapter details the microstructural results obtained on additions of different carbides to PCD. The carbides investigated were molybdenum carbide (Mo<sub>2</sub>C), chromium carbide (Cr<sub>3</sub>C<sub>2</sub>), titanium carbide (TiC) and an equal mixture of vanadium carbide and titanium carbide. The aim of the chapter was to determine the structure and location of the carbide

precipitation in the PCD, as well as the stability of the carbide during tool use. The stability tests were carried out using hot stage XRD.

## 4.2 Experimental

Table 4.1 shows the supplier and average particle size of the various carbides that were used in the experiments.

**Table 4.1: Source and Particle size of the various carbide powders**

<b>Powder Material</b>	<b>Source</b>	<b>Average Particle Size</b>
Vanadium carbide	HC Starck	3.08 $\mu\text{m}$
Chromium carbide	Sigma Aldrich	2.67 $\mu\text{m}$
Titanium carbide	Sigma Aldrich	3.27 $\mu\text{m}$
Molybdenum carbide	Sigma Aldrich	2.82 $\mu\text{m}$

The carbides were ball milled with the diamond powder (average grain size of 10  $\mu\text{m}$ ) in the same way as for the VC enhanced PCD. WC was introduced into the diamond powder by the abrasion of the WC milling media during the ball milling process. The diamond mixture was then placed onto a WC-Co substrate and sintered at 1400 °C and 6.8 GPa using a high pressure vehicle.

## 4.3 Results

### 4.3.1 Mo<sub>2</sub>C addition to PCD

The microstructure of the PCD containing 3wt% (1.17vol%) Mo<sub>2</sub>C showed the PCD to be well sintered (refer to Figure 4.1). There appears to be three phases, i.e. a dark grey phase associated with diamond, a lighter grey phase due to the presence of the binder and an off-white brighter phase. On closer investigation, EDS analysis shows that both the Mo<sub>2</sub>C and the WC seems to have precipitated in the binder pools (shown in Figure 4.2). The EDS analysis, however, does not differentiate whether the Mo<sub>2</sub>C precipitates on its own next to the WC particles or whether it combines with the tungsten to form a mixed carbide.

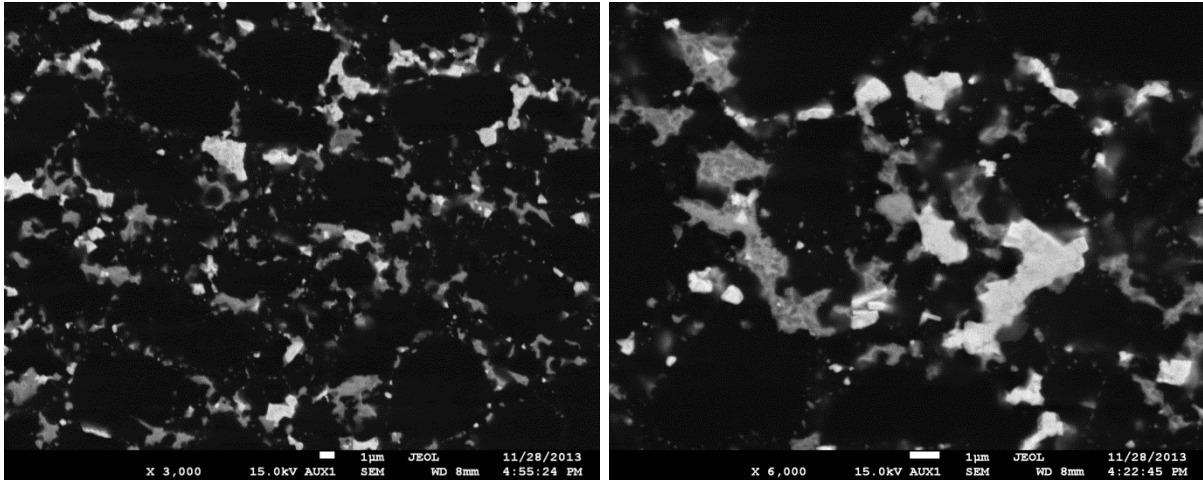
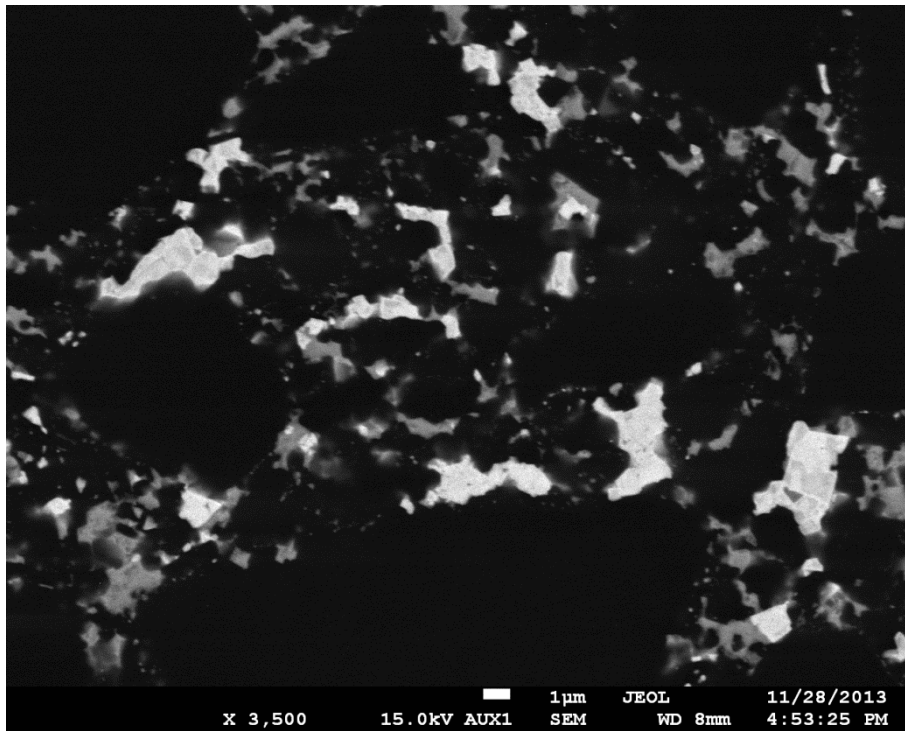
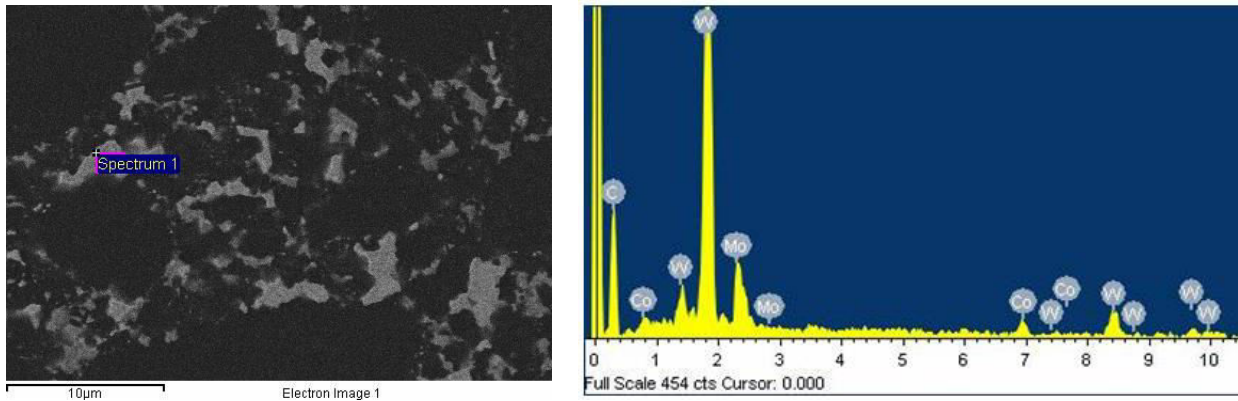


Figure 4.1: SEM microstructures of PCD containing 3wt% Mo<sub>2</sub>C

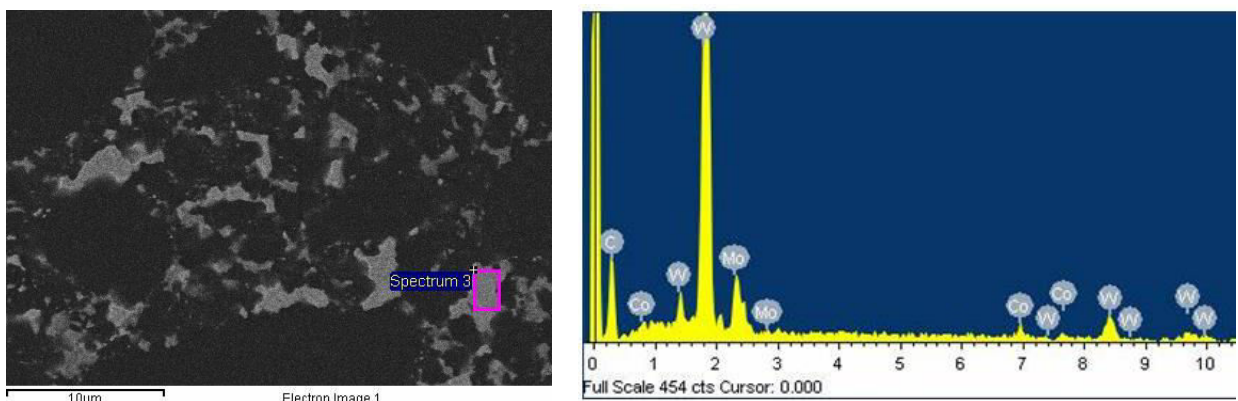


(a)





(b)



(c)

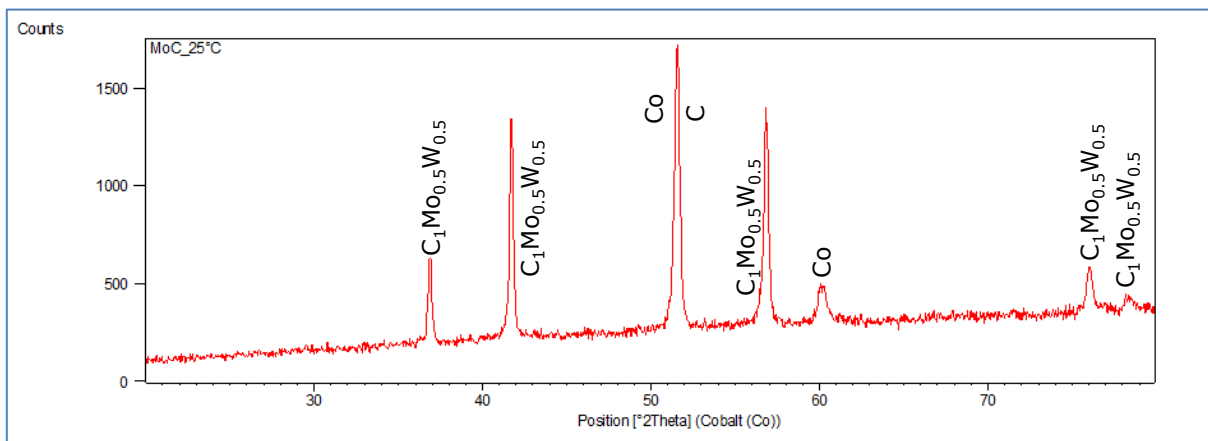
**Figure 4.2: SEM microstructure of PCD containing 3wt% Mo<sub>2</sub>C: (a) microstructure of the PCD showing binder pools, (b) and (c) EDS analysis of binder pools showing the presence of Mo<sub>2</sub>C**

Table 4.2 shows the EDS semi-quantification of the PCD binder pools in the 3wt% Mo<sub>2</sub>C enhanced PCD. The atomic % cannot be used to quantify the stoichiometry of the phases present due to the overwhelming presence of carbon from the diamond.

**Table 4.2: EDS semi-quantification of the PCD binder pools in the 3wt% Mo<sub>2</sub>C enhanced PCD**

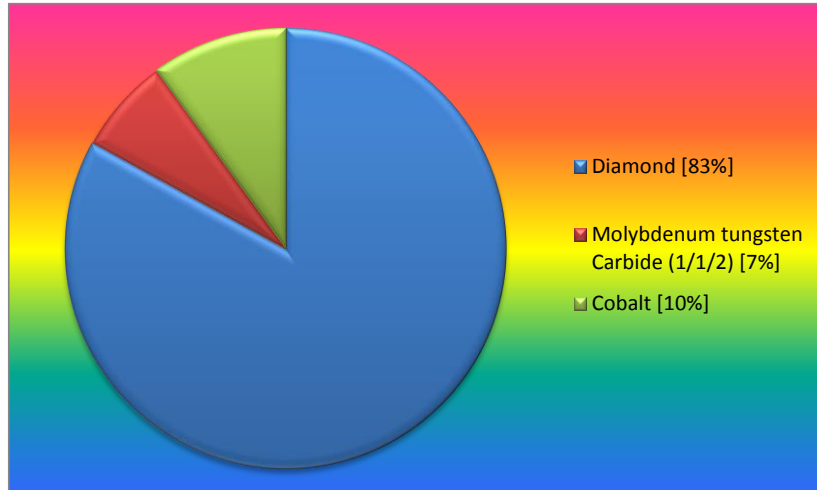
Element	Atomic (%)					
	1 – Fig 2b	2 – Fig 2c	3	4	5	6
C	85.61	81.62	70.62	68.28	60.70	80.86
O	-	-	15.94	12.59	22.49	-
Co	2.44	2.95	3.61	4.47	2.06	16.13
Mo	3.38	3.59	2.53	3.12	4.59	1.01
W	8.58	11.84	7.29	11.54	10.16	2.00

Figure 4.3 shows the XRD pattern of the 3wt% Mo<sub>2</sub>C enhanced PCD. According to the XRD analysis, the molybdenum seems to have combined with the tungsten in equal ratio to form a Mo<sub>0.5</sub>W<sub>0.5</sub>C mixed carbide. According to the XRD pattern, the PCD contains no free WC. All of the tungsten in the PCD seems to have combined with the Mo to form the Mo<sub>0.5</sub>W<sub>0.5</sub>C mixed carbide.



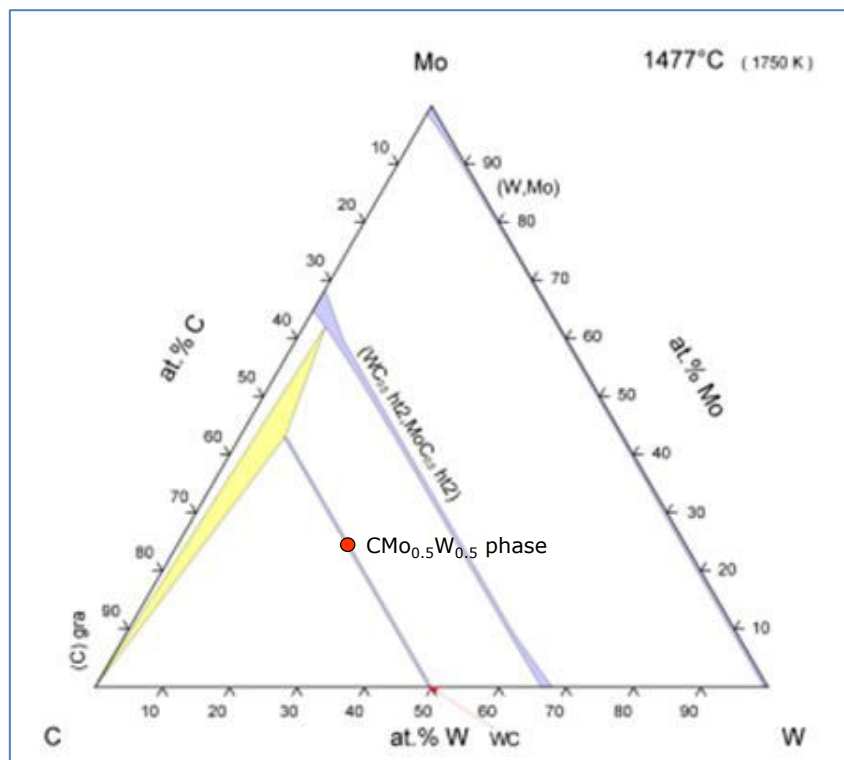
**Figure 4.3: XRD pattern of PCD containing 3wt% Mo<sub>2</sub>C taken at 25 °C**

Figure 4.4 shows the XRD quantification of the PCD containing 3wt% Mo<sub>2</sub>C performed using the Reference Intensity Ratio (RIR) method. The PCD contains 7% CMo<sub>0.5</sub>W<sub>0.5</sub>, 10% Co and 83% diamond.



**Figure 4.4: XRD quantification of the PCD containing 3wt% Mo<sub>2</sub>C**

From the Mo-W-C ternary phase diagram shown in Figure 4.5, there is clearly no spread in the carbon content at a Mo:W ratio of 50:50. Furthermore, the molybdenum and tungsten is shown to form a solid solution. The observed CMo<sub>0.5</sub>W<sub>0.5</sub> phase was plotted on the solid solution line and this shows agreement with the XRD phase identified as CMo<sub>0.5</sub>W<sub>0.5</sub> using the ICSD database.



**Figure 4.5: Mo-W-C Ternary Phase Diagram [89]**

Hot stage XRD analysis was carried out on the Mo<sub>2</sub>C enhanced PCD. Table 4.3 shows the phases formed as a function of temperature. The XRD pattern for the temperature ranging from 350 °C to 900 °C is the same as the pattern taken at room temperature. Figure 4.6 shows the XRD pattern of the 3wt% Mo<sub>2</sub>C enhanced PCD taken at 950 °C. The PCD appears to have slightly graphitized as evidenced by the appearance of a small graphite peak. The phases present in the XRD pattern are constant from 950 °C to 1100 °C. The binder phase seems to consist of tungsten dissolved in cobalt.

**Table 4.3: XRD phases present in the Mo<sub>2</sub>C enhanced PCD and the Standard PCD during heat treatment** (Appendix Three shows all the XRD patterns)

Temperature	Phases Present (Mo <sub>2</sub> C PCD)	Phases Present (Std PCD)
25°C	Diamond, Co, CMoW	WC, CoW, diamond
350°C	Diamond, Co, CMoW	-
400°C	Diamond, Co, CMoW	-
450°C	Diamond, Co, CMoW	-
500°C	Diamond, Co, CMoW	-
550°C	Diamond, Co, CMoW	-
600°C	Diamond, Co, CMoW	-
650°C	Diamond, Co, CMoW	-
700°C	Diamond, Co, CMoW	WC, CoW, diamond
750°C	Diamond, Co, CMoW	WC, CoW, diamond
800°C	Diamond, Co, CMoW	WC, CoW, diamond
850°C	Diamond, Co, CMoW	WC, CoW, diamond
900°C	Diamond, Co, CMoW	WC, CoW, diamond
950°C	Diamond, Graphite, CMoW, CoW	WC, CoW, Co <sub>3</sub> W, diamond, graphite
1000°C	Diamond, Graphite, CMoW, CoW	-
1050°C	Diamond, Graphite, CMoW, CoW	-
1100°C	Diamond, Graphite, CMoW, CoW	-
25°C (post treatment)	Diamond, Graphite, CMoW, Co	WC, CoW, Co <sub>3</sub> W, diamond, graphite

CMoW denotes C<sub>1</sub>Mo<sub>0.5</sub>W<sub>0.5</sub>, CoW denotes Co<sub>0.87</sub>W<sub>0.13</sub>,

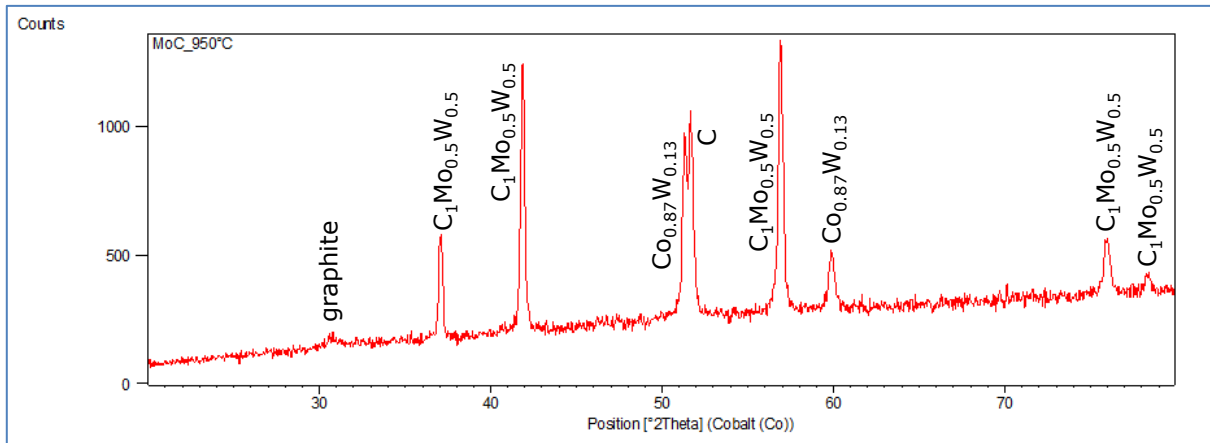


**Figure 4.6: XRD pattern of 3wt% enhanced  $Mo_2C$  PCD taken at 950 °C**

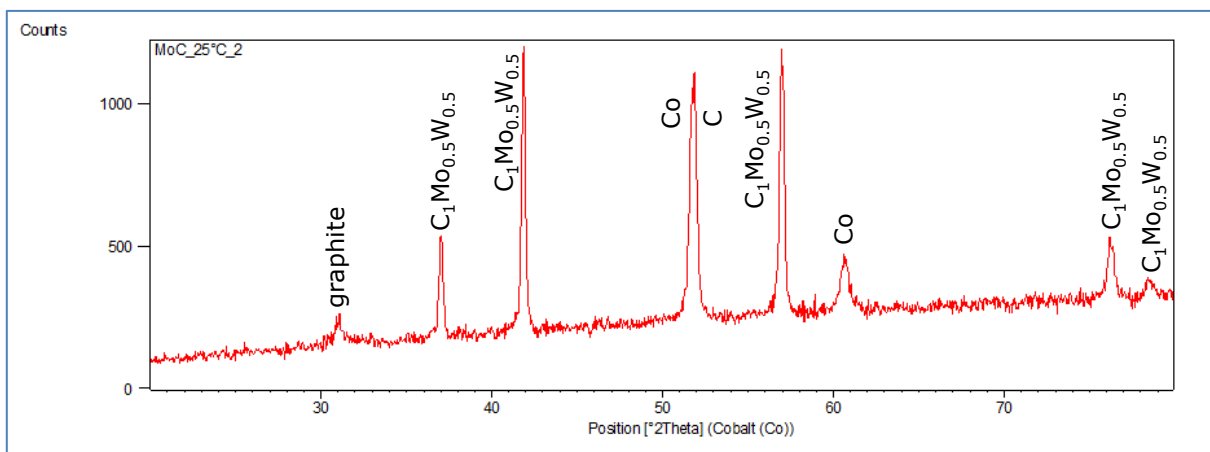


**Figure 4.7: XRD pattern of 3wt% enhanced  $Mo_2C$  PCD taken at 25 °C post heat treatment**

Figure 4.8 and Table 4.4 shows the SEM and EDS analysis of the  $Mo_2C$  enhanced PCD post heat treatment. Macro cracking of the PCD is clearly visible in Figure 4.8. The binder seems to have seeped out of the PCD structure and formed 'blob' like formations on the surface of the PCD. Area (A) shows a combination of carbon, cobalt, tungsten and molybdenum. Area (B) displays a cobalt particle containing some oxygen, surrounded by diamond.

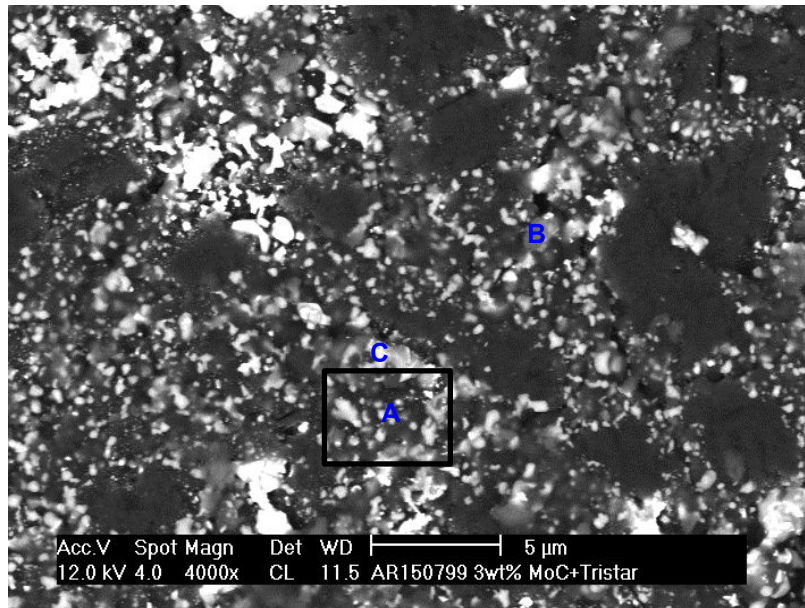


**Figure 4.8: SEM and EDS analysis of the Mo<sub>2</sub>C enhanced PCD post heat treatment**

**Table 4.4: EDS analysis of the various phases in the heat treated Mo<sub>2</sub>C enhanced PCD, values in atomic %**

Area	Carbon	Cobalt	Tungsten	Molybdenum	Oxygen
A	95.65	3.58	0.48	0.30	-
B	89.89	6.64	-	-	3.47
C	83.53	12.15	2.11	2.20	-

#### 4.3.2 TiC addition to PCD

Figure 4.9 shows the SEM microstructure of PCD containing 3wt% (2.16vol%) TiC. The PCD seems well sintered, with TiC carbide deposits occurring in the binder pools. The carbide deposits show a phase contrast that is both darker than the tungsten carbide particles and the cobalt binder.

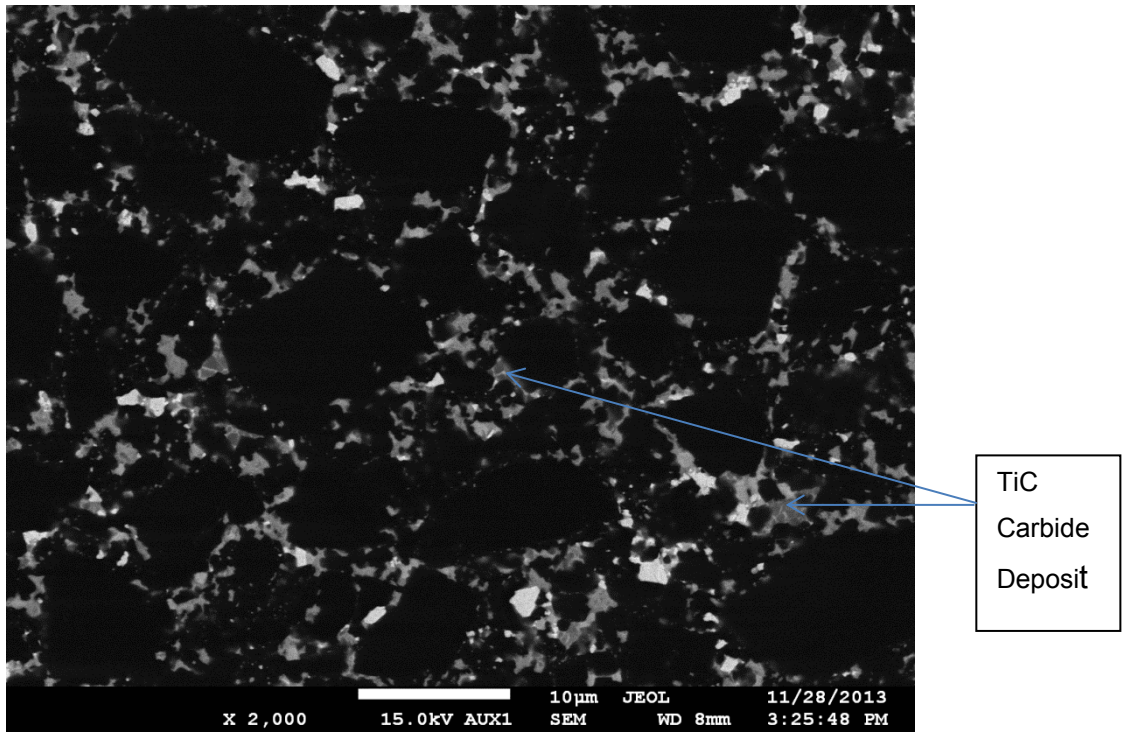
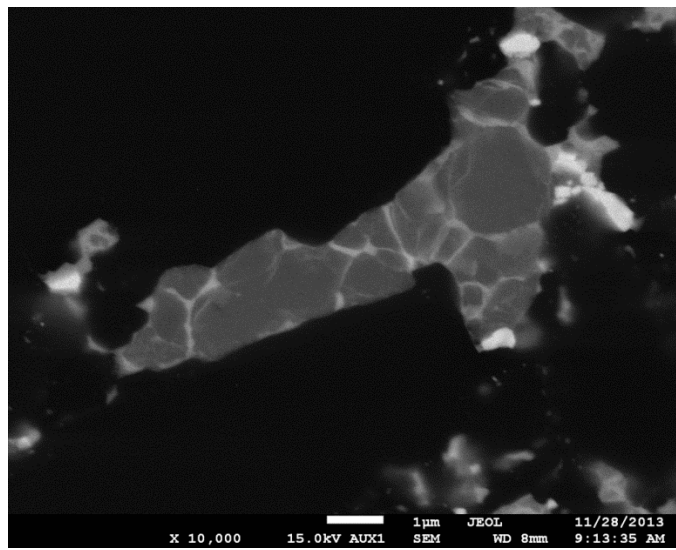
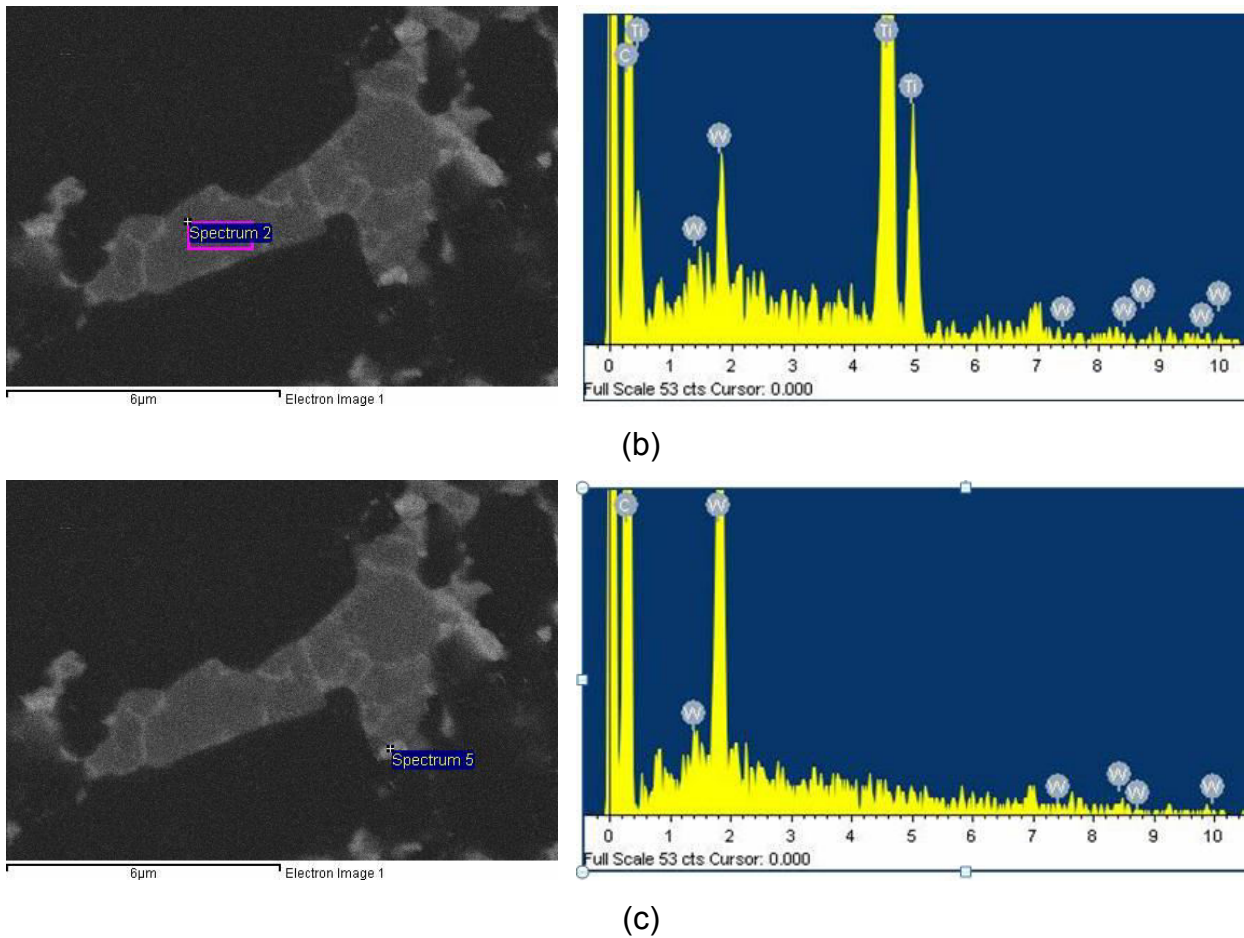


Figure 4.9: SEM microstructure of PCD containing 3wt% TiC



(a)



**Figure 4.10: SEM microstructure of a binder pool in the 3wt% TiC enhanced PCD: (a) microstructure of the binder pool, (b) EDS spectrum of the TiC carbide particulate, (c) EDS spectrum of WC deposit**

Figure 4.10 shows the SEM microstructure of a binder pool with the TiC carbide deposits displacing the cobalt binder. Generally, a PCD compact with a microstructure such as this should display a higher resistance to thermal degradation due to the reduction in the amount of cobalt present in the microstructure. It is known that high amounts of cobalt enhance thermal degradation due to the cobalt interacting with the surrounding diamond and enhancing the conversion of diamond into graphite. The binder is frequently removed to enhance the thermal stability of the compact [27]. Yancong et al. observed that the addition of TiC to PCD increases the thermal stability of the material [107]. They explained the phenomenon by the reduction of the cobalt binder.



According to the EDS spectrum in Figure 4.10, the darker grey deposits in the binder pool seems to be predominantly TiC, whilst the light grey phase seems to be WC. The EDS data for the images shown in Figure 4.10 is shown in Table 4.5. The high carbon content observed in both the EDS spectra for Figure 4.10(b) and (c) is due to the overwhelming presence of the neighbouring diamond particles. Additional EDS analysis was performed on the deposits in the binder pools (refer to Table 4.6). The carbon content of the TiC deposit is expected to be 50%, but the observed value was found to be much higher. This is mainly due to the EDS analysis not being as accurate because the technique measures an excitation volume of 10  $\mu\text{m}$  which includes the surrounding area. In the PCD matrix, the surrounding area is diamond.

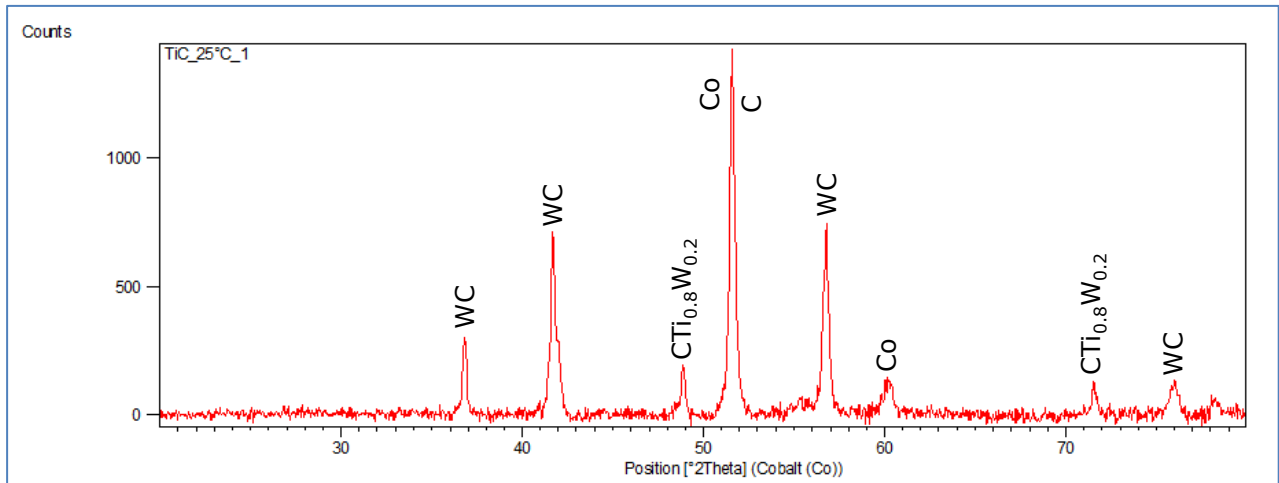
**Table 4.5: EDS data for the images shown in Figure 4.10**

Element	Figure 4.10(b) – atomic %	Figure 4.10(c) – atomic %
C	79.09	99.35
Ti	20.54	-
W	0.37	0.65

**Table 4.6: EDS analysis (atomic %) of the binder pools**

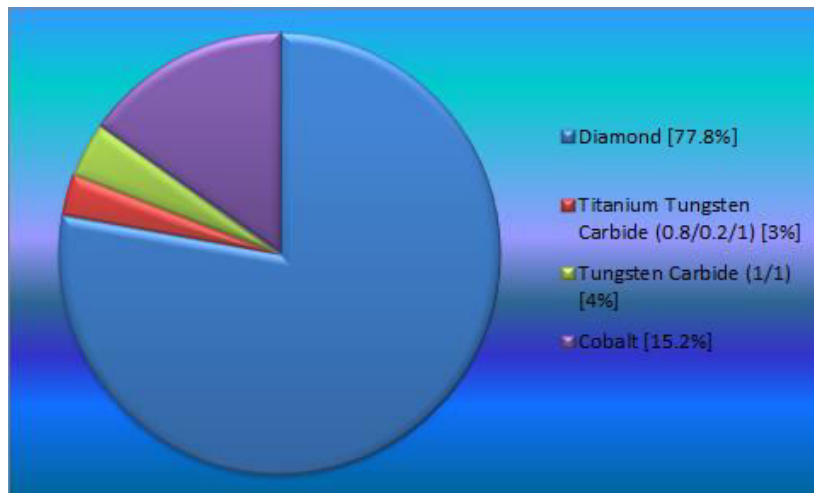
Element	Binder (1)	Binder (2)	Binder (3)	Binder (4)
C	60.06	82.37	83.73	85.98
Co	-	1.47	-	-
Ti	39.29	14.77	15.28	13.38
W	0.65	1.39	0.98	0.64

Figure 4.11 shows the XRD pattern of the PCD containing 3wt% TiC. According to the pattern, the PCD contains free WC particles (as observed in the microstructure) and a mixed  $\text{Ti}_{0.8}\text{W}_{0.2}\text{C}$  (according to the ICSD database) phase.



**Figure 4.11: XRD pattern of PCD containing 3wt% TiC taken at 25 °C**

Figure 4.12 shows the XRD quantification of the PCD containing 3wt% TiC performed using the Reference Intensity Ratio (RIR) method. The PCD contains 3%  $Ti_{0.8}W_{0.2}C$ , 4% WC, 15.2% Co and 77.8% diamond.



**Figure 4.12: XRD quantification of the PCD containing 3wt% TiC**

Hot stage XRD analysis was carried out on the TiC enhanced PCD to determine the onset of graphitisation. Table 4.7 shows the phases formed as a function of temperature. The XRD pattern remains the same from room temperature to 850 °C. At 900 °C, the binder phase comprises  $Co_{0.87}W_{0.13}$  (refer to Figure 4.13).

**Table 4.7: XRD phases present in the TiC enhanced PCD and the Standard PCD during heat treatment** (Appendix Four shows all the XRD patterns)

Temperature	Phases Present	Phases Present (Std PCD)
25°C	Diamond, Co, WC, CTiW	WC, CoW, diamond
350°C	Diamond, Co, WC, CTiW	-
400°C	Diamond, Co, WC, CTiW	-
450°C	Diamond, Co, WC, CTiW	-
500°C	Diamond, Co, WC, CTiW	-
550°C	Diamond, Co, WC, CTiW	-
600°C	Diamond, Co, WC, CTiW	-
650°C	Diamond, Co, WC, CTiW	-
700°C	Diamond, Co, WC, CTiW	WC, CoW, diamond
750°C	Diamond, Co, WC, CTiW	WC, CoW, diamond
800°C	Diamond, Co, WC, CTiW	WC, CoW, diamond
850°C	Diamond, Co, WC, CTiW	WC, CoW, diamond
900°C	Diamond, CoW, WC, CTiW	WC, CoW, diamond
950°C	Diamond, Graphite, CoW, WC, CTiW	WC, CoW, Co <sub>3</sub> W, diamond, graphite
1000°C	Diamond, Graphite, CoW, WC, CTiW	-
1050°C	Diamond, Graphite, Co <sub>3</sub> Ti, WC, CTiW	-
1100°C	Diamond, Graphite, Co <sub>3</sub> Ti, WC, CTiW	-
25°C (post treatment)	Diamond, Graphite, Co, WC, CTiW	WC, CoW, Co <sub>3</sub> W, diamond, graphite

CTiW denotes C<sub>1</sub>Ti<sub>0.8</sub>W<sub>0.2</sub>, CoW denotes Co<sub>0.87</sub>W<sub>0.13</sub>

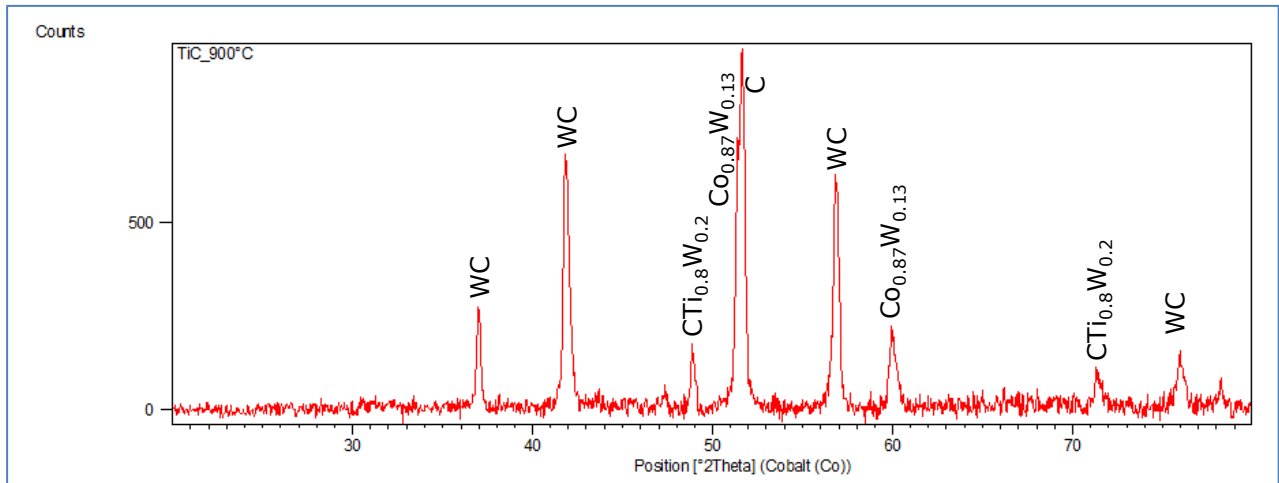


**Figure 4.13: XRD pattern of 3wt% enhanced TiC taken at 900 °C**

Figure 4.14 shows the XRD pattern of the TiC enhanced PCD taken at 950 °C. The pattern shows additional peaks for graphite.

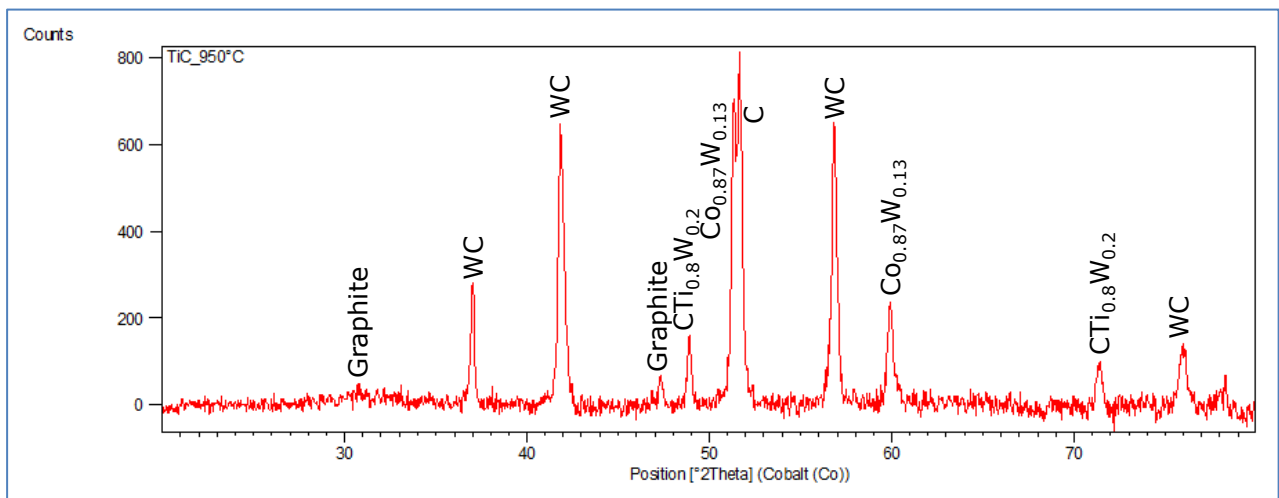


**Figure 4.14: XRD pattern of 3wt% enhanced TiC taken at 1000 °C**

The XRD pattern for the TiC enhanced PCD exposed to 1100 °C shows the presence of  $\text{Co}_3\text{Ti}$  as the binder (refer to Figure 4.15). This is most probably due to the peak shift at higher temperatures because the XRD pattern taken at 25 °C post heat treatment shows the binder present in the PCD to be cobalt (refer to Figure 4.16). Furthermore, there are no additional peaks present for  $\text{Co}_3\text{Ti}$  to substantiate the formation of another phase. It

can therefore be concluded that the cobalt binder does not change phase and is constant throughout the heat treatment.

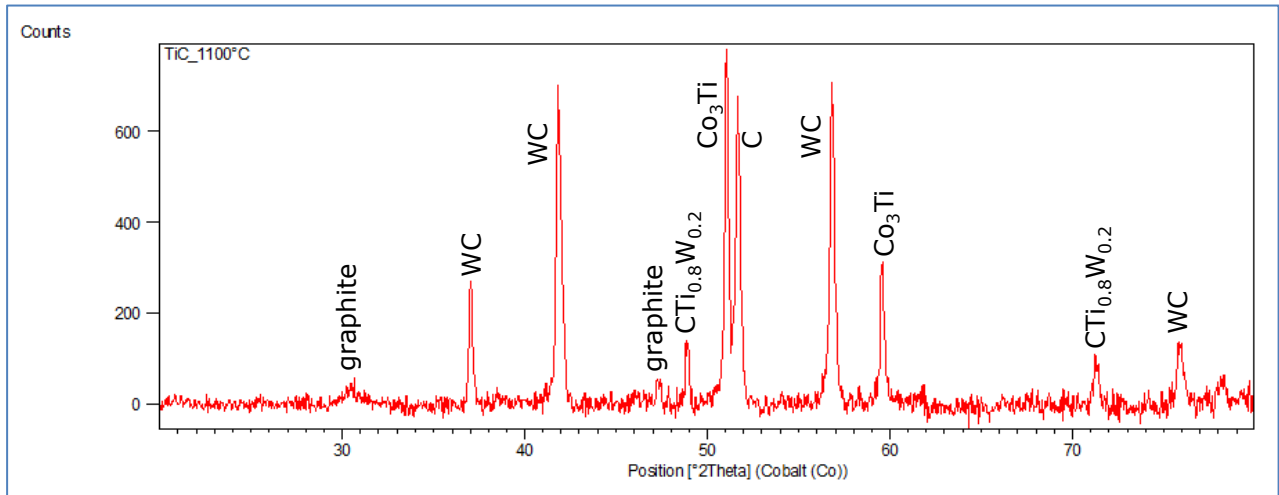


**Figure 4.15: XRD pattern of 3wt% enhanced TiC taken at 1100 °C**

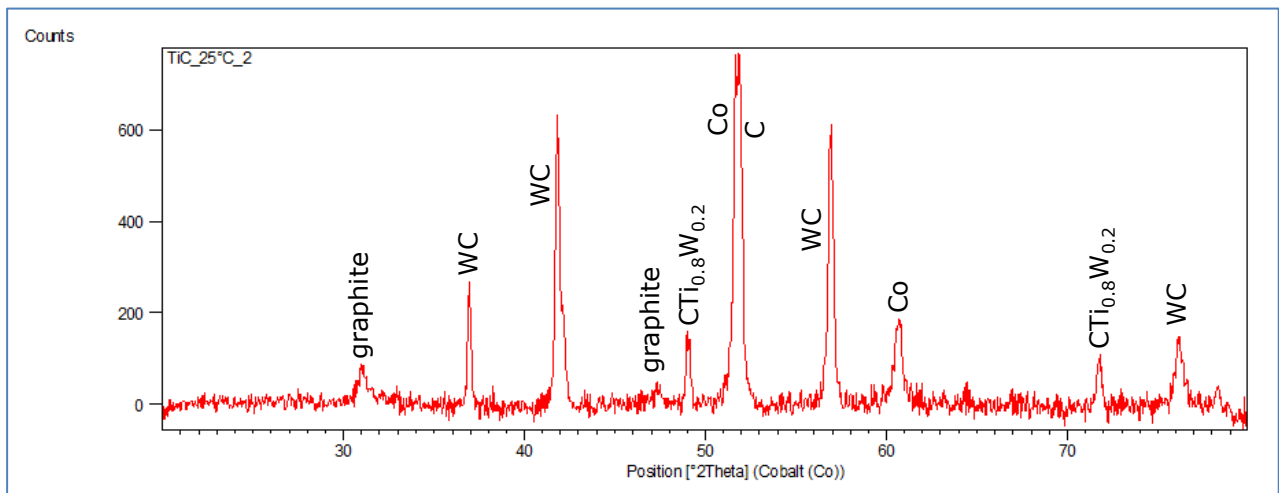


**Figure 4.16: XRD pattern of 3wt% enhanced TiC taken at 25 °C post heat treatment**

Figure 4.17 shows the TiC enhanced PCD XRD pattern of the diamond peak at various temperatures. At 900 °C (i.e. red curve), the diamond peak contains a shoulder peak which is associated with the cobalt binder. At 950 °C, the diamond peak begins to separate into two different constituents, i.e. the diamond and the binder (i.e. the blue curve). The green curve taken at 1000 °C shows the clear separation of the binder peak

and the diamond peak. This observation is more pronounced at 1100 °C (i.e. the grey curve).

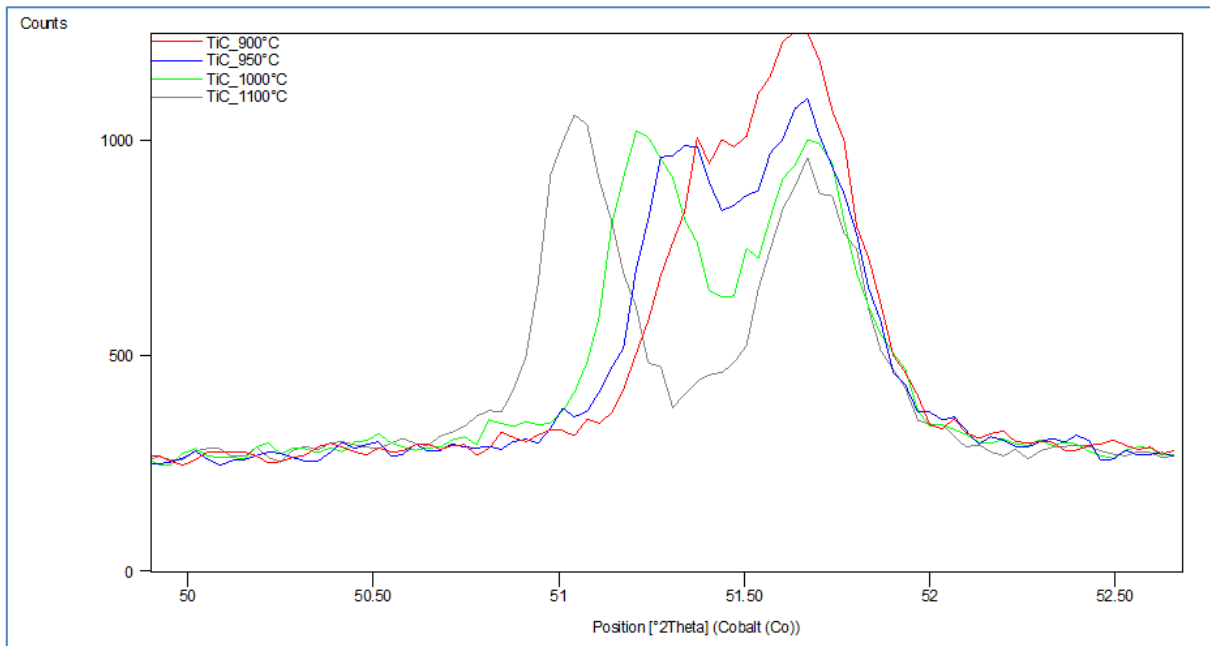


**Figure 4.17: XRD pattern of 3wt% enhanced TiC – overlay of the diamond peak**

The observed de-convolution of the diamond peak is due to the thermal expansion differences between the diamond and the binder. Due to the large differences in thermal expansion between the diamond and the binder, a slight displacement in the diamond peak is expected as compared to a large displacement in the cobalt peak. According to measured values appearing in Table 4.8, an average displacement of  $0.12^{\circ}2\theta$  was observed for the diamond peak. The peak displacement for the binder increased progressively from  $0.18^{\circ}2\theta$  to  $0.54^{\circ}2\theta$  as the temperature increased from 900 °C to 1100 °C.

**Table 4.8: Peak Displacement Calculation for the diamond peak and the binder peak**

Peak	25 °C	900 °C	950 °C	1000 °C	1100 °C
Diamond Peak					
Peak position	51.56°2 $\theta$	51.69°2 $\theta$	51.65°2 $\theta$	51.70°2 $\theta$	51.66°2 $\theta$
Displacement	-	0.13°2 $\theta$	0.09°2 $\theta$	0.14°2 $\theta$	0.10°2 $\theta$
Binder Peak					
Peak position	51.56°2 $\theta$	51.38°2 $\theta$	51.28°2 $\theta$	51.20°2 $\theta$	51.02°2 $\theta$
Displacement	-	0.18°2 $\theta$	0.28°2 $\theta$	0.36°2 $\theta$	0.54°2 $\theta$

The SEM image of the TiC enhanced PCD post heat treatment is shown in Figure 4.18. Macro cracking is present on the PCD surface, and the binder seepage from within the PCD is quite evident. Table 4.9 shows the EDS analysis of the various phases present in the heat treated TiC enhanced PCD. Area (a) shows a particle containing carbon, cobalt, titanium, tungsten and oxygen. Area (b) is a SiO<sub>2</sub> and Al<sub>2</sub>O<sub>3</sub> contaminant probably arising from the furnace tool holder. Area (c) shows the presence of carbon, cobalt, titanium, tungsten and oxygen.

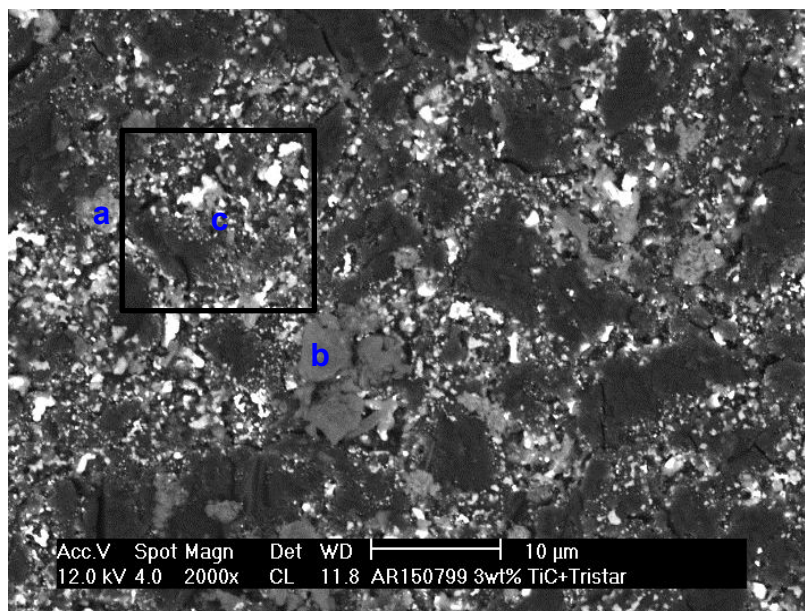


**Figure 4.18: SEM and EDS analysis of the TiC enhanced PCD post heat treatment**

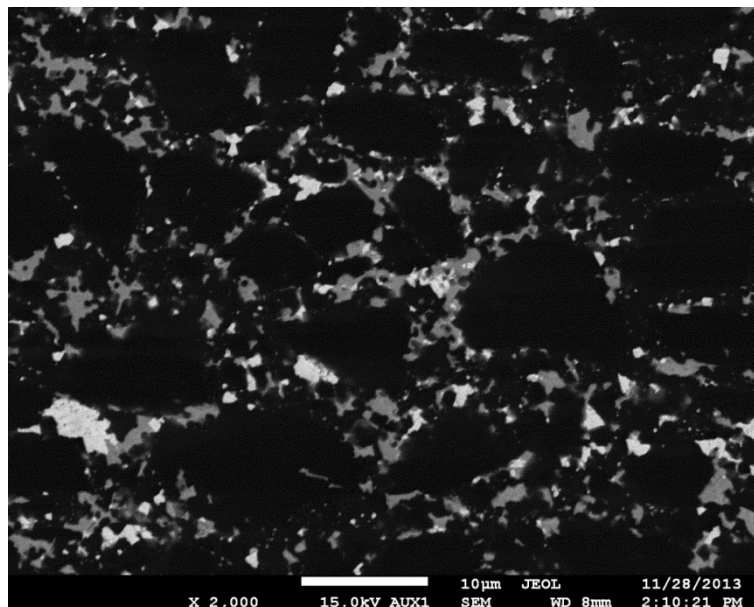
**Table 4.9: EDS Analysis of the TiC enhanced heat treated PCD, values in atomic %**

Area	Carbon	Cobalt	Tungsten	Titanium	Oxygen	Aluminium	Silicon
a	25.88	1.53	2.40	18.74	51.45	-	-
b	39.41	1.12	-	-	36.92	17.68	4.87
c	93.96	1.88	0.77	0.62	2.78	-	-

#### 4.3.3 Cr<sub>3</sub>C<sub>2</sub> addition to PCD

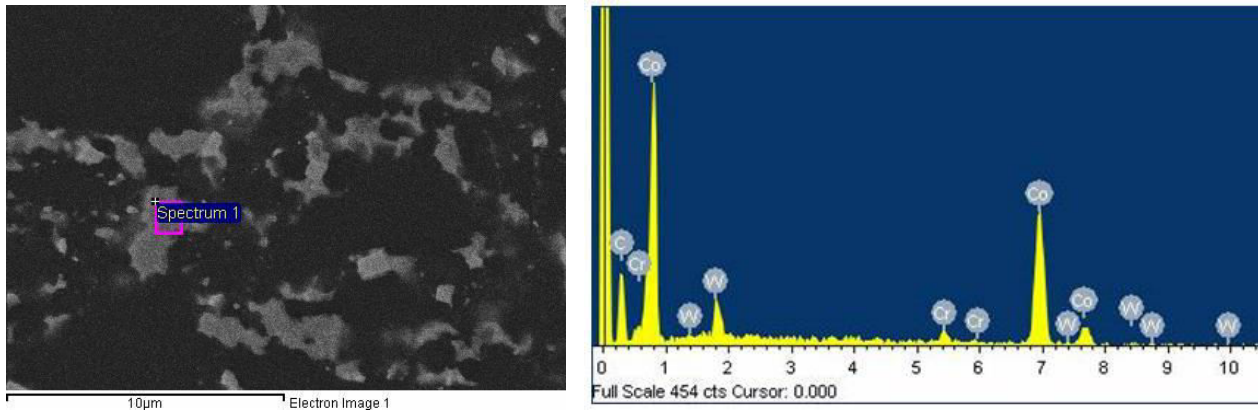
Middlemiss et al. investigated the behaviour of PCD containing Cr<sub>3</sub>C<sub>2</sub> additions [108]. They found that the addition of Cr<sub>3</sub>C<sub>2</sub> to PCD increased the abrasion resistance of the PCD without compromising the impact resistance of the material. The addition of Cr<sub>3</sub>C<sub>2</sub> was also found to suppress the formation of large tungsten carbide grains at the WC-Co PCD interface.

Figure 4.19 shows the SEM microstructure of PCD containing 3wt% (1.60vol%) Cr<sub>3</sub>C<sub>2</sub>. The PCD seems well sintered, with light grey WC deposits appearing in the binder pools. Besides the appearance of these WC deposits, the binder pools seem to have no other carbide phases within them.

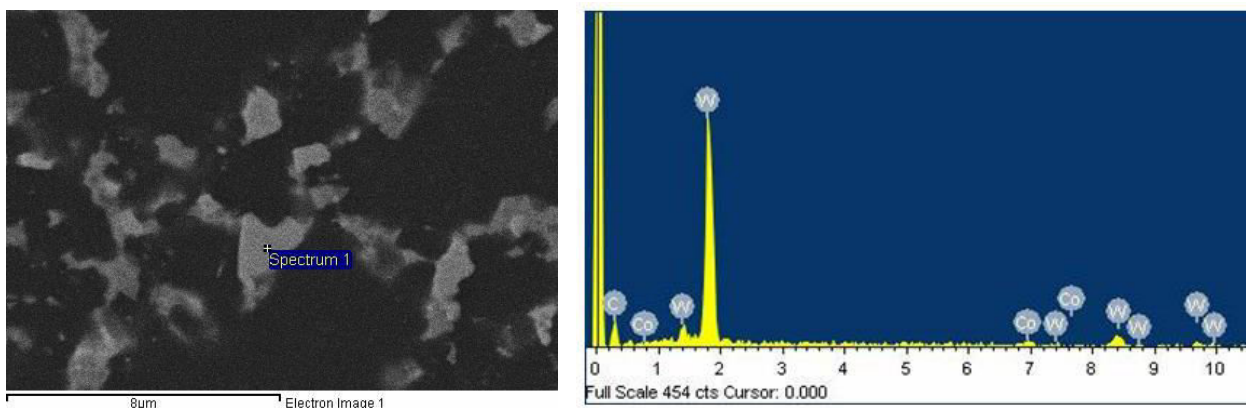


**Figure 4.19: SEM microstructure of PCD containing 3wt% Cr<sub>3</sub>C<sub>2</sub>**





(a)



(b)

**Figure 4.20: EDS Spectra of the binder pools for the  $\text{Cr}_3\text{C}_2$  enhanced PCD**

The EDS spectra in Figure 4.20 show the binder pools to consist primarily of cobalt, tungsten, carbon and chromium. It would seem that the chromium is distributed in the PCD as a solid solution with the cobalt binder. The EDS analysis confirms the light grey deposits to be WC. Table 4.10 shows the EDS semi-quantification analysis of the EDS spectra shown in Figure 4.19.

**Table 4.10: EDS data for the spectra shown in Figure 4.19**

Element	Figure 4.19 (a) atomic %	Figure 4.19(b) atomic %
C	60.82	72.40
Cr	1.44	-
Co	36.39	4.64
W	1.35	22.96

Figure 4.21 shows the XRD pattern of the PCD containing 3wt%  $\text{Cr}_3\text{C}_2$ . The phases present are WC,  $\text{Co}_{0.87}\text{W}_{0.13}$  and Diamond. There is noticeably no evidence on the XRD pattern that a  $(\text{Cr,W})\text{C}_x$  mixed carbide phase forms in the PCD compact. The cobalt binder appears in the fcc phase and is stabilised by the tungsten atoms in the lattice.

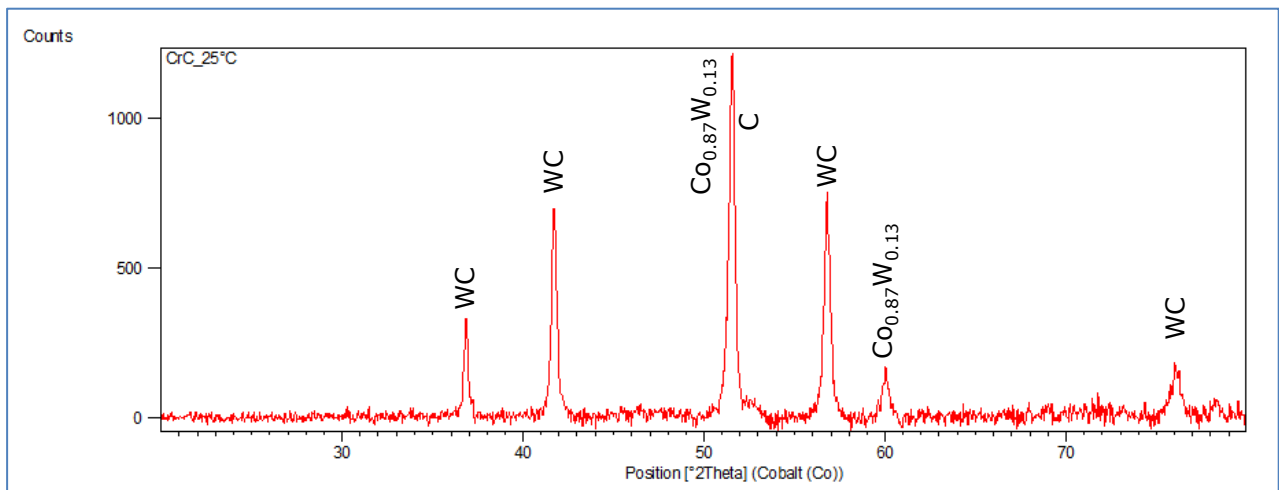


**Figure 4.21: XRD pattern of PCD containing 3wt%  $\text{Cr}_3\text{C}_2$**

Figure 4.22 shows the XRD quantification of the PCD containing 3wt%  $\text{Cr}_3\text{C}_2$  performed using the Reference Intensity Ratio (RIR) method. The PCD contains 4% WC, 2%  $\text{Co}_{0.87}\text{W}_{0.13}$  and 93.9% diamond. The ratio of Co:W in the binder is 75:25 which is typically what is generally observed in standard PCD.

Hot stage XRD was performed on the  $\text{Cr}_3\text{C}_2$  enhanced PCD to determine the onset of graphitisation and any change in the phases present in the PCD. Table 4.11 shows the XRD phases present in the  $\text{Cr}_3\text{C}_2$  enhanced PCD and the standard PCD during heat

treatment. The XRD pattern remains the same from room temperature to 650 °C. At 700 °C, the XRD pattern shows the appearance of a CrW phase at 49.36°2θ (refer to Figure 4.23).

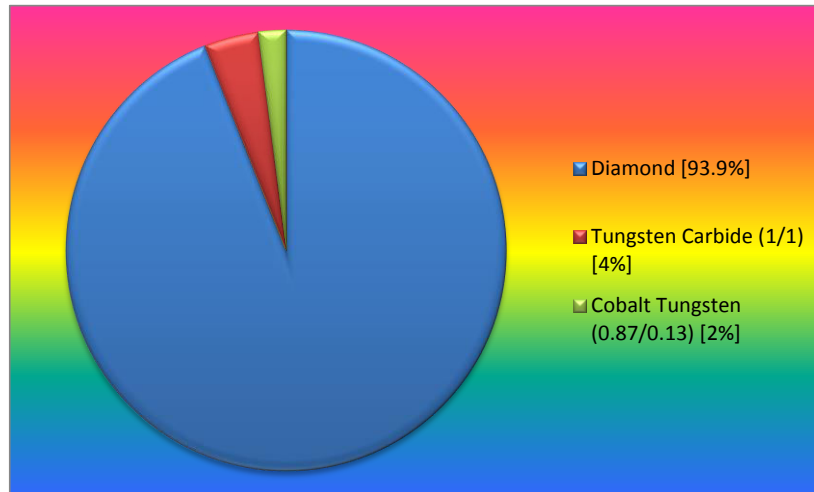


**Figure 4.22: XRD quantification of the PCD containing 3wt% Cr<sub>3</sub>C<sub>2</sub>**

At 750 °C, the cobalt seems to have oxidised to form CoO<sub>4</sub>W (refer to Figure 4.24). The oxidation of the cobalt could be due to an oxygen leak during the experiment, since no other samples exhibited any signs of oxidation. The phases present were constant from 750 °C to 1100 °C, with the intensity of the oxide phase increasing as a function of temperature. Figure 4.25 shows the XRD pattern of the PCD taken at 1100 °C, and Figure 4.26 shows the overlay of the CoO<sub>4</sub>W peak at the different temperatures. As the temperature increases, the CoO<sub>4</sub>W peak intensity also increases. It can be inferred from the graph that the higher the temperature, the greater the amount of oxide formed. The onset of oxidation seems to begin at 750 °C. Interestingly, there is no evidence of graphitisation in the XRD pattern taken at any of the temperatures. It is possible that the graphite which may have formed would have reacted with the oxygen present, and subsequently been removed by the formation of the gaseous products.

**Table 4.11: XRD phases present in the Cr<sub>3</sub>C<sub>2</sub> enhanced PCD and the Standard PCD during heat treatment** (Appendix Five shows all the XRD patterns)

Temperature	Phases Present	Phases Present (Std PCD)
25°C	Diamond, CoW, WC	WC, CoW, diamond
350°C	Diamond, CoW, WC	-
400°C	Diamond, CoW, WC	-
450°C	Diamond, CoW, WC	-
500°C	Diamond, CoW, WC	-
550°C	Diamond, CoW, WC	-
600°C	Diamond, CoW, WC	-
650°C	Diamond, CoW, WC	-
700°C	Diamond, CoW, WC, CrW	WC, CoW, diamond
750°C	Diamond, CoW, WC, CrW, CoO <sub>4</sub> W	WC, CoW, diamond
800°C	Diamond, CoW, WC, CrW, CoO <sub>4</sub> W	WC, CoW, diamond
850°C	Diamond, CoW, WC, CrW, CoO <sub>4</sub> W	WC, CoW, diamond
900°C	Diamond, CoW, WC, CrW, CoO <sub>4</sub> W	WC, CoW, diamond
950°C	Diamond, Co <sub>0.87</sub> W <sub>0.13</sub> , WC, CrW, CoO <sub>4</sub> W	WC, CoW, Co <sub>3</sub> W, diamond, graphite
1000°C	Diamond, CoW, WC, CrW, CoO <sub>4</sub> W	-
1050°C	Diamond, CoW, WC, CrW, CoO <sub>4</sub> W	-
1100°C	Diamond, CoW, WC, CrW, CoO <sub>4</sub> W	-
25°C (post treatment)	Diamond, CoW, WC, CrW, CoO <sub>4</sub> W	WC, CoW, Co <sub>3</sub> W, diamond, graphite

CoW denotes Co<sub>0.87</sub>W<sub>0.13</sub>

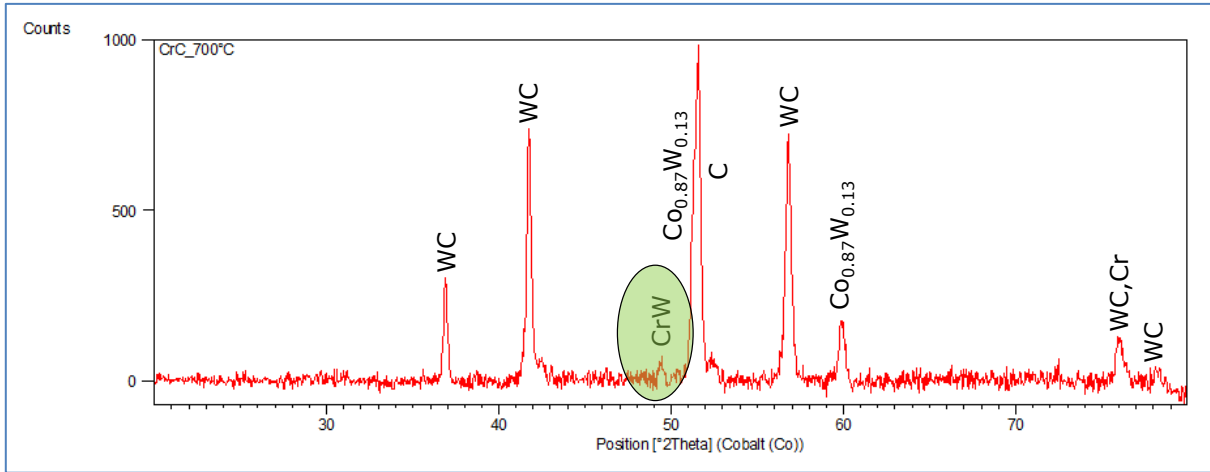


Figure 4.23: XRD pattern of PCD containing 3wt% Cr<sub>3</sub>C<sub>2</sub> taken at 700 °C

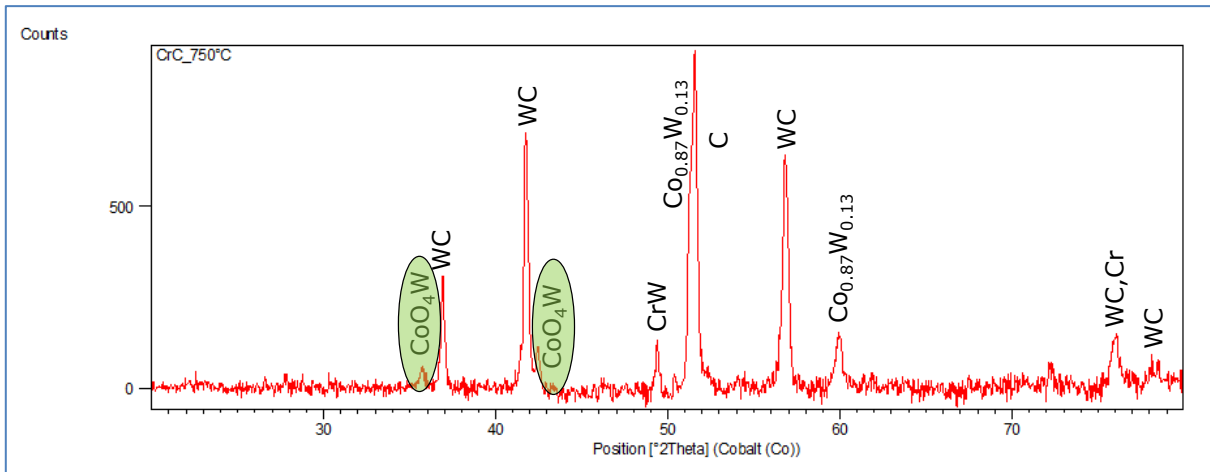
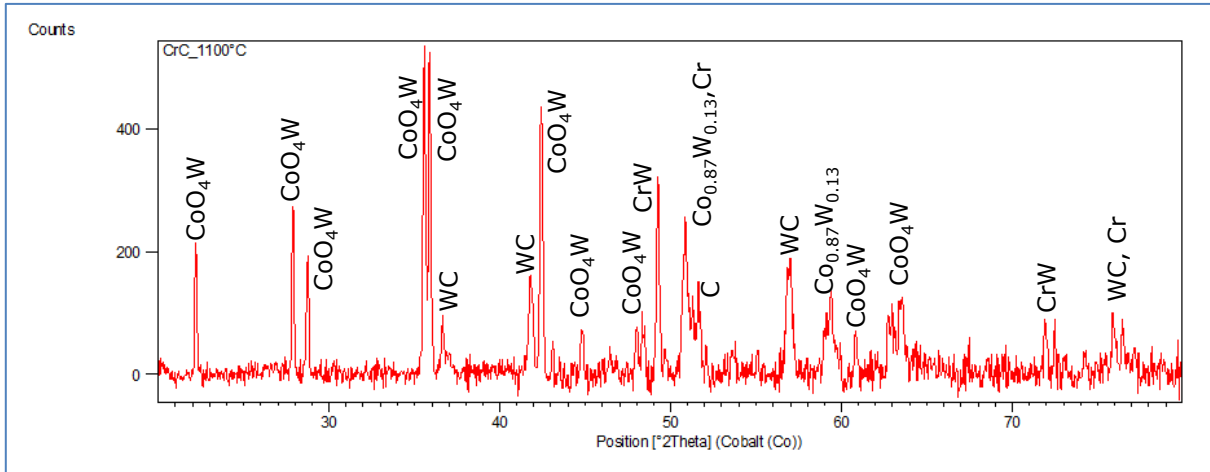
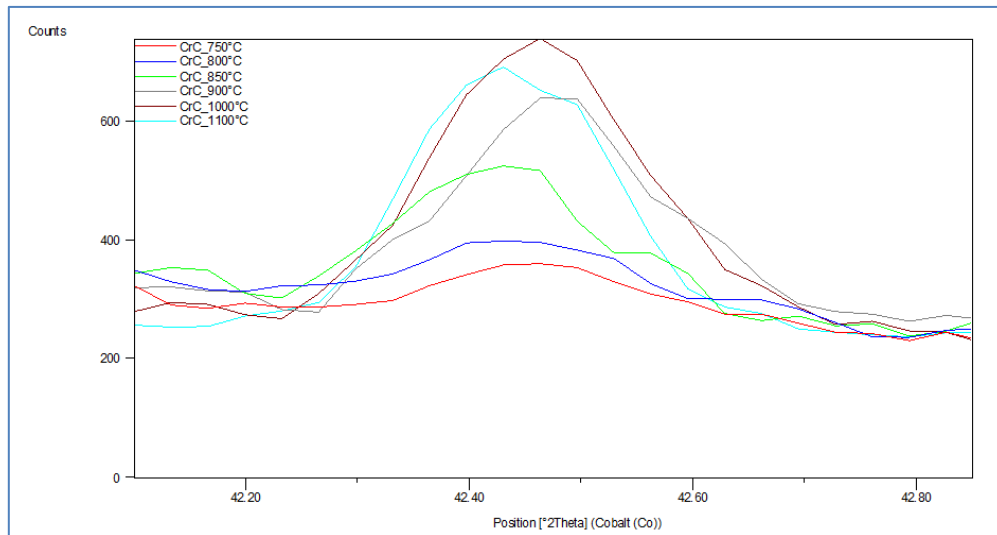


Figure 4.24: XRD pattern of PCD containing 3wt% Cr<sub>3</sub>C<sub>2</sub> taken at 750 °C



**Figure 4.25: XRD pattern of PCD containing 3wt%  $\text{Cr}_3\text{C}_2$  taken at 1100 °C**



**Figure 4.26: XRD overlay of the  $\text{CoO}_4\text{W}$  peak at different temperatures**

Figure 4.27 shows the SEM and EDS analysis of the  $\text{Cr}_3\text{C}_2$  enhanced PCD post heat treatment. The surface of the PCD seems to portray a 'cauliflower' type structure. The EDS analysis of the surface is shown in Table 4.12. The predominant constituent across the surface of the PCD is the presence of oxygen. There appears to be tremendous seepage of the binder from within the PCD as well as oxidation of the cobalt.

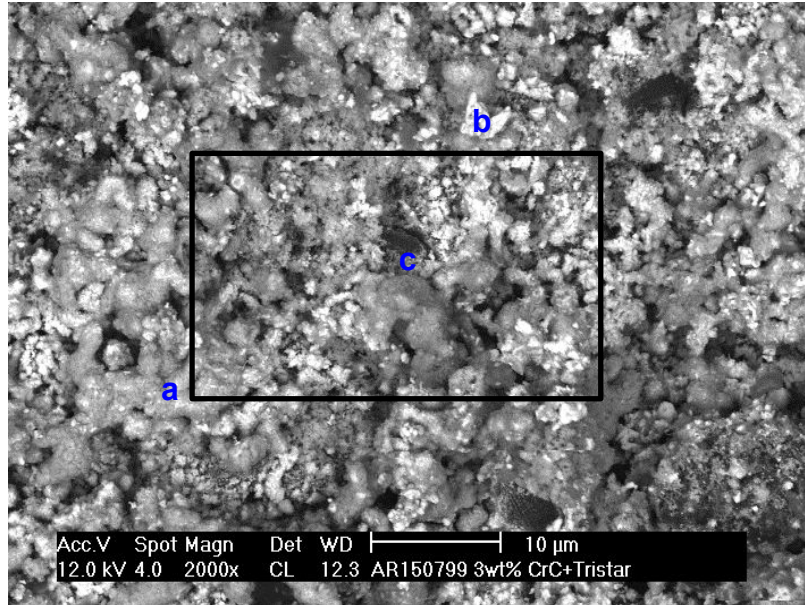


**Figure 4.27: SEM and EDS analysis of the Cr<sub>3</sub>C<sub>2</sub> enhanced PCD post heat treatment**

**Table 4.12: EDS Analysis of the Cr<sub>3</sub>C<sub>2</sub> enhanced heat treated PCD, values in atomic %**

Area	Carbon	Cobalt	Tungsten	Chromium	Oxygen
a	7.65	17.04	5.86	-	69.44
b	-	7.48	16.23	-	76.28
c	28.80	14.78	5.56	3.64	47.22

#### 4.3.4 TiC-VC addition to PCD

The addition of a combination of TiC and VC to PCD was investigated. According to Hashe et al [53], the properties of the WC-Co material was enhanced by the TiC-VC additive. His work revealed that the addition of TiC controlled the grain growth of the cubic carbide phase.

Figure 4.28 shows the SEM microstructure of the PCD containing 1.5wt% TiC and 1.5wt% VC. The microstructure seems well sintered with carbide deposits in the binder pools clearly visible. The EDS analysis (refer to Table 4.13) shows carbide deposits in some areas of the PCD (e.g. area (a)). Area (c) shows the presence of carbon, tungsten,

titanium and vanadium. According to the EDS analysis of area (c), the ratio of Ti:V is close to 1:1.

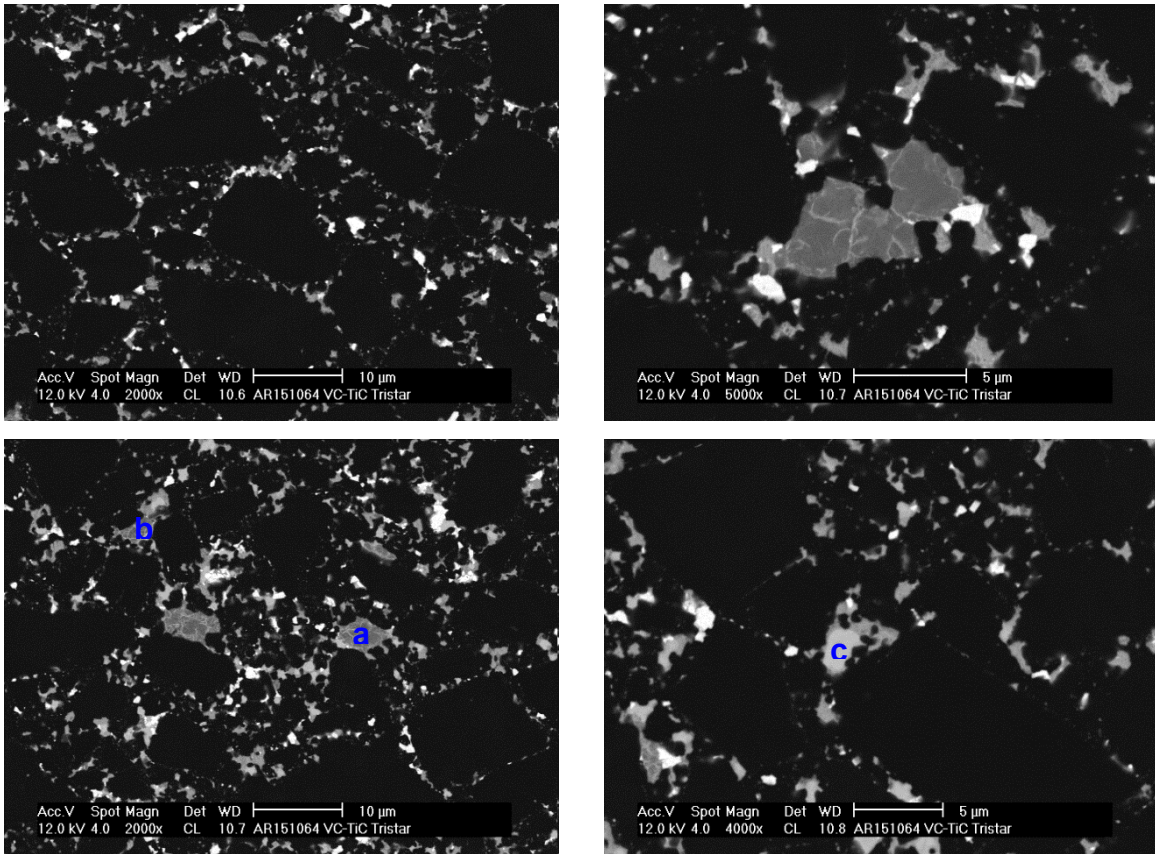


**Figure 4.28: SEM microstructures of PCD containing 1.5wt% TiC and 1.5wt% VC**

**Table 4.13: EDS Analysis of the PCD containing 1.5wt% TiC and 1.5wt% VC, values in atomic %**

Area	Carbon	Cobalt	Tungsten	Titanium	Vanadium
a	78.70	1.86	1.38	18.06	-
b	74.20	4.95	9.43	7.48	3.94
c	78.75	-	9.54	5.30	6.41

Figure 4.29 shows the XRD pattern of PCD containing 1.5wt% VC and 1.5wt% TiC. In the previous chapter, it was observed that the VC combines with W to form a mixed carbide (V,W) $C_x$  phase with the absence of WC in the sintered PCD. According to the XRD ICSD database, the VC-TiC enhanced PCD indicates the formation of both  $C_2TiV$  and  $C_2TiW$



phases. In Figure 4.29, the Ti combines with the VC to form a combined  $C_2TiV$  phase with the absence of WC in the phase. The formation of this phase without the incorporation of WC seems a bit improbable. On closer inspection of the new formed phases (refer to Figure 4.30), it is observed that the phases do not appear exactly where it is supposed to be when compared to the reference peak. The peaks seem slightly shifted. Therefore it is plausible that a mixed  $(Ti,V,W)C_x$  phase could have formed, which is supported by EDS analysis.

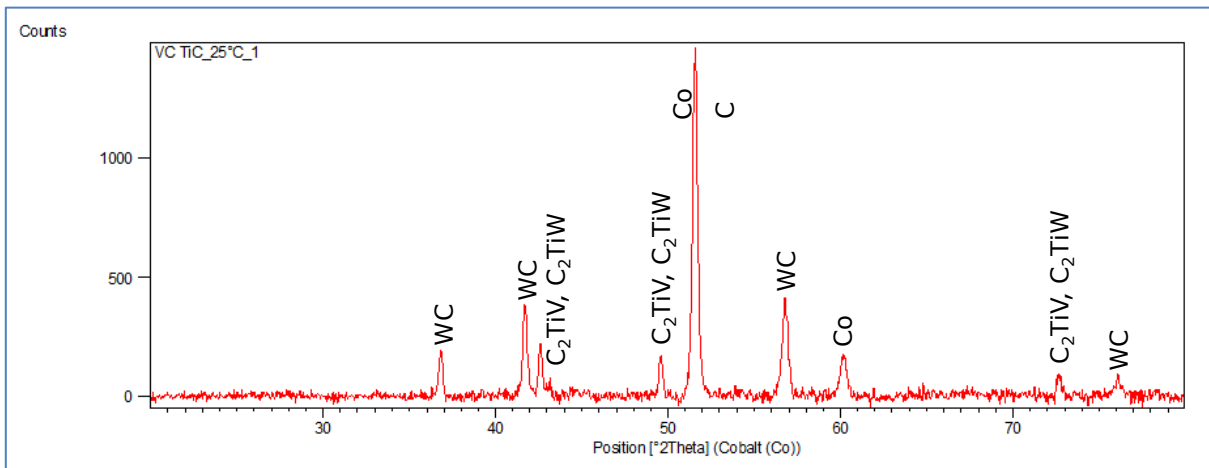


**Figure 4.29: XRD pattern of PCD containing 1.5wt% VC and 1.5wt% TiC**

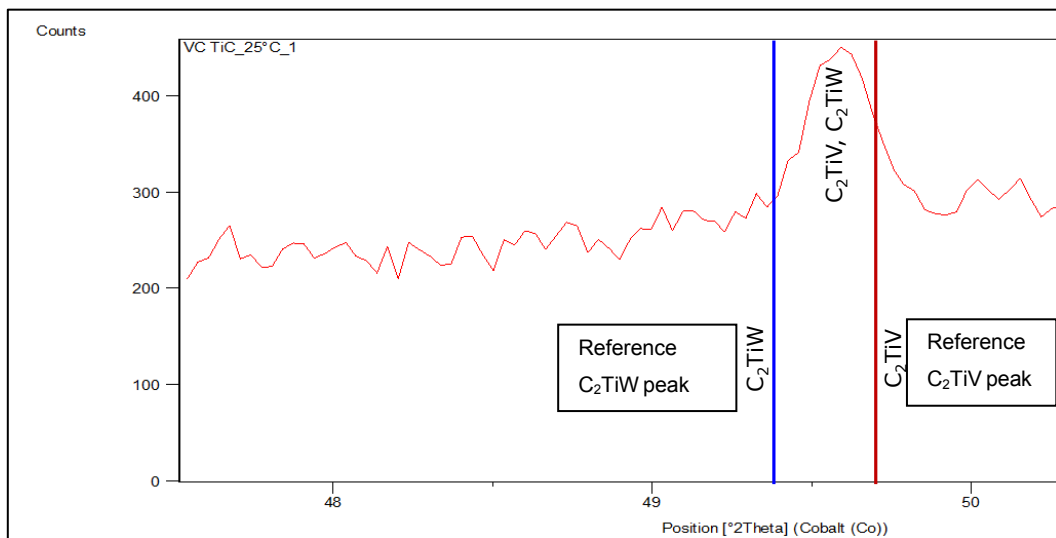


**Figure 4.30: XRD pattern of the  $C_2TiV$  and  $C_2TiW$  phases showing peak shift**

Hot stage XRD was performed on the VC-TiC enhanced PCD to determine the onset of graphitisation and any change in the phases present in the PCD. Table 4.14 shows the XRD phases present in the VC-TiC enhanced PCD and the standard PCD during heat treatment. The XRD pattern remains the same from room temperature to 750 °C. At 750 °C, according to the ICSD database, the XRD pattern shows the appearance of tungsten dissolved in the cobalt binder. However, the  $\text{Co}_{0.87}\text{W}_{0.13}$  peak seems to have shifted in the XRD pattern taken at 25 °C post heat treatment. Hence, the appearance of the  $\text{Co}_{0.87}\text{W}_{0.13}$  peak must be due to peak shift at high temperatures.

The onset of graphitisation occurs at approximately 950 °C, similar to the VC enhanced PCD. Figure 4.31 shows the XRD pattern of PCD containing 1.5wt% VC and 1.5wt% TiC taken at 25 °C post heat treatment. There seems to be no change in the appearance of the phases present.

The SEM images and EDS analysis of the VC-TiC enhanced PCD post heat treatment is shown in Figure 4.32 and Table 4.15 respectively. Macro cracking is evident on the surface of the PCD. Area (a) shows a (Ti,V,W)C<sub>x</sub> mixed carbide particle.

**Table 4.14: XRD phases present in the VC-TiC enhanced PCD and the Standard PCD during heat treatment** (Appendix Six shows all the XRD patterns)

Temperature	Phases Present	Phases Present (Std PCD)
25°C	Diamond, Co, WC, (Ti,V,W)Cx	WC, CoW, diamond
350°C	Diamond, Co, WC, (Ti,V,W)Cx	-
400°C	Diamond, Co, WC, (Ti,V,W)Cx	-
450°C	Diamond, Co, WC, (Ti,V,W)Cx	-
500°C	Diamond, Co, WC, (Ti,V,W)Cx	-
550°C	Diamond, Co, WC, (Ti,V,W)Cx	-
600°C	Diamond, Co, WC, (Ti,V,W)Cx	-
650°C	Diamond, Co, WC, (Ti,V,W)Cx	-
700°C	Diamond, Co, WC, (Ti,V,W)Cx	WC, CoW, diamond
750°C	Diamond, CoW, WC, (Ti,V,W)Cx	WC, CoW, diamond
800°C	Diamond, CoW, WC, (Ti,V,W)Cx	WC, CoW, diamond
850°C	Diamond, CoW, WC, (Ti,V,W)Cx	WC, CoW, diamond
900°C	Diamond, CoW, WC, (Ti,V,W)Cx	WC, CoW, diamond
950°C	Diamond, CoW, WC, (Ti,V,W)Cx, graphite	WC, CoW, Co <sub>3</sub> W, diamond, graphite
1000°C	Diamond, CoW, WC, (Ti,V,W)Cx, graphite	-
1050°C	Diamond, CoW, WC, (Ti,V,W)Cx, graphite	-
1100°C	Diamond, CoW, WC, (Ti,V,W)Cx, graphite	-
25°C (post treatment)	Diamond, Co, WC, (Ti,V,W)Cx, graphite	WC, CoW, Co <sub>3</sub> W, diamond, graphite

CoW denotes Co<sub>0.87</sub>W<sub>0.13</sub>

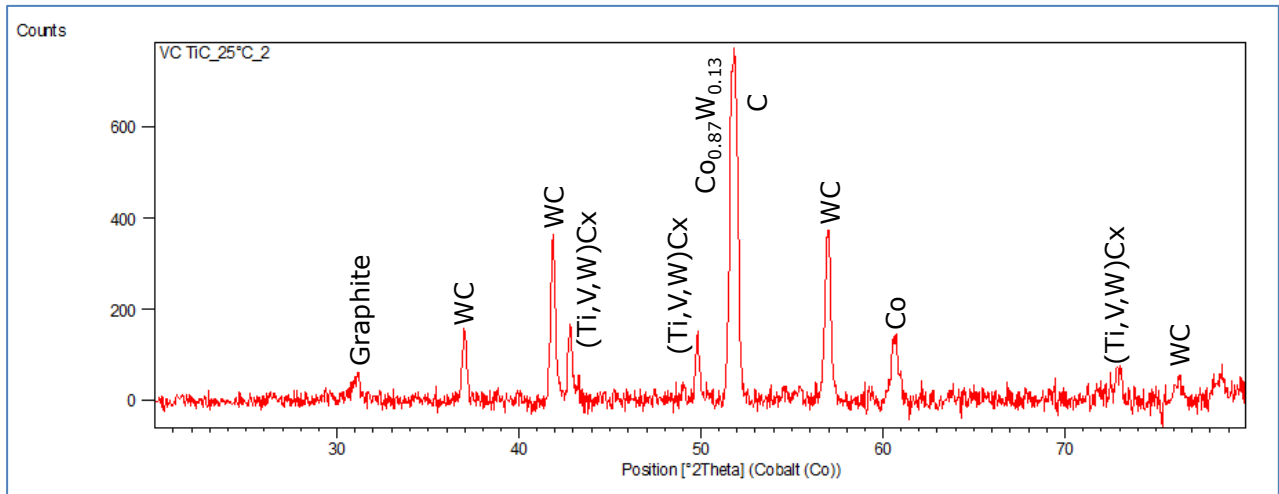


**Figure 4.31: XRD pattern of PCD containing 1.5wt% VC and 1.5wt% TiC taken at 25°C post heat treatment**

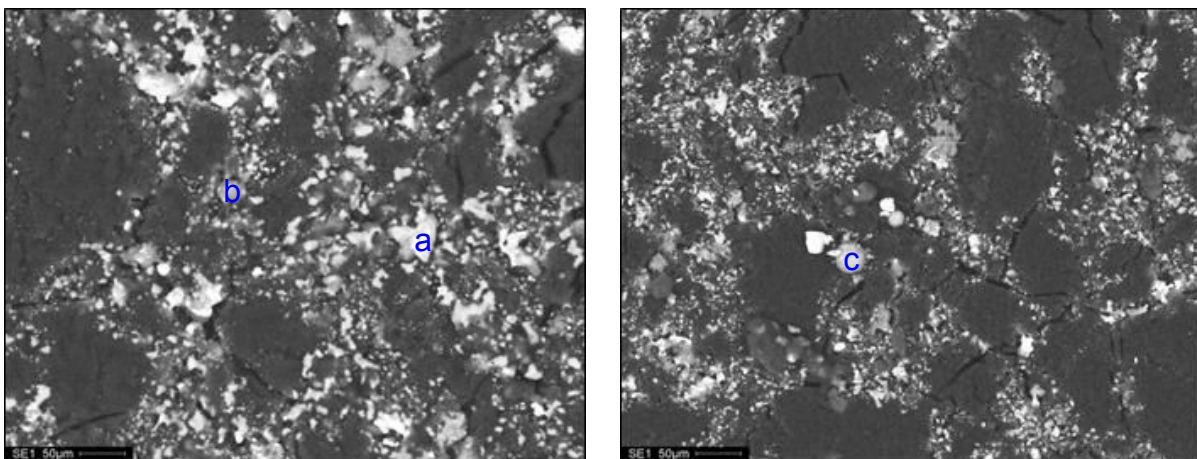


**Figure 4.32: SEM and EDS analysis of the VC-TiC enhanced PCD post heat treatment**

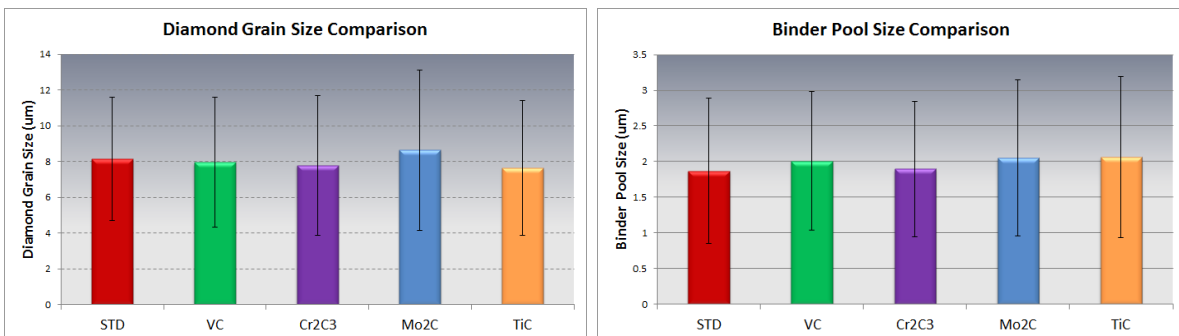
**Table 4.15: EDS Analysis of the various phases in the heat treated VC-TiC enhanced heat treated PCD, values in atomic %**

Area	Carbon	Cobalt	Tungsten	Titanium	Vanadium	Oxygen
a	68.14	7.79	9.94	4.97	9.16	-
b	82.05	2.29	2.62	1.07	1.54	10.43
c	52.33	40.33	-	-	-	7.34

#### 4.3.5 Image Analysis of PCD containing various Carbides

Image analysis was carried out on PCD containing the various metal carbides (refer to Figure 4.33). The addition of the carbide does not seem to affect the diamond grain size nor the binder pool size. The diamond area is significantly decreased on addition of the carbide, with the PCD containing  $\text{Cr}_3\text{C}_2$  showing the lowest diamond density. Carbide additions to PCD reduces the overall amount of diamond present in the PCD compact, and hence an observed decrease in the diamond area. The addition of  $\text{Cr}_3\text{C}_2$  was theoretically supposed to increase the diamond density since it is believed that the  $\text{Cr}_3\text{C}_2$  would disassociate to release chromium and the bonded carbon atoms. Chromium would then go into solution with the cobalt binder and the carbon would be used to enhance the diamond density. However, this phenomenon is not observed.

The diamond area and binder area are inter-related. According to the graph in Figure 4.33, PCD containing  $\text{Cr}_3\text{C}_2$  shows the highest binder content. This is expected since  $\text{Cr}_3\text{C}_2$  does not form a carbide precipitate but rather remains in solution with the cobalt. It must be noted that the diamond content of the  $\text{Cr}_3\text{C}_2$ ,  $\text{Mo}_2\text{C}$  and  $\text{TiC}$  additives are significantly less than the diamond density of the PCD compact containing VC. It could be possible that the sintering of the PCD containing  $\text{Cr}_3\text{C}_2$ ,  $\text{Mo}_2\text{C}$  and  $\text{TiC}$  was not as good as the PCD containing VC.



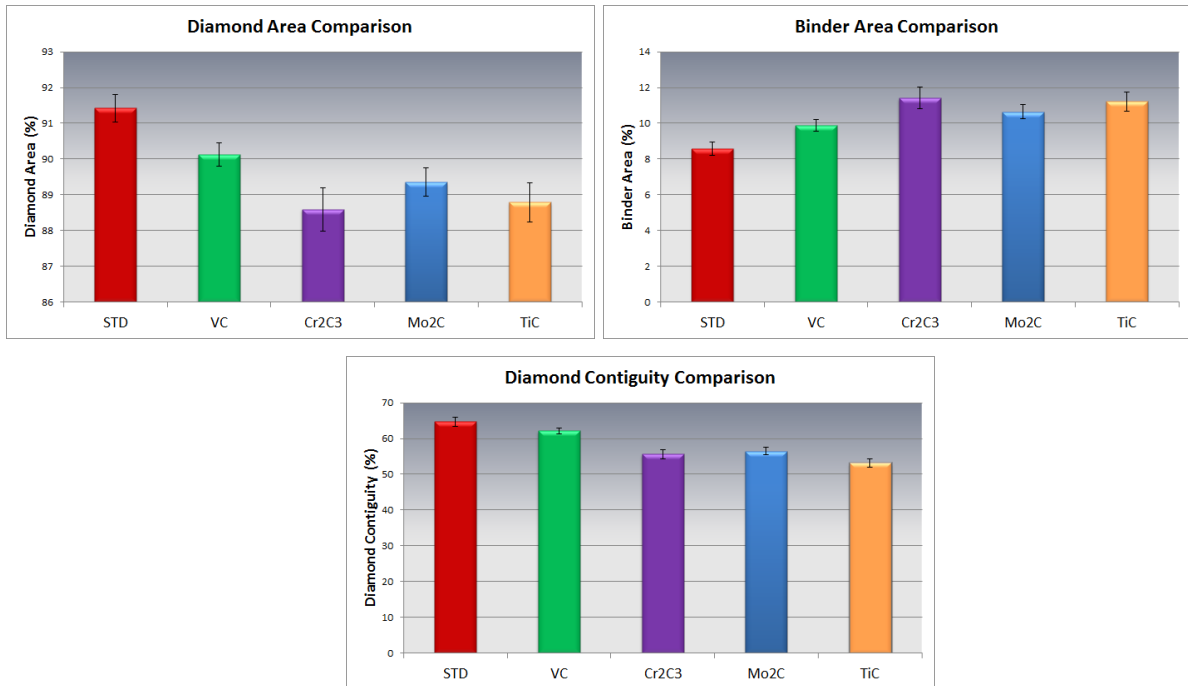


**Figure 4.33: Image Analysis Data for PCD containing different carbides**

The diamond contiguity seems to have slightly decreased with PCD containing the carbide additive. This observation does not necessarily mean that the performance of the PCD compact would be compromised, it probably means that the behaviour mechanism of the PCD would be different. Some PCD compacts fail by the removal of the diamond grains whilst others fail by trans-granular cracking.

#### 4.3.6 Vertical Borer testing of VC-TiC enhanced PCD

The standard PCD, VC enhanced PCD and the VC-TiC enhanced PCD cutters were tested on the vertical borer to compare the respective performance. According to the graph shown in Figure 4.34, the VC-TiC enhanced PCD shows superior durability compared to both the standard PCD and the VC enhanced PCD. The wear resistance of the VC enhanced PCD and the VC-TiC enhanced PCD seemed similar with both cutters showing an improvement over the standard PCD. The VB test shown in Figure 4.34 was a more aggressive test as compared to the VB test previously shown (i.e. Figure 2.54), hence the observed difference in the cutting length. Please note that there is no standard procedure for the VB test. The results will differ depending on the type of test parameters used, and should be used for comparison purposes only.

The wear scar images shown in Figure 4.35 very clearly indicate the susceptibility of the standard PCD to chip and spall. The VC enhanced PCD shows slight spalling on the surface whereas the VC-TiC enhanced PCD shows a smooth wear of the PCD.

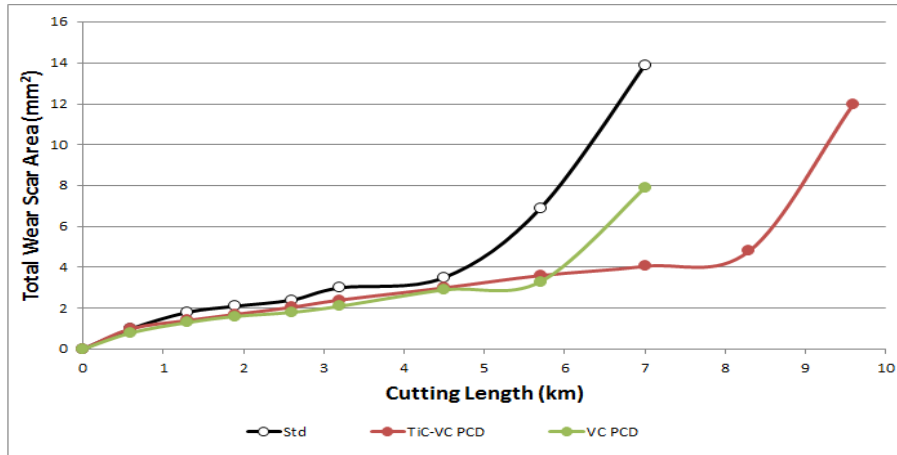


**Figure 4.34: Graph showing the vertical borer comparison between the standard PCD, VC enhanced PCD and VC-TiC enhanced PCD**

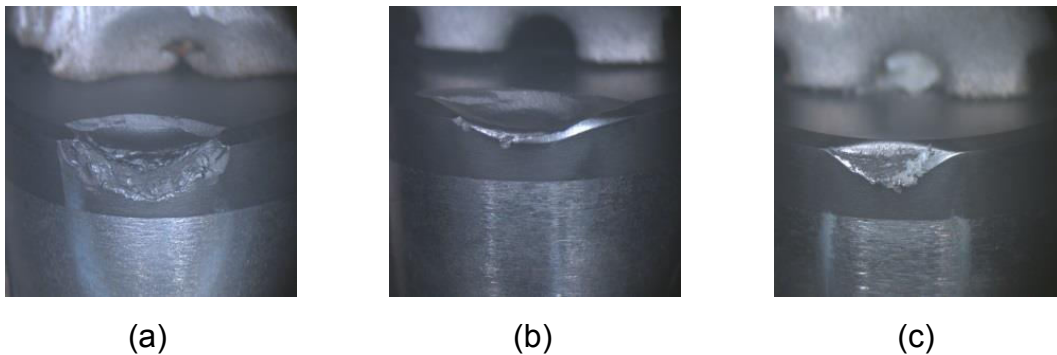


**Figure 4.35: Optical images of the wear scar post VB: (a) Standard PCD, (b) VC enhanced PCD, (c) VC-TiC enhanced PCD**

#### 4.4 Discussion

For the Mo<sub>2</sub>C enhanced PCD, the microstructural analysis of the PCD compact showed the presence of carbide deposits in the binder. On further investigation, EDS analysis revealed the elemental composition to be a combination of carbon, cobalt, molybdenum and tungsten. The XRD pattern showed the carbide deposits to be of similar composition

to  $\text{Mo}_{0.5}\text{W}_{0.5}\text{C}$ . According to the Mo-W-C phase diagram, a solid solution forms between molybdenum and tungsten.

Interestingly, the XRD pattern of the  $\text{Mo}_2\text{C}$  enhanced PCD showed the presence of pure cobalt binder in the PCD. In both the standard PCD and VC enhanced PCD, the binder either comprised  $\text{Co}_{0.87}\text{W}_{0.13}$  or  $\text{Co}_{0.793}\text{V}_{0.207}$ . Closer analysis of the pattern showed the cobalt binder to contain an fcc structure, even though it did not seem to be stabilized by molybdenum substitution into the crystal lattice.

Figure 4.36 shows the XRD overlay of the diamond peak at room temperature, 1100 °C and at 25 °C post heat treatment for the 3wt%  $\text{Mo}_2\text{C}$  enhanced PCD. The blue graph shows the XRD trace at room temperature. There is a slight shoulder on the diamond peak that is owing to the overlap with the cobalt binder. The green graph shows the XRD trace at 1100 °C. The diamond peak and the binder peak appear to be de-convoluted, and the red graph shows the XRD trace at 25 °C post heat treatment. The shoulder on the diamond peak appears more pronounced in the red graph. Peak separation at 1100 °C is due to the difference in thermal expansion between the diamond and the binder.

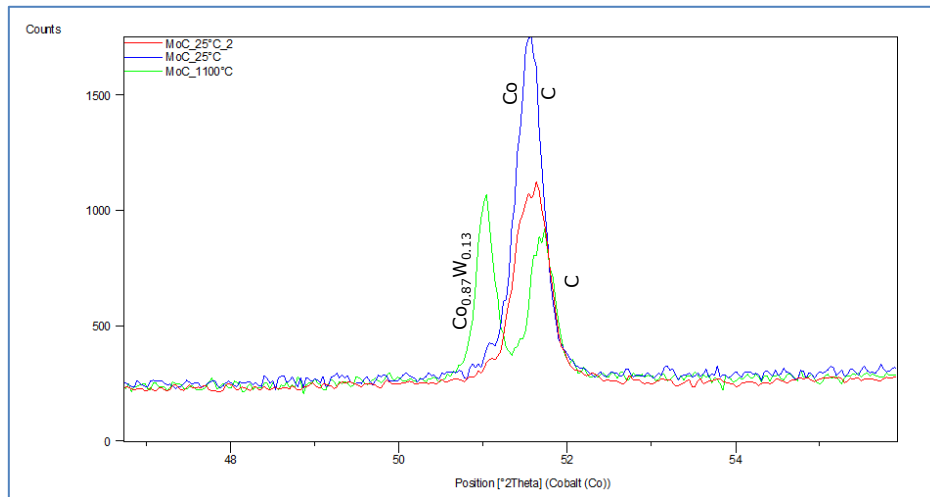


**Figure 4.36: XRD overlay of the diamond peak at room temperature (blue), 1100 °C (green) and at 25 °C post heat treatment (red) for the 3wt%  $\text{Mo}_2\text{C}$  enhanced PCD**

For the TiC enhanced PCD, the  $\text{CTi}_{0.8}\text{W}_{0.2}$  mixed carbide phase seemed to have formed. Both the  $\text{CTi}_{0.8}\text{W}_{0.2}$  mixed carbide and WC phases were observed to deposit in the binder



pools. The SEM image of the  $\text{Cr}_3\text{C}_2$  enhanced PCD showed no evidence of a mixed  $(\text{Cr,W})\text{C}_x$  deposit in the binder pools. In fact, there was no evidence of any  $\text{Cr}_3\text{C}_2$  deposits within the PCD either. From the observations, it is inferred that the  $\text{Cr}_3\text{C}_2$  dissolved in the cobalt binder and went into solution with the binder. The EDS analysis (refer to Figure 4.20) substantiates this conclusion as the graph shows the presence of chromium in the binder pools. Zackrisson et al. state that for  $\text{Cr}_3\text{C}_2$  additions larger than 2vol%, the most obvious effect on the microstructure was the formation of a  $\text{Cr}_7\text{C}_3$  phase [109]. In this study a  $\text{Cr}_3\text{C}_2$  concentration of 1.60vol% was used, and this explains the observation that no  $\text{Cr}_3\text{C}_2$  or  $(\text{Cr,W})\text{C}_x$  was formed in the PCD. The presence of the chromium in the binder phase probably results in the solution hardening of the binder phase which assists in the improvement of the abrasion resistance of the compact, as observed by Middlemiss et al. on their granite log test results.

Heat treatment of the  $\text{Cr}_3\text{C}_2$  enhanced PCD showed excessive oxidation of the cobalt binder possibly due to an oxygen leak. In addition, seepage of the cobalt from within the PCD was also observed. Figure 4.37 shows the SEM comparison of the microstructures of the various carbides used in the study post heat treatment. In the  $\text{Mo}_2\text{C}$  and  $\text{TiC}$  enhanced PCD, the diamond grains can still be seen. However in the  $\text{Cr}_3\text{C}_2$  enhanced PCD, there is predominantly cobalt oxide on the surface of the PCD.

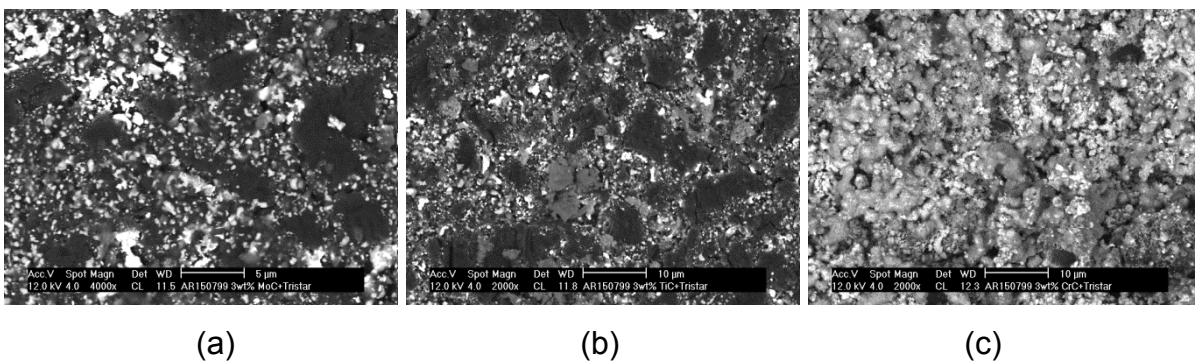


**Figure 4.37: SEM comparison of the microstructures post heat treatment: (a)  $\text{Mo}_2\text{C}$  enhanced PCD, (b)  $\text{TiC}$  enhanced PCD and (c)  $\text{Cr}_3\text{C}_2$  enhanced PCD**

Figure 4.38 shows the overlay of the graphite peak appearing in the VC- $\text{TiC}$  enhanced PCD and in the VC enhanced PCD. According to the XRD pattern, the peak height and

area of graphite for the VC enhanced PCD is 106.58cts & 40.96cts, whereas the peak height and area of graphite (002 peak) for the VC-TiC enhanced PCD is 69.81cts & 35.78cts. According to the observed results, it would appear that the VC-TiC enhanced PCD seems slightly more resistant to graphitisation.

The wetting angle of TiC in cobalt seems much larger than the wetting angle of VC in cobalt (refer to Figure 4.39). Hashe et al. concluded that TiC is not expected to easily go into solution with cobalt [53]. This implies that TiC would likely be a more efficient barrier against the cobalt reacting with the diamond to form graphite. It is therefore plausible to speculate that the VC-TiC enhanced PCD would be more thermally resistant as evidenced by the XRD pattern shown in Figure 4.38.

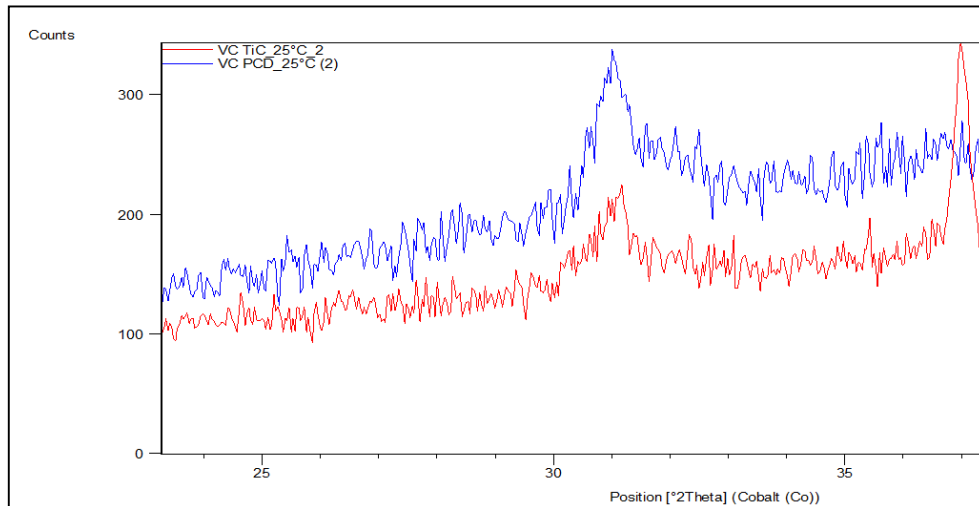


**Figure 4.38: Overlay of the graphite (002) peak appearing in the VC-TiC enhanced PCD and in the VC enhanced PCD**

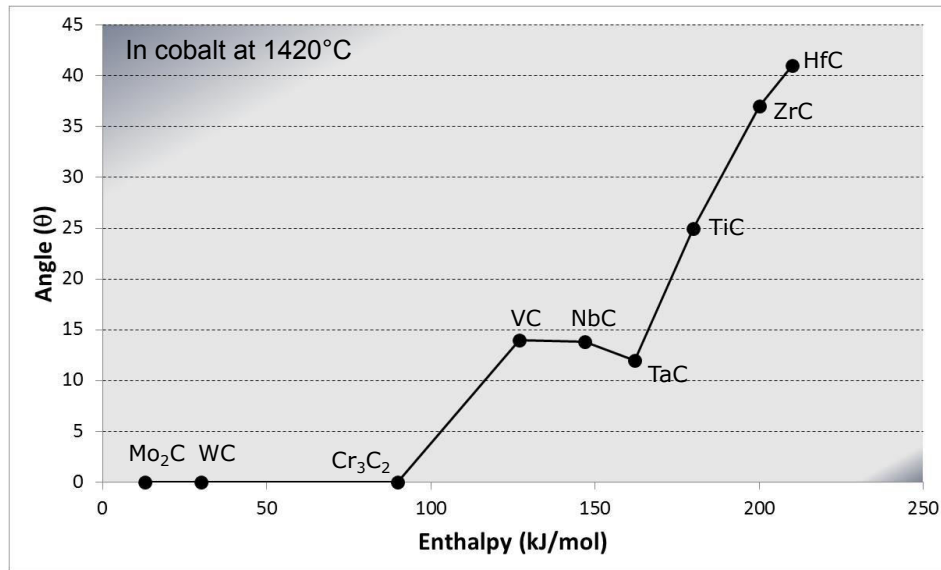


**Figure 4.39: Wetting of Metallic carbides by liquid cobalt [60]**

According to both SEM analysis and XRD analysis shown, WC was found in the Cr<sub>3</sub>C<sub>2</sub> enhanced PCD, Mo<sub>2</sub>C enhanced PCD, TiC enhanced PCD and in the VC-TiC enhanced PCD. The wetting angle of TiC with cobalt is substantially higher and therefore TiC is not expected to easily go into solution with the cobalt. This could reduce the interaction between TiC and WC (which is in solution with the cobalt) and hence result in residual WC remaining in the sintered PCD. Interestingly, the VC enhanced PCD shows no evidence of residual WC in the sintered PCD for concentrations greater than 3wt% VC, but in combination with TiC, the VC-TiC enhanced PCD shows the definite presence of WC in the sintered PCD.

Luyckx et al. observed that both VC and Cr<sub>3</sub>C<sub>2</sub> are effective grain growth inhibitors for WC-Co, with VC being more effective [106]. Although the hardness of Cr<sub>3</sub>C<sub>2</sub> is not as high as VC or TiC (refer to Table 4.16 [38]), the dissolution of Cr<sub>3</sub>C<sub>2</sub> into the cobalt binder suggests solution hardening of the cobalt binder by the presence of Cr<sub>3</sub>C<sub>2</sub>.

**Table 4.16: Micro Hardness of Metal Carbides**

<b>Metal Carbide</b>	<b>Micro Hardness (kg/mm<sup>2</sup>)</b>
Diamond	7000 <sup>a</sup>
VC <sub>0.97</sub>	2900
TiC	2900
WC	2100
Mo <sub>2</sub> C	1500
Cr <sub>3</sub> C <sub>2</sub>	1300

a [67]

#### 4.5 Conclusion

Various carbides such as molybdenum carbide (Mo<sub>2</sub>C), chromium carbide (Cr<sub>3</sub>C<sub>2</sub>), titanium carbide (TiC) and an equal mixture of vanadium carbide and titanium carbide were added to PCD. The resulting microstructure and stability of the carbide were investigated. Surprisingly, the Cr<sub>3</sub>C<sub>2</sub> did not seem to react with the WC in the PCD to form a mixed carbide. It was previously shown that both the 3wt% and 5wt% VC enhanced PCD displayed no evidence of the presence of WC in the sintered PCD. However, the strong presence of WC in the PCD containing Cr<sub>3</sub>C<sub>2</sub> or TiC is evidently visible. In addition, the Cr<sub>3</sub>C<sub>2</sub> seemed to have disassociated and entered into solution with the cobalt binder. The Mo<sub>2</sub>C and WC seemed to have reacted to form a solid solution giving rise to a mixed carbide phase, namely Mo<sub>0.5</sub>W<sub>0.5</sub>C.

XRD analysis showed that the carbides that formed were stable up to 1100 °C, with the onset of graphitization at 950 °C. According to the ICSD database, the addition of a combination of TiC and VC led to the formation of two carbides, namely C<sub>2</sub>TiV and C<sub>2</sub>TiW. Further investigation showed that it was likely that a mixed carbide phase, namely (Ti,V,W)C<sub>x</sub>, formed. Vertical borer test results showed that the VC-TiC enhanced PCD exhibited superior durability. An additional patent was filed by Kaveshini Naidoo et al. with the publication number: US2015151410A1 that described the performance improvement of the VC-TiC enhanced PCD.

#### 4.6 Recommendations

The thesis focussed predominantly on the microstructural analysis of various carbide additives to PCD. Additional work should be done to qualify the behavioural performance of the PCD containing different carbide additives and a comparison made as to which carbide additive displays the highest performance.

## CHAPTER FIVE

### GRAIN GROWTH OF PCD

#### 5.1 Background

Fine grain structures have unique properties such as high tensile and fatigue strengths, as well as a high resistance to crack growth [110]. There is generally a drive to move to finer and finer structures in order to enhance the properties of the material, especially the abrasion resistance [111]. One of the major challenges faced when moving to finer grain sizes is grain growth. Generally grains grow according to the Ostwald ripening process whereby smaller crystals dissolve and redeposit onto larger crystals to create a more homogeneous structure [112]. This occurs due to the larger particles being more energetically favourable as compared to the smaller particles. Equation 5-1 best describes the process of the LSW (Lifshitz, Slyozov and Wagner) coarsening process.

$$\langle R \rangle^3 - \langle R \rangle_0^3 = \frac{8\gamma c_\infty v^2 D}{9R_g T} t \quad \dots\dots\dots \text{Equation 5-1 [112]}$$

Where:

- $\langle R \rangle_0$  = initial average radius of all the particles
- $\langle R \rangle$  = average radius of all the particles
- $\gamma$  = particle surface tension or surface energy
- $c_\infty$  = solubility of the particle material
- $v$  = molar volume of the particle material
- $D$  = diffusion coefficient of the particle material
- $R_g$  = ideal gas constant
- $T$  = absolute temperature and
- $t$  = time.

Sometimes, grains do not grow in a homogeneous way. Some grains would grow faster than others, and this results in abnormal grain growth. Grain growth is the increase in the size of grains or crystallites in a material at high temperature. It is a phenomenon that occurs as a result of the movement of grain boundaries. There are two types of grain growth, viz. continuous grain growth and discontinuous or abnormal grain growth.

Abnormal grain growth, also known as secondary recrystallisation, occurs when a small number of grains in a matrix grow at a higher rate as compared to the remaining grains in the matrix. The result is a microstructure dominated by a few large grains. This is most likely attributed to a thermodynamic instability that occurs at a three-grain boundary junction of one large grain  $D$  with two smaller adjoining grains  $d$  if  $D/d > 2$ . All the growth then occurs in  $D$  and not in  $d$ . This process actually has an incubation time for  $D$  to grow until it is  $2d$  in size and then secondary recrystallisation sets in.

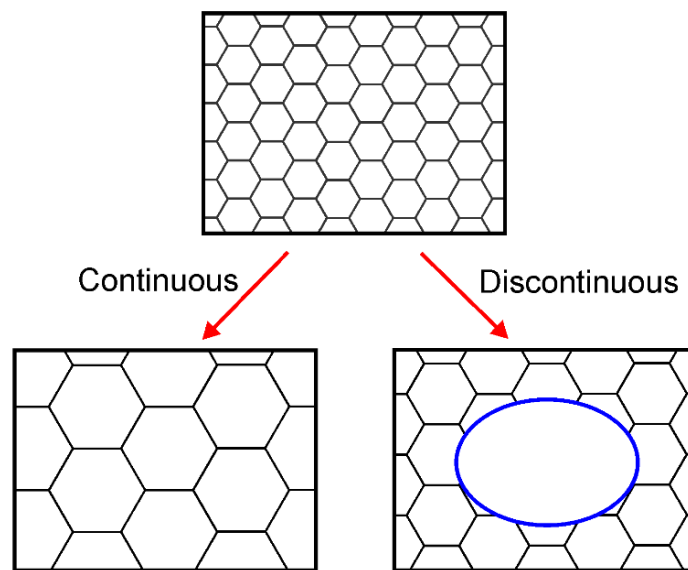


**Figure 5.1: Continuous and Discontinuous (abnormal) grain growth**

Konyashin et al. observed that WC coarsening in WC-Co hard metals was strongly suppressed by decreasing the carbon content in the material and additionally increasing the tungsten content in the binder. Furthermore, it was found that the activation energy of WC coarsening in the alloy with medium carbon content varied from 163 to 177 kcal/mol which resulted in greater coarsening of the WC particles, whereas the activation energy in the alloy with low carbon content was found to be 98 kcal/mol which resulted in less coarsening of the WC particles.

Marshall et al. found that both vanadium and chromium inhibited grain growth in WC-Co carbide [51]. Vanadium appeared to have a stronger tendency to segregate to the WC-Co interface than chromium, resulting in vanadium segregating more on the fine grains

during sintering. WC grains in the chromium doped samples tended to have a more prismatic appearance whilst WC grains in the vanadium doped samples tended to be more rounded.

Weidow et al. investigated the effect of vanadium, chromium and manganese additions on the microstructure of WC-Co [113]. Vanadium was found to be the most effective grain growth inhibitor followed by chromium. WC-Co carbides containing vanadium had the highest hardness, followed by chromium. The addition of manganese to the WC-Co showed no significant improvement from the reference. Furthermore, WC-Co containing vanadium showed the highest increase in WC/WC grain boundaries.

It is proposed that the grain growth inhibition due to VC doping is closely related to the formation of the (W,V)C<sub>x</sub> layers [49]. Jaroenworuluck et al. believe that the retardation of the grain growth of carbide grains is closely related to the segregation of vanadium at the WC/Co interfaces [114].

Thus far, the most successful way of controlling the WC grain growth is the addition of small amounts of grain growth inhibitor, typically metallic carbides such as VC, Cr<sub>3</sub>C<sub>2</sub>, NbC, or TaC [115], [116], [117], [58], [118]. Morton et al. found the most effective grain growth inhibitor to be VC, and the least effective grain growth inhibitor to be Zr/HfC with the following trend in between: VC > Cr<sub>3</sub>C<sub>2</sub> > NbC > TaC > TiC > Zr/HfC [119].

Grain growth is an important phenomenon observed in the sintering of fine grain PCD, especially PCD with a grain size of 1 μm and below. Although normal grain growth (NGG) is expected and observed in fine grain PCD, the presence of abnormal grain growth (AGG) still remains a challenge to overcome. AGG in PCD negatively affects both the properties of the material as well as the electrical discharge machining (EDM) of the compact.

Various researchers have investigated methods to reduce the occurrence of AGG in PCD, some successful and some not. Akaishi et al. found that the addition of a small amount of cubic boron nitride to the starting diamond powder suppressed grain growth



[120]. Yu et al. observed that the addition of Ni-Zr to PCD having a grain size of 0.5-1.5  $\mu\text{m}$  resulted in the in-situ formation of ZrC which suppressed grain growth [49]. Shin et al. found that the addition of approximately 30% WC powder to the diamond effectively suppressed the formation of AGG in PCD but resulted in the decrease of abrasion resistance of the compact [121]. They furthermore observed that the largest faceted planes of the abnormally grown crystals were octahedral planes  $\{111\}$ . In addition, they observed that AGG was extensive at the corners of the tantalum cupping material due to the increase in pressure naturally applied to the corner.

McKie et al. found that the use of diamond enhanced carbide substrates suppressed the AGG in PCD [122]. They had the similar observation to Shin et al. in that they observed that some of the larger grains were not always single crystals but comprised of inter-grown crystals.

In this chapter, two types of carbides were added to fine grain PCD, viz. VC and  $\text{Cr}_3\text{C}_2$ . The aim of the investigation was to assess the effect of the individual grain refiner on the grain growth of PCD.

## 5.2 Experimental

The vanadium (3wt%, 1.85vol%) and chromium (3wt%, 1.60vol%) carbides were combined with the diamond powder (with average grain size of 0.5  $\mu\text{m}$ ) in the same way as for the VC enhanced PCD. The mixture was sintered at 1400 °C and 6.8 GPa using a high pressure vehicle. The sintered PCD was optically analysed using the Olympus SZX7 Stereo Microscope attached to an Olympus SC30 camera, and the microstructure was analysed using a Jeol 7500 SEM. Grain size measurements were done using Scandium software and the elemental composition of the constituents in the PCD was measured using the PW2400 XRF.

## 5.3 Results

### 5.3.1 Analysis of the 0.5 $\mu\text{m}$ Standard PCD Compact

Figure 5.2 shows the optical image of the 0.5  $\mu\text{m}$  sintered PCD compact showing areas of abnormal grain growth (AGG) and normal grain growth (NGG) of the diamond crystallites. The grain growth is predominant along the WC-Co interface and along the canister material, with the centre of the PCD devoid of any AGG areas. The AGG region was approximately 250-300  $\mu\text{m}$  thick. The SEM image of the 0.5  $\mu\text{m}$  sintered PCD compact showing AGG at the WC-Co/diamond interface is shown in Figure 5.3. Large grains in the order of 100 – 400  $\mu\text{m}$  are clearly seen. The results shown are indicative of the grain size. For a more accurate analysis, the line intercept method would have to be applied.

Figure 5.4 shows the SEM image of the 0.5  $\mu\text{m}$  sintered PCD compact showing normal grain growth. The grain size is considerably smaller than the grains appearing in the AGG region, generally less than 1  $\mu\text{m}$ . There are a few large cobalt pools present in the microstructure. Conversely, Figure 5.5 shows the SEM image of the 0.5  $\mu\text{m}$  sintered PCD compact with large grains in the AGG region clearly visible. The large grains are separated by the cobalt binder. There seems to be cobalt pools and tungsten carbide trapped within the large grain. This occurrence is typical of an increased growth rate of particles. Essentially, the diffusion of the metal binder away from the growing crystal is slower than the growth rate of the crystal, and hence some of the metal binder becomes trapped within the growing crystal.

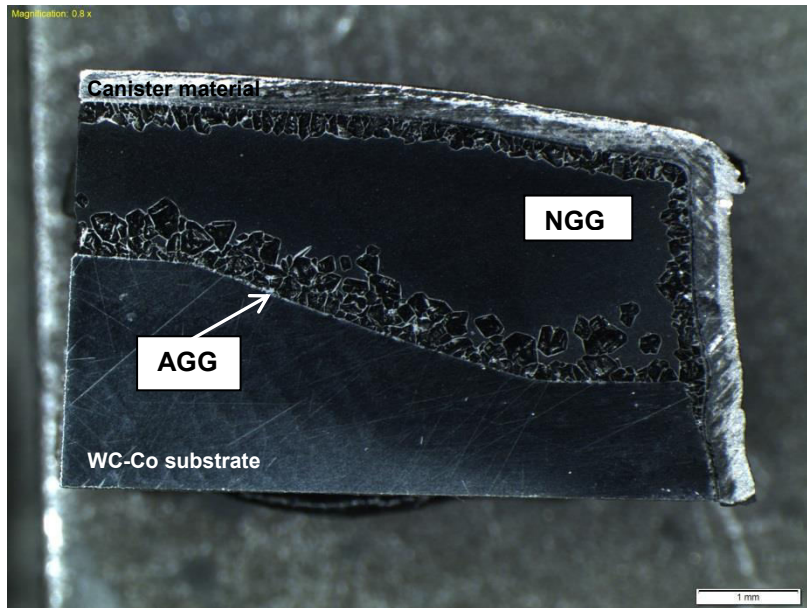
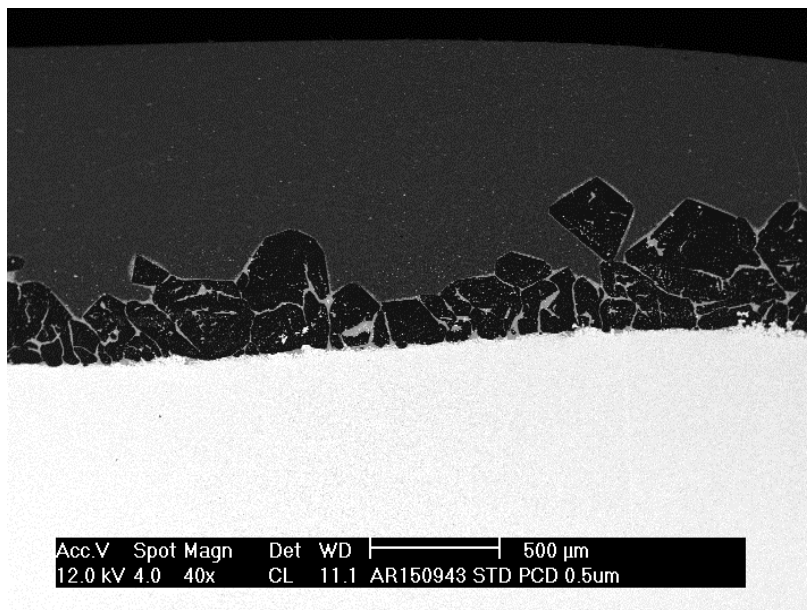
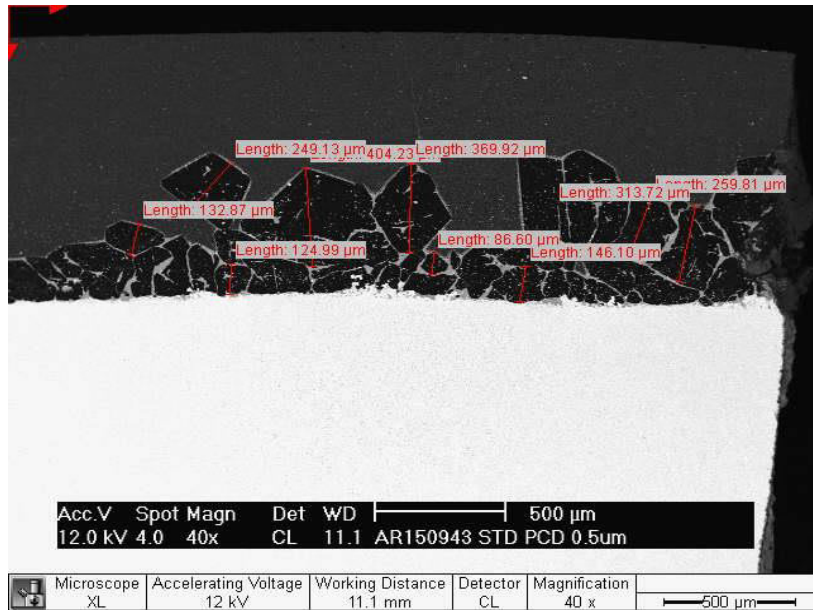


Figure 5.2: Optical image of the 0.5  $\mu\text{m}$  sintered PCD showing areas of abnormal grain growth (AGG) and normal grain growth (NGG) of the diamond crystallites

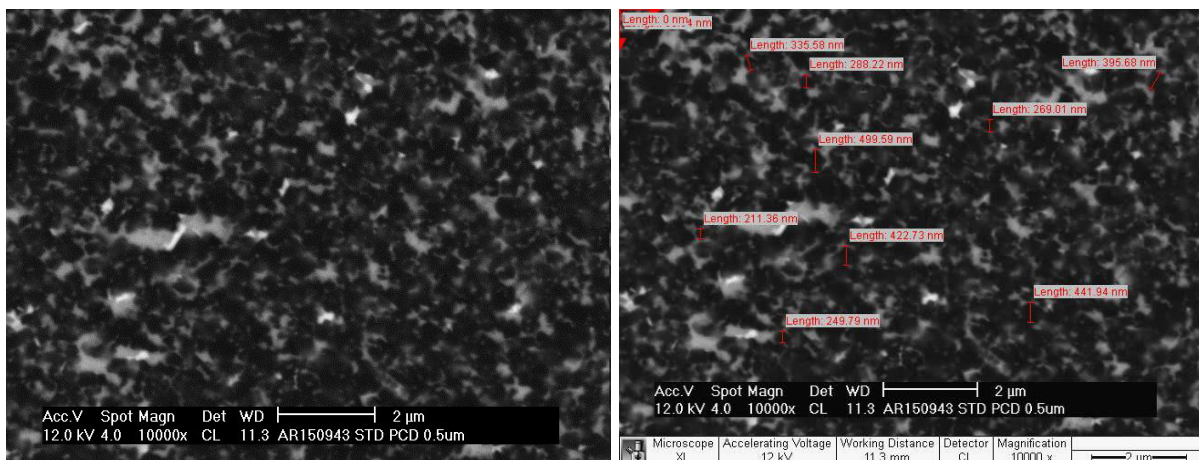


(a)



(b)

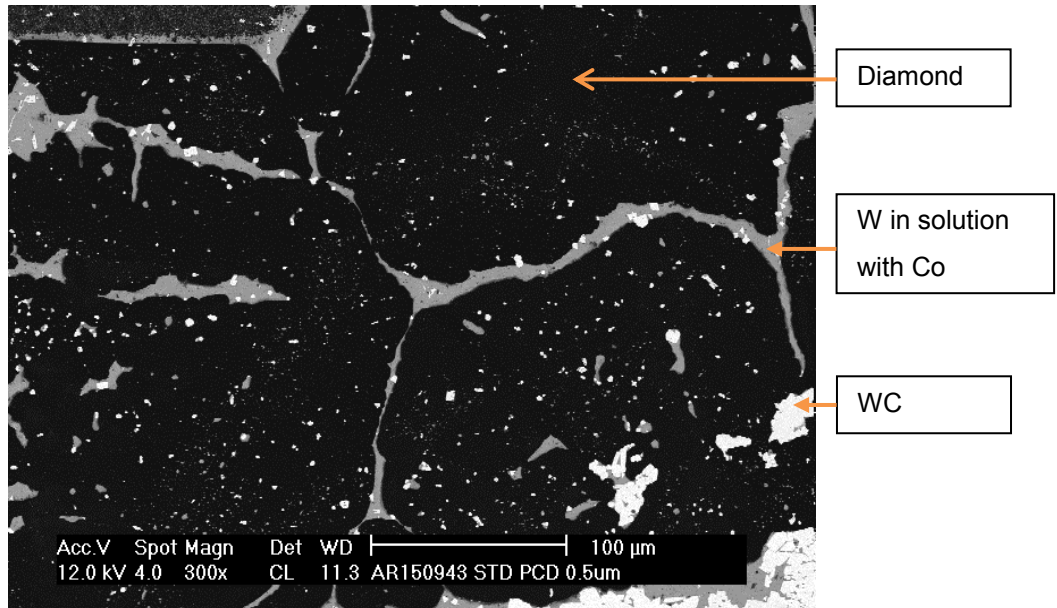
**Figure 5.3: SEM image of the 0.5 μm sintered PCD compact showing AGG at the WC-Co/diamond interface: (a) AGG at the interface, (b) Measurement of grain size**



(a)

(b)

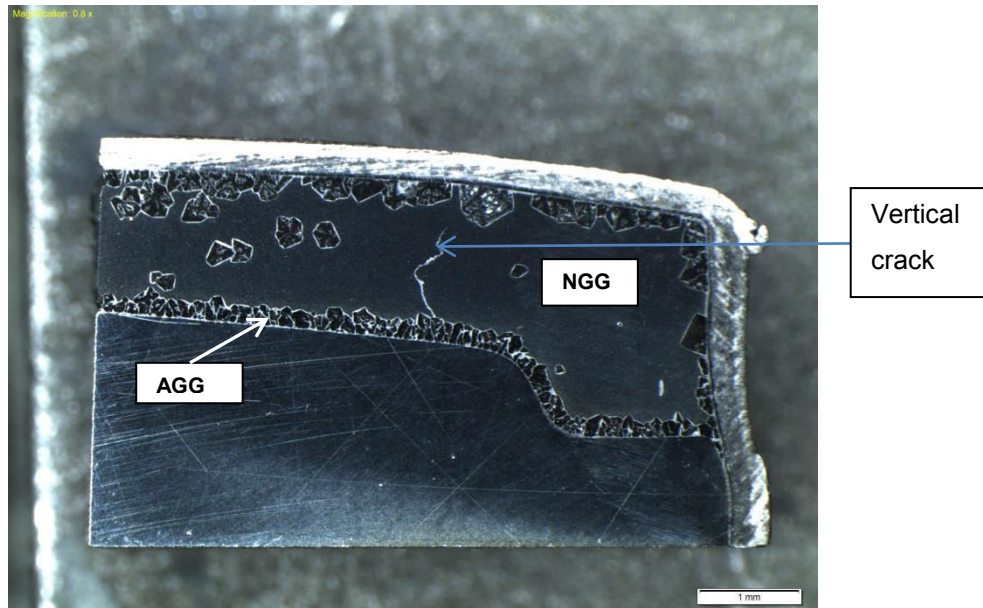
**Figure 5.4: SEM image of 0.5 μm sintered PCD showing normal grain growth: (a) Bulk PCD, (b) Measurement of grains**



**Figure 5.5: SEM image of 0.5 μm sintered PCD showing large grains in the AGG region**

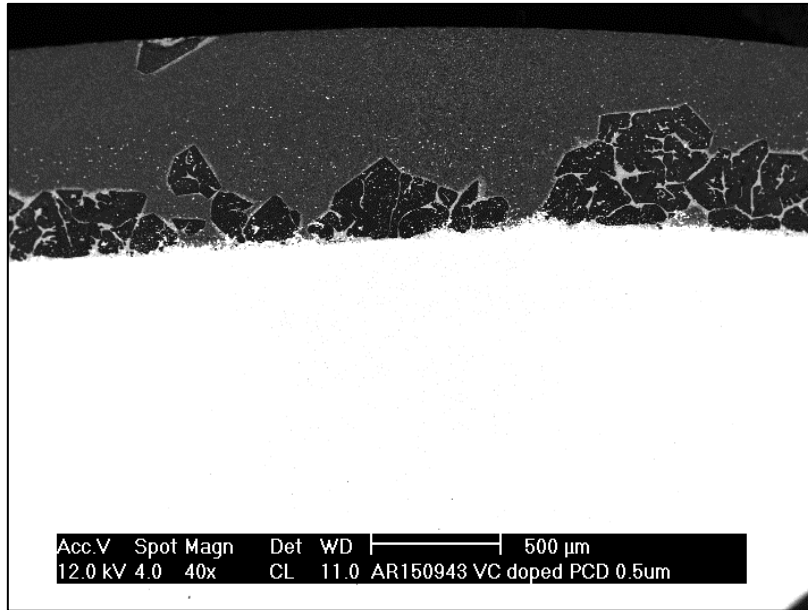
### 5.3.2 Analysis of the 0.5 μm PCD Compact containing 3wt% VC

Figure 5.6 shows the optical image of a 0.5 μm sintered PCD doped with 3wt% VC. AGG is visible along the WC-Co/diamond interface as well as along the canister material. Interesting, larger grains are present in the bulk of the PCD. This phenomenon was not observed in the standard sintered PCD. In addition, there seems to be a vertical crack initiating at the AGG near the substrate propagating into the bulk PCD. Scratches appearing on the WC-Co substrate are quite common and usually arise during sample preparation.

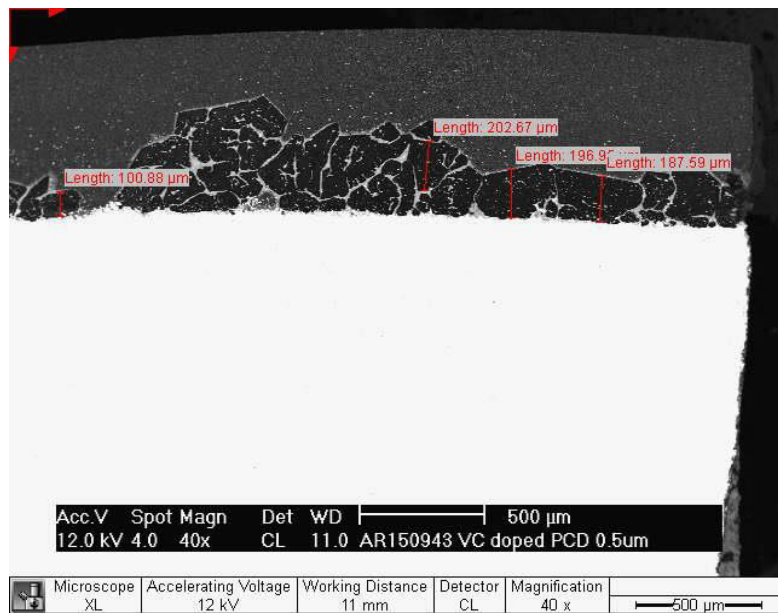


**Figure 5.6: Optical image of the 0.5  $\mu\text{m}$  sintered PCD doped with 3wt% VC**

Figure 5.7 shows the SEM image of the 0.5  $\mu\text{m}$  sintered PCD compact doped with 3wt% VC. AGG is present at the WC-Co/diamond interface. The magnitude of the grain size at the interface is in the order of 100-200  $\mu\text{m}$ , slightly finer than the grain size of the standard PCD. The AGG region was approximately 250-300  $\mu\text{m}$  thick. An image of the NGG in the bulk PCD is shown in Figure 5.8. The grain size is considerably smaller than the grains appearing in the AGG region, approximately  $\approx 0.5 \mu\text{m}$ . However, in the centre of the image, two abnormally grown grains are visible with an approximate grain size of 1  $\mu\text{m}$ .



(a)



(b)

**Figure 5.7: SEM image of the 0.5 μm sintered PCD compact doped with 3wt% VC, showing AGG at the WC-Co/diamond interface: (a) AGG at the interface, (b) Measurement of grain size**

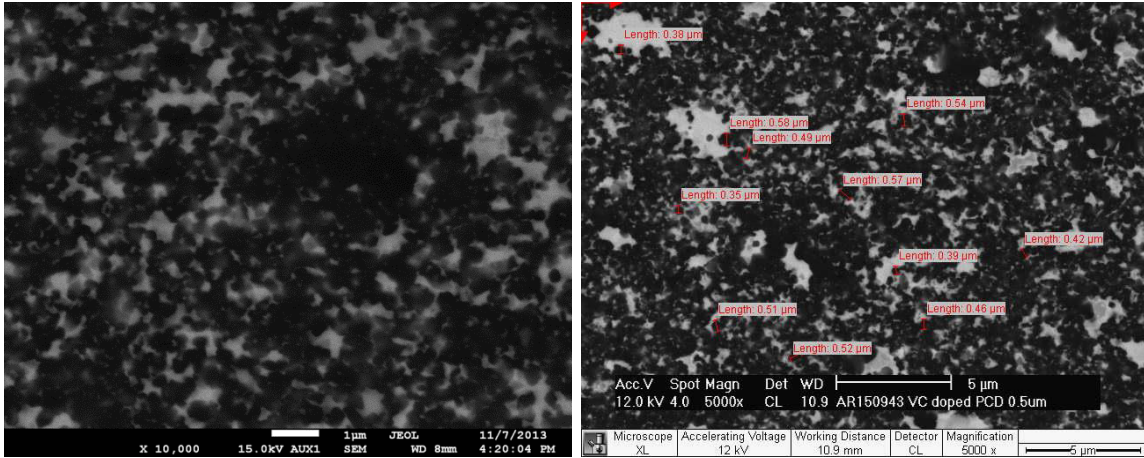


**Figure 5.8: SEM image of 0.5  $\mu\text{m}$  sintered PCD doped with 3wt% VC showing normal grain growth**

Figure 5.9 shows a high magnification SEM image of the AGG region in the 0.5  $\mu\text{m}$  PCD doped with 3wt% VC. The cobalt pools appear as thin continuous regions surrounding the diamond grains. Various tungsten carbide deposits are visible within the grain. Ordinarily, WC would not be expected to be present in a PCD containing 3wt% VC, but due to the excessive grain growth, the WC seems to have become trapped in the growing grain instead of combining with the VC to form the mixed carbide phase.

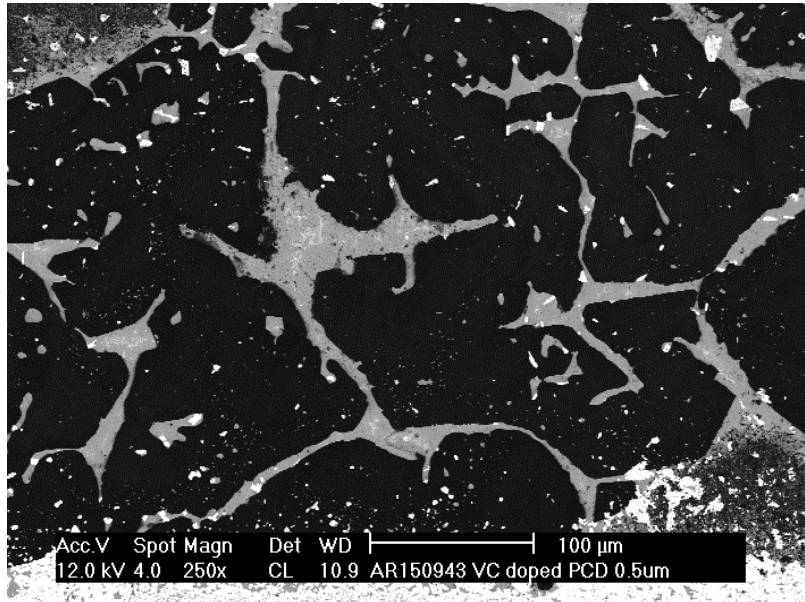


**Figure 5.9: SEM image of 0.5  $\mu\text{m}$  sintered PCD doped with 3wt% VC showing large grains in the AGG region**



### 5.3.3 Analysis of the 0.5 $\mu\text{m}$ PCD Compact containing 3wt% $\text{Cr}_3\text{C}_2$

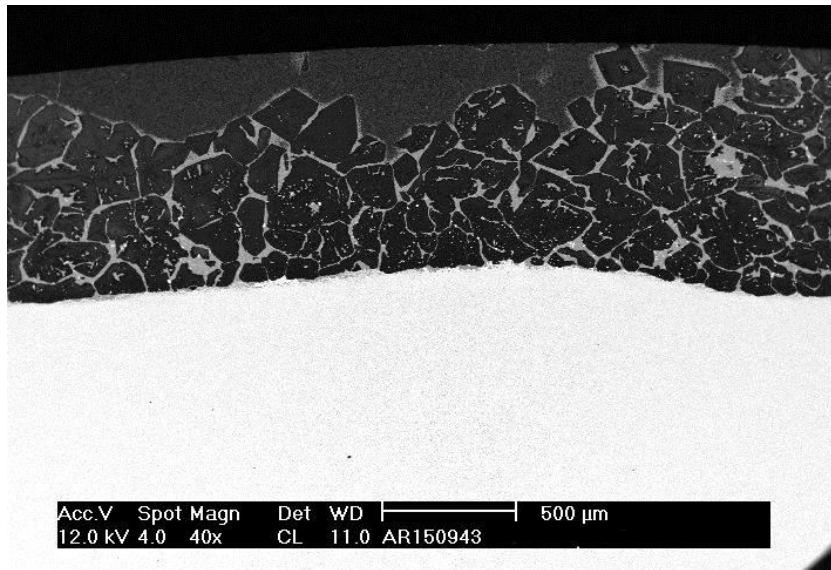
Figure 5.10 shows the optical image of the 0.5  $\mu\text{m}$  sintered PCD doped with 3wt%  $\text{Cr}_3\text{C}_2$ . Tremendous grain growth is observed along the WC-Co/diamond interface, at the canister interface as well as at the corner of the canister material. AGG also appears in the bulk of the PCD.



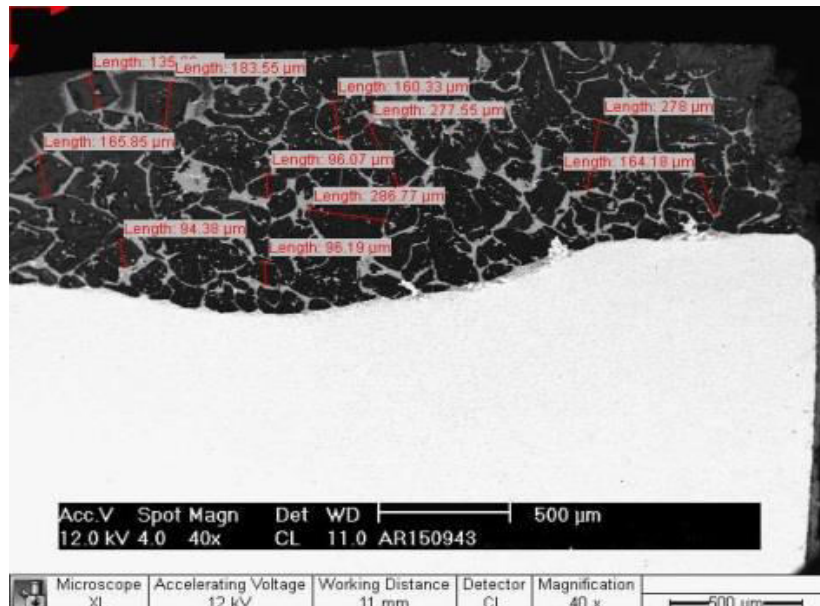
**Figure 5.10: Optical image of the 0.5  $\mu\text{m}$  sintered PCD doped with 3wt%  $\text{Cr}_3\text{C}_2$**

The SEM image of the 0.5  $\mu\text{m}$  sintered PCD compact doped with 3wt%  $\text{Cr}_3\text{C}_2$  is shown in Figure 5.11. The AGG seems to almost comprise the entire PCD table, with the size of the abnormally grown grains ranging from 100-250  $\mu\text{m}$ . The AGG region was approximately 650-700  $\mu\text{m}$  thick. The extent of AGG observed in the  $\text{Cr}_3\text{C}_2$  doped PCD far exceeds the AGG detected in both the VC doped PCD and standard PCD.

Figure 5.12 shows the SEM image of 0.5  $\mu\text{m}$  sintered PCD doped with 3wt%  $\text{Cr}_3\text{C}_2$  showing normal grain growth. The grain size appears  $<0.5 \mu\text{m}$ . The microstructure is not homogeneous with large binder pools present in the PCD. Some of these binder pools consist of a mixture of fine agglomerated particles. There was no evidence of  $\text{Cr}_3\text{C}_2$  precipitation.



(a)



(b)

**Figure 5.11: SEM image of the 0.5 μm sintered PCD compact doped with 3wt% Cr<sub>3</sub>C<sub>2</sub>, showing AGG at the WC-Co/diamond interface: (a) AGG at the interface, (b) Measurement of grain size**

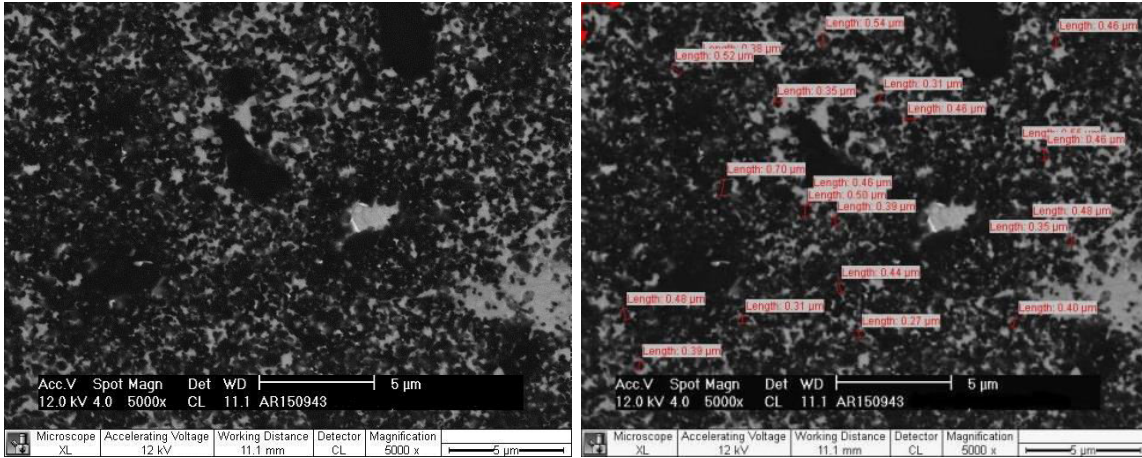


**Figure 5.12: SEM image of 0.5 μm sintered PCD doped with 3wt% Cr<sub>3</sub>C<sub>2</sub> showing normal grain growth**

Figure 5.13 shows the SEM image of the larger grains appearing at the WC-Co interface. According to EDS analysis, the binder pools consist of both tungsten and chromium dissolved in the cobalt. In addition, there appears to be WC precipitates present in the binder pools.

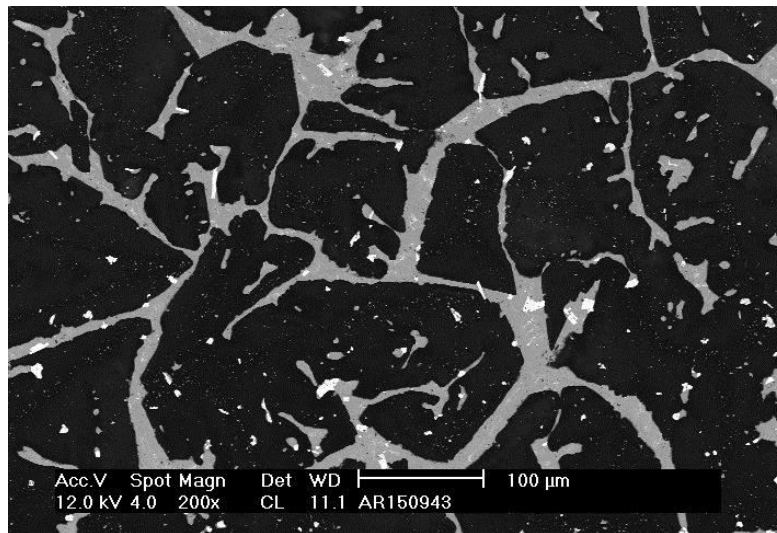


**Figure 5.13: SEM image of 0.5 μm sintered PCD doped with 3wt% Cr<sub>3</sub>C<sub>2</sub> showing large grains in the AGG region**

## 5.4 Discussion

Using the Gibbs/Thompson equation, McKie et al. determined the solubility curve for diamond in the cobalt liquid (refer to Figure 5.14).

$$C = C_o \exp \left[ \frac{4\gamma_{sl}\Omega}{kT} \frac{1}{r} \right] \quad \text{Equation 5-2: Gibbs/Thompson equation}$$

Where,  $r$  is the grain size of the particles,  $\gamma_{sl}$  is the solid–liquid interfacial energy,  $\Omega$  is the atomic volume,  $T$  is the temperature and  $k$  is the Boltzmann constant.  $C_o$  is the equilibrium concentration above an infinitively large particle. The equation shows that the solubility increases strongly with reducing grain size.

The dotted line indicates the carbon solubility at equilibrium. From the graph in Figure 5.14, it is clear that the solubility of the diamond in the cobalt binder increases as the particle size decreases. There is a substantial increase in the solubility of the diamond particle at  $0.5 \mu\text{m}$  and an exponential increase in the solubility at less than  $0.2 \mu\text{m}$ . This graph explains the AGG observed in the PCD samples under investigation.

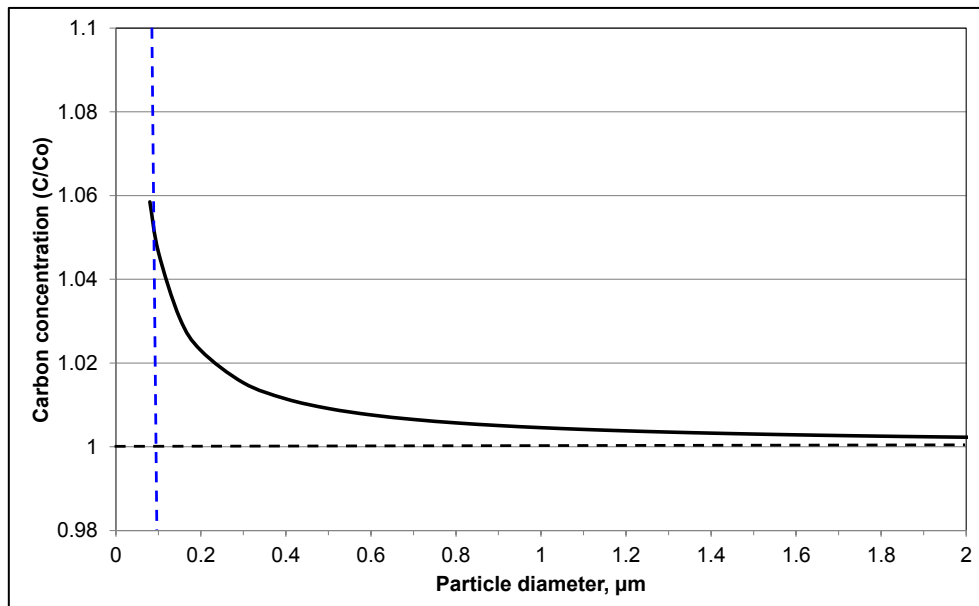
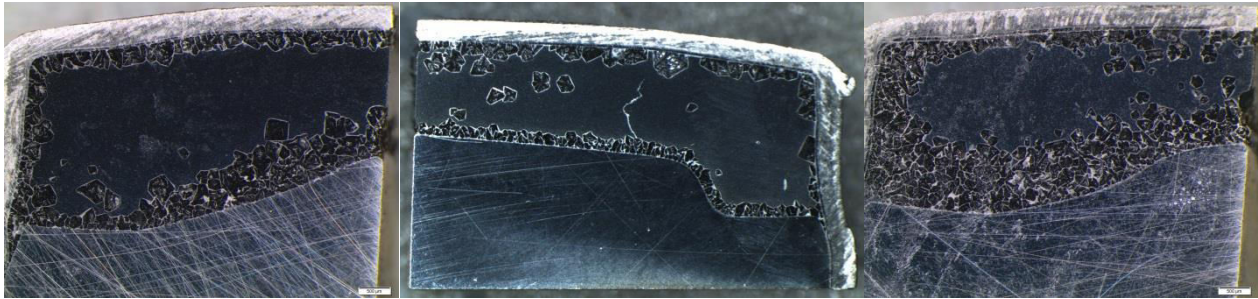


**Figure 5.14: Solubility curve of diamond in the cobalt liquid [122]**

Both VC and  $\text{Cr}_3\text{C}_2$  seem to be effective grain growth inhibitors when added to tungsten carbide. One of the mechanisms is believed to be the segregation of both the carbide additive to the WC/Co interface thereby reducing the grain mobility of the WC particle, and thus hindering grain growth [123] [124]. Jaroenworarluck et al. suggests that the segregation of VC at the WC/Co interface leads to the faceting of the interface reducing grain growth [114]. G. Gille et al. explains another mechanism where the solubility of the WC grains in the binder reduces when adding grain growth inhibitors [125]. They concluded that limited solubility decreases the solution re-precipitation which reduces grain growth.

In this study, doping with VC was found to be slightly beneficial in terms of reducing AGG, whereas addition of  $\text{Cr}_3\text{C}_2$  promoted AGG (refer to Figure 5.15). The reduction of AGG when using VC as a dopant can be explained by one of the mechanisms outlined above. Perhaps the VC segregates to the diamond/Co interface thereby reducing the mobility of the carbon atoms at the surface of the diamond particle. Or perhaps the solubility of carbon in the cobalt binder is reduced as a result of the addition of VC, and this reduces the extent of AGG in the PCD.

Figure 5.16 shows the TEM analysis of a coarse grain PCD sample containing 3wt% VC addition. This was previously explained in Section 2.4.2.3. The mixed carbide deposit can be clearly seen at the diamond/Co interface. Furthermore, vanadium atoms are present in the cobalt binder, therefore it is likely that these atoms segregate at the diamond/Co interface thereby influencing grain growth.

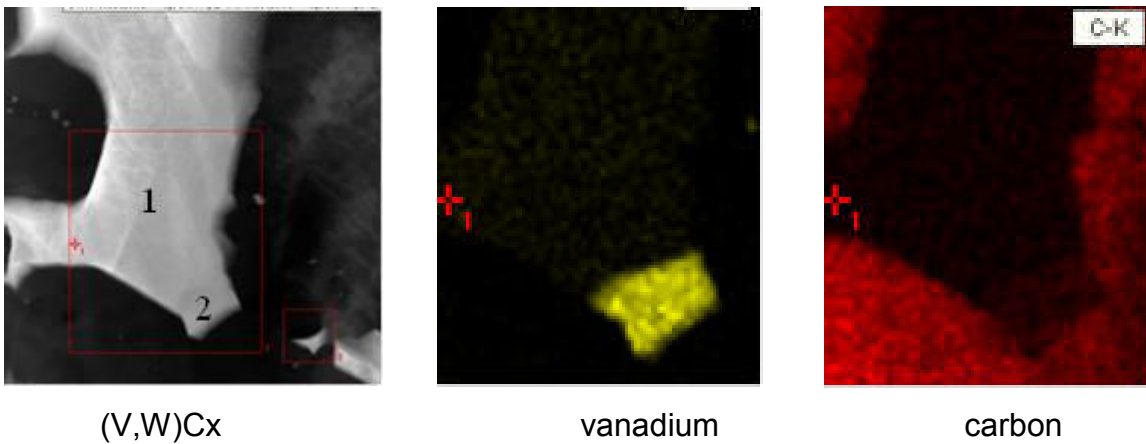


(a)

(b)

(c)

**Figure 5.15: AGG comparison of: (a) Std PCD, (b) VC doped PCD and (c)  $\text{Cr}_3\text{C}_2$  doped PCD**



(V,W)Cx

vanadium

carbon

**Figure 5.16: TEM analysis of the 3wt% VC addition to coarse grain PCD**

Weidow et al. [113] state that chromium lowers the magnetic saturation of the binder phase and in so doing, the carbon activity was found to be higher in the WC-Co material. A material with a higher carbon activity is generally known to have a larger WC coarsening rate during sintering which then results in a larger grain size [126] [127] [128]. It is also known that the WC grain size increases with an increase in the carbon addition [129].

Based on the conclusions drawn by fellow researchers on the increase in carbon activity and WC coarsening rate when  $\text{Cr}_3\text{C}_2$  is added to WC-Co, it can be assumed that the similar phenomenon occurs in PCD, i.e. the presence of chromium increases the carbon activity in the binder phase of the PCD during sintering thus promoting grain growth.

## 5.5 Conclusion

Vanadium carbide and chromium carbide are widely used in the sintering of WC-Co materials to control the extent of grain growth. In this study, the effect of these dopants on the sintering of fine grain PCD was assessed. The additives were admixed into the diamond powder (grain size of 0.5  $\mu\text{m}$ ) prior to sintering at 1400  $^{\circ}\text{C}$  and 6.8 GPa.

Optical images of the standard sintered PCD showed abnormal grain growth at the WC-Co/Diamond interface and at the region next to the canister material. Normal grain growth was present in the bulk of the PCD. The addition of VC to the PCD slightly reduced the extent of AGG whereas the addition of  $\text{Cr}_3\text{C}_2$  to the PCD significantly exaggerated AGG grain growth within the PCD.

The grain size of the AGG in the standard PCD ranged from 100-400  $\mu\text{m}$  (AGG region of 250-300  $\mu\text{m}$ ), the VC doped PCD showed an AGG size of 100-200  $\mu\text{m}$  (AGG region of 250-300  $\mu\text{m}$ ) and the  $\text{Cr}_3\text{C}_2$  doped PCD showed an AGG size of 100-250  $\mu\text{m}$  (AGG region of 650-700  $\mu\text{m}$ ).

It is assumed that the slight reduction of AGG in the VC doped PCD is due to the segregation of the vanadium to the diamond/Co interface thereby reducing the mobility of the carbon atoms at the surface of the diamond particle. Or perhaps the solubility of carbon in the cobalt binder is reduced as a result of the addition of VC, and this reduces the extent of AGG in the PCD. It was previously mentioned and shown that VC enhanced PCD exhibited superior performance to the standard PCD. It is therefore expected that the performance of the PCD containing VC in the fine grain material would be superior in terms of both abrasion resistance and impact resistance due to the reduced amount of AGG.

The exaggerated AGG present in the  $\text{Cr}_3\text{C}_2$  doped PCD is likely due to the increase in the carbon activity in the PCD.

## 5.6 Recommendations

It is recommended that further work be done to investigate the effect of  $\text{Cr}_3\text{C}_2$  additions to PCD on the carbon activity of the PCD.

In this study, both the VC and  $\text{Cr}_3\text{C}_2$  were admixed into the diamond powder prior to sintering of the PCD, and the resultant PCD microstructure was found to be inhomogeneous with frequent deposits of large binder pools, clustered fine diamond grains and large (V,W) $\text{C}_x$  deposits.

It would be more preferable if the carbide additive was coated onto the diamond particle using a technique such as sol gel in order to enhance the homogeneity of the sintered PCD. Coating of the dopant onto the individual diamond grain would produce a finer grain size of the dopants and more effective interaction of the dopants with the cobalt binder and diamond grains. This may results in a more effective control of grain growth.



## CHAPTER SIX

### CONCLUSIONS AND RECOMMENDATIONS

#### 6.1 Summary and Conclusions

Vanadium carbide is used extensively in the carbide industry to control the grain growth of tungsten carbide particles. In doing so, the properties of the tungsten carbide tool is enhanced especially the hardness and wear resistance of the material. Based on the results observed in the carbide industry, it was decided to use vanadium carbide as an additive in PCD.

Different methods of addition of vanadium carbide were investigated such as infiltration of vanadium carbide into the diamond layer using a vanadium carbide powder bed, infiltration of vanadium powder into the diamond layer, and admixing of the vanadium carbide powder with the diamond powder. Both the infiltration methods resulted in inadequate sintering of the PCD and this was primarily due to insufficient cobalt binder being infiltrated into the diamond layer to promote sintering. The cobalt binder shim was placed beneath the vanadium carbide powder bed and the aim was for the cobalt to carry the vanadium carbide into the diamond layer as it diffused through. Hence, the vanadium carbide was admixed into the diamond powder at various concentration levels.

The 1wt% vanadium carbide admix showed the formation of a  $C_2VW$  mixed carbide (according to the ICSD XRD database) with the presence of tungsten carbide particles clearly visible in the PCD. The 3wt% and 5wt% vanadium carbide additive showed a major reduction in the amount of tungsten carbide present in the PCD. In addition, a  $(V,W)C_x$  mixed carbide phase was formed.

Both SEM and TEM analysis were used to determine the microstructure of the vanadium carbide enhanced PCD and the location of the mixed carbide deposits. TEM analysis revealed that the  $(V,W)C_x$  phase deposited at the diamond-binder interface. The stoichiometry of the  $(V,W)C_x$  mixed carbide phase was confirmed using Energy Dispersive X-ray Spectroscopy (EDS) analysis. Molar volume calculations yielded no

increase in volume with the formation of the mixed carbide, hence there was no need for concern regarding the expansion within the PCD table on formation of the (V,W)C<sub>x</sub> phase.

Mechanical testing proved that the vanadium carbide enhanced PCD possesses improved behaviour properties. The sandstone milling test revealed the vanadium carbide enhanced PCD to be more thermally stable with approximately 40% improvement, whilst both the Paarl Granite Turning test and Vertical borer tests showed the PCD to be more wear resistant. The reason for the superior performance of the vanadium carbide enhanced PCD was explained by the precipitation hardening of the (V,W)C<sub>x</sub> phase within the PCD and the segregation of the (V,W)C<sub>x</sub> towards the Co/diamond interface. A patent was filed by Kaveshini Naidoo et al. with the publication number: US2010285335A1 that described the performance improvement of the vanadium carbide enhanced PCD.

Interrupted high temperature and high pressure runs were performed in order to determine the formation temperature of the mixed carbide. The runs were unsuccessful due to inadequate sintering of the diamond powder, and the resultant compacts could not be further analysed. A powder mix containing vanadium carbide, tungsten carbide and diamond was therefore heat treated in a tube furnace at three different temperatures, namely 1200 °C, 1300 °C and 1400 °C to determine the optimum formation temperature of the (V,W)C<sub>x</sub> mixed carbide phase. Results indicated that as the temperature increased, the quantity of the mixed carbide phase also increased.

The stability of the (V,W)C<sub>x</sub> mixed carbide phase was also investigated using hot stage X-ray Diffraction (XRD), and was found to be stable up to the temperature investigated, i.e. 1100 °C. This finding implies that the presence of the mixed carbide would not be compromised at high temperatures during tool use but would continue to enhance the performance of the PCD. In addition, the vanadium carbide enhanced PCD showed a reduced amount of graphite being formed during hot stage XRD analysis. This suggests that the vanadium carbide enhanced PCD would be more thermally stable during tool use as compared to the conventional PCD.

Since the addition of vanadium carbide to PCD yielded a positive result both in terms of the reduction of the amount of graphite being formed and improved performance, other carbide additives such as molybdenum carbide, chromium carbide and titanium carbide were investigated. Surprisingly, the chromium carbide additive did not react with the tungsten to form a mixed carbide, but rather seemed to have entered into solution with the binder. Hot stage XRD results of the carbide additives showed that the onset of graphitisation to be 950 °C which is similar to the vanadium carbide enhanced PCD.

It was shown on numerous occasions that the addition of titanium carbide to the vanadium carbide enhanced the properties of the tungsten carbide tool by controlling the grain growth of the vanadium carbide particle. The addition of titanium carbide to the vanadium carbide enhanced PCD led to the formation of a proposed mixed (Ti,V,W)C<sub>x</sub> phase. Vertical borer test results showed that the VC–TiC enhanced PCD exhibited superior durability. An additional patent was filed by Kaveshini Naidoo et al. with the publication number: US2015151410A1 that described the performance improvement of the VC-TiC enhanced PCD.

There is a major challenge in the synthesis of fine grained PCD, with a diamond grain size of less than 0.5 µm. It is known that as the grain size of the PCD decreases, the grain growth of diamond particles within the PCD increases. The abnormal grain growth (AGG) normally occurs at the WC-Co/diamond interface or alongside the canister material. Since both vanadium carbide and chromium carbide are effective grain growth inhibitors in the carbide industry, it was decided to use these additives in the sintering of PCD containing a 0.5 µm diamond grain size.

It was found that the addition of vanadium carbide to the PCD slightly reduced the extent of AGG whereas the addition of chromium carbide to the PCD significantly exaggerated AGG within the PCD. The grain size of the AGG in the standard PCD ranged from 100-400 µm (AGG region of 250-300 µm), the VC doped PCD showed an AGG size of 100-200 µm (AGG region of 250-300 µm) and the Cr<sub>3</sub>C<sub>2</sub> doped PCD showed an AGG size of 100-250 µm (AGG region of 650-700 µm). The exaggerated AGG present in the

chromium carbide doped PCD is likely due to the increase in the carbon activity in the PCD.

## 6.2 Recommendations

Although various concentrations of vanadium carbide were investigated, it is recommended that the performance of the PCD doped with different quantities of vanadium carbide be investigated in order to establish what the optimum VC dopant concentration regime is. It is also recommended that ab initio calculations be done prior to the concentration study.

A heat treatment study was performed using 3wt% vanadium carbide additions to PCD. The temperatures investigated were 1200 °C, 1300 °C and 1400 °C. It is recommended that heat treatment experiments of the diamond powder containing 3wt% VC be broadened to include the formation temperature of the (V,W)C<sub>x</sub> phase.

The thesis predominantly focussed on the addition of vanadium carbide to PCD. Although the addition of other carbides such as molybdenum carbide, chromium carbide and titanium carbide were investigated, insufficient work was performed. It is hence recommended that additional work be done to qualify the behavioural performance of the PCD containing different carbide additives and a comparison made as to which carbide additive displays the highest performance.

Very interesting findings were made regarding the effect of vanadium carbide and chromium carbide on the abnormal grain growth of PCD. It is recommended that further work be done to investigate the effect of chromium carbide additions to PCD on the carbon activity of the PCD. The method of addition of the carbide additive to the 0.5 µm diamond grain size powder was inadequate, as it led to large carbide deposits within the PCD. These carbide deposits would act as major flaws in the PCD and would most definitely negatively affect the performance of the PCD. Other methods of addition such as sol gel coating of the additive onto the diamond particle should also be investigated.

In addition, the performance of the fine grain PCD containing the carbide additives should be investigated.

## REFERENCES

- [1] G.H.Citel, "Cutting tool materials for high performance machining," *Industrial Diamond Review*, vol. 4, pp. 107-111, 1996.
- [2] I.E. Glark and P.A. Bex, "The use of PCD for petroleum and mining drilling," *Journal of Industrial Diamond Review*, vol. 1, pp. 43-49, 1999.
- [3] C. Suryanarayana, J.J. Moore and R. P. Radtke, "Novel methods of brazing dissimilar materials," *Advanced Materials & Processes*, vol. 3, pp. 29-31, 2001.
- [4] Halliburton, "Polycrystalline-Diamond-Compact (PDC) Bits Drill Out Casing-Float Equipment," [Online]. Available: [http://www.halliburton.com/public/cem/contents/papers\\_and\\_articles/web/h/h05105\\_wp.pdf](http://www.halliburton.com/public/cem/contents/papers_and_articles/web/h/h05105_wp.pdf). [Accessed 24 March 2015].
- [5] Varel, "Roller Cone Bits," [Online]. Available: <http://www.varelintl.com/content/documents/Roller%20Cone%20Catalog%202012.pdf>. [Accessed 24 March 2015].
- [6] F. Bellin, "The current state of PDC bit technology Part 1 of 3: Development and application of polycrystalline diamond compact bits have overcome complex challenges from the difficulty of reliably mounting PDC cutters in bit bodies to accelerated thermal wear," *World Oil*, vol. 1, no. 9, pp. 41-46, 2010.
- [7] D. E. Scott, "The history and impact of synthetic diamond cutters and diamond enhanced inserts on the oil and gas industry," *1st international industrial diamond conference, Barcelona, Spain*, pp. 20-21, Oct 2005.
- [8] Oil & Gas Journal, "Roller Cones vs. Diamonds: A Reversal of Roles," 2006. [Online]. Available: <http://www.ogj.com/articles/print/volume-104/issue-7/supplement-to-oil-gas-journal/advances-in-drill-bit-technology/roller-cones-vs-diamonds-a-reversal-of-roles.html>. [Accessed 25 March 2015].
- [9] F. P. Bundy, *Mater. Res. Soc. Symp.*, vol. 19, p. 383, 1995.
- [10] R. Nilen, *Phase diagram for Diamond Synthesis*, 2010.
- [11] Tai, C.M. Sung and M. Fong, "Reactivities of transition metals with carbon: Implications to the mechanism of diamond synthesis under high pressure,"

- Internation Journal of Refractory Metals & Hard Materials*, vol. 15, pp. 237-256, 1997.
- [12] S.M. Ozbayraktar, A.H. Ras and K. Naidoo, "The role of superhard materials in the efficient use of energy," Verona, Italy, 2008.
- [13] R.H. Rocco and W.A. Wentorf, "Diamond Tool Machining". USA Patent US Patent 3745623, 1973.
- [14] Element Six, "PCD precision cutting tool materials," [Online]. Available: [http://www.e6.com/wps/wcm/connect/E6\\_Content\\_EN/Home/Materials+and+products/Synthetic+Polycrystalline+Diamond+%28PCD%29//pcd+precision+cutting+tool+materials](http://www.e6.com/wps/wcm/connect/E6_Content_EN/Home/Materials+and+products/Synthetic+Polycrystalline+Diamond+%28PCD%29//pcd+precision+cutting+tool+materials). [Accessed 24 March 2015].
- [15] M. Yahiaouia, L. Gerbaudb, J.Y. Parisa, J. Denapea and A. Dourfayec, "A study on PDC drill bits quality," *Wear*, vol. 298, pp. 32-41, 2012.
- [16] R Bodkin, *Site visit to West Texas*, Texas, 2006.
- [17] Element Six, "Synthetic diamond to increase ROP, tool life and profitability in Oil & Gas," [Online]. Available: [http://www.e6.com/wps/wcm/connect/E6\\_Content\\_EN/Home/Applications/Drilling+cushing+sawing+and+milling/Oil+and+gas+drilling/](http://www.e6.com/wps/wcm/connect/E6_Content_EN/Home/Applications/Drilling+cushing+sawing+and+milling/Oil+and+gas+drilling/). [Accessed 24 March 2015].
- [18] R.H. Wentorf, R.C. De Vries and F.P. Bundy, "Sintered superhard materials," *Science*, no. 208, pp. 873-80, 1980.
- [19] L.E. Hibbs, Jr. and R.H. Wentorf, "Borazon and diamond compact tools," *High temp – high pressures*, vol. 6, pp. 409-13, 1974.
- [20] K. Nikolova, *Drilling efficiency and Stability Comparison Between Tricone, PDC and Kymera Drill Bits*, University of Stavange, MSc Thesis, 2014.
- [21] V. Astakhov, *Drills - Science and Technology of advanced Operations*, Taylor and Francis Group, 2014.
- [22] T. Biggs, "The band structure of blue and yellow diamonds," [Online]. Available: <http://www.webexhibits.org/causesofcolor/11A0.html>. [Accessed 31 March 2015].
- [23] J. E. Field, *The Properties of Natural and Synthetic Diamond*, New York: Academic Press Ltd, 1992.
- [24] R. M. German, *Sintering Theory and Practice*, 1 ed., Wiley-Interscience, 1996.

- [25] M. Akhaishi, H. Kanda, Y. Sato, N. Setaka, T. Ohsawa and O. Fukunaga, "Sintering behaviour of the diamond-cobalt system at high temperature and pressure," *Journal of Materials Science*, vol. 17, p. 193 – 198, 2005.
- [26] Y. Zhang, "High pressure and high temperature sintering of fine-grained," *High Pressure Research*, vol. 29, no. 2, pp. 325-334, 2009.
- [27] R.L. Ladi, C.E. Wells, B.K. Kataria and S.W. Almond, "Chemical agents for leaching polycrystalline diamond elements". United States Patent US2012/0152064, 2012.
- [28] T. Nakai and S.I. Yazu, "Diamond sintered body for tools and method of manufacturing same". USA Patent US4636253 A, 1987.
- [29] P. Harold, Bovenkerk and P. D. Gigl, "High pressure bonding of diamond or boron nitride with sintering aid, leaching, porosity". USA Patent US4288248 A, 1981.
- [30] K. Davis, R. Frazier and J. Fischer, "Sonochemical leaching of polycrystalline diamond". USA Patent US20070169419 A1, 2007.
- [31] K. Naidoo, J.H. Liversage, D.E. Scott, H.S.L. Sithebe, B.A. Kaiser and M.L. Fish, "Polycrystalline diamond element". USA Patent US20120061149 A1, 2012.
- [32] K. Naidoo, J.H. Liversage, D.E. Scott, H.S.L. Sithebe, B.A. Kaiser and M.L. Fish, "Polycrystalline diamond element". USA Patent US20120055717 A1, 2012.
- [33] K. Naidoo, G.J. Davies and J.L. Myburgh, "Method of making polycrystalline diamond material". USA Patent US20130291443 A1, 2013.
- [34] C.S. Montross and K. Naidoo, "Polycrystalline diamond material". USA Patent US20130326963 A1, 2013.
- [35] K. Naidoo, "Polycrystalline diamond material". USA Patent US20130333300 A1, 2013.
- [36] W. Hong-tao and Z. Shi, "Study on mechanism of thermal damage on PCD compacts induced by induction heating," *Materials Science and Technology*, vol. 13, no. 5, 2005.
- [37] R. C. Weast, Handbook of Chemistry and Physics, 52 ed., Ohio: The Chemical Rubber Co., 1972.
- [38] L. Toth, Transition Metal Carbides and Nitrides, New York: Academic Press, 1971.
- [39] Massachusetts Institute of Technology, "Material Properties," [Online]. Available:



<http://web.mit.edu/course/3/3.11/www/modules/props.html>. [Accessed 8 May 2015 May 2015].

- [40] A.N. Popandopula and A.N. Gerashchenko, "Carbide phase and red hardness of cast-high vanadium tungsten-molybdenum high-speed steel," *Metalovedenie i Termicheskaya Obrabotka Metallov*, vol. 9, pp. 70-71, 1975.
- [41] X. Qi, Z. Jia, Q. Yang and Y. Yang, "Effects of vanadium additive on structure property and tribological performance of high chromium cast iron hardfacing metal," *Surface & Coatings Technology*, 2011.
- [42] X. Qi, Z. Jia, Q. Yang and Y. Yang, "Effect of cerium on the as-cast microstructure of a hypereutectic high chromium cast iron," *Materials Letters*, vol. 62, no. 17, pp. 3024-3027, 2008.
- [43] S.G. RamaRao and A.V. Sapate, "Erosive wear behaviour of weld hardfacing high chromium cast irons: effect of erodent particles," *Tribol. Int.*, vol. 39, p. 206, 2006.
- [44] S. Z Wei, J. H Zhu and L. J Xu, "Research on wear resistance of high speed steel," *Mater. Sci. Eng*, vol. 404, p. 138–145, 2005.
- [45] Y.H. Qu, J.D. Xing and X.H. Zhi, "Effect of vanadium and carbon on microstructure and abrasive wear resistance of high speed steel," *Tribol. Int*, vol. 39, p. 641–648, 2006.
- [46] Y. Li, J.A. Wilson, A.J. Craven, P.S. Mitchell, D.N. Crowther and T.N. Baker, "Dispersion strengthening in vanadium microalloyed steels processed by simulated thin slab casting and direct charging Part 1 – Processing parameters, mechanical properties and microstructure," *Materials Science and Technology*, vol. 23, no. 5, pp. 509-518, 2007.
- [47] K. Liu, *Tungsten Carbide - Processing and Applications*, InTech, 2012.
- [48] J. Weidow, J. Zackrisson, B. Jansson and H. Andrén, "Characterisation of WC-Co with cubic carbide additions," *Int. Journal of Refractory Metals & Hard Materials*, vol. 27, p. 244–248, 2009.
- [49] I. Sugiyama, Y. Mizumukai, T. Taniuchi, K. Okada, F. Shirase, T. Tanase, Y. Ikuhara and T. Yamamoto, "Formation of (W,V)Cx layers at the WC/Co interfaces in the VC-doped WC–Co cemented carbide," *International Journal of Refractory*

- Metals and Hard Materials*, vol. 30, pp. 185-187, 2012.
- [50] N. Al-Aqeeli, "Characterization of nano-cemented carbides Co-doped with vanadium and chromium carbides," *Powder Technology*, vol. 273, p. 47–53, 2015.
- [51] J.M. Kusoffsky and A. Marshall, "Binder phase structure in fine and coarse WC–Co hard metals with Cr and V carbide additions," *International Journal of Refractory Metals and Hard Materials*, vol. 40, pp. 27-35, 2013.
- [52] C. Osborne, L. Cornish and S. Luyckx, "On the preparation of fine  $V_8C_7$ –WC and  $V_4C_3$ –WC powders," *Int J Refract Met Hard Mater*, vol. 15, pp. 163-168, 1997.
- [53] N.G. Hashe, J.H. Neethling, P.R. Berndt, H. Andren and S Norgren, "A comparison of the microstructures of WC–VC, TiC–Co and WC–VC–Co cemented carbides," *Journal of Refractory Metals and Hard Materials*, vol. 25, no. 3, pp. 207-213, 2007.
- [54] N.G. Hashe, S. Norgren, H.O. Andrén, J.H. Neethling and P.R. Berndt, "The influence of sintering in nitrogen gas on the microstructure of a WC–VC–TiC–Co cemented carbide," *Int J Refract Met Hard Mater*, vol. 26, pp. 404-410, 2008.
- [55] N.G. Hashe, J.H. Neethling, H.O. Andrén and P.R. Berndt, "Reduction of carbide grain growth in WC–VC–Co by sintering in nitrogen atmosphere," *Int J Refract Met Hard Mater*, pp. 20-25, 2009.
- [56] N. G Hashe, S. M. Norgren, H. O. Andrén and J. H. Neethling, "Characterization of WC–(W,V)C–Co made from pre-alloyed (W,V)C," *Int. Journal of Refractory Metals & Hard Materials*, vol. 27, pp. 229-233, 2009.
- [57] Y. Wang, E. Pauty, S. Lay and C. H. Allibert, "Microstructure evolution in the cemented carbides WC–Co II. Cumulated effects of Cr additions and of the C/W ratio on the crystal features of the WC grains," *Phys Status Solidi*, vol. 193, pp. 284-293, 2002.
- [58] H.R. Lee, D.J. Kim, N.M. Hwang and D.Y. Kim, "Role of vanadium carbide additive during sintering of WC–Co: mechanism of grain growth inhibition," *J Am Ceram Soc*, vol. 86, no. 1, pp. 152-154, 2003.
- [59] E.A. Brandes and G.B. Brook, *Smithells Metals Reference Book*, 1949.
- [60] L. Ramqvist, "Wetting of metallic carbides by liquid copper, nickel, cobalt and iron," *International Journal of Powder Metallurgy*, vol. 1, no. 4, 1965.

- [61] T. B. Massalski, Binary Alloy Phase Diagrams, 2nd Ed ed., Ohio: ASM International, 1990.
- [62] A. V. Andreyev, "The wetting and bonding of diamond films by high melting point metals in the range of diamond thermodynamic stability," *Diamond and Related Materials*, vol. 3, pp. 1262-1264, 1994.
- [63] "Fill 3D Orbitals," [Online]. Available: [https://www.google.co.za/search?q=copper+d+orbitals&biw=1194&bih=759&tbm=isch&tbo=u&source=univ&sa=X&ei=dbqjVYKvO\\_GU7Qbdg5DoDQ&ved=0CCgQsAQ&dpr=0.95#tbn=isch&q=titanium+d+orbitals&imgsrc=zTCuhgxVhl\\_qbM%3A](https://www.google.co.za/search?q=copper+d+orbitals&biw=1194&bih=759&tbm=isch&tbo=u&source=univ&sa=X&ei=dbqjVYKvO_GU7Qbdg5DoDQ&ved=0CCgQsAQ&dpr=0.95#tbn=isch&q=titanium+d+orbitals&imgsrc=zTCuhgxVhl_qbM%3A). [Accessed 13 July 2015].
- [64] J.E. Westraadt, N. Dubrovinskaia, J.H. Neethling, L. Sigalas, "Thermally stable polycrystalline diamond sintered with calcium carbonate," *Diamond and related materials*, vol. 16, pp. 1929 - 1935, 2007.
- [65] Tool Dynamics, "The application of Vanadium Carbide," [Online]. Available: <http://www.tool-dynamics.com/literature/papers/000.php>. [Accessed 12 July 2015].
- [66] Wikipedia, "Hardness of the elements," [Online]. Available: [http://en.wikipedia.org/wiki/Hardnesses\\_of\\_the\\_elements\\_\(data\\_page\)](http://en.wikipedia.org/wiki/Hardnesses_of_the_elements_(data_page)). [Accessed 9 May 2015].
- [67] Ted Pella Inc., "Microscopy Products for Science and Industry," [Online]. Available: [https://www.tedpella.com/company\\_html/hardness.htm](https://www.tedpella.com/company_html/hardness.htm). [Accessed 9 May 2015].
- [68] J.Y. Huang, Y.K. Wu, and H.Q. Ye, "Phase transformation of cobalt induced by ball milling," *Appl. Phys. Lett.*, vol. 3, no. 16, pp. 308-310, 1995.
- [69] A. Guillermet, "Critical Evaluation of the Thermodynamic Properties of Cobalt," *International Journal of Thermophysics*, vol. 8, no. 4, pp. 481-510, 1987.
- [70] X.H. Qu, J.X. Gao, M.L. Qin and C.M. Lei, "Application of a wax-based binder in PIM of WC–TiC–Co cemented carbides," *Int J Refract Met Hard Mater*, vol. 23, pp. 273-277, 2005.
- [71] K. Bonny, P. de Baets, J. Vleugels, S. Haung, O. van der Biest and B. Lauwers, "Impact of Cr<sub>3</sub>C<sub>2</sub>/VC addition on the dry sliding friction and wear response of WC-Co cemented carbides," *Wear*, vol. 267, pp. 1642-1652, 2009.

- [72] F. Arenas, I.B. de Arenas, J. Ochoa and S.A. Cho, "Influence of VC on the microstructure and mechanical properties of WC±Co sintered cemented carbides," *International Journal of Refractory Metals & Hard Materials*, vol. 17, pp. 91-97, 1999.
- [73] A.M. Soleimanpour, P. Abachi and A. Simchi, "Microstructure and mechanical properties of WC–10Co cemented carbide containing VC or (Ta, Nb)C and fracture toughness evaluation using different models," *International Journal of Refractory Metals and Hard Materials*, vol. 31, pp. 141-146, 2012.
- [74] R.M. German, *Liquid Phase Sintering*, Springer Science & Business Media, 2013.
- [75] Y. Jin, B. Huang, C. Liu and Q. Fu, "Phase evolution in the synthesis of WC–Co–Cr<sub>3</sub>C<sub>2</sub>–VC nanocomposite powders from precursors," *International Journal of Refractory Metals and Hard Materials*, vol. 41, pp. 169-173, 2013.
- [76] A. Can, E.M. Mochubele, J.G. Davies and J.L. Myburgh, "Coated abrasive materials and method of manufacture". South Africa Patent AU2012202109, 3 May 2012.
- [77] K. H. Wong, "X-ray diffraction," [Online]. Available: <http://ap.polyu.edu.hk/apakhwon/Lecture%2001%20-%20X-ray%20Diffraction.pdf>. [Accessed 10 November 2013 November 2013].
- [78] K. Majumdar, "Theory of X-ray Diffraction," [Online]. Available: [http://faculty.gvsu.edu/majumdak/public\\_html/OnlineMaterials/XRay.pdf](http://faculty.gvsu.edu/majumdak/public_html/OnlineMaterials/XRay.pdf). [Accessed 10 November 2013 November 2013].
- [79] ASDL, "Introduction to X-ray Diffraction (XRD)," [Online]. Available: [http://www.asdlib.org/onlineArticles/ecourseware/Bullen\\_XRD/LearningActivity\\_Diffraction\\_BraggsLaw.pdf](http://www.asdlib.org/onlineArticles/ecourseware/Bullen_XRD/LearningActivity_Diffraction_BraggsLaw.pdf). [Accessed 16 November 2013 November 2013].
- [80] D. Goodhew and P.J. Chescoe, *The Operation of Transmission and Scanning Electron Microscopes*, 1 ed., Oxford University Press, 1990.
- [81] Riverside, University of California, "Introduction to Energy Dispersive X-ray Spectrometry (EDS)," [Online]. Available: <http://micron.ucr.edu/public/manuals/EDS-intro.pdf>. [Accessed 23 November 2013 November 2013].
- [82] Malvern, "Laser Diffraction Particle Sizing," [Online]. Available:

- [http://www.malvern.com/labeng/technology/laser\\_diffraction/particle\\_sizing.htm](http://www.malvern.com/labeng/technology/laser_diffraction/particle_sizing.htm).  
[Accessed 17 November 2013 November 2013].
- [83] L. Salvo, P. Cloetens and E. Maire, "X-ray micro-tomography an attractive characterisation technique in materials science," France, 2003.
- [84] H. Proudhon, "Using X-ray micro-tomography," [Online]. Available: [http://mms2.ensmp.fr/tribo\\_paris/lectures/wemesurf\\_tomo\\_seminar\\_handouts.pdf](http://mms2.ensmp.fr/tribo_paris/lectures/wemesurf_tomo_seminar_handouts.pdf).  
[Accessed 30 November 2013 November 2013].
- [85] C. J. Barrett, "Nanotechnology: A Brief Overview," [Online]. Available: <http://barrett-group.mcgill.ca/tutorials/nanotechnology/nano02.htm>. [Accessed 30 November 2013 November 2013].
- [86] F. Hofer, "The principles of TEM," [Online]. Available: <http://portal.tugraz.at/portal/page/portal/felmi/research/TEM%20and%20Nanoanalysis/Principles%20of%20TEM>. [Accessed 30 November 2013 November 2013].
- [87] L. Salvo, P. Cloetens and E. Maire, "On the contiguity of carbide phase in WC–Co hardmetals," *International Journal of Refractory Metals & Hard Materials*, vol. 21, p. 241–244, 2003.
- [88] About.com Chemistry, "Tungsten or Wolfram Facts," [Online]. Available: <http://chemistry.about.com/od/elementfacts/a/tungstenwolfram.htm>. [Accessed 6 December 2013 December 2013].
- [89] ASM International, "ASM Alloy Phase Diagram Database," ASM International, [Online]. Available: [http://www.asminternational.org/home/-/journal\\_content/56/10192/15469013/DATABASE](http://www.asminternational.org/home/-/journal_content/56/10192/15469013/DATABASE). [Accessed 20 March 2017].
- [90] G.A. Roberts, J.C. Hamaker and A.R. Johnson, *Tool Steels*, 3rd Edition, ASM International, 1962.
- [91] WebElements, "Web Elements," [Online]. Available: <http://www.webelements.com/cobalt/physics.html>. [Accessed 6 December 2013 December 2013].
- [92] L.I. Frayman, "Advancements in Cemented Carbide Products & Processing," [Online]. Available: <http://www.generalcarbide.com/PDF/APMI1-8-09.pdf>. [Accessed 6 December 2013 December 2013].

- [93] S. Lay, J. Thibault, S. Hamar-Thibault, "Structure and role of the interfacial layers in VC-rich WC–Co cermets," *Philos Mag*, vol. 83, pp. 1175-1190, 2003.
- [94] W. G. Christensen M M. Christensen and G. Wahnstrom, "Strength and reinforcement of interfaces in cemented carbides," *International Journal of Refractory Metals & Hard Materials*, vol. 24, pp. 80-88, 2006.
- [95] Z. Sun, R. Ahuja and J.E. Lowther, "Mechanical properties of vanadium carbide and a ternary vanadium," *Solid State Communications*, vol. 150, 2010.
- [96] K. Naidoo and H.S.L. Sithebe, "Polycrystalline diamond (PCD materials". United Staes of America Patent 20100285335, 5 May 2008.
- [97] H. J. Citel, "Cutting tool materials for high performance machining," *Industrial Diamond Review*, vol. 1, pp. 17-21, 2001.
- [98] J. Sung, "Graphite to diamond transition underhigh pressure: A kinetics approach," *Journal of Materials Science*, vol. 35, pp. 6041-6054, 2000.
- [99] R.L. Mehan and L.E. Hibbs, "Thermal degradation of sintered diamond compacts," *Journal of Material Science*, vol. 24, pp. 942-950, 1989.
- [100] KnowledgeDoor, "Linear Thermal Expansion Coefficient Navigation," [Online]. Available:  
[http://www.knowledgedoor.com/2/elements\\_handbook/linear\\_thermal\\_expansion\\_coefficient.html](http://www.knowledgedoor.com/2/elements_handbook/linear_thermal_expansion_coefficient.html). [Accessed 2 June 2017].
- [101] Diamond Materials, "Thermal Properties of CVD Diamond," [Online]. Available:  
[http://www.diamond-materials.com/EN/cvd\\_diamond/thermal\\_properties.htm](http://www.diamond-materials.com/EN/cvd_diamond/thermal_properties.htm). [Accessed 2 June 2017].
- [102] B.N. Masina, A.Forbes, O.M. Ndwandwe, G. Hearne, B.W. Mwakikunga and G. Katumba, "Thermally induced defects in a polycrystalline diamond layer on a tungsten carbide substrate," *Physica B: Condensed Matter*, vol. 404, no. 22, pp. 4485-4488, 2009.
- [103] H. R. Lee, D. J. Kim, N. M. Hwang and D. Y. Kim, "Role of vanadium carbide additive during sintering of WC–Co: mechanism of grain growth inhibition," *J Am Ceram Soc*, vol. 86, no. 1, pp. 152-154, 2003.
- [104] T. B. Massalski, "Co-V Phase Diagram," in *Binary Alloy Phase Diagrams*, Ohio,

- ASM International, 1992, pp. 1255-1257.
- [105] J. Weidow and H. Andren, "Grain and phase boundary segregation in WC-Co with small V, Cr or Mn additions," *Acta Materialia*, vol. 10, pp. 3888-3894, 2010.
- [106] S. Luyckx and M. Z. Alli, "Comparison between  $V_8C_7$  and  $Cr_3C_2$  as grain refiners for WC-Co," *Materials and Design*, vol. 22, pp. 507-510, 2001.
- [107] L. Yancong and Y. Jixiang, "Effect of intercrystalline phase of grown PCD to its thermal stability," *DIAMOND & ABRASIVES ENGINEERING*, no. 2, pp. 30-33, 2006.
- [108] S. Middlemiss, "Polycrystalline diamond with improved abrasion resistance". United States Patent US2004/0140132, 2004.
- [109] J. Zackrisson, B. Jansson, G. S. Uphadyaya and H.O. Andren, "WC-Co based cemented carbides with large  $Cr_3C_2$  additions," *International Journal of Refractory Metals & Hard Materials*, vol. 16, pp. 417-422, 1998.
- [110] L. Liu, T. Huang, Y. Xiong, A. Yang, Z. Zhao, R. Zhang and J. Li, "Cast structure and mechanical properties of fine grained superalloy K4169 addition of refiners," *Materials Science and Technology*, vol. 3, pp. 268-274, 1987.
- [111] P. V. Krakhmalev, "Abrasion of ultrafine WC-Co by fine abrasive particles," *Trans. Nonferrous Met. SOC. China*, vol. 17, pp. 1287-1293, 2007.
- [112] I. Lifshitz and V. Slyozov, "The Kinetics of Precipitation from Supersaturated Solid Solutions," *Journal of Physics and Chemistry of Solids*, vol. 19, no. 1, pp. 35-50, 1961.
- [113] J. Weidow, S. Norgren, H.O. Andrén, "Effect of V, Cr and Mn additions on the microstructure of WC-Co," *Int. Journal of Refractory Metals & Hard Materials*, vol. 27, pp. 817-822, 2009.
- [114] A. Jaroenworarluck, T. Yamamoto, Y. Ikuhara and T. Sakuma, "Segregation of vanadium at the WC/Co interface in VC-doped WC-Co," *J. Mater. Res*, vol. 13, no. 9, pp. 2450-2452, 1998.
- [115] Z.Z. Fang, X. Wang, T. Ryu, K.S. Hwanga and H.Y. Sohn, "Synthesis, sintering, and mechanical properties of nanocrystalline cemented tungsten carbide—a review," *International Journal of Refractory Metals*, vol. 27, no. 2, pp. 288-299,

2009.

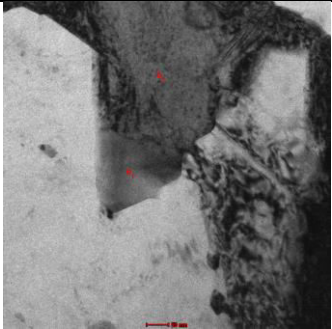
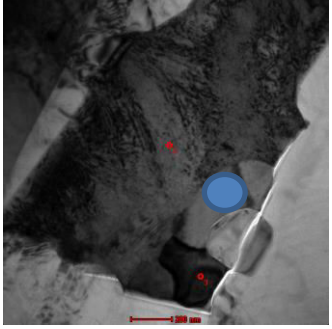
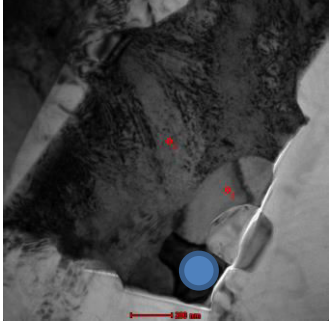
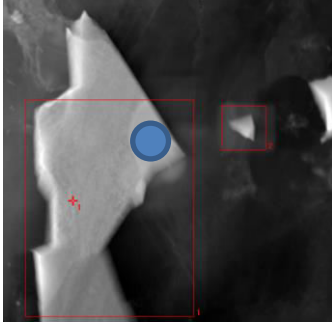

- [116] B.K. Kim, G.H. Ha, G.G Lee and D.W Lee, "Structure and properties of nanophase WC/Co/VC/TaC hardmetal," *Nanostructure Materials*, vol. 9, pp. 233-236, 1997.
- [117] S.G. Huang, R.L. Liu, L. LiL, O Van der Biest and J. Vleugel, "NbC as grain growth inhibitor and carbide in WC–Co hard metals," *Int J Refract Met Hard Mater*, vol. 26, no. 5, pp. 389-395, 2008.
- [118] Z.X. Guo, J. Xiong, M. Yang, X.Y. Song and C.J, Jiang, "Effect of Mo<sub>2</sub>C on the microstructure and properties of WC–TiC–Ni cemented carbide," *Int J Refract Met Hard Mater*, vol. 26, no. 6, pp. 601-605, 2008.
- [119] C.W. Morton, D.J. Wills and K. Stjernberg, "The temperature ranges of maximum effectiveness of grain growth inhibitors in WC alloys," *Int J Refract Met Hard Mater*, vol. 23, pp. 287-293, 2005.
- [120] M. Akaishi, T. Ohsawa and S.Y Amaoka, "Synthesis of Fine-Grained Polycrystalline Diamond Compact and Its Microstructure," *Journal of the American Ceramic Soceity*, vol. 74, no. 1, pp. 5-10, 1991.
- [121] T. Shina, J. Oha, K.H. Ohb and D.N. Leeb, "The mechanism of abnormal grain growth in polycrystalline diamond during high pressure-high temperature sintering," *Diamond and Related Materials*, vol. 13, pp. 488-494, 2004.
- [122] A. McKie, M. Herrmann, I. Sigalas, K. Sempf and R. Nilen, "Suppression of abnormal grain growth in fine grained polycrystalline diamond materials (PCD)," *Int. Journal of Refractory Metals and Hard Materials*, vol. 41, pp. 66-72, 2013.
- [123] A. Azcona, J.M. Ordonez and F.C. Sanchez, "Hot isostatic pressing of ultrafine tungsten carbide-cobalt hardmetals," *Journal of Materials Science* , vol. 37, pp. 4189-4195, 2002.
- [124] Sugiyama, Y. Mizumukai, T. Taniuchi, K. Okada, F. Shirase, T. Tanase, I. Sugiyama and Y. Mizumukai, "Formation of (W,V)C<sub>x</sub> layers at the WC/Co interfaces in the VC-doped WC–Co cemented carbide," *International Journal of Refractory Metals and Hard Materials*, vol. 30, pp. 185-187, 2012.
- [125] G. Gille, B. Szesny and Leitner, "Cemented Carbides and Hard Materials," *14th Int Plansee seminar'97*, vol. 2.



- [126] V. Chabretou, C.H. Allibert and J.M. Missiaen, "Quantitative analysis of the effect of the binder phase composition on grain growth in WC–Co sintered materials," *Journal of Material Science*, vol. 38, pp. 2581-2590, 2003.
- [127] I. Borgh, P. Hedström, A. Borgenstam, J. Ågren and J. Odqvist, "Effect of carbon activity and powder particle size on WC grain coarsening during sintering of cemented carbides," *International Journal of Refractory Metals and Hard Materials*, vol. 42, pp. 30-35, 2014.
- [128] Y. Wang, M. Heusch, S. Lay, C.H. Allibert, "Microstructure evolution in the cemented carbides WC–Co I. Effect of the C/W ratio on the morphology and defects of the WC grains," *Phys Status Solidi A*, vol. 193, pp. 271-283, 2002.
- [129] C. Wei, X. Song, J. Fu, X. Lv, H. Wang, Y. Gao, S. Zhao and X. Liu, "Effect of Carbon Addition on Microstructure and Properties of WC–Co Cemented Carbides," *Journal of Material Science and Technology*, vol. 28, no. 9, pp. 837-843, 2012.

## APPENDIX ONE: EDS QUANTIFICATION OF THE BINDER POOLS USING THE TEM

### EDS 1

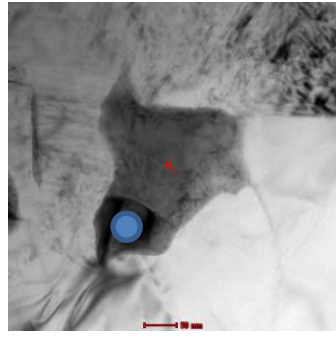
Analysis	Element	Composition (at%)	Image
EDS 1	Carbon	57.64	
	Cobalt	1.51	
	Vanadium	31.65	
	Tungsten	9.20	
EDS 2	Carbon	93.57	
	Cobalt	0.41	
	Vanadium	4.55	
	Tungsten	1.47	
EDS 3	Carbon	88.21	
	Cobalt	0	
	Vanadium	8.61	
	Tungsten	3.18	
EDS 4	Carbon	84.79	
	Cobalt	0.42	
	Vanadium	11.41	
	Tungsten	3.38	
EDS 5	Carbon	87.77	



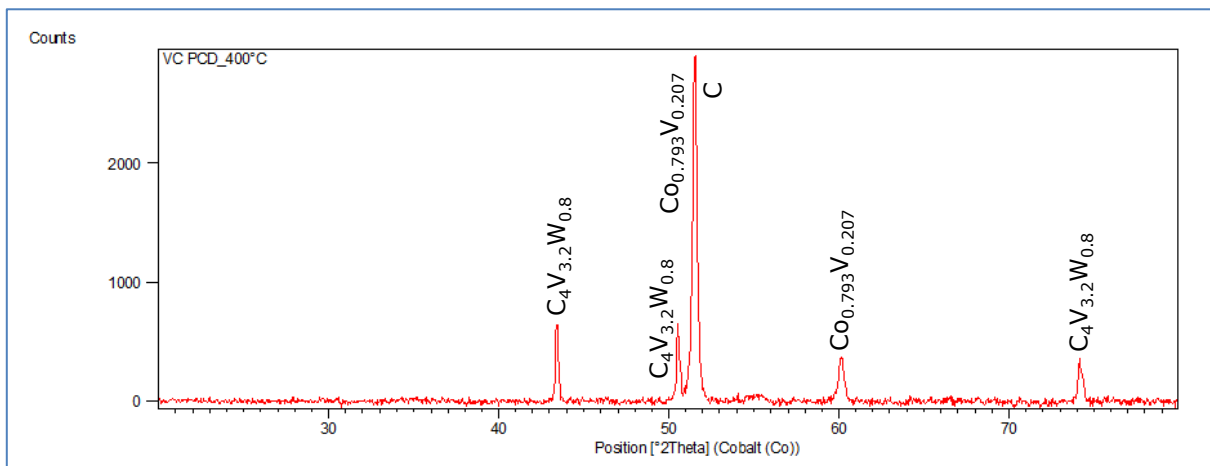
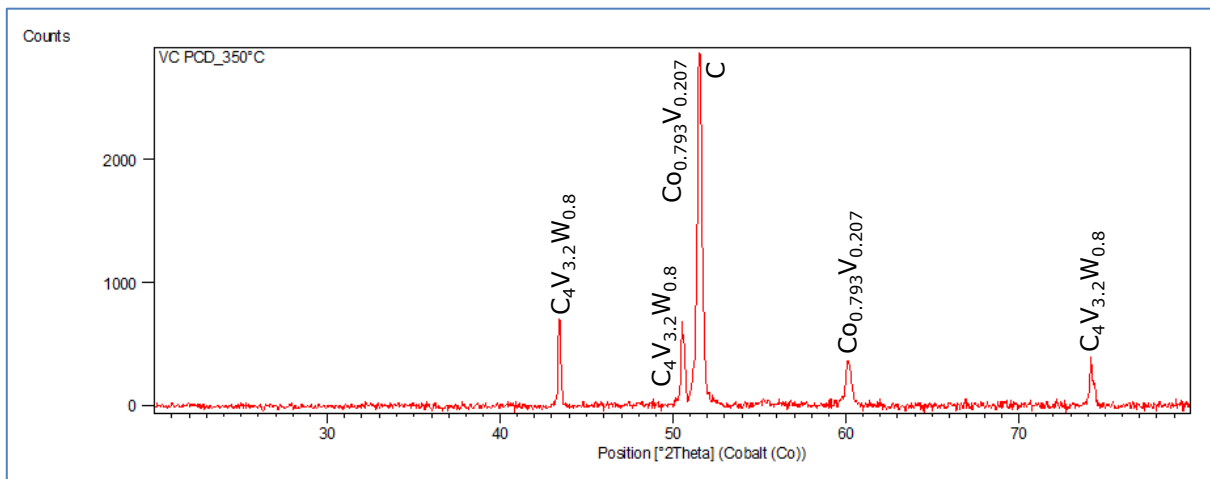
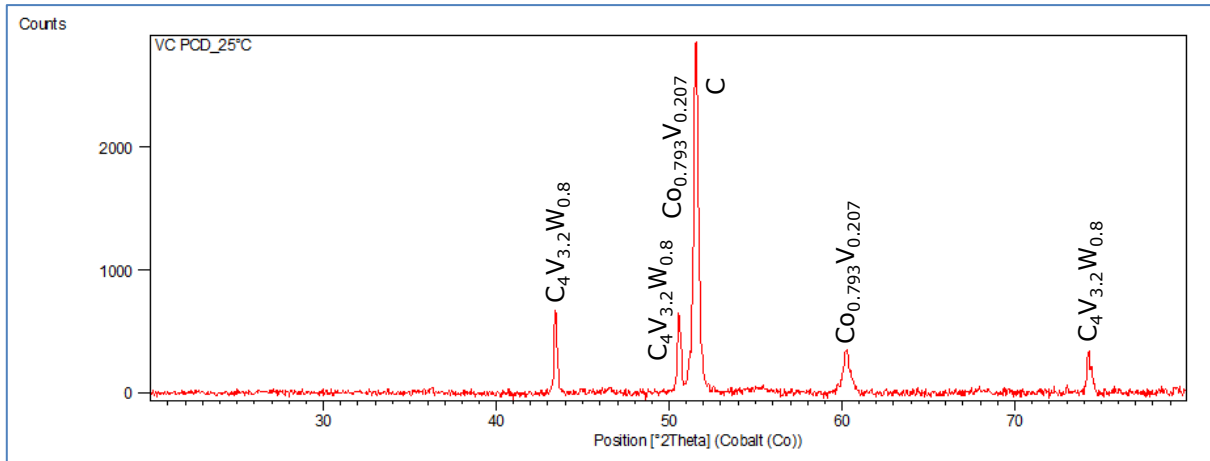
---

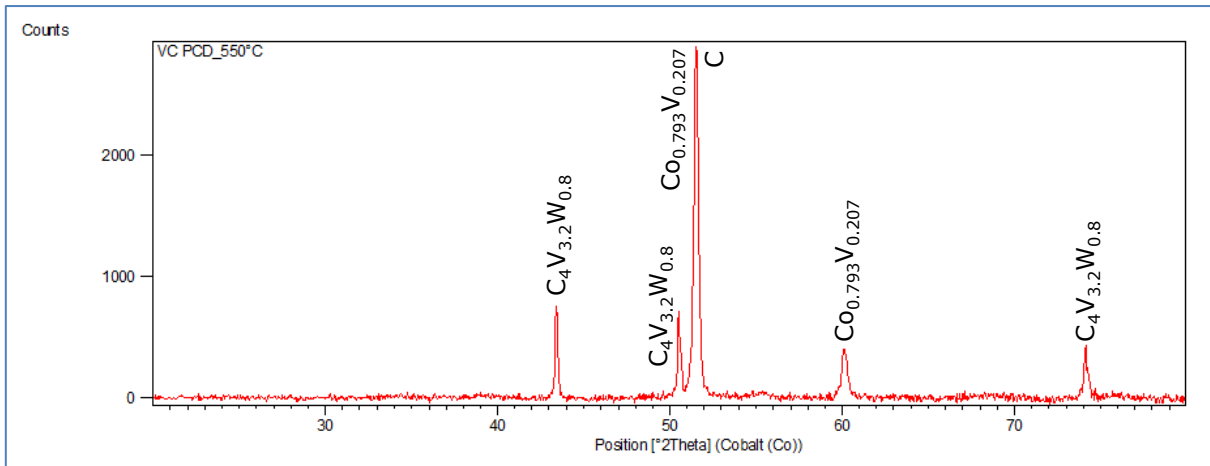
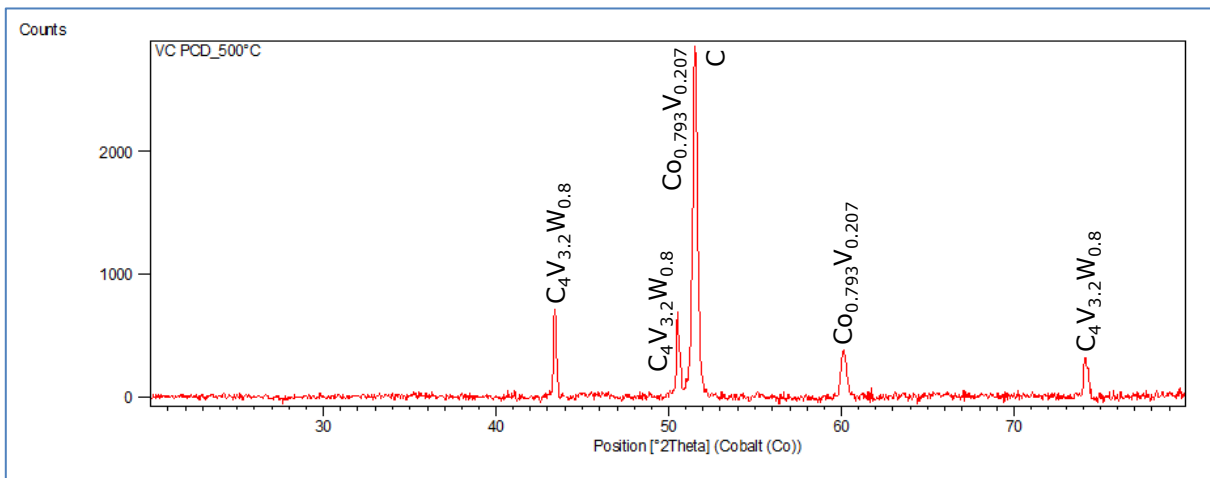
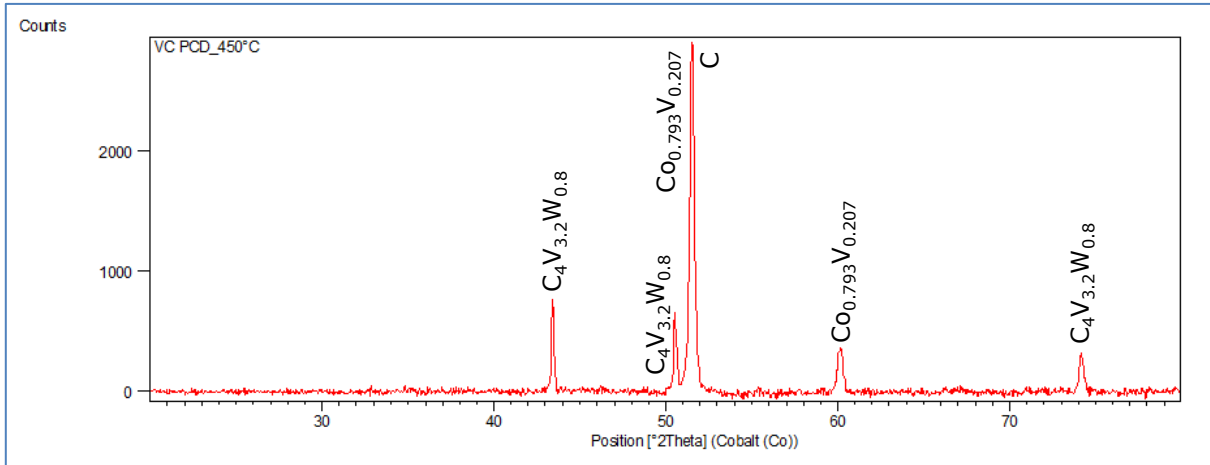
	Cobalt	0.56
	Vanadium	8.87
	Tungsten	2.80
EDS 6	Carbon	89.57
	Cobalt	0
	Vanadium	9.01
	Tungsten	1.42

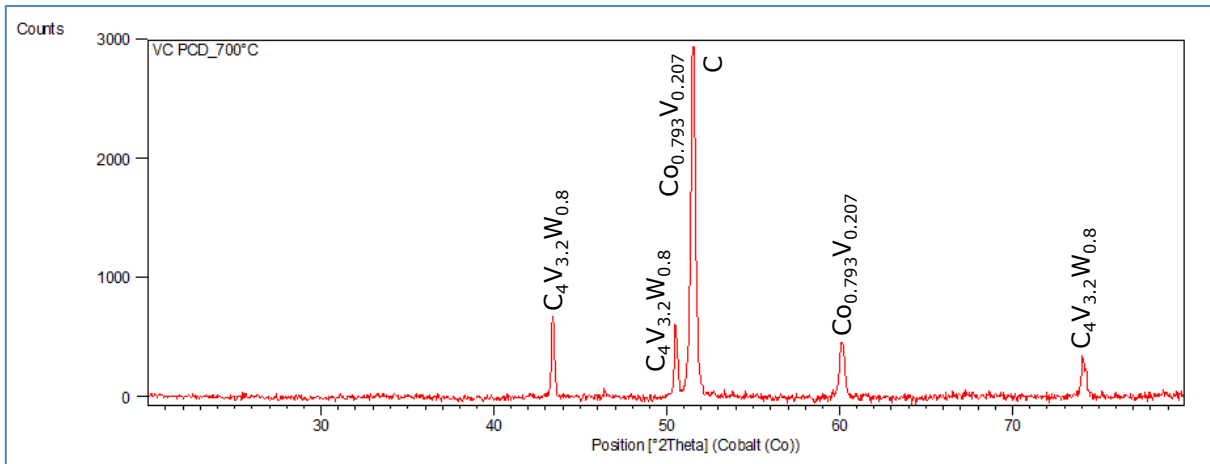
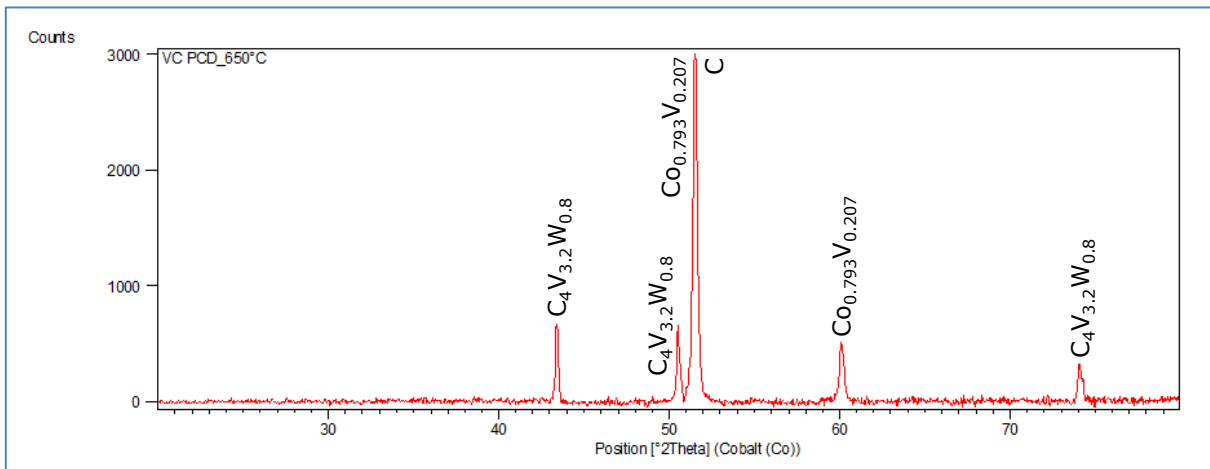
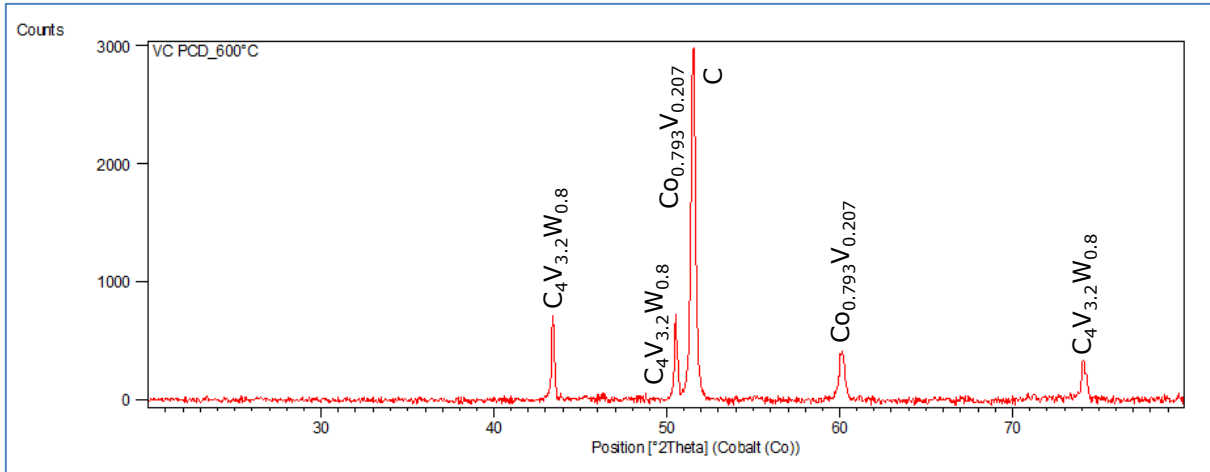
---

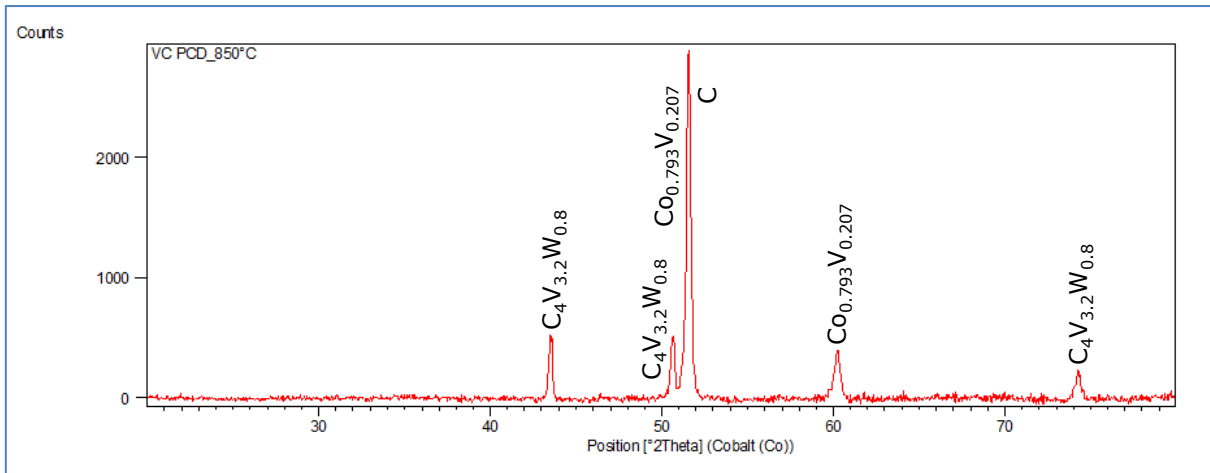
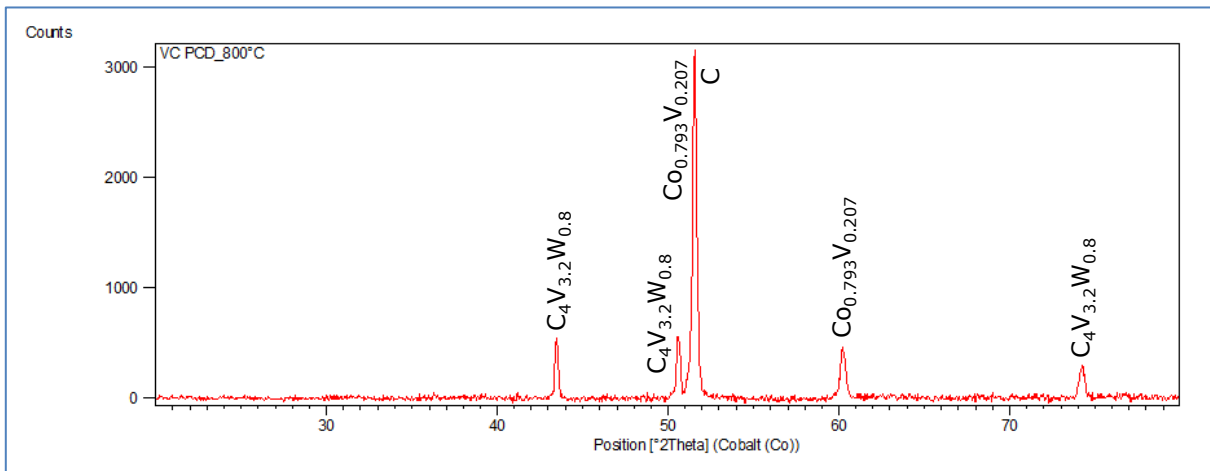
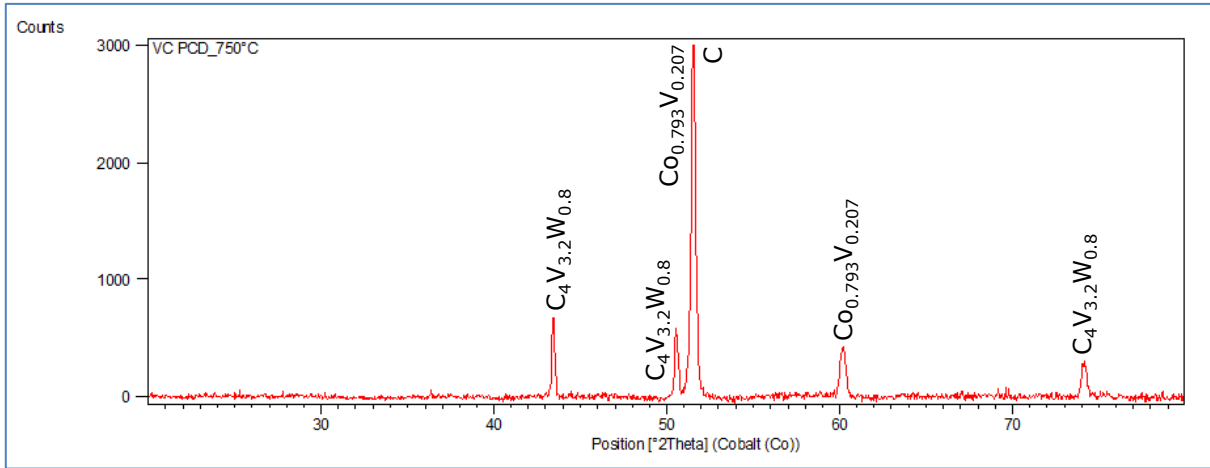


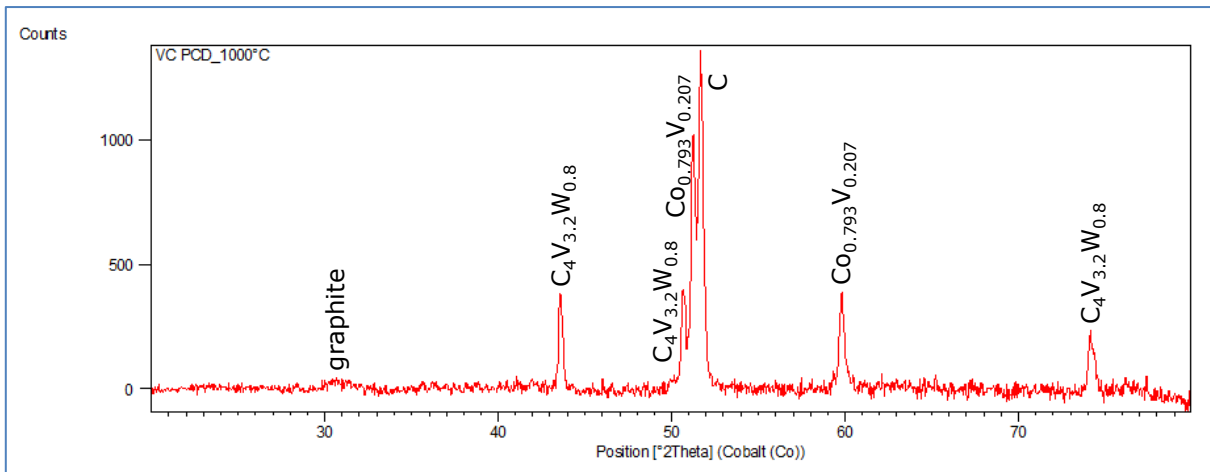
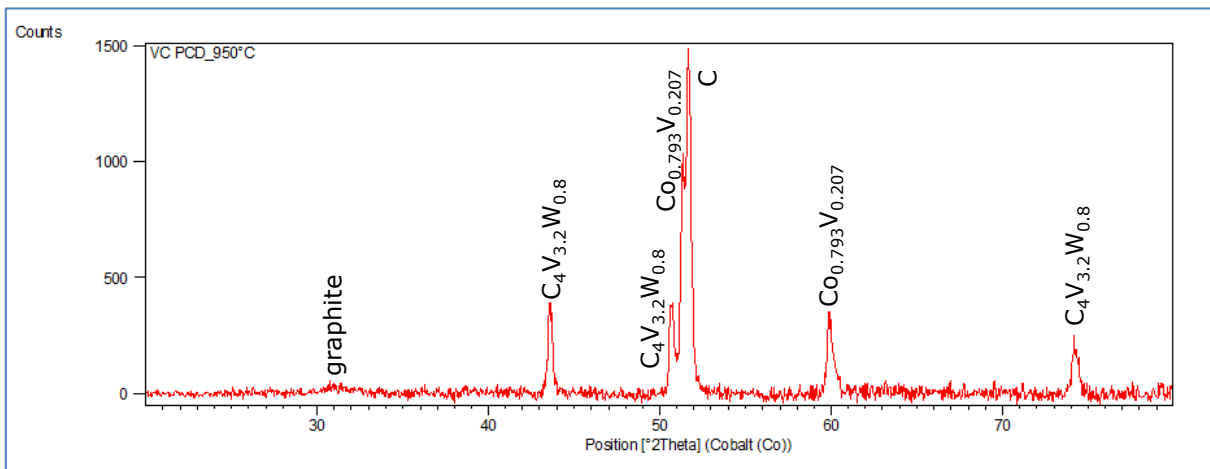
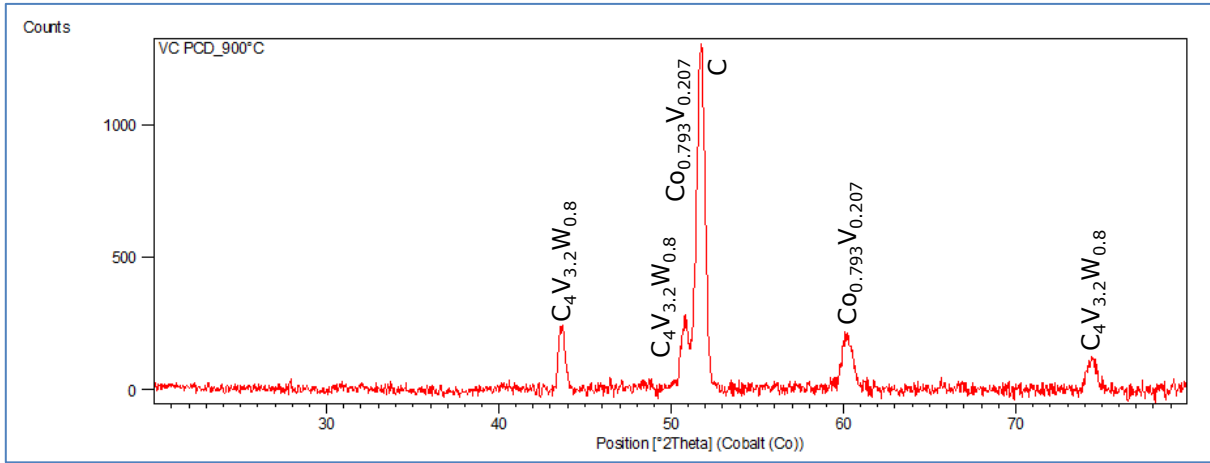
## APPENDIX TWO: HEAT TREATMENT OF VC ENHANCED PCD



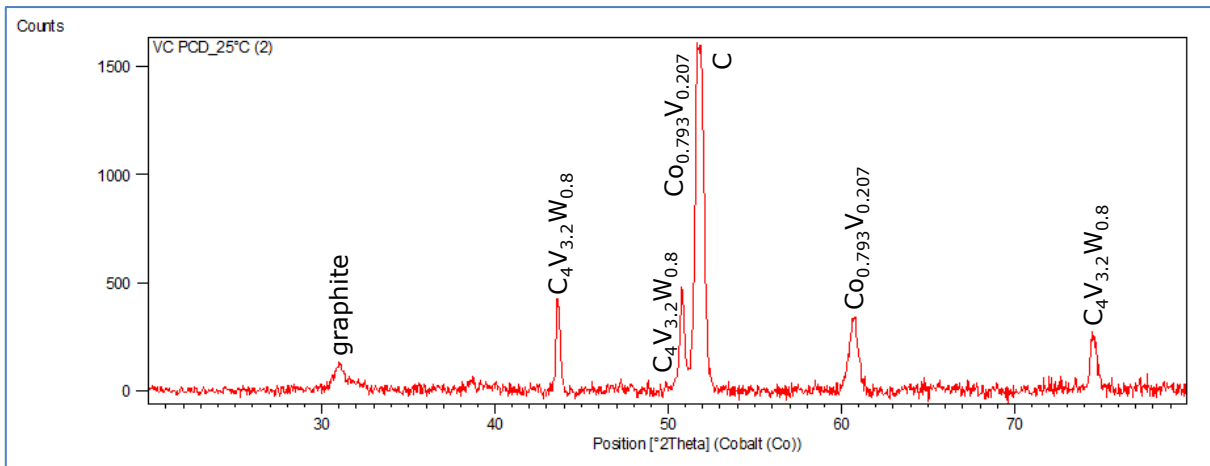
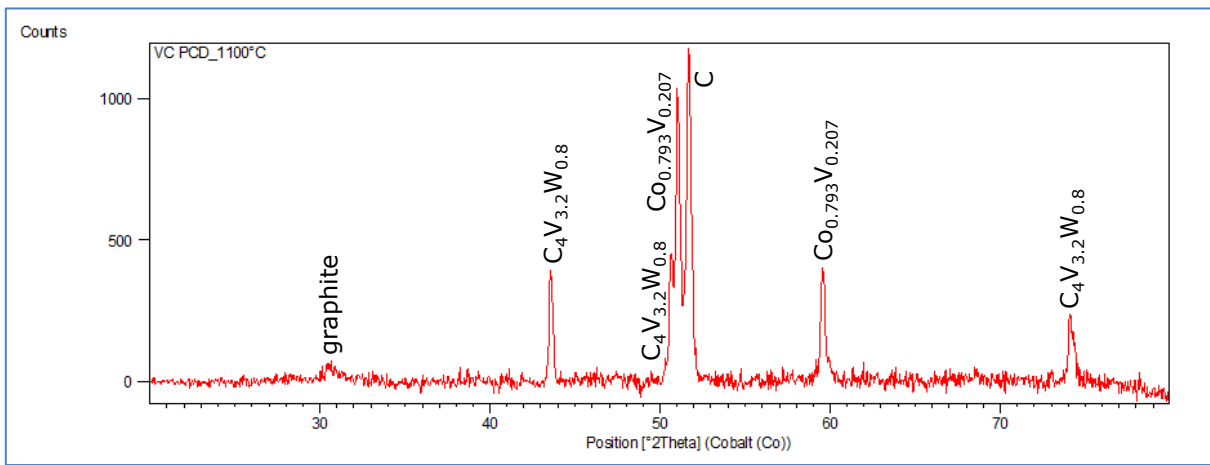
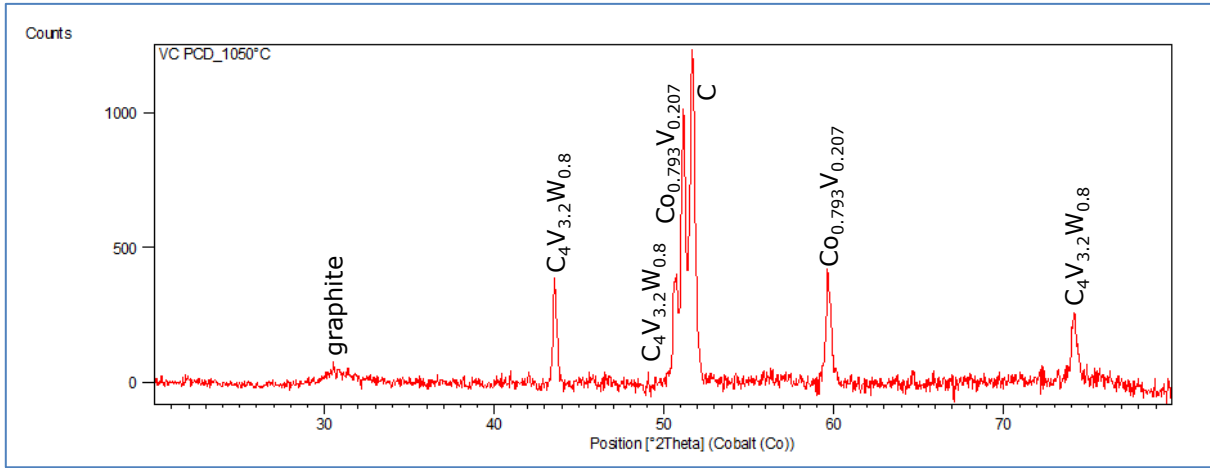




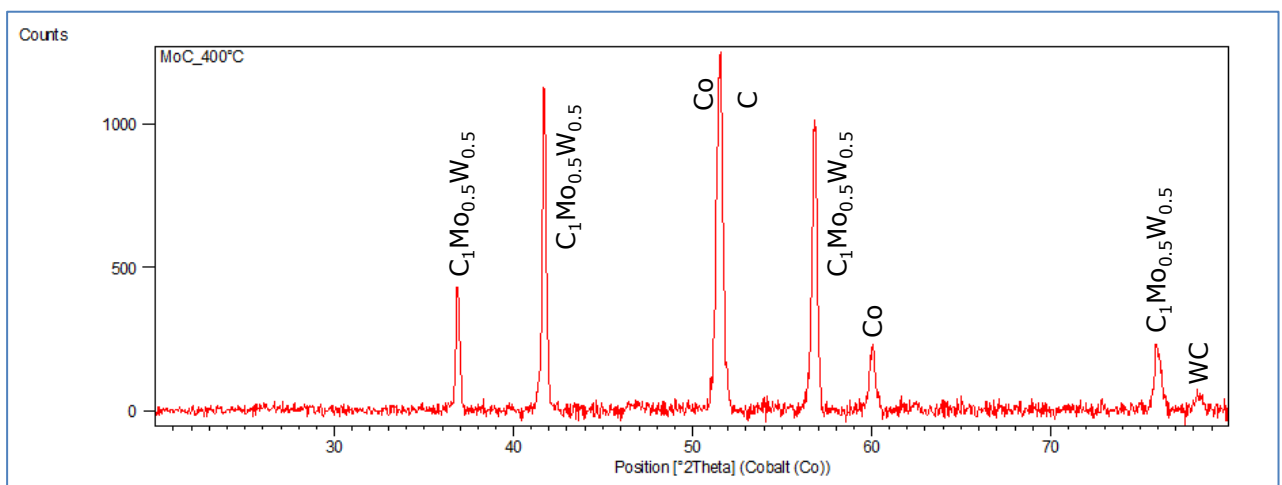
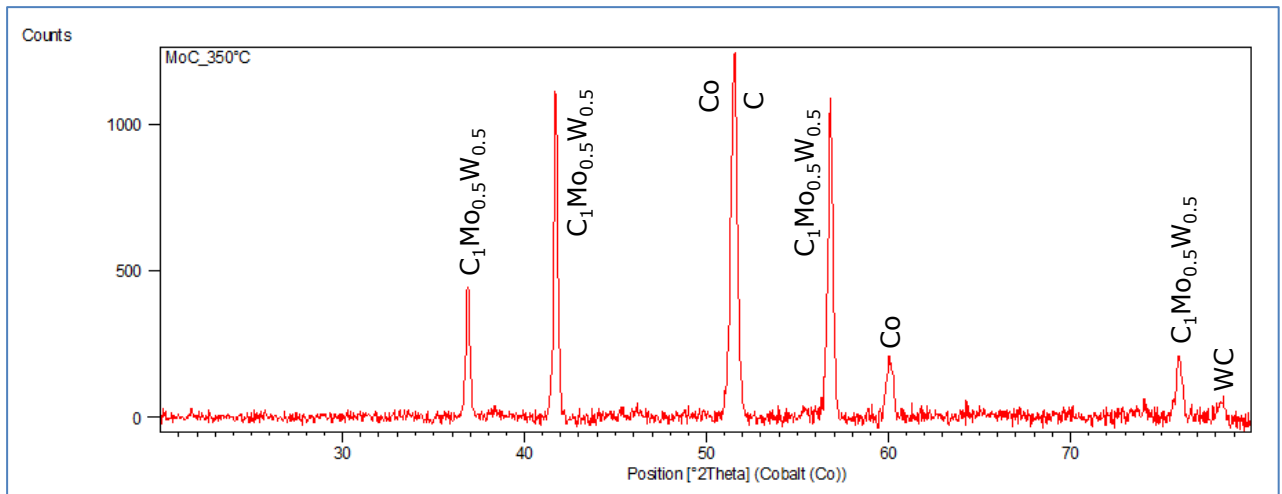
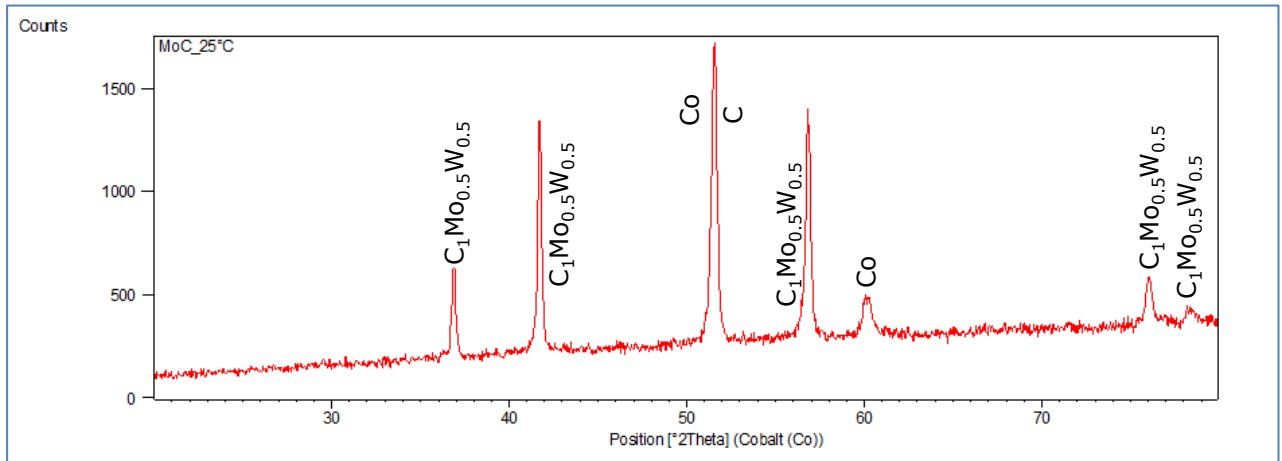


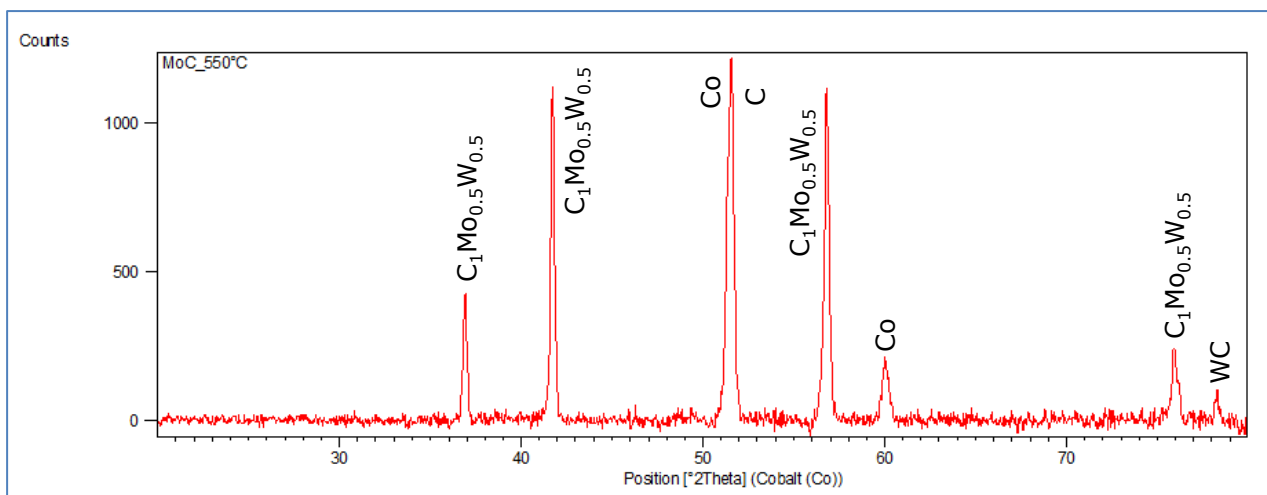
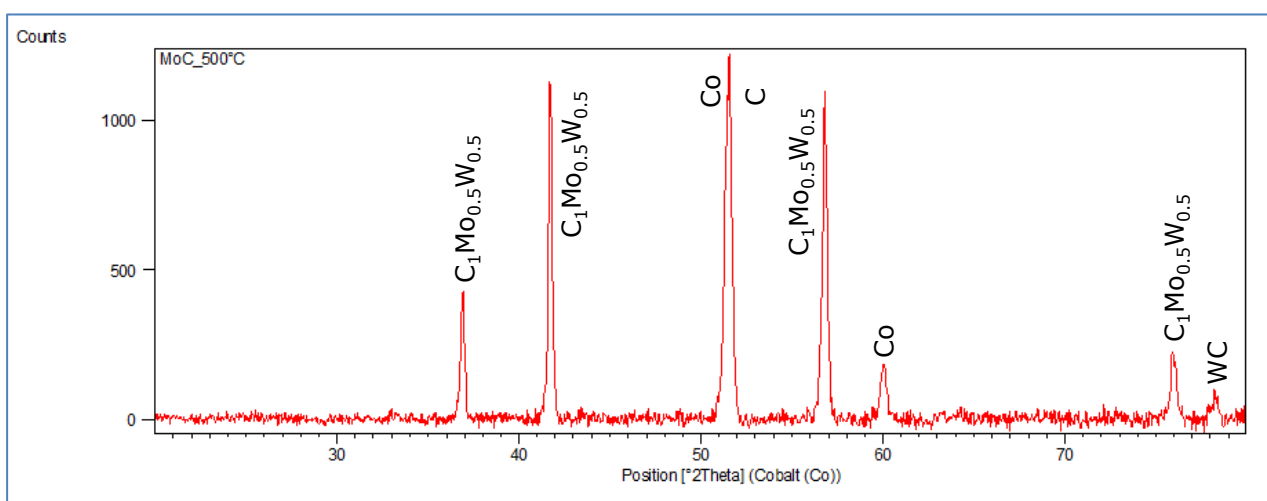
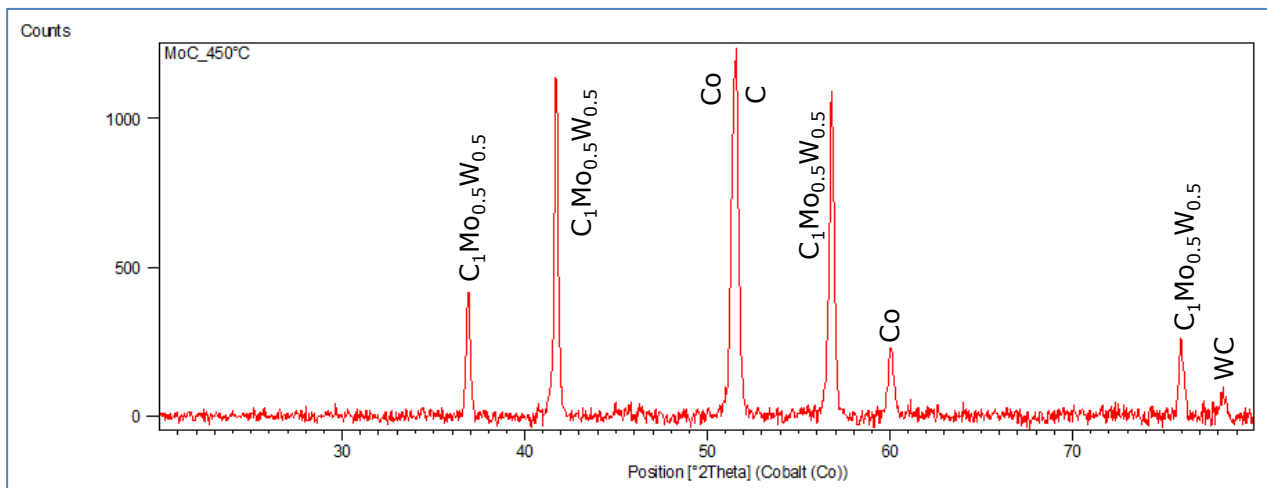


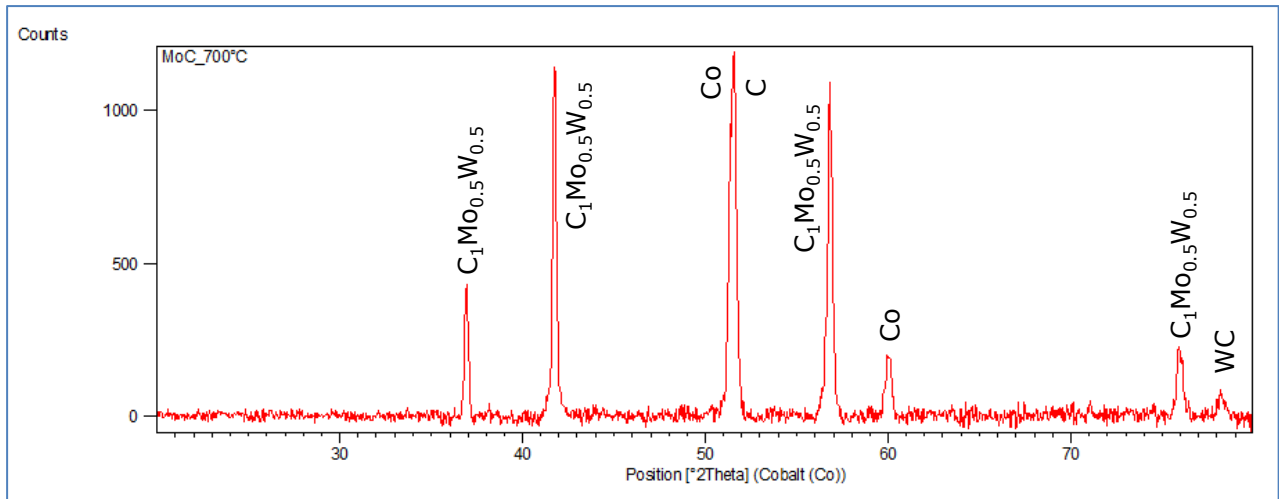
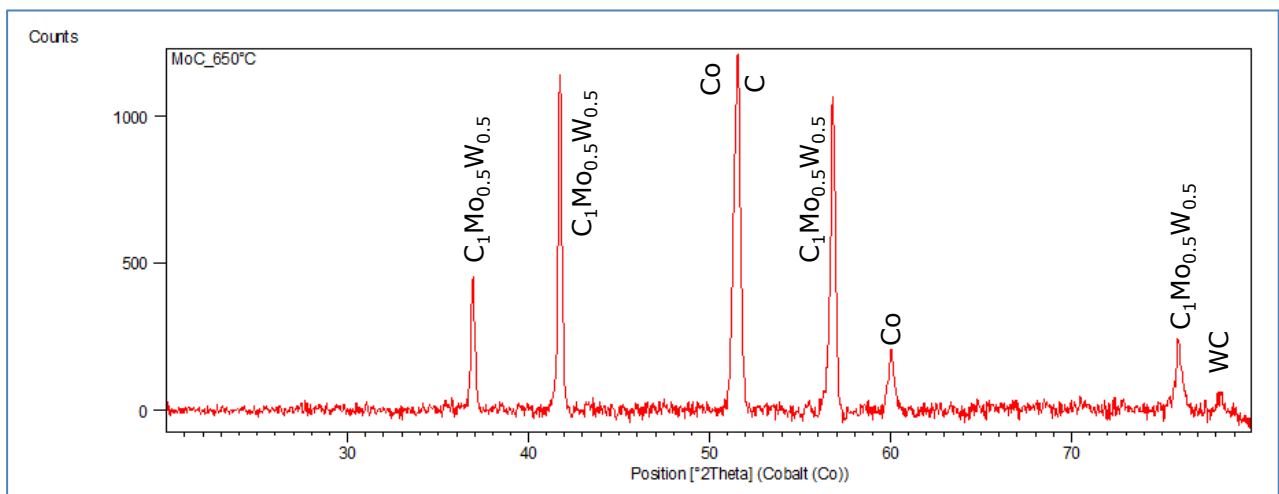
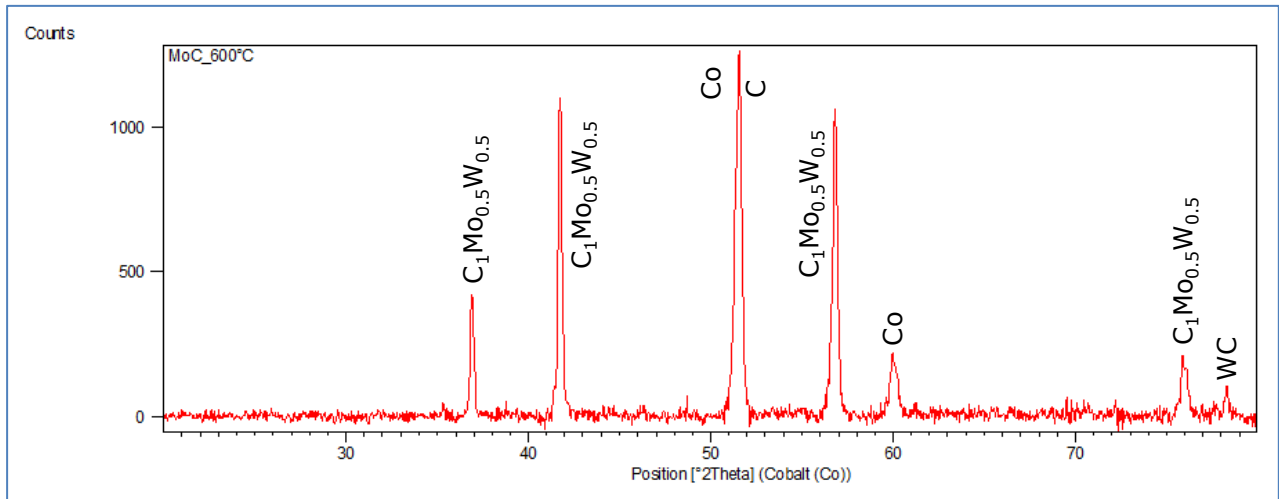


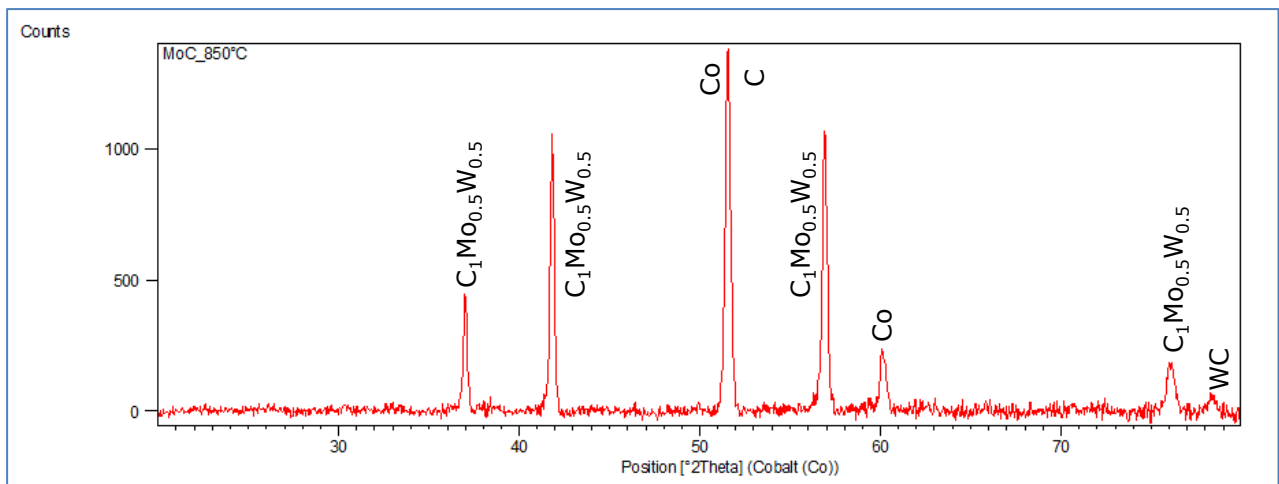
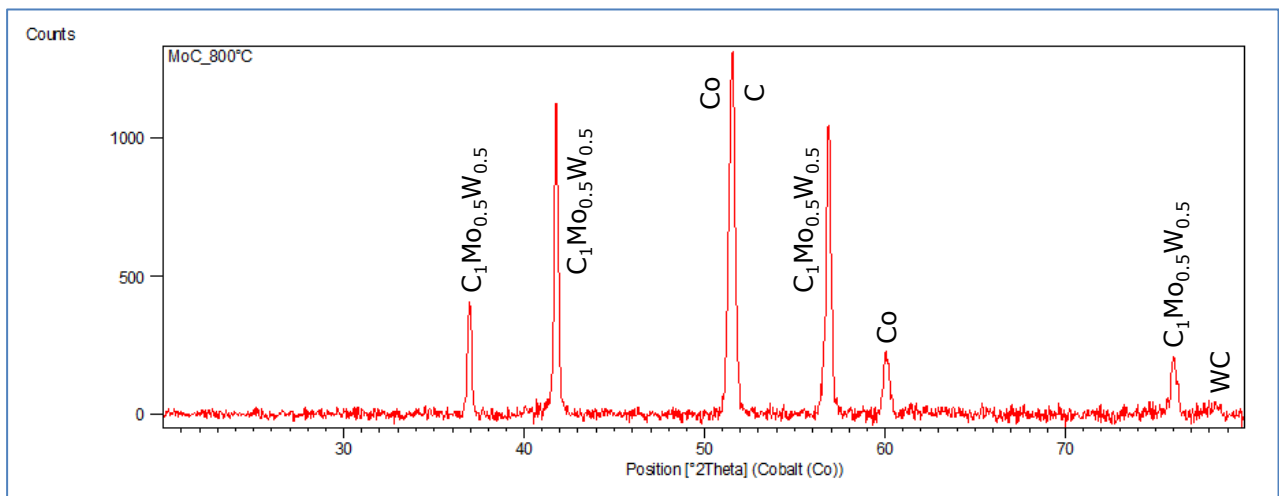
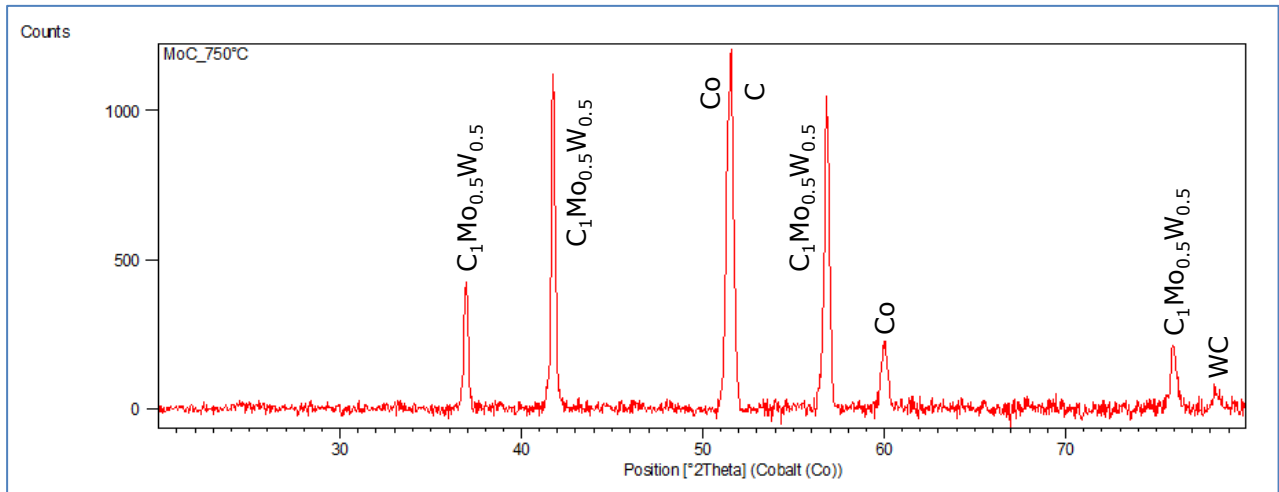


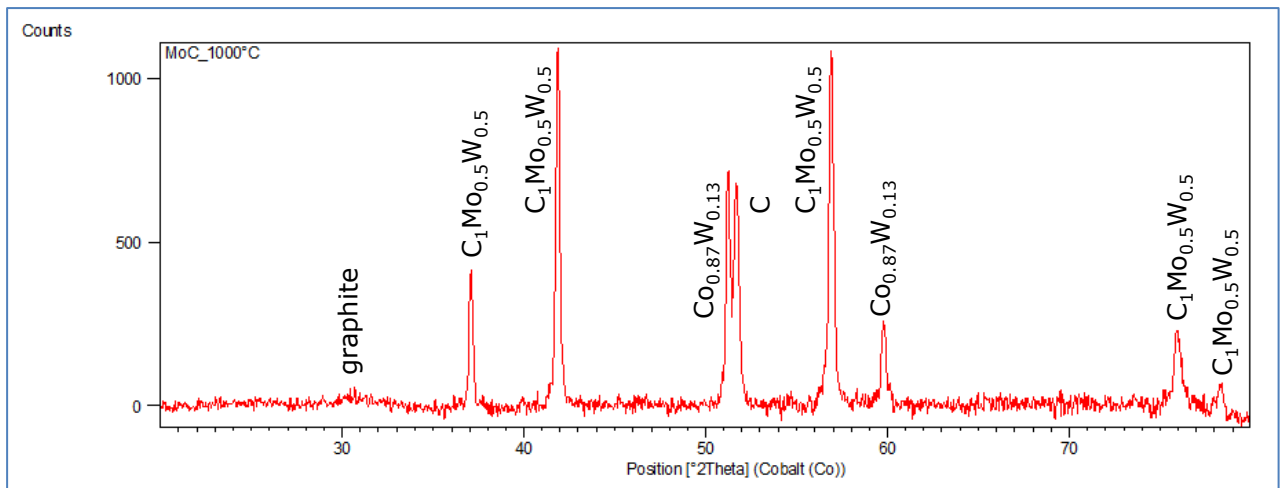
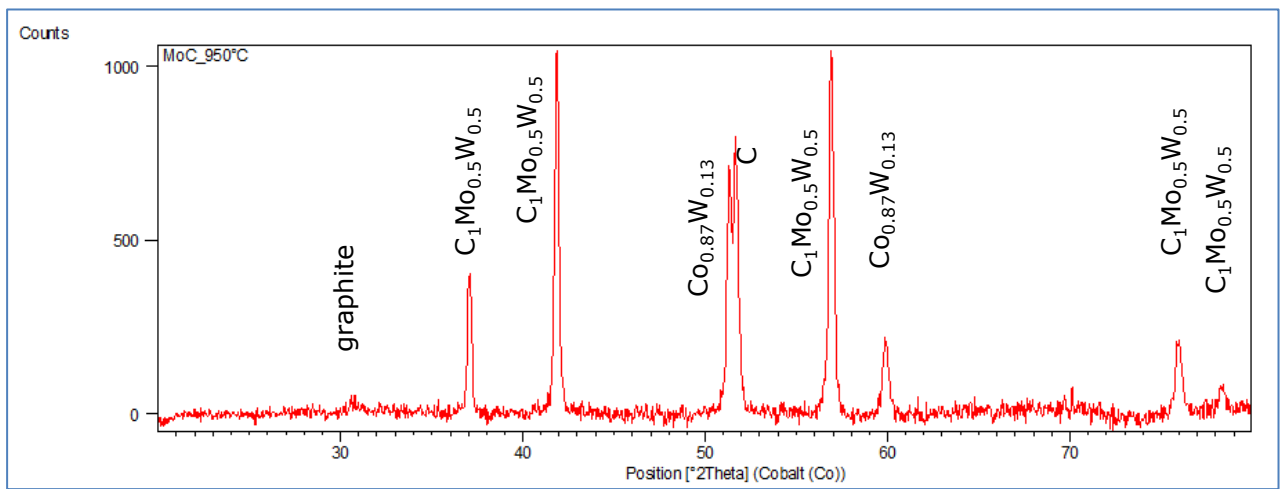
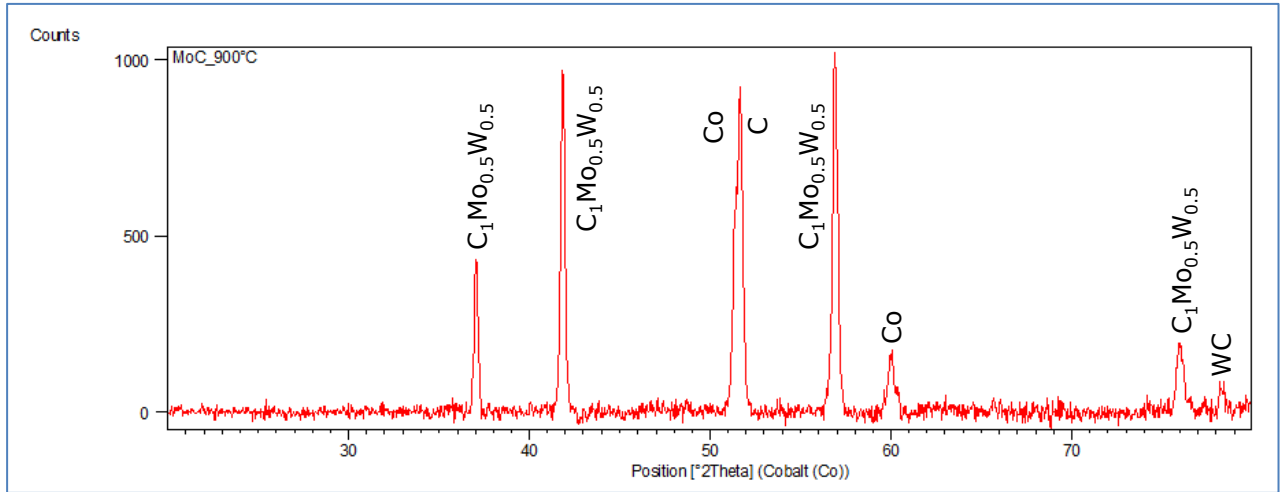
### APPENDIX THREE: XRD Patterns for the Mo<sub>2</sub>C enhanced PCD during heat treatment

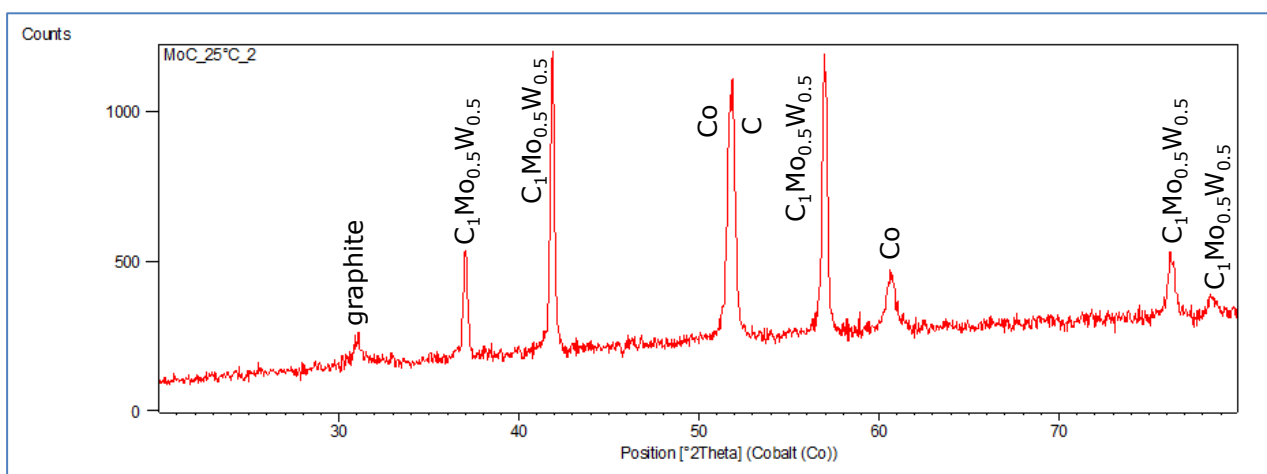
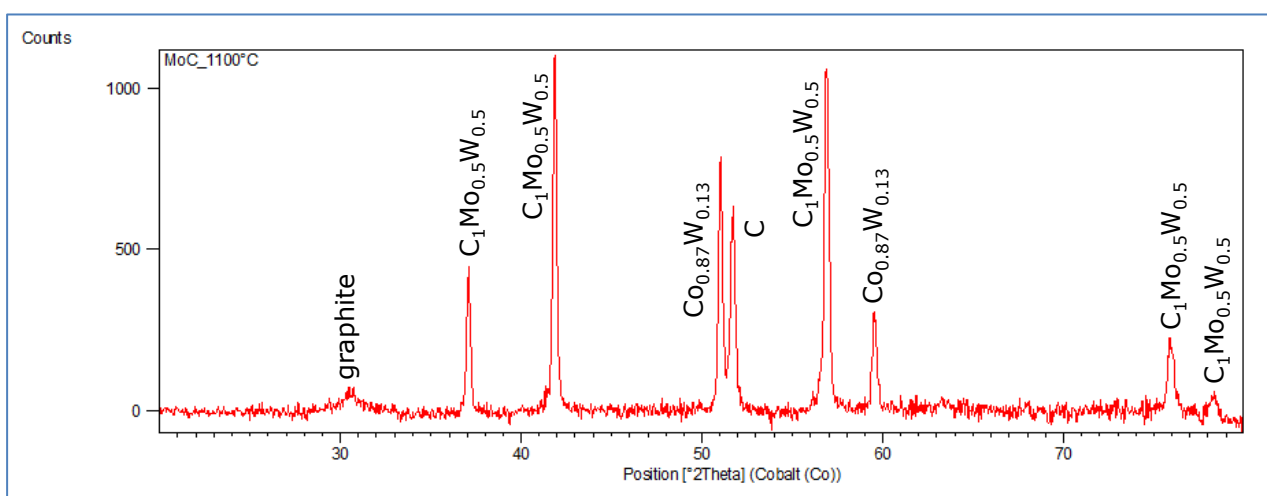
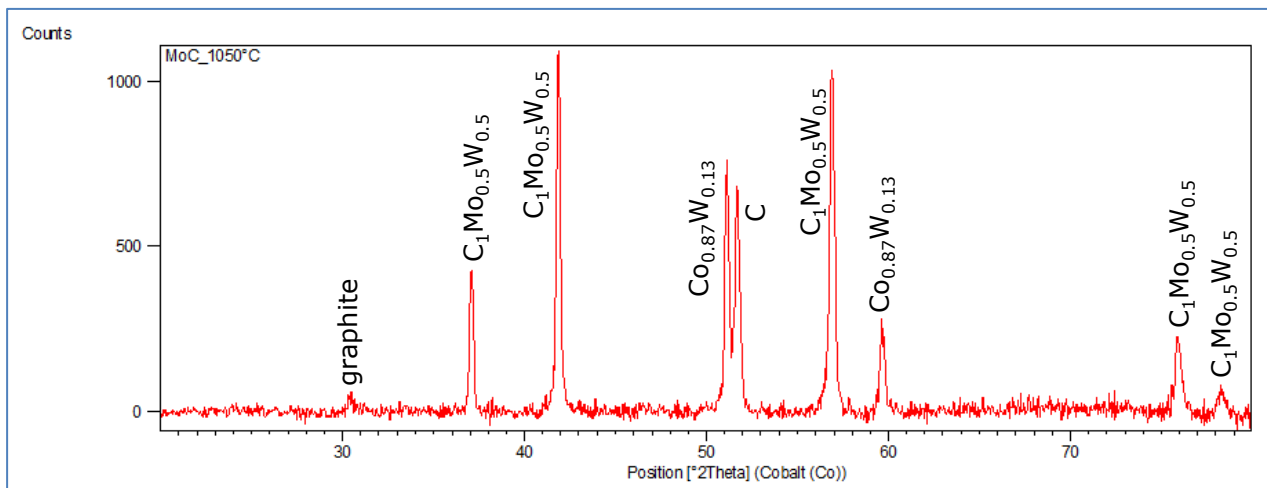




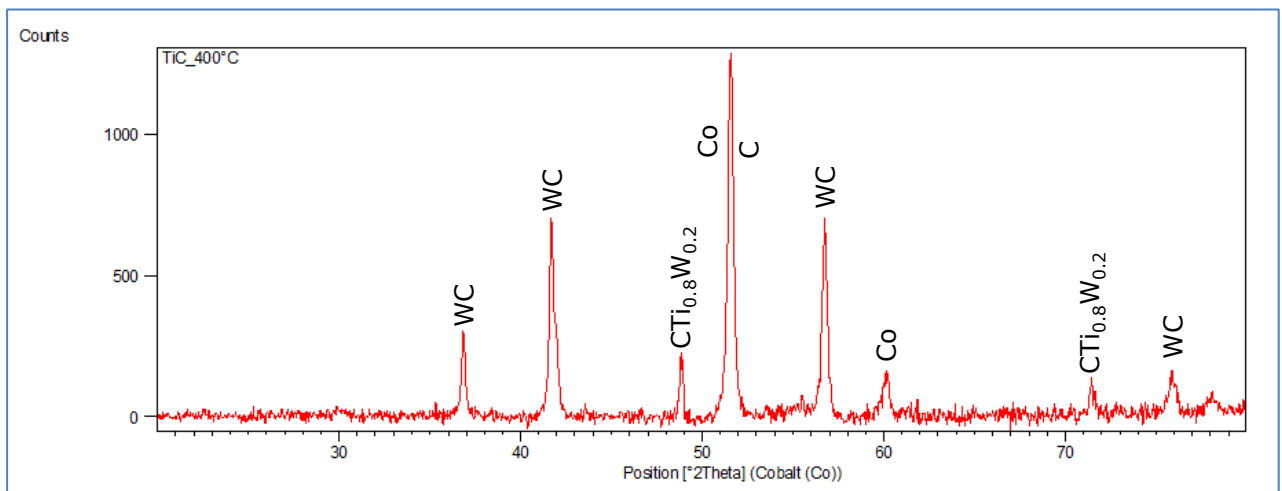
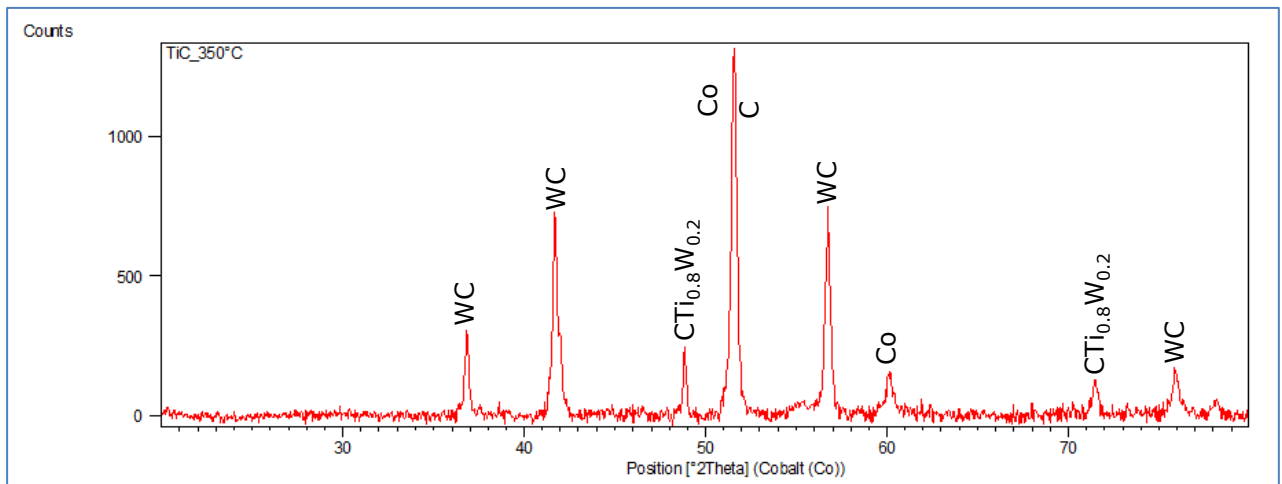
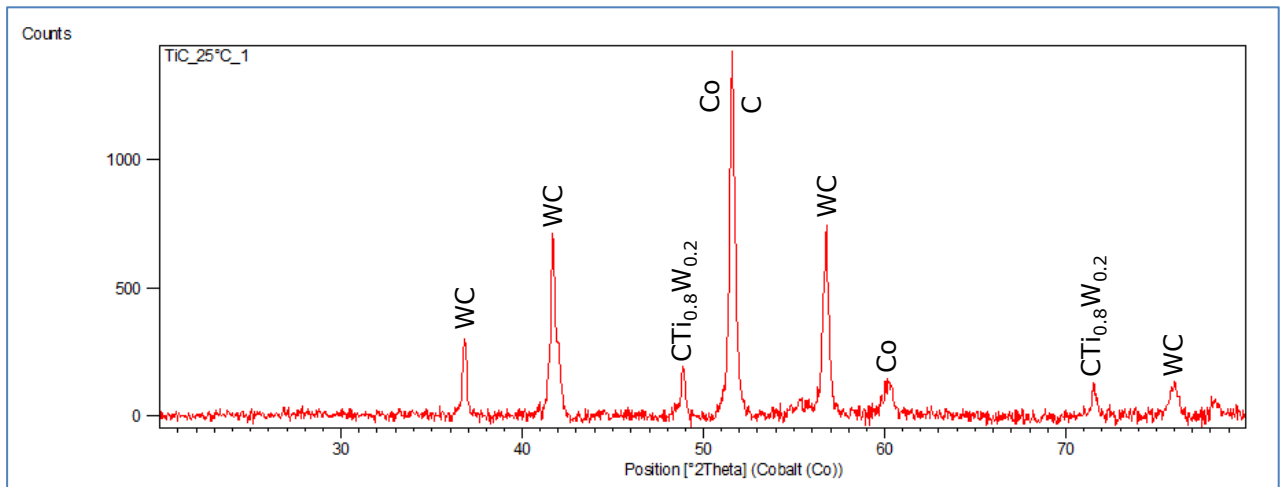




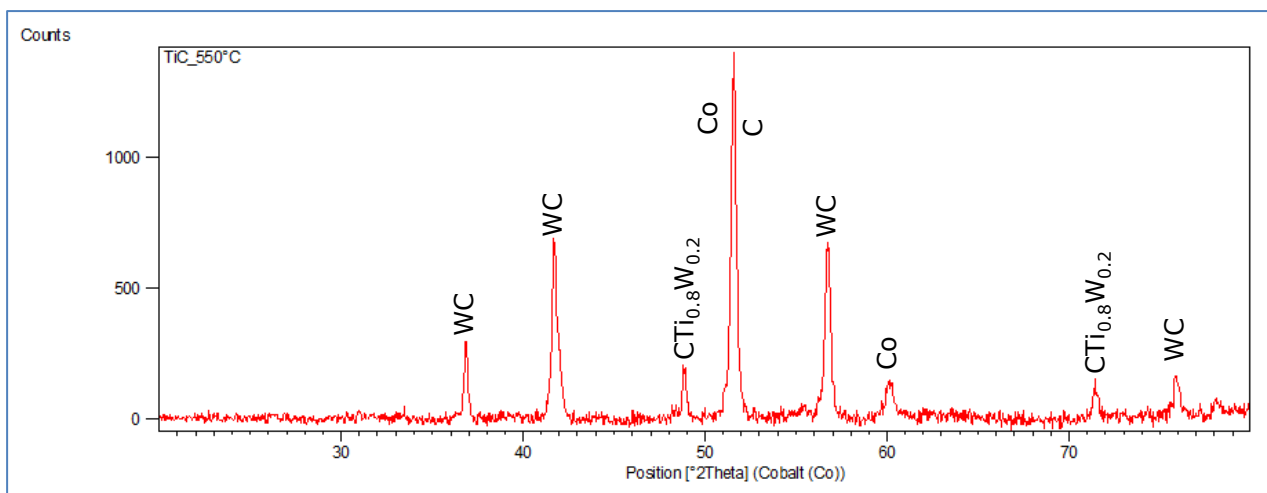
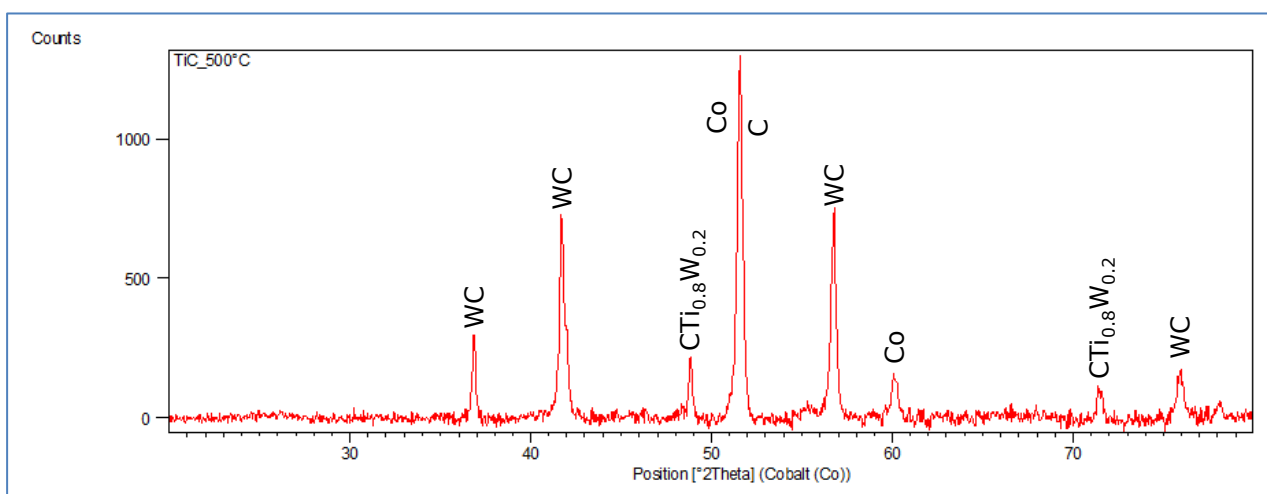
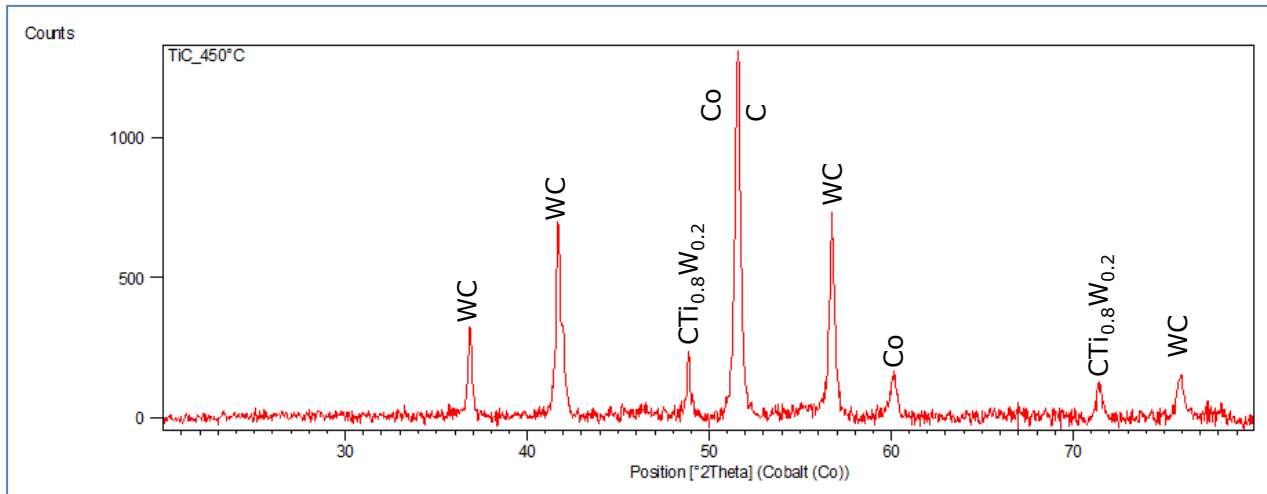


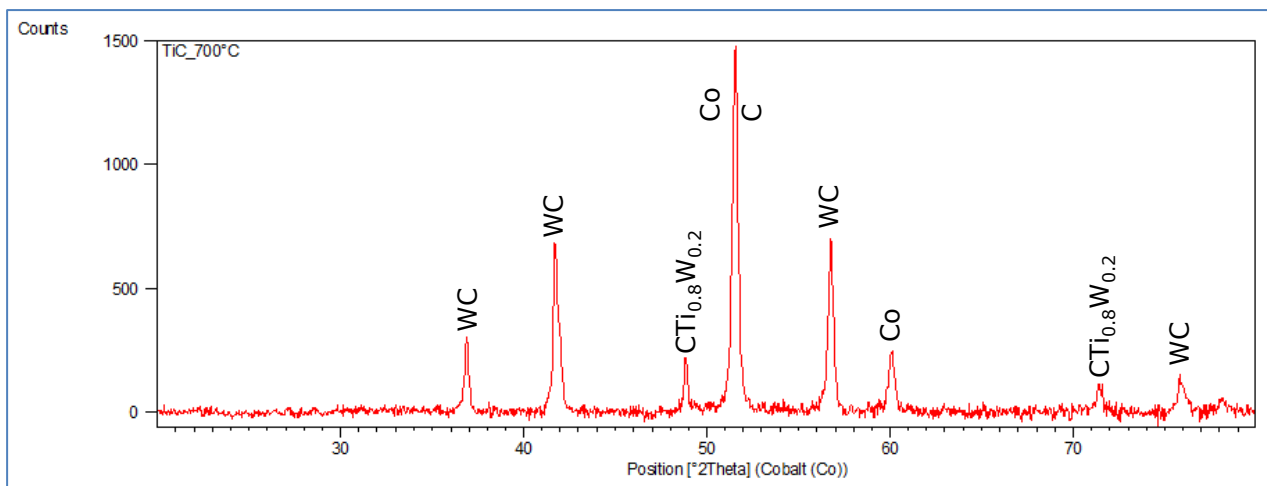
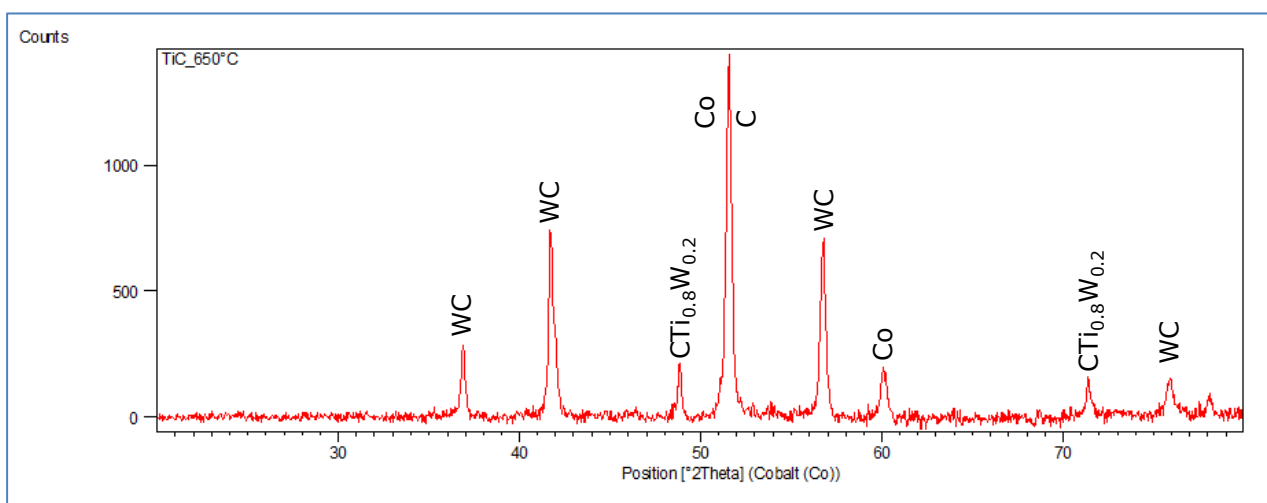
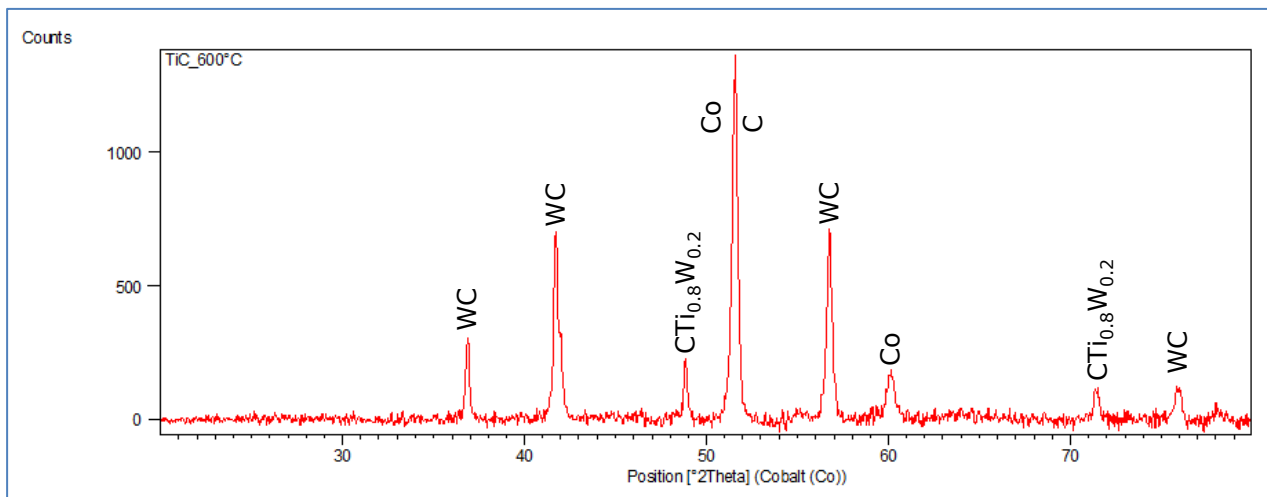


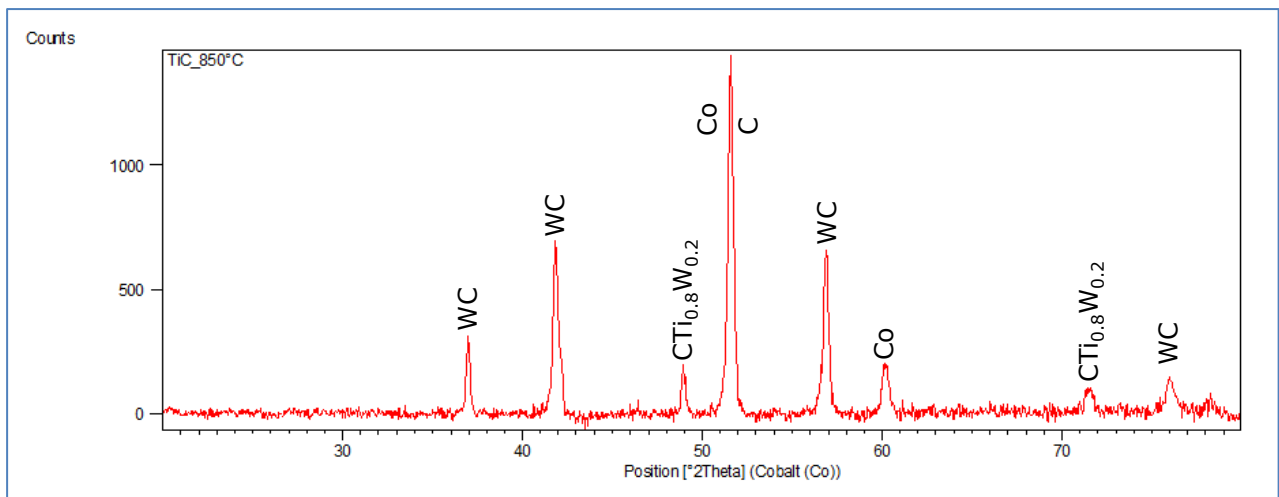
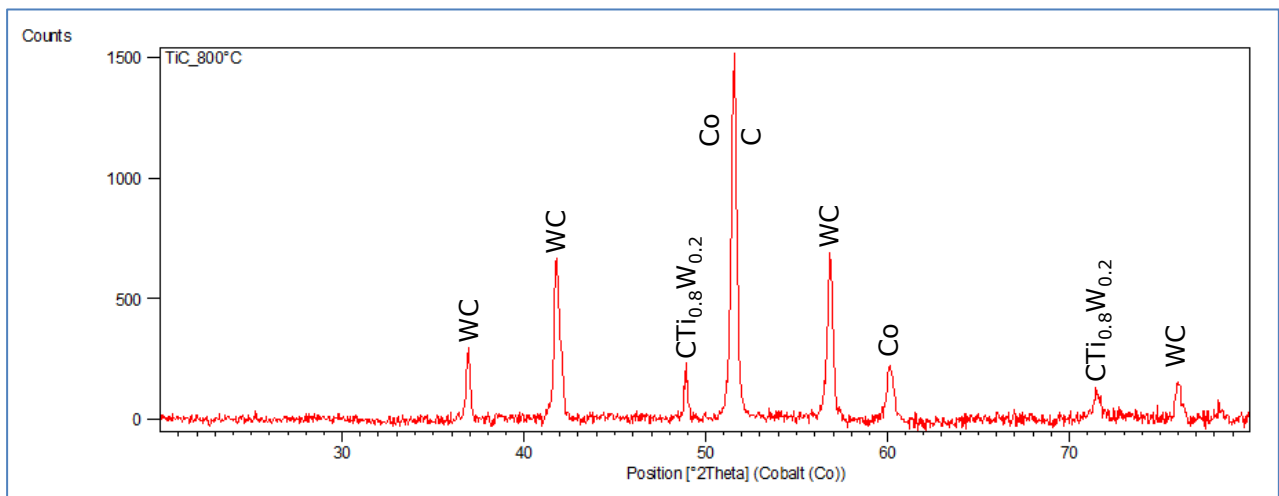
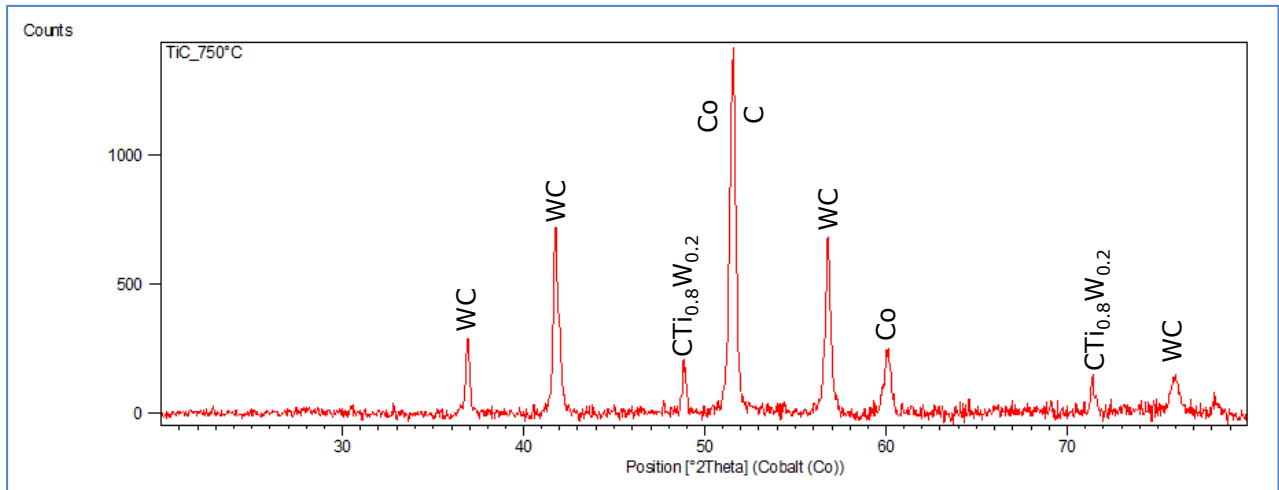
## APPENDIX FOUR: XRD PATTERNS FOR THE TIC ENHANCED PCD DURING HEAT TREATMENT

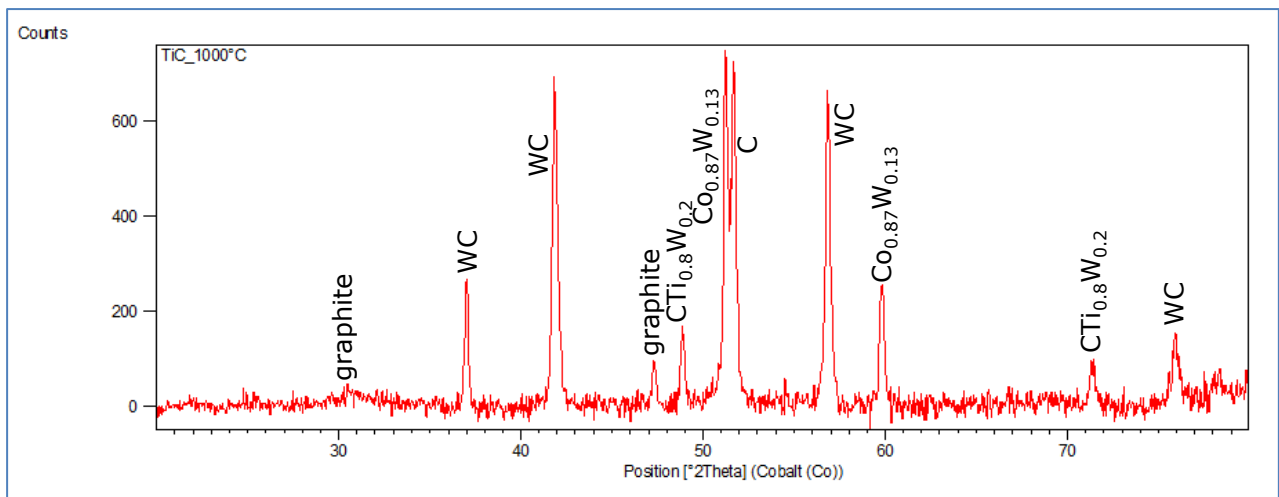
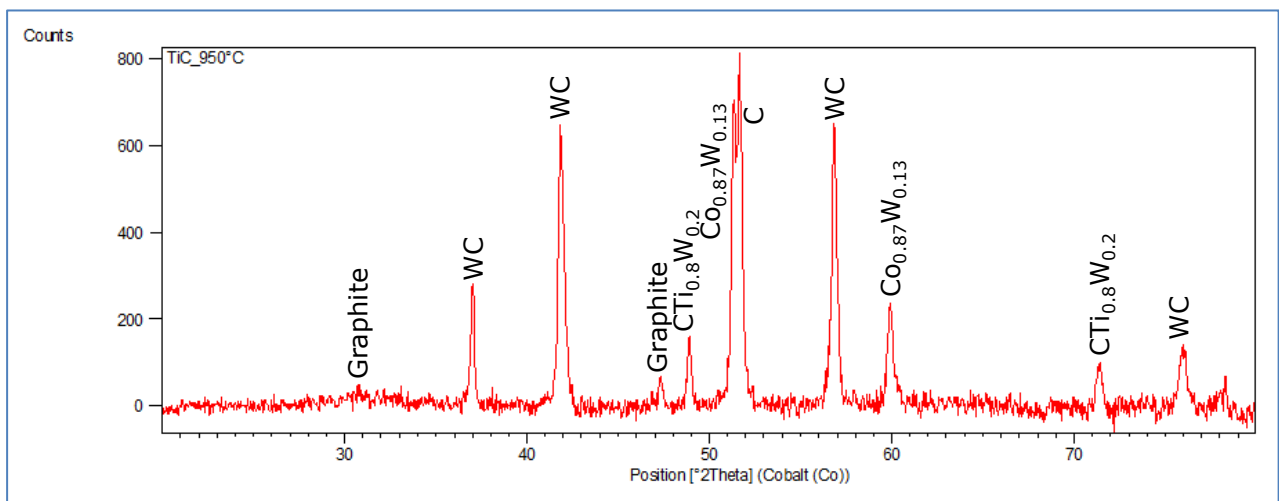
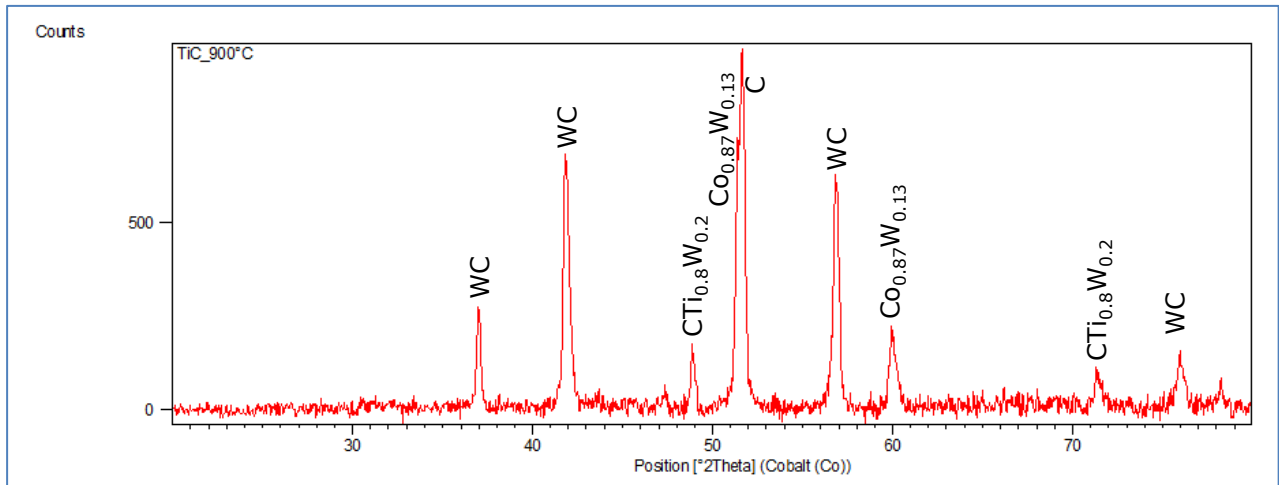


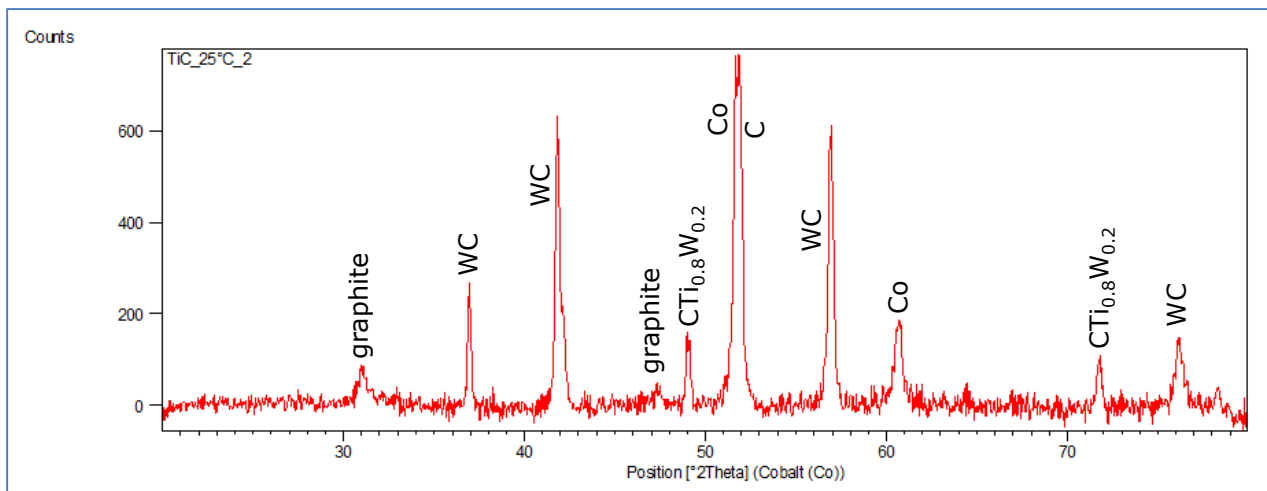
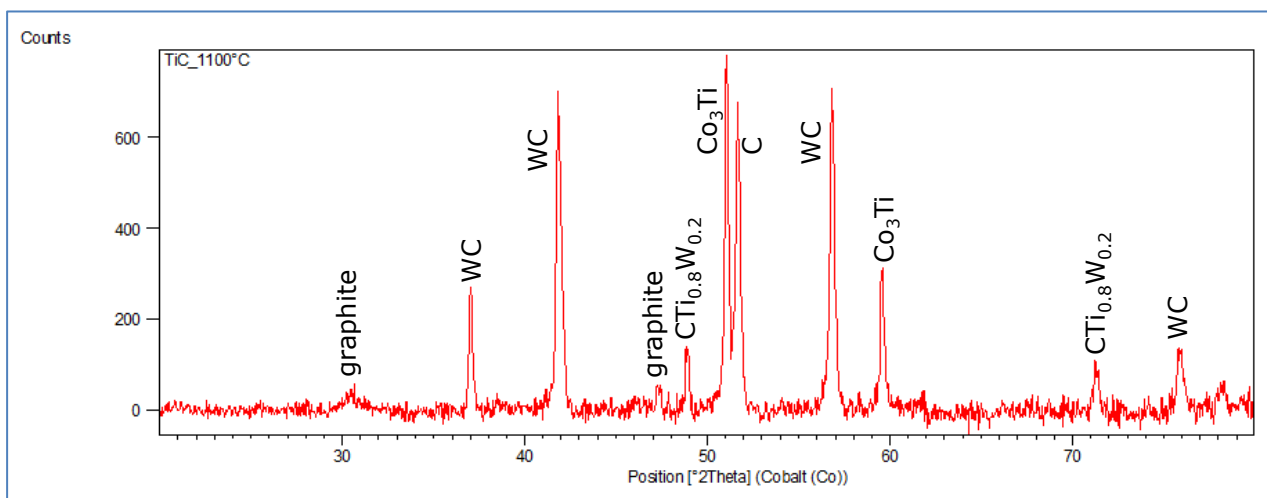
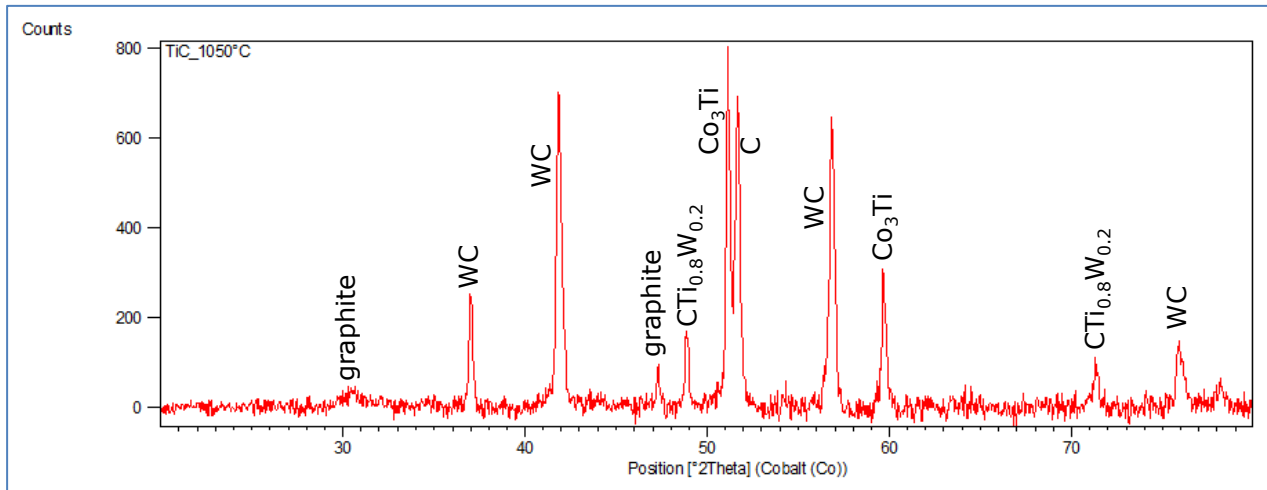




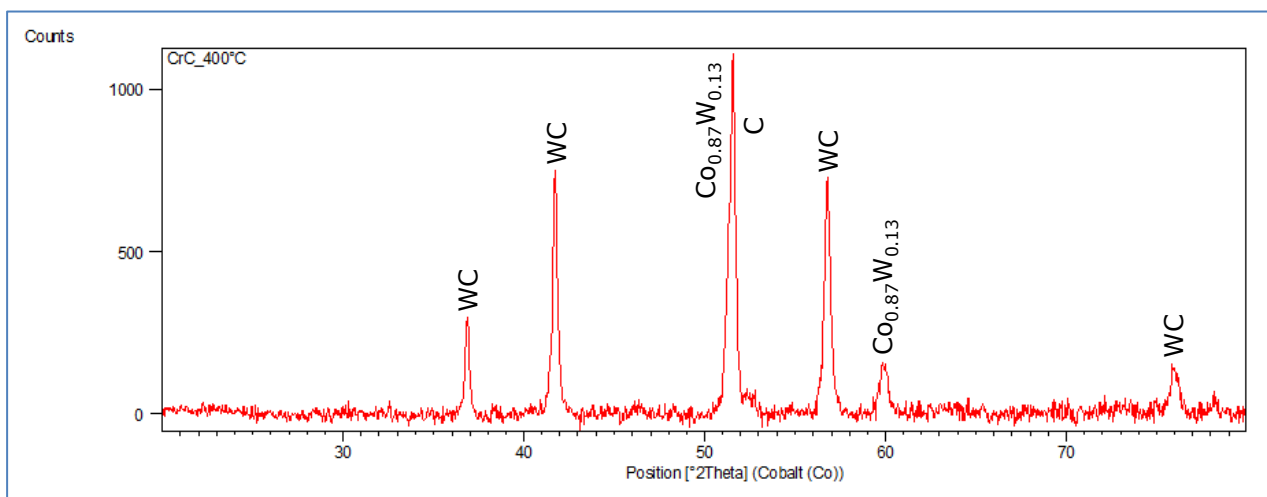
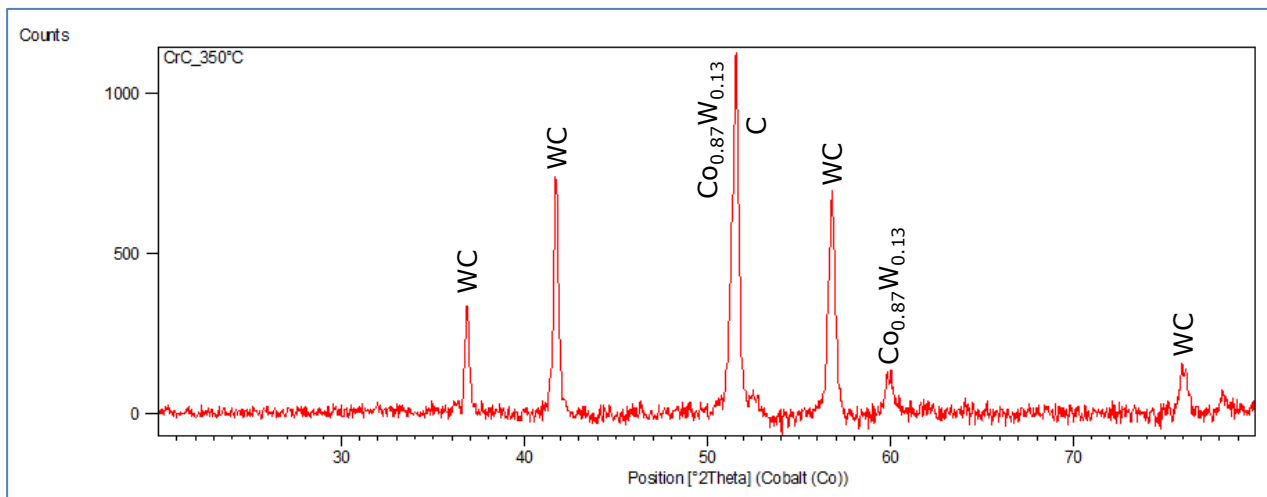
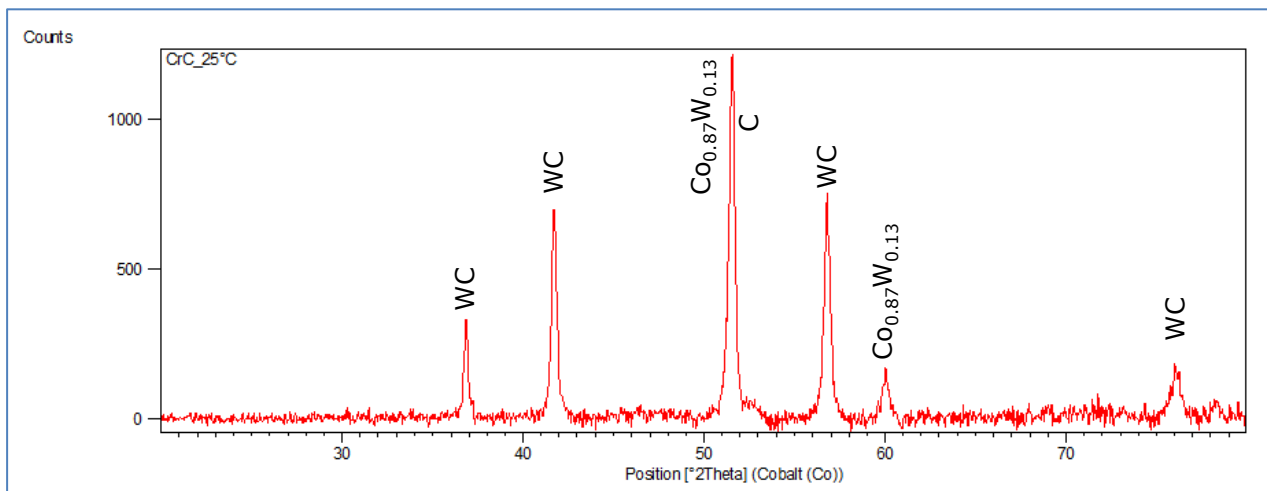


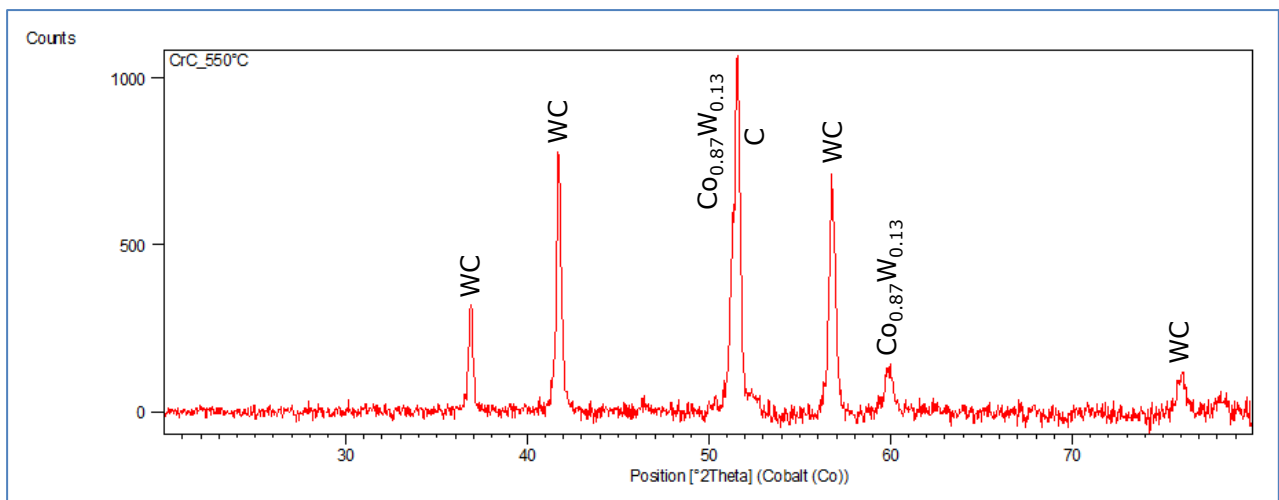
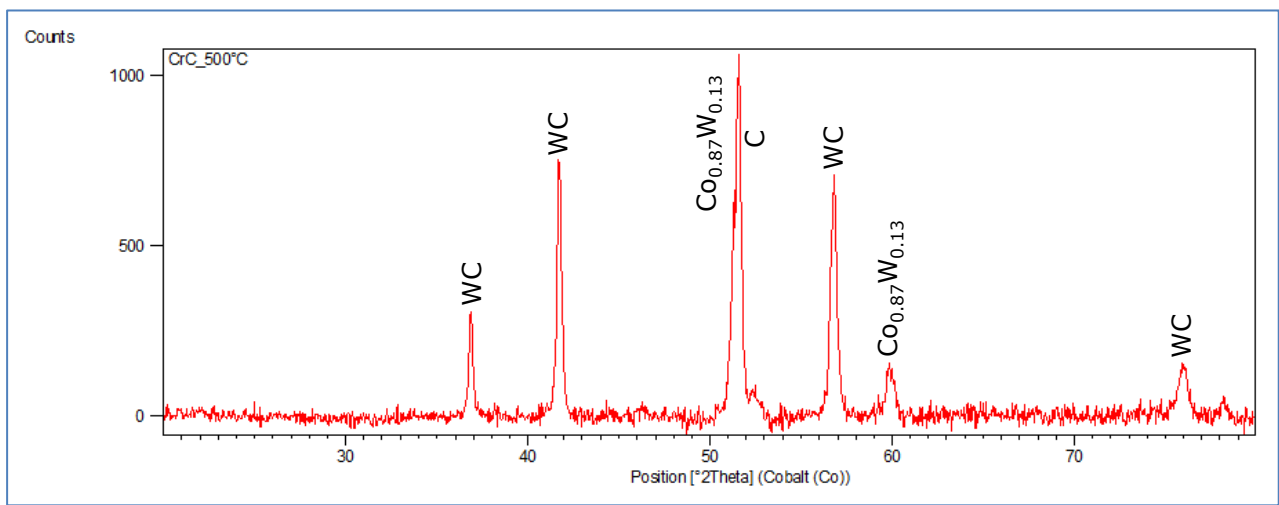
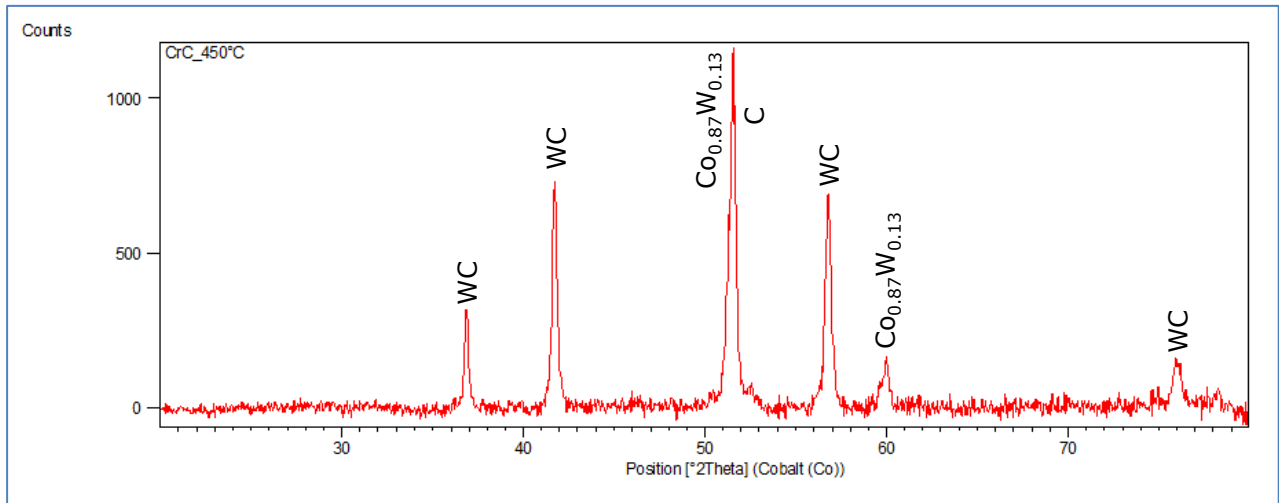


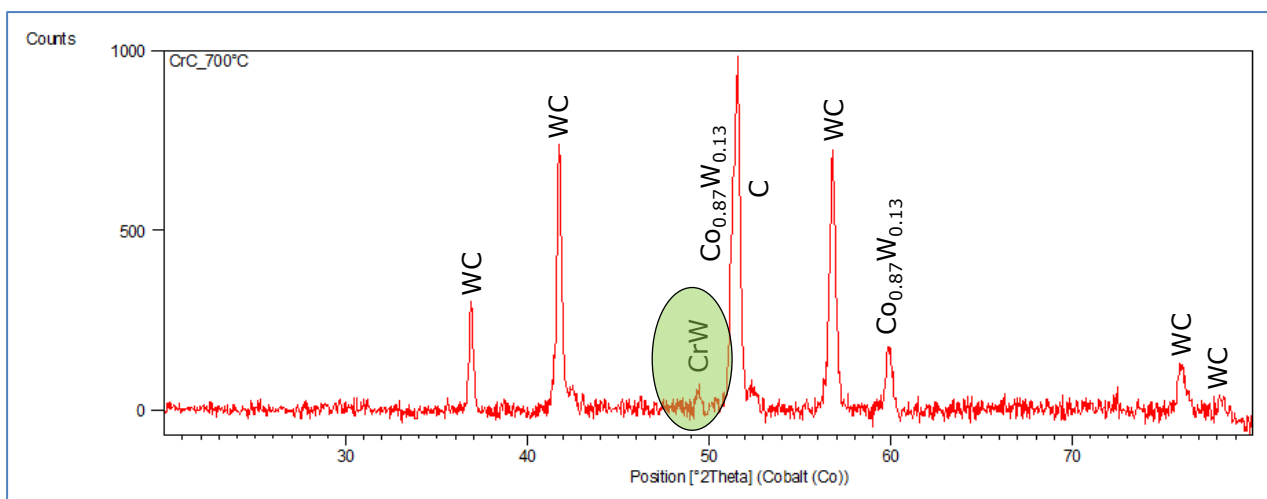
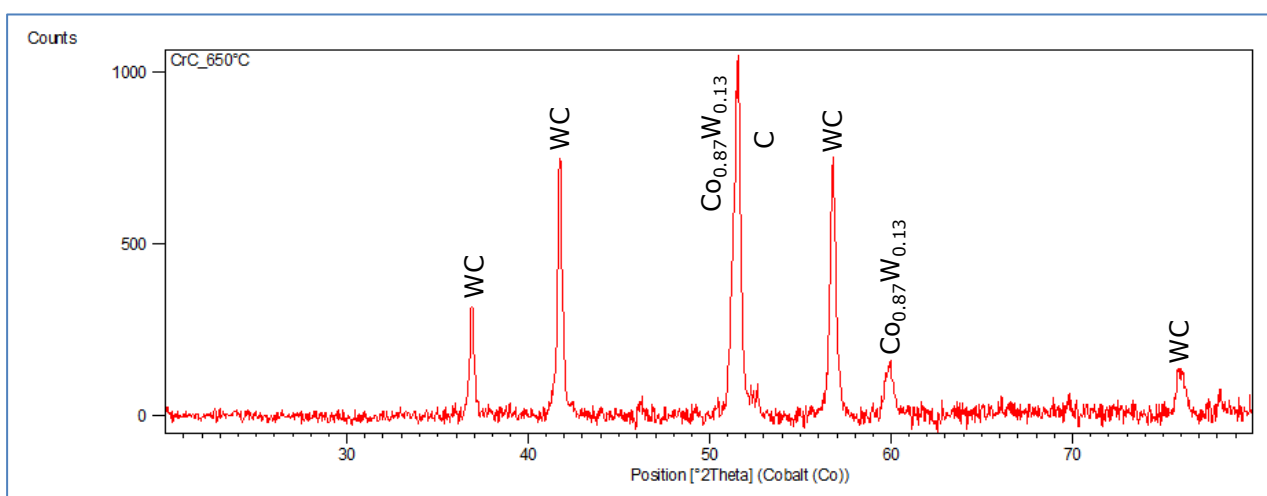
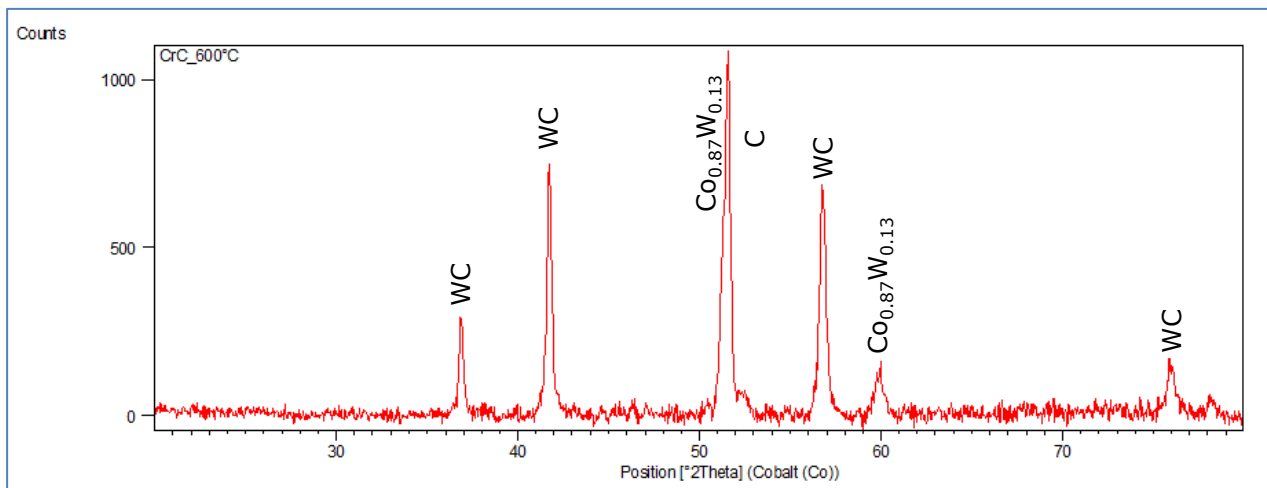




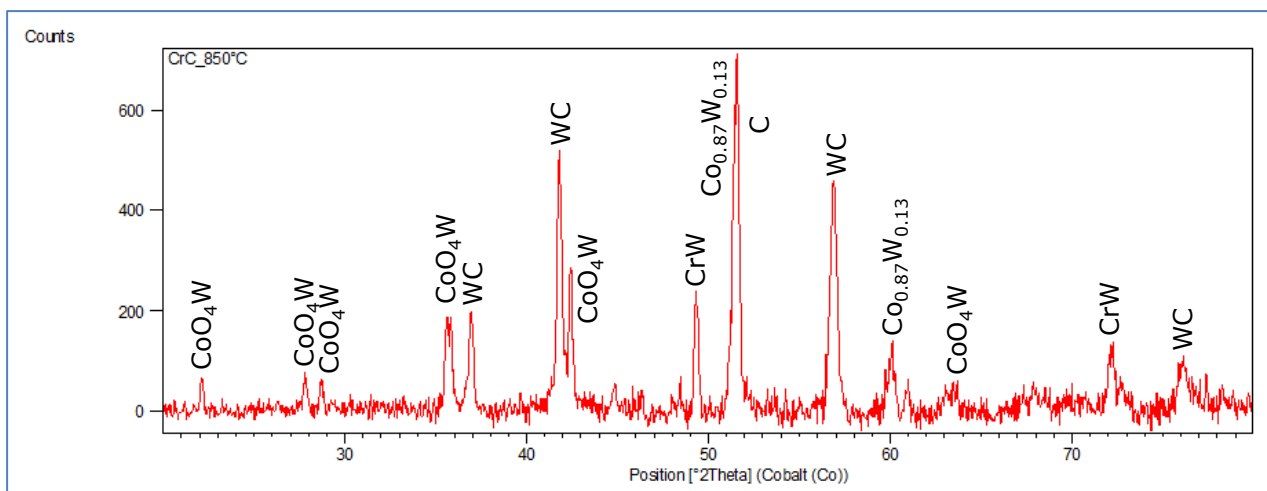
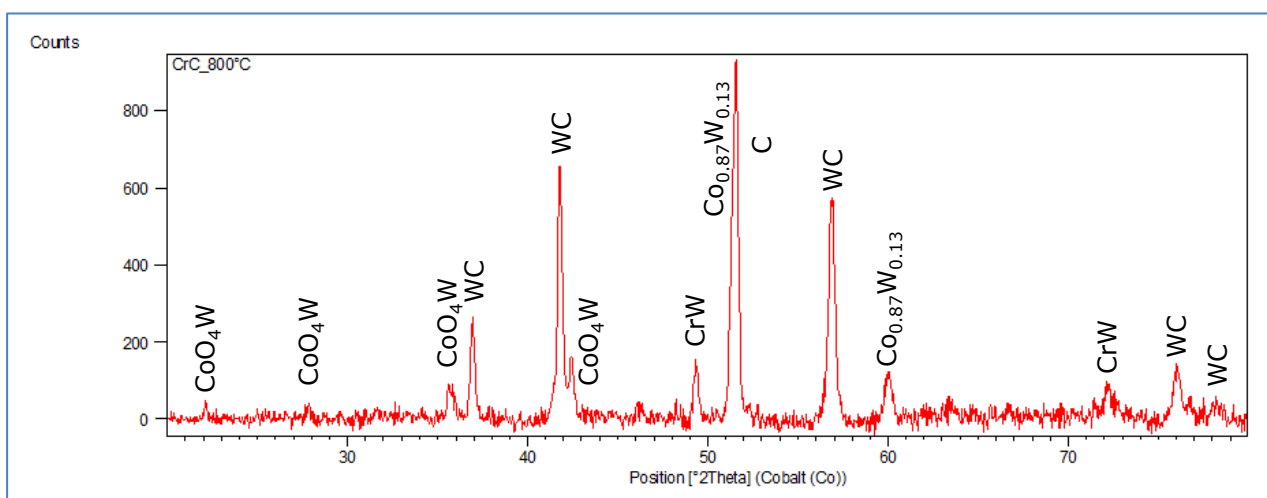
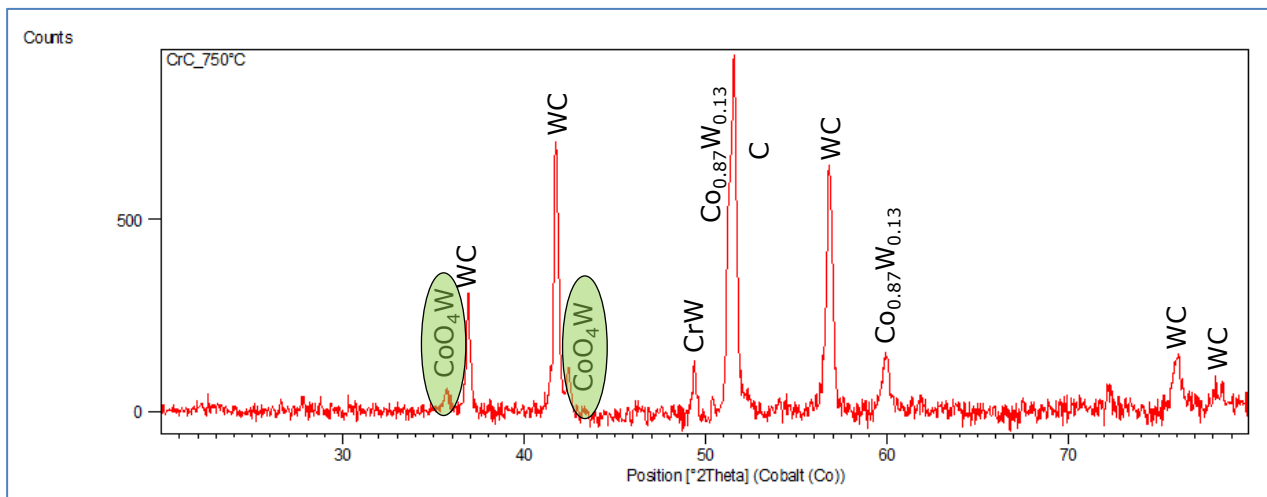
## APPENDIX FIVE: XRD PATTERNS FOR THE $\text{Cr}_3\text{C}_2$ ENHANCED PCD DURING HEAT TREATMENT

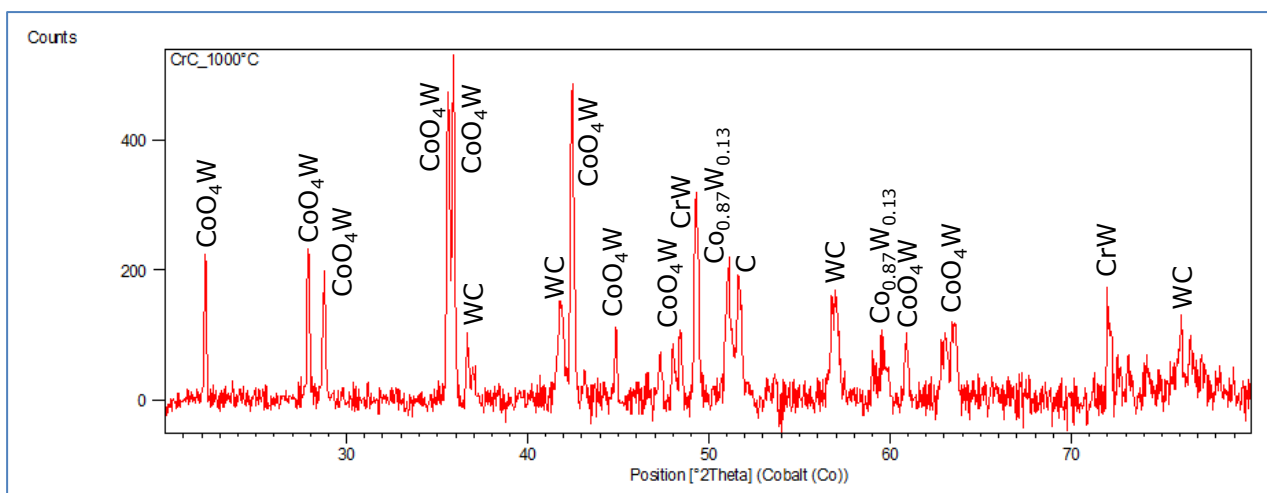
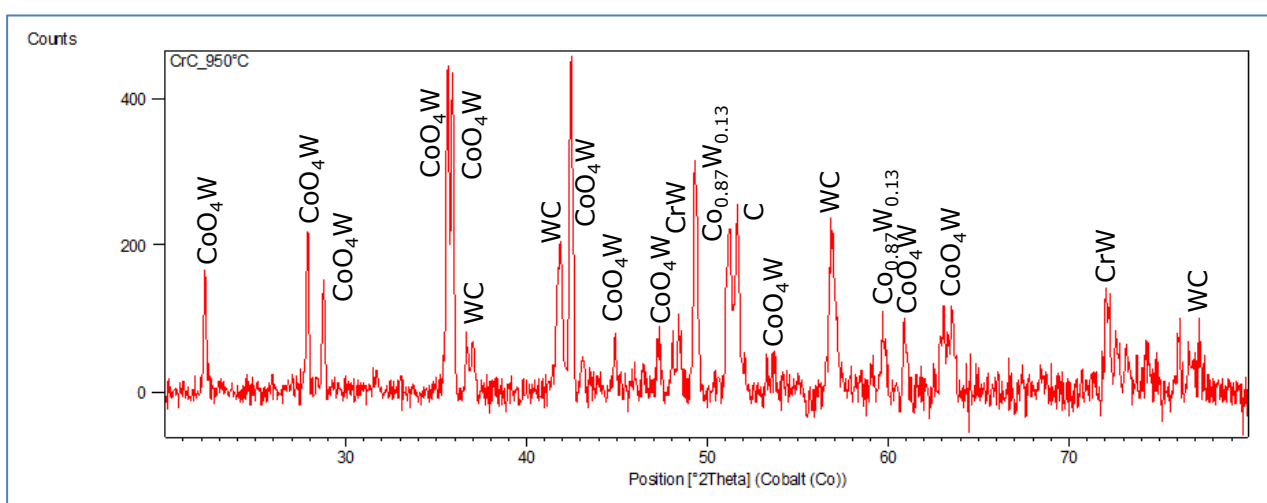
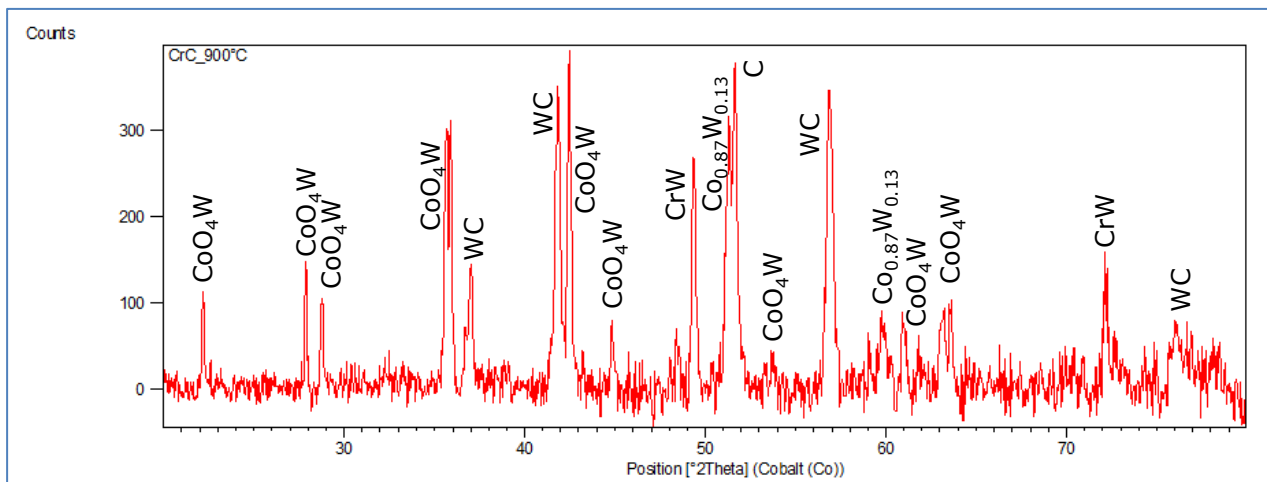


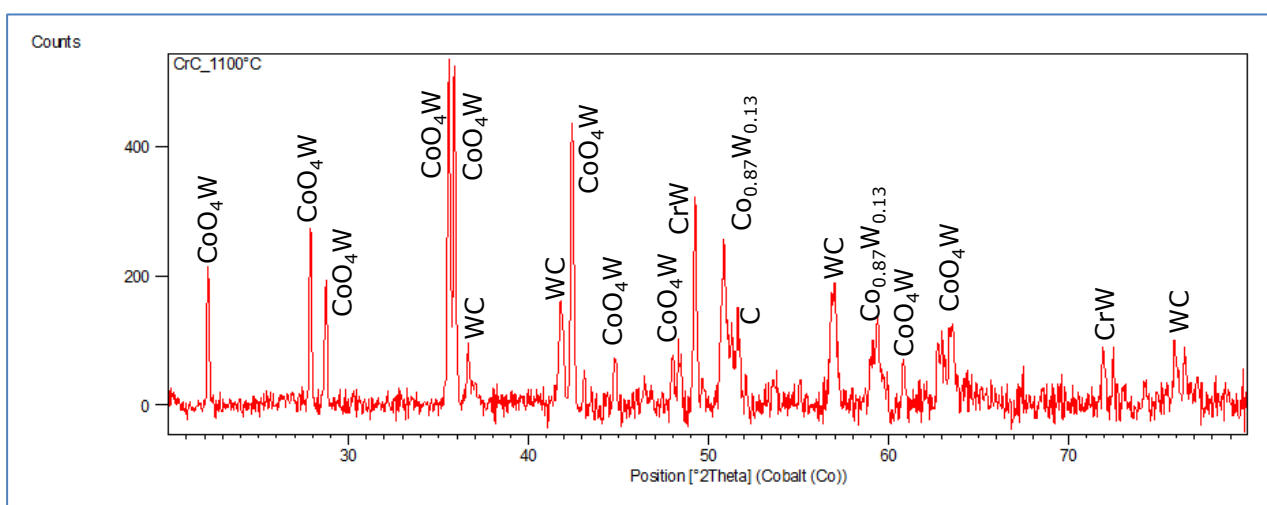
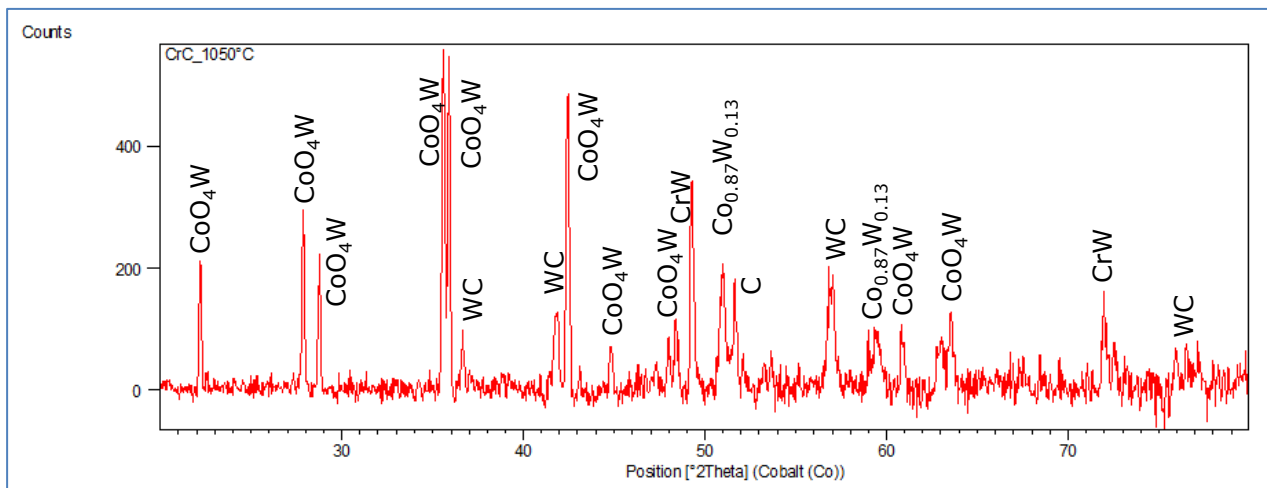




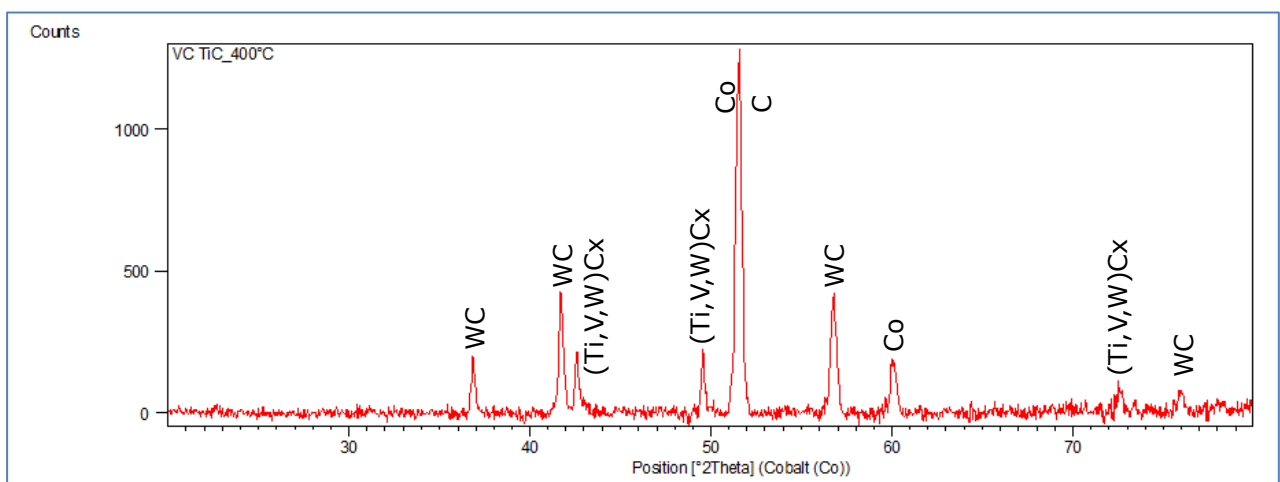
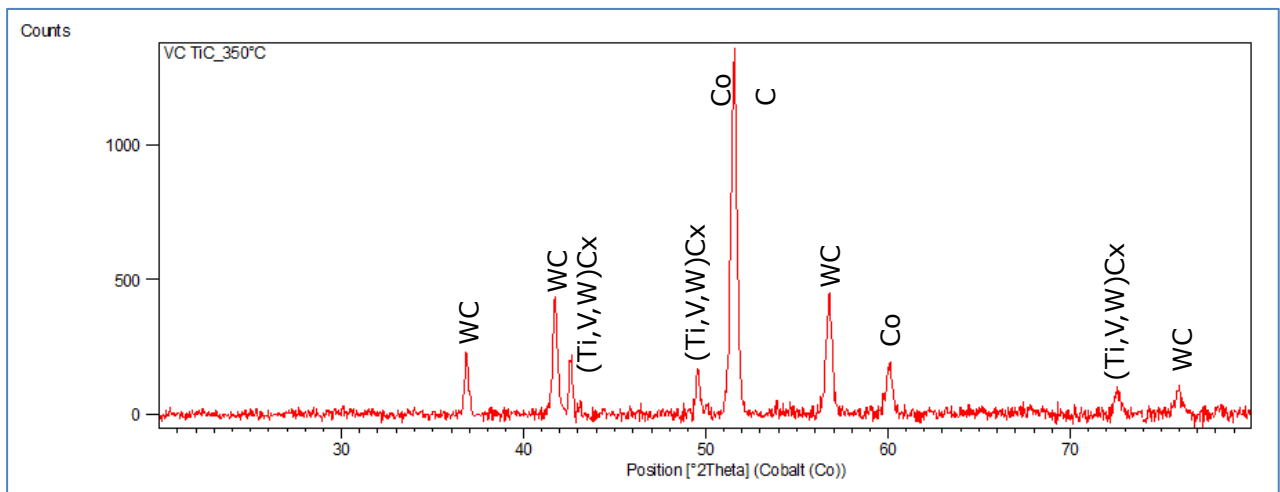
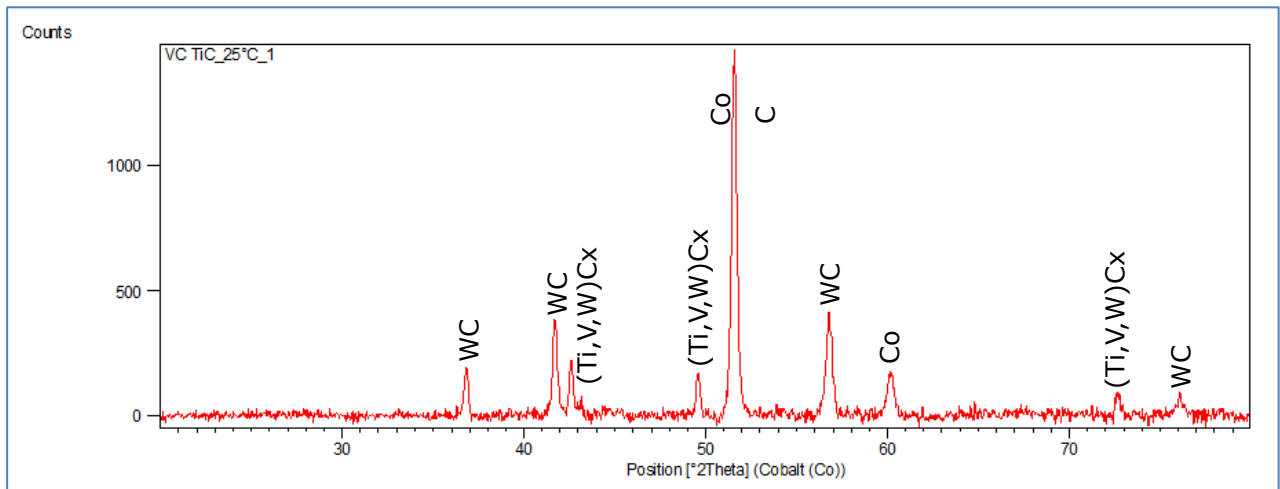


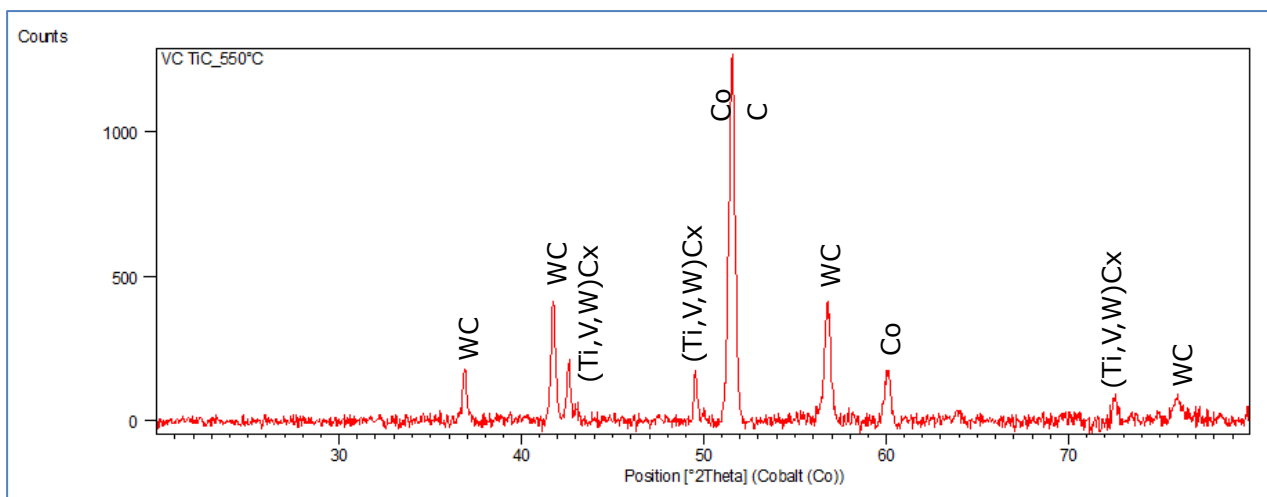
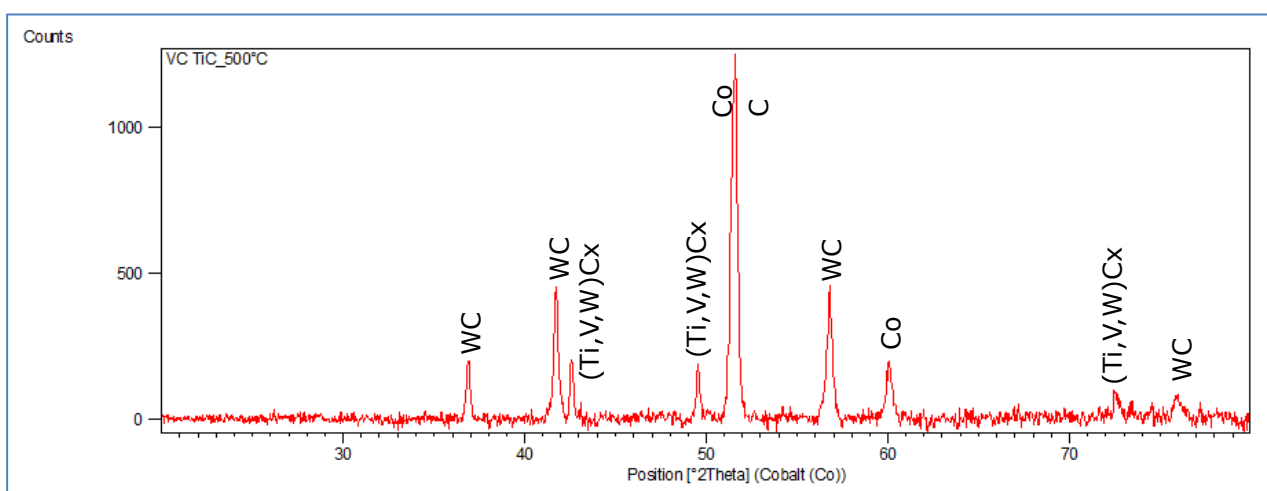
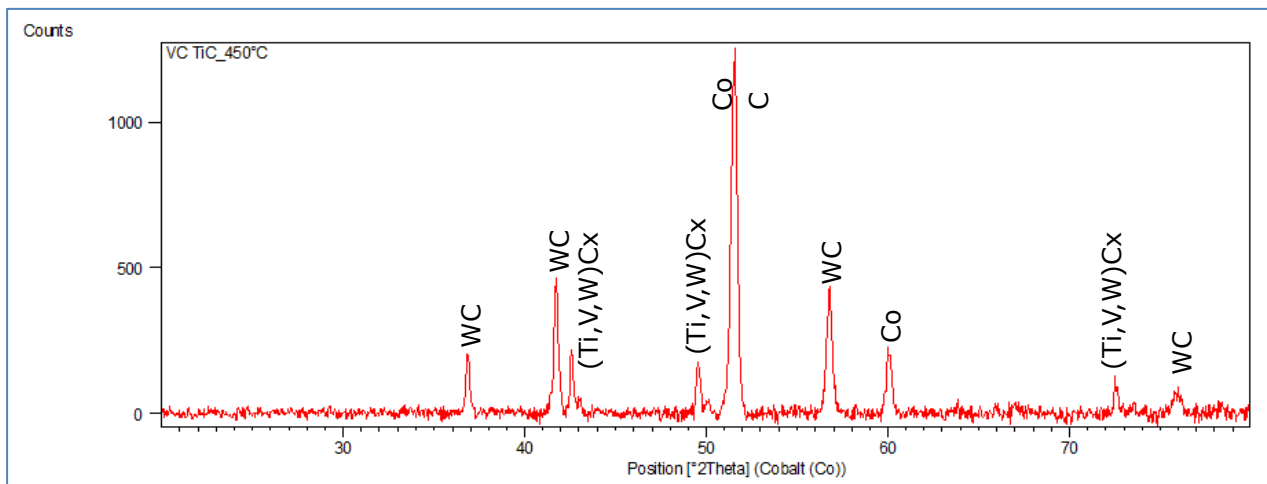


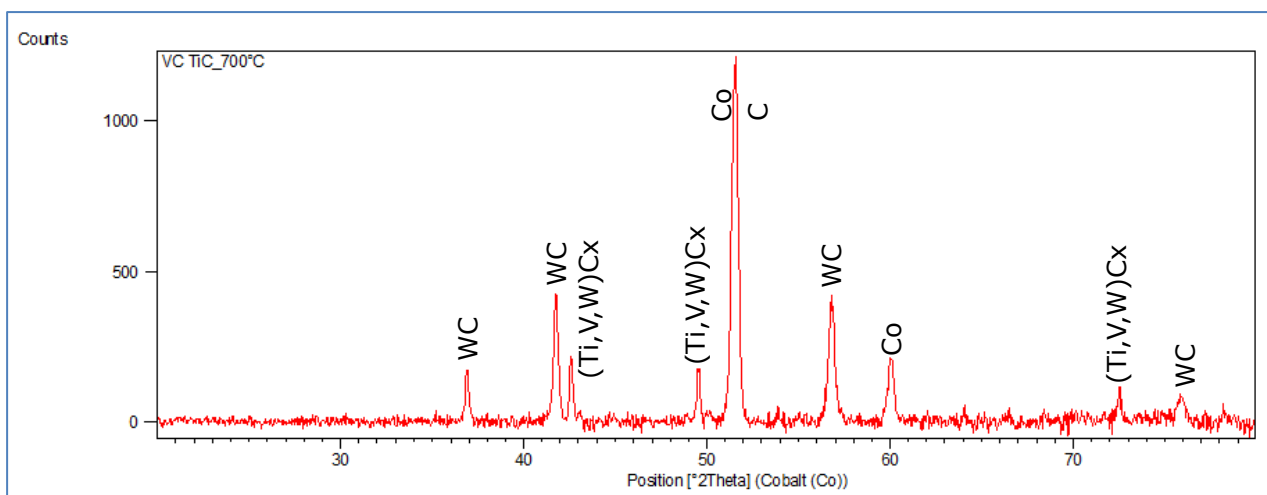
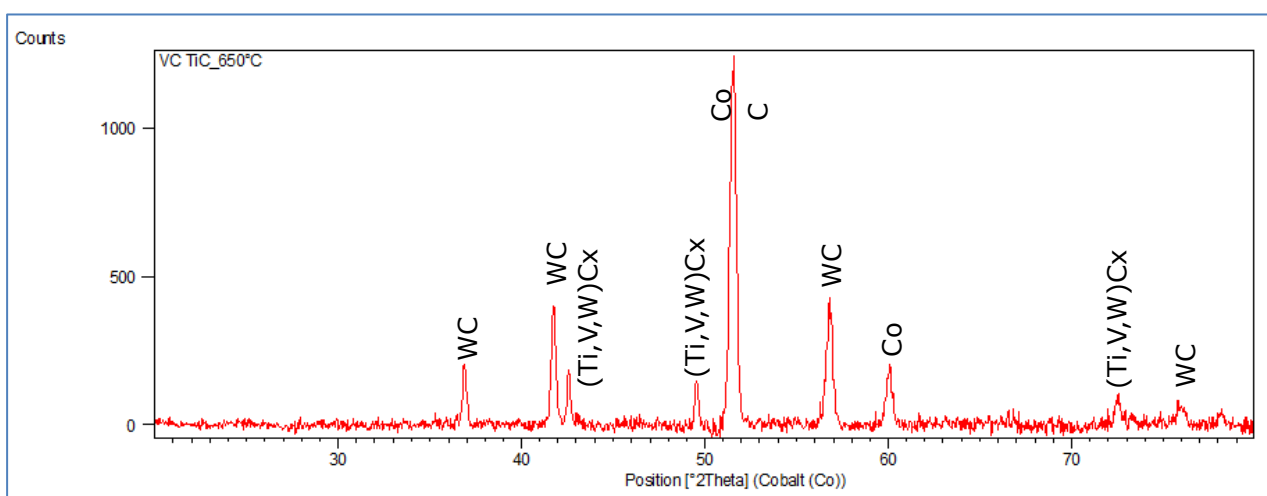
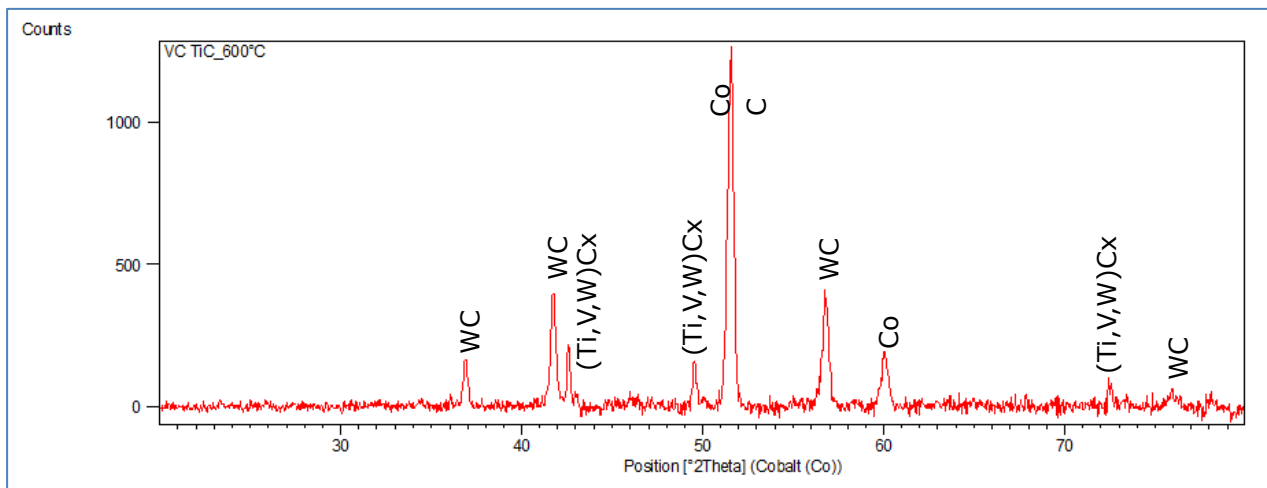


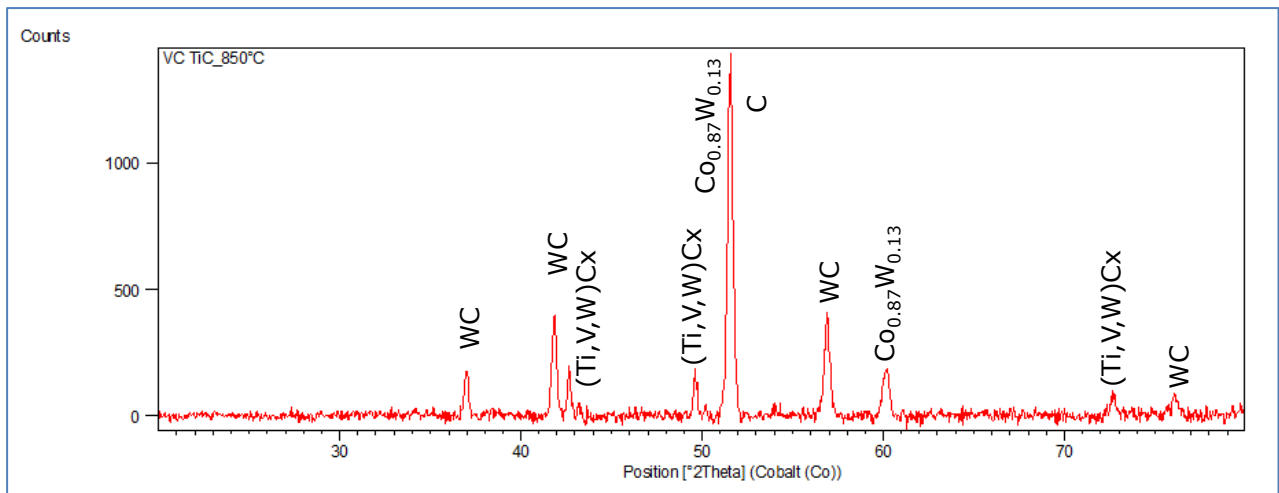
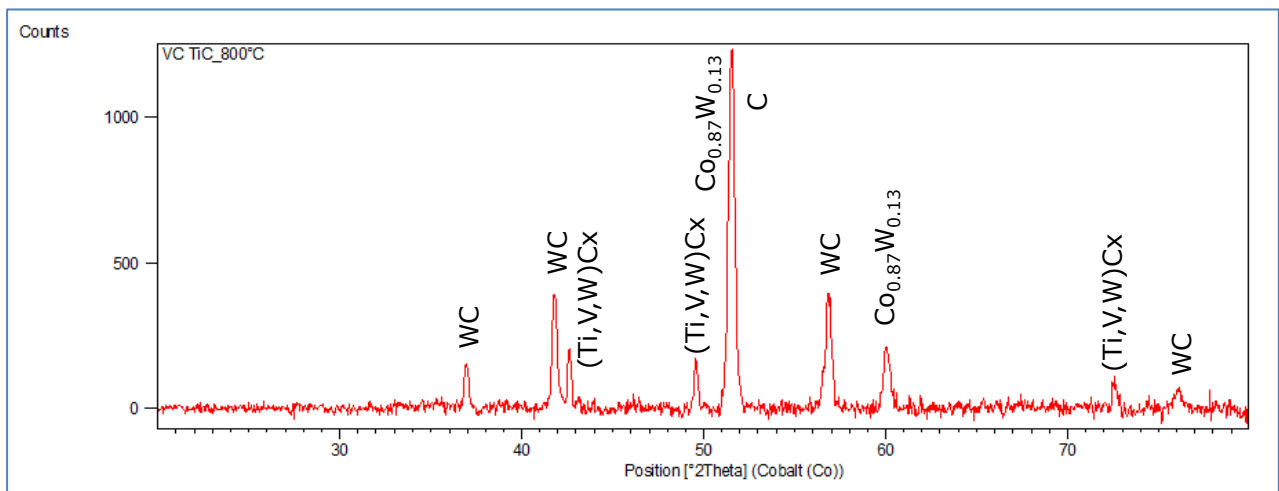
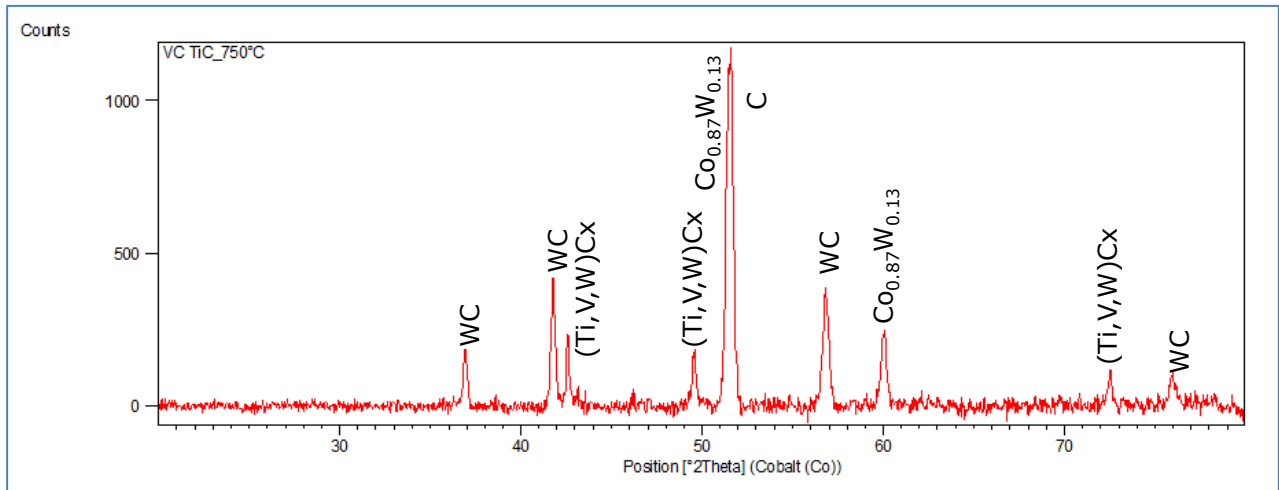


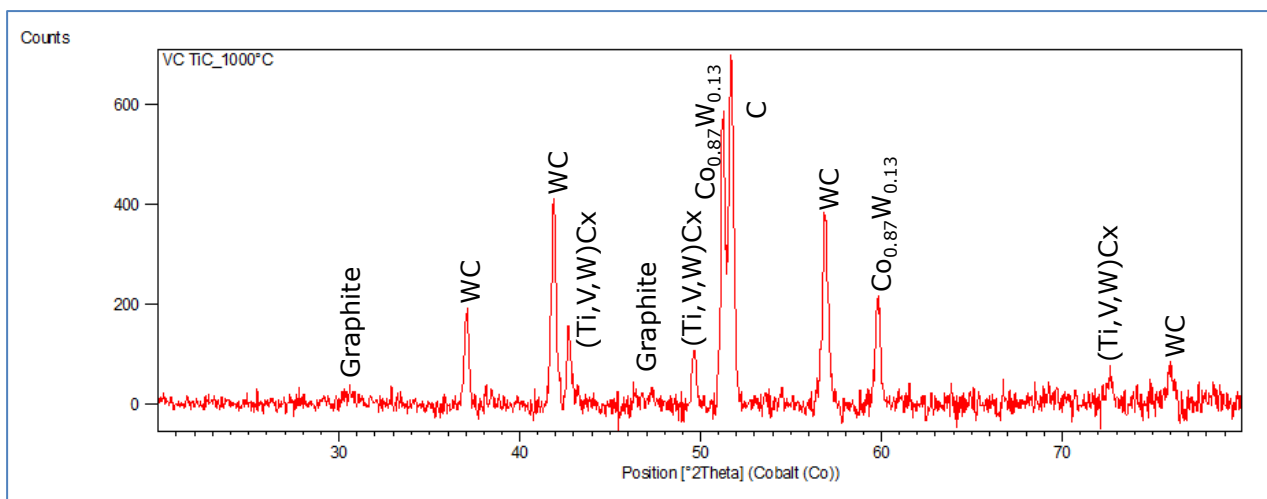
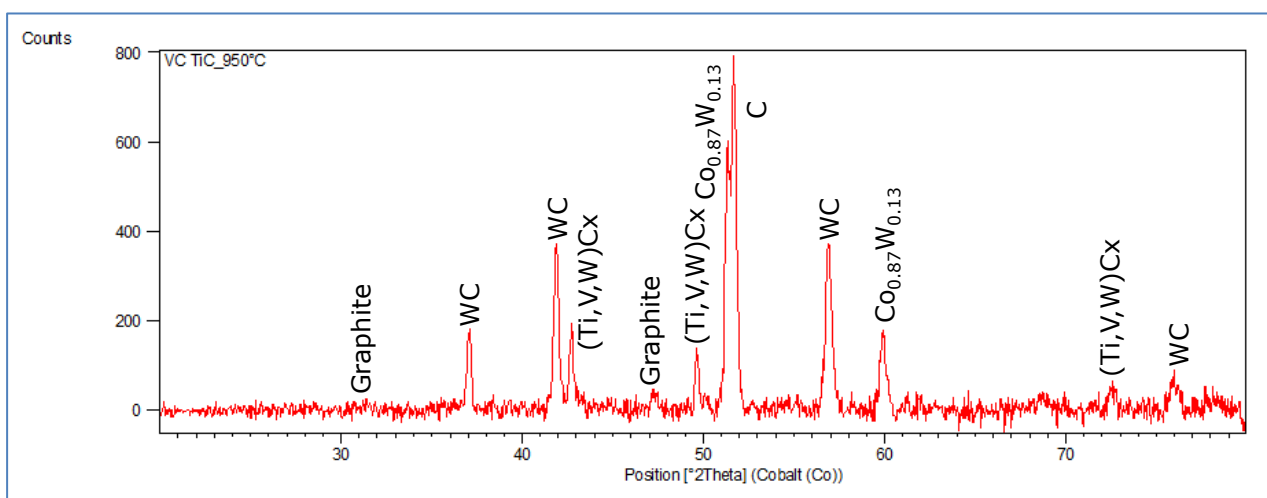
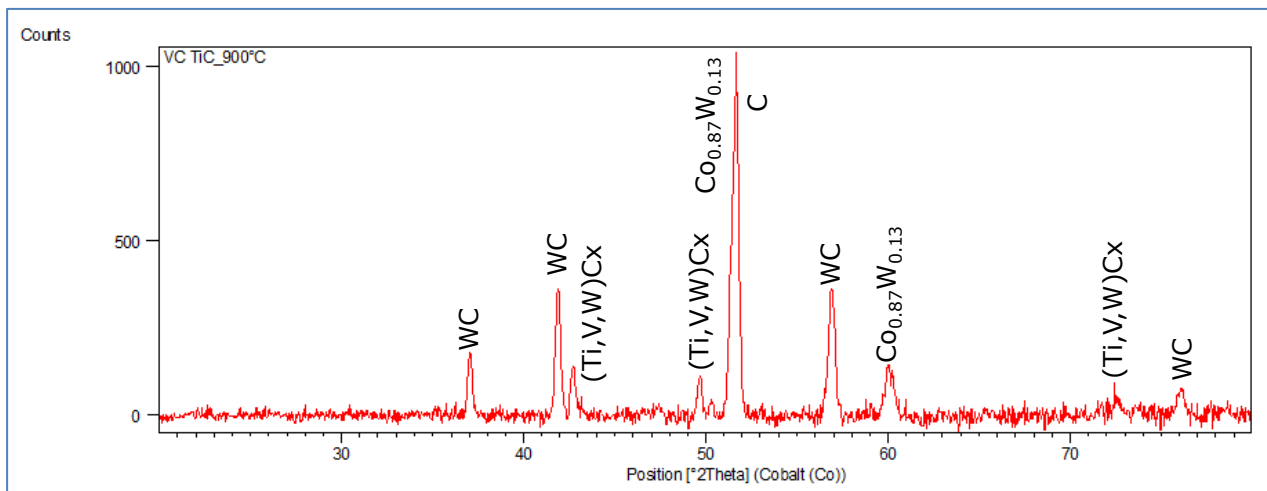
## APPENDIX SIX: XRD PATTERNS FOR THE VC-TiC ENHANCED PCD DURING HEAT TREATMENT



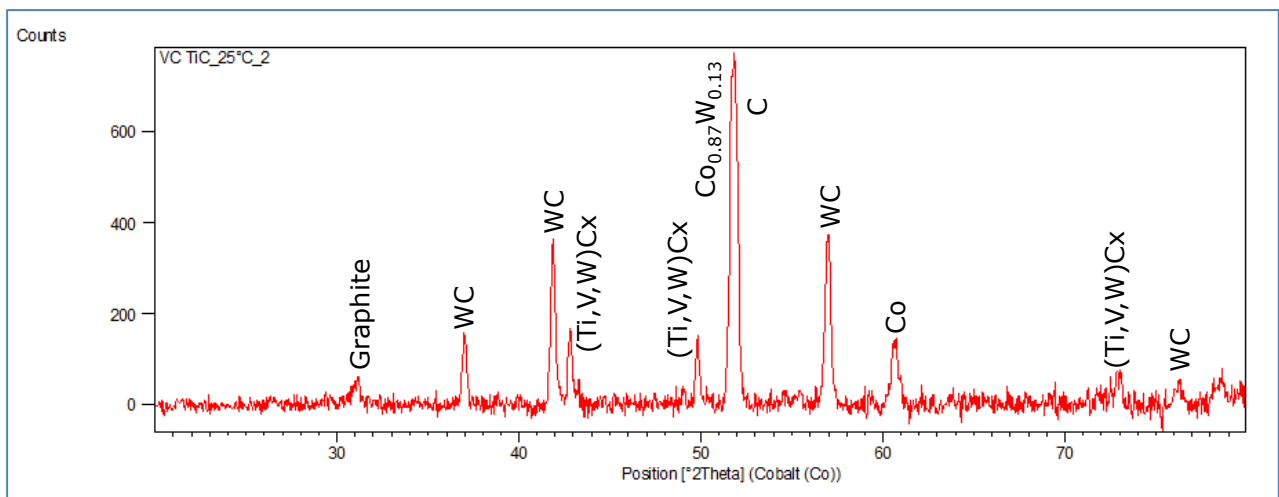
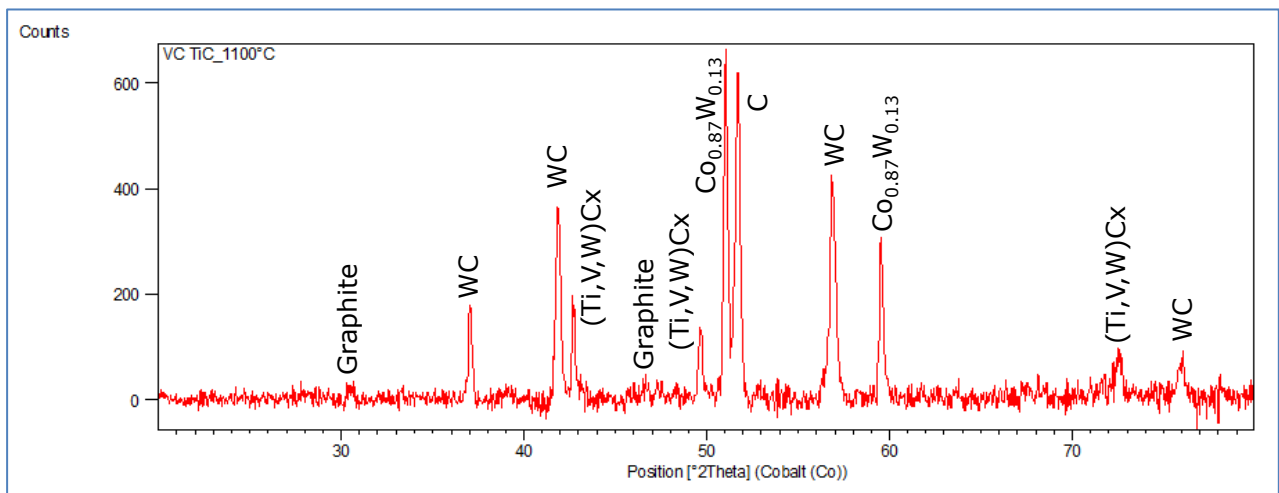
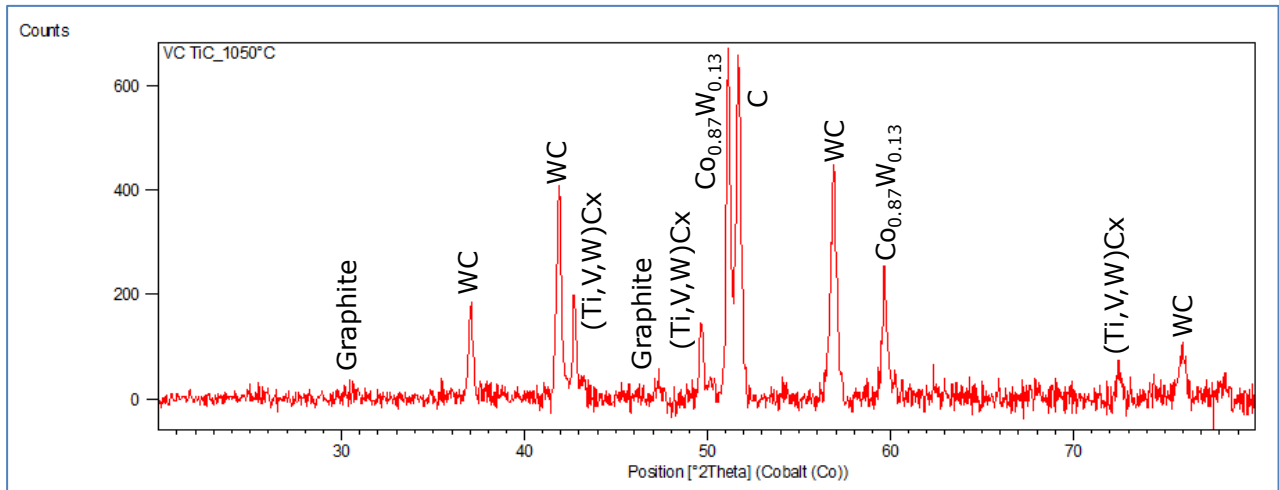












APPENDIX SEVEN



US 20100285335A1

(19) **United States**

(12) **Patent Application Publication**  
**Sithebe et al.**

(10) **Pub. No.:** US 2010/0285335 A1

(43) **Pub. Date:** Nov. 11, 2010

(54) **POLYCRYSTALLINE DIAMOND (PCD) MATERIALS**

(30) **Foreign Application Priority Data**

Feb. 5, 2007 (ZA) ..... 200701063

(76) **Inventors:** **Humphrey Samkelo Lungisani**  
**Sithebe, Springs (ZA); Kaveshini**  
**Naidoo, Elma Park (ZA)**

**Publication Classification**

**Correspondence Address:**  
**FROMMER LAWRENCE & HAUG**  
**745 FIFTH AVENUE- 10TH FL.**  
**NEW YORK, NY 10151 (US)**

(51) **Int. CL**  
**C04B 35/56** (2006.01)  
**B32B 18/00** (2006.01)

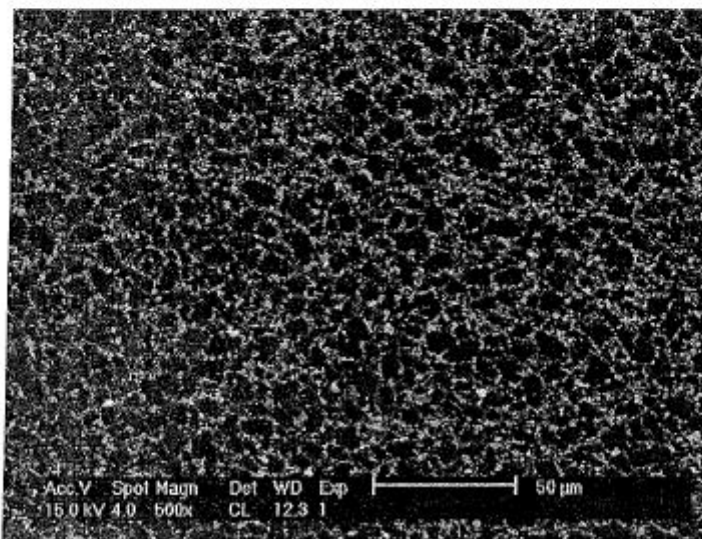
(52) **U.S. CL** ..... **428/698; 501/87**

(21) **Appl. No.:** **12/523,644**  
(22) **PCT Filed:** **Feb. 5, 2008**  
(86) **PCT No.:** **PCT/IB08/50407**

(57) **ABSTRACT**

The invention is for a polycrystalline diamond material comprising a first phase of bonded diamond particles and a second phase interspersed through the first phase. The second phase contains vanadium in the form of the metal or vanadium carbide or vanadium tungsten carbide or two or more of these forms and may be present in the polycrystalline diamond material in the range 1 to 8 percent by mass of the material.

§ 371 (c)(1),  
(2), (4) Date: **Jul. 27, 2010**





US 20150151410A1

(19) **United States**

(12) **Patent Application Publication**  
**Naidoo et al.**

(30) **Pub. No.: US 2015/0151410 A1**  
(43) **Pub. Date: Jun. 4, 2015**

(54) **POLYCRYSTALLINE DIAMOND**

**Publication Classification**

(71) Applicants: **Kaveshini Naidoo, Gauteng (ZA);  
Humphrey Samkelo Lungisani  
Sitsebe, Gauteng (ZA)**

(51) **Int. Cl.**  
*B24D 99/00* (2006.01)  
*B24D 18/00* (2006.01)  
*E21B 10/567* (2006.01)

(72) Inventors: **Kaveshini Naidoo, Gauteng (ZA);  
Humphrey Samkelo Lungisani  
Sitsebe, Gauteng (ZA)**

(52) **U.S. Cl.**  
CPC ..... *B24D 99/005* (2013.01); *E21B 10/567*  
(2013.01); *B24D 18/0009* (2013.01)

(21) Appl. No.: **14/616,638**

(22) Filed: **Feb. 6, 2015**

(57) **ABSTRACT**

A PCD body comprises a skeletal mass of inter-bonded diamond grains defining interstices between them. At least some of the interstices contain a filler material comprising a metal catalyst material for diamond, the filler material containing Ti, W and an additional element M selected from the group consisting of V, Y, Nb, Hf, Mo, Ta, Zr, Cr, and the rare-earth elements. The content of Ti within the filler material is at least 0.1 weight % and at most 20 weight %. The content of M within the filler material is at least 0.1 weight % and at most 20 weight %, and the content of W within the filler material is at least 5 weight % and at most 50 weight % of the filler material.

**Related U.S. Application Data**

(63) Continuation of application No. 13/107,590, filed on May 13, 2011, now abandoned.

